C-GLYCOSYLFLAVONES AGAINST ALZHEIMER'S DISEASE: FROM DISCOVERY TO MECHANISM OF ACTION

A DISSERTATION SUBMITTED TO THE GRADUATE DIVISION OF
THE UNIVERSITY OF HAWAIʻI AT MĀNOA IN PARTIAL
FULFILLMENT OF THE
REQUIREMENTS FOR THE DEGREE OF

DOCTOR OF PHILOSOPHY

IN

MOLECULAR BIOSCIENCES AND BIOENGINEERING

MAY 2018

By

Zhibin Liang

Dissertation Committee:

Qing X. Li, Chairperson
Jon-Paul Bingham
Robert A. Nichols
Jinzeng Yang
Philip G. Williams

Keywords: *C*-Glycosylflavone, Drug Discovery, Molecular Mechanism, Pharmacology, Neuroscience, Alzheimer's Disease

ACKNOWLEDGMENT

I would like to thank many people who have given assistance, support, and encouragement during my dissertation research. I would like to express the deep gratitude to my faculty advisor, Dr. Qing X. Li (UH MBBE), for his endless support, enlightened mentorship, and academic training during my entire Ph.D. journey. I would also like to thank the other committee members, Dr. Philip Williams (UH Chemistry), Dr. Robert Nichols (UH CMB), Dr. Jon-Paul Bingham (UH MBBE), and Dr. Jinzeng Yang (UH HNFAS), for their interest, advice, and critique on my research projects. Thanks also go to the former and present members of the Li Lab for their helpful discussions that inspire advances of my research. Special thanks to the UH Proteomics Core fellows, Dr. Margaret Baker and Ms. Sofia Doello, for the active collaboration on the proteomics project, and Ms. Gladys Leong for the research support. I would like to acknowledge my collaborators Dr. Yong-Soo Kim (UH HNFAS) and Dr. Ching Yuan Hu (UH HNFAS) for the assistance of mammalian cell culture, Dr. James Brewbaker (UH TPSS) for kindly providing corn silk samples, Dr. Wei Wen Su (UH MBBE) for the assistance of bioluminescence measurement, and. Mr. Wesley Yoshida (UH Chemistry) for acquiring the NMR data.

Lastly and most importantly, I would like to dedicate this dissertation to my wife, Dr. Bei Zhang, who is always my partner, soulmate, supporter, and colleague during the joyful and frustrating time of my life. I would also like to dedicate to my parents who are always there being the source of the keenest love and strength in my life.

ABSTRACT

Alzheimer's disease (AD) is the most common neurodegenerative disease worldwide and is the sixth leading cause of death in the U.S. Current AD medications only temporarily relieve symptoms, and none can prevent, cure, or even slow AD. There is an urgent demand for effective drugs for AD prevention and treatment. *C*-Glycosylflavones, a class of phytochemicals, display diverse benefits to human health and recently noted for their neuroprotective effects. They are a novel and valuable source of anti-AD agents. Identification and validation of therapeutic targets of *C*-glycosylflavones for neuroprotection against AD are crucial to convey the mechanistic understanding of these agents in pharmaceutical applications. The principal objectives of the dissertation research aim to unravel the mechanistic basis of natural and synthetic *C*-glycosylflavones for potential AD therapies. Different research strategies such as target/phenotype-based screening and chemical proteomics approaches were adopted and integrated into an innovative drug discovery paradigm for target identification and validation of *C*-glycosylflavones.

Our efforts to search for natural anti-AD agents led to the discovery that a *C*-glycosylflavone called isoorientin from corn silks is neuroprotective. Isoorientin selectively inhibits glycogen synthase kinase-3β (GSK-3β), an enzyme most relevant to AD tauopathy. Molecular docking and enzyme kinetics indicated that isoorientin selectively inhibits GSK-3β via a substrate competition rather than the common ATP competition. Cellular studies demonstrated that isoorientin effectively attenuates tau hyperphosphorylation and amyloid neurotoxicity in human SH-SY5Y cells. By applying computer-aided drug design approach, novel analogues of *C*-glycosylflavones as GSK-3β inhibitors were synthesized. The new analogues show significant improvements of potency and passive membrane permeability compared to isoorientin. In addition, they have distinct kinase

selectivity to GSK-3β and effectively block GSK-3β–mediated tau and amyloid neurotoxicities. Finally, by harnessing the chemical proteomics and bioinformatics technologies, we revealed that *C*-glycosylflavones are novel multitarget ligands for potential AD prevention.

Collectively, the present dissertation elaborates a hypothesis-driven research on AD drug discovery. The new findings and knowledge gained through this study will broaden the understanding of mechanism of actions of *C*-glycosylflavones for potential AD therapies.

TABLE OF CONTENTS

LIST OF TABLES

LIST OF FIGURES

LIST OF ABBREVIATIONS

Aβ42	β-amyloid fragment peptide 1-42
AD	Alzheimer's disease
ADMET	absorption, distribution, metabolism, excretion and toxicity
ADP	adenosine diphosphate
AKT1	v-akt murine thymoma viral oncogene homolog 1
AM1	austin model 1
AMPK	AMP-activated protein kinase with subunits
amu	atomic mass units
ANP	adenylyl imidodiphosphate
APOE	apolipoprotein E
APP	amyloid precursor protein
ATP	adenosine triphosphate
BACE1	beta-site APP cleaving enzyme; β-secretase
BBB	blood-brain barrier
BCIP/NBT	5-bromo-4-chloro-3-indolyl-phosphate/nitro blue tetrazolium
BLAST	basic local alignment search tool
Bn	benzyl
br	broad
BSA	bovine serum albumin
c	concentration in g/100 mL
ºC	degrees Celsius
C_8	octyl
C_{18}	octadecyl
calcd	calculated
CALM1	calmodulin-1
CAMK	Ca^{2+}/calmodulin-dependent protein kinase
CDK	cyclin-dependent kinase
CDK5/p25	cyclin-dependent kinase 5 with subunit p25
CDK5/p35	cyclin-dependent kinase 5 with subunit p35

CGF	*C*-glycosylflavone
ChIP	chromatin immunoprecipitation
CID	collision induced dissociation
CK	casein kinase
CLK1	dual specificity protein kinase 1
CLogP	calculated logarithm of partition coefficient
cmpd	compound
CNS	central nervous system
CRISPR-Cas9	clustered regularly interspaced short palindromic repeats and CRISPR-associated protein 9
CS	corn silks
C-terminus	carboxyl terminus
1D	one-dimensional
2D	two-dimensional
3D	three-dimensional
d	doublet
D	configurational descriptor (Fisher system)
DAD	diode array detector
DAPK1	death-associated protein kinase 1
DCM	dichloromethane
dd	doublet of doublets
ddd	doublet of doublet of doublets
δ	chemical shift (in ppm)
DIPEA	*N,N*-diisopropylethylamine
DMF	*N*,*N*-dimethylformamide
DMSO	dimethyl sulfoxide
DNA	deoxyribonucleic acid
DNA-PK	DNA-dependent protein kinase
dq	doublet of quartets
dt	doublet of triplets
DTT	dithiothreitol
E	entegen (descriptor in Cahn-Ingold-Prelog system)
EC_{50}	half maximum effective concentration

EDCI	1-(dimethylaminopropyl)-3-ethylcarbodiiminde
EDTA	ethylenediaminetetraacetic acid
ELISA	enzyme-linked immunosorbent assay
ERK	extracellular signal regulated kinase
ESI	electrospray ionization
Et	ethyl
ETD	electron-transfer dissociation
EtOAc	ethyl acetate
expt	experimental
FBS	fetal bovine serum
FDA	Food and Drug Administration
FDR	false discovery rate
FTD	frontotemporal dementia
GO	gene ontology
GSK-3	glycogen synthase kinase-3
HCTU	2-(6-chloro-1-H-benzotriazole-1-yl)-1,1,3,3-tetramethylaminium hexafluorophosphate
HEPES	4-(2-hydroxyethyl)piperazine-1-ethanesulfonic acid
HPLC	high performance liquid chromatography
HR	high-resolution
HTS	high-throughput screening
Hz	hertz
IAA	iodoacetamide
IC_{50}	half maximum inhibitory concentration
ISO	isoorientin
iTRAQ	isobaric tags for relative and absolute quantitation
IUPAC	International Union of Pure and Applied Chemistry
^{n}J	coupling constant via n bonds
JNK	c-Jun N-terminal kinase
KEGG	Kyoto Encyclopedia of Genes and Genomes
K_i	inhibition constant
K_m	Michaelis–Menten constant
L	configuratonal descriptor (Fisher system)

LC	liquid chromatography
LG3BP	galectin-3-binding protein
QTOF-MS	quadrupole time-of-flight-mass spectrometry
LiPE	ligand-lipophilic efficiency
m	multiplet
$[M]^+$	molecular ion
$[M+H]^+/[M+Na]^+/[M+K]^+$	pseudomolecular ions
MALDI	matrix-assisted laser desorption ionization
MARK	microtubule affinity-regulating kinase
MAPK	mitogen-activated protein kinase
MAPT	microtubule-associated protein tau
Me	methyl
MeCN	acetonitrile
MeOH	methanol
MEP	methylerythritol phosphate
MF	molecular formula
MHz	megahertz
MM2	molecular mechanics model 2 method
MMFF94	Merck molecular force field 94 method
MMTS	methylmethanethiosulfate
MS	mass spectrometry
MS/MS; MS^n	tandem mass spectrometry
MW	molecular weight
MWCO	molecular weight cut-off
m/z	mass to charge ratio
NCBI	National Center for Biotechnology Information
NF-κB	nuclear factor kappa-light-chain-enhancer of activated B cells
NFT	neurofibrillary tangle
NMR	nuclear magnetic resonance
N-terminus	amino terminus
p38	p38 mitogen-activated protein kinase
p70S6Kβ	p70 ribosomal protein S6 kinase beta

PAMPA	parallel artificial membrane permeability assay
PBS	phosphate buffered saline
P_e	effective permeability coefficients
PDA	photodiode array
PDB	protein data bank
PDK1	phosphoinositide-dependent kinase 1
pH	activity coefficient of H^+ in aqueous solution
Ph	phenyl
PHF	paired helical filament
PhMe	toluene
PI3K	phosphoinositide 3-kinase
pK_a	logarithmic acidity constant
PKA	protein kinase A
PKC	protein kinase C
PMSF	phenylmethanesulfonyl fluoride
PPI	protein-protein interaction
ppm	part per million
PRKG1	cGMP-dependent protein kinase 1
PSEN	presenilin
q	quartet
qd	quartet of doublets
qPCR	quantitative polymerase chain reaction
QqQ	triple quadrupole
R	placeholder for side-chains
R	rectus (descriptor in Cahn-Ingold-Prelog system)
RA1L2	heterogeneous nuclear ribonucleoprotein A1-like 2
RMSD	root-mean-square deviation
RNA-seq	RNA sequencing
ROCK	Rho-associated, coiled-coil containing protein kinase
ROS	reactive oxygen species
RP	reversed-phase
RSK2	ribosomal protein S6 kinase 2

rt	room temperature
s	singlet
S	sinister (descriptor in Cahn-Ingold-Prelog system)
SAR	structure-activity relationship
SD	standard deviation
SDS-PAGE	sodium dodecyl sulfate-polyacrylamide gel electrophoresis
SEM	standard error of the mean
SGLT	sodium glucose co-transporter
SILAC	stable isotope labeling with amino acids in cell culture
STK33	serine/threonine-protein kinase 33
t	triplet
TCEP	tris(2-carboxyethyl)phosphine
TCM	traditional Chinese medicine
TDZD	thiadiazolidinone
TEAB	triethylammonium bicarbonate
$[TEMPO]^+[BF4]^-$	4-acetamido-2,2,6,6-tetramethyl-1-oxopiperidinium tetrafluoroborate
$TMSCHN_2$	trimethylsilyldiazomethane
TOF	time-of-flight
TPK	tau-protein kinase
t_R	retention time
UHPLC	ultra-high performance liquid chromatography
UniProt	universal protein resource
UV	ultraviolet
vis	visible
V_{max}	maximum reaction rate
VRK2	vaccinia related kinase 2
Z	zusammen (descriptor in Cahn-Ingold-Prelog system)

LIST OF ACADEMIC ACCOMPLISHMENTS

Peer-Reviewed Publications:

1. **Liang, Z.**; Zhang, B.; Su, W.W.; Williams, P.G.; Li, Q.X. (2016) *C*-Glycosylflavones alleviate tau phosphorylation and amyloid neurotoxicity through GSK3β inhibition. *ACS Chemical Neuroscience* *7*, 912–923.
2. Zhang, B.; Rapolu, M.; Kumar, S.; Gupta, M.; **Liang, Z.**; Han, Z.; Williams, P.G.; Su, W.W. (2017) Coordinated protein co-expression in plants by harnessing the synergy between an intein and a viral 2A peptide. *Plant Biotechnology Journal* *15*, 718–728.
3. **Liang, Z.**; Li, Q.X. (2018) π-Cation interactions in molecular recognition: Perspectives on pharmaceuticals and pesticides. *Journal of Agricultural and Food Chemistry* *66*, 3315–3323.
4. Doello, S.; **Liang, Z.**; Cho, I.K.; Kim, J.B.; Li, Q.X. (2018) Cytotoxic effects of 24-methylenecycloartanyl ferulate on A549 non-small cell lung cancer cells through MYBBP1A up-regulation and AKT and Aurora B kinase inhibition. *Journal of Agricultural and Food Chemistry* *66*, 3726–3733.
5. **Liang, Z.**; Li, Q.X. (2018) Discovery of selective, substrate-competitive, and passive membrane permeable glycogen synthase kinase-3β inhibitors: Synthesis, biological evaluation, and molecular modeling of new *C*-glycosylflavones. *ACS Chemical Neuroscience*, DOI: 10.1021/acschemneuro.8b00010.

Professional Conference Presentations:

1. **Liang, Z.**; Li, Q.X. "Neuroprotective compounds from corn silks alleviate amyloid cytotoxicity in SH-SY5Y cells." Poster presentation at the 7th International Chemical Congress of Pacific Basin Societies (Pacifichem 2015) on Advances in Functional Foods and Flavor Chemistry Research, Honolulu, HI, USA, December 15–20, 2015.
2. **Liang, Z.**; Li, Q.X. "A novel mechanism of action of a corn silk flavone for Alzheimer's drug discovery." Oral presentation at the 28th Annual CTAHR Student Research Symposium at UH-Manoa, Honolulu, HI, USA, April 8–9, 2016.
3. **Liang, Z.**; Zhang, B.; Su, W.W.; Williams, P.G.; Li, Q.X. "Glycosylflavone as glycogen synthase kinase-3β inhibitor alleviates tau hyperphosphorylation and amyloid neurotoxicity." Poster presentation at the 2016 Hawaii Neuroscience Symposium, Honolulu, HI, USA, August 20, 2016.

4. **Liang, Z.**; Li, Q.X. "Glycosylflavone as glycogen synthase kinase-3β inhibitor alleviates tau hyperphosphorylation and amyloid neurotoxicity." Poster presentation at the 252nd American Chemical Society National Meeting on Current Topics in Biochemistry, Philadelphia, PA, USA, August 21–25, 2016.
5. **Liang, Z.**; Li, Q.X. "Discovery of novel selective GSK3beta inhibitors for Alzheimer's disease treatment." Poster presentation at the 29th Annual CTAHR Student Research Symposium at UH-Manoa, Honolulu, HI, USA, April 7–8, 2017.
6. **Liang, Z.**; Li, Q.X. "Computer-aided drug discovery of selective GSK3β inhibitors inspired by natural products for Alzheimer's disease." Oral presentation at the 58th Annual Meeting of the American Society of Pharmacognosy, Portland, OR, USA, July 29–August 2, 2017.
7. **Liang, Z.**; Li, Q.X. "Selective GSK3β inhibitors reduce tau and amyloid burdens: promising drug candidates help fight Alzheimer's." Oral and poster presentations at the 18th International Conference on Alzheimer's Drug Discovery, Jersey City, NJ, USA, September 11–12, 2017.
8. **Liang, Z.**; Morisseau, C.; Hwang, S.H.; Hammock, B.D.; Li, Q.X. "A dual-inhibitor of soluble epoxide hydrolase and p38 kinase alleviating tau hyperphosphorylation and amyloid neurotoxicity for potential treatment of neuroinflammation in Alzheimer's disease." Poster presentation at the 2018 Experimental Biology Conference on Drug Discovery and Development, San Diego, CA, USA, April 21–25, 2018.

Awards and Honors:

1. (2016) American Chemical Society Division of Biological Chemistry Travel Award
2. (2016) CTAHR Best PhD Oral Presentation Award, University of Hawaii at Manoa
3. (2017) CTAHR Best PhD Poster Presentation Award, University of Hawaii at Manoa
4. (2017) CTAHR Three-Minute Elevator Pitch Best PhD Presentation Award and People's Choice Award, University of Hawaii at Manoa
5. (2017) American Society of Pharmacognosy the Lynn Brady Travel Award
6. (2017) Alzheimer's Drug Discovery Foundation Young Investigator Scholarship
7. (2018) University of Hawaii at Manoa OVCR PhD Student Award for Excellence in Research

CHAPTER 1

1. INTRODUCTION

1.1. Neurological Pathologies of Alzheimer's Disease

Alzheimer's disease (AD) is a progressive and irreversible neurodegenerative disease worldwide. The AD syndrome is attributed to the gradual loss of neurons, particularly in the hippocampus and neocortex where brain regions involved in memory, cognition, language, emotion, and motor skills.[1] According to the latest statistics, AD is the sixth leading cause of death in the U.S. and one-third of seniors dies with AD. The direct cost of AD patients in the U.S. was approximately $259 billion in 2017, and it is estimated that such costs will rise to $1.1 trillion by 2050.[2] In Hawaii, AD affects 11% of people over the age of 65. Caring for AD patients places a huge burden on Hawaii families. While millions of people suffer from this fatal disease, the four drugs approved by the United States Food and Drug Administration (FDA) marginally improve cognition of AD patients. The consensus is that these medications only temporarily relieve symptoms, but none can prevent, halt, cure, or even slow AD.[3] There is a critical and urgent demand for effective drugs for AD prevention and treatment.

Although the exact etiology remains poorly understood, current advances in AD research implicate that a complexity of genetic, aging, and environmental factors appears to be causative. Many gene mutations associated with amyloid precursor protein (*APP*) are known to cause the early-onset, familial AD that follows a Mendelian inheritance pattern, but it only accounts for less than 5% of incident cases.[4-5] Mutations in *MAPT* gene encoding tau protein also give rise to certain familial tauopathies such as frontotemporal dementia (FTD) closely relevant to AD.[6-7] In contrast, over 95% of AD is characterized as late-onset or sporadic that follows non-Mendelian inheritance.

For example, individuals caring copies of the ε4 allele of apolipoprotein E (*APOE4*) significantly increase risk for sporadic AD.[8-9] Besides genetics, environmental stress, traumatic brain injury, and aging-associated incidence are also potential risk factors for AD.[10-11]

Mounting evidence indicates that AD is a form of neurodegeneration associated with abnormal protein production and aggregation, which is categorized as a proteopathy. In AD brains, the prevalent presence of senile plaques and neurofibrillary tangles (NFTs) accompanied by synaptic dysfunction and neuroinflammation are the molecular characteristics.[1, 10] Senile plaques are extracellular deposits of β-amyloid (Aβ) peptide, which are a pathological hallmark of AD. In familial AD, mutations in *APP* or *presenilin* (*PSEN1* and *PSEN2*) genes significantly promote APP processing by β/γ-secretases, leading to enhanced production of toxic Aβ peptides.[4] Accumulation of Aβ forms toxic aggregates impairing neuronal functions. Aβ aggregates interfere with the neurotransmitter receptors, disrupt the synaptic transmission, and eventually trigger neurotoxic events such as formation of reactive oxygen species (ROS), Ca^{2+} dysregulation, mitochondrial damage, neuroinflammation, and neuronal loss. These genetic and molecular observations are thus the basis of the "amyloid cascade hypothesis of AD".[5]

On the other hand, NFTs composing intracellular hyperphosphorylated tau proteins are another major hallmark in AD pathology. Tau protein, an important microtubule-associated protein mainly expressed in neurons, stabilizes the integrity and functionality of microtubules in the neuronal cytoskeleton and maintains healthy axonal transport.[12] In adult human brains, there are six isoforms of tau generated by alternative mRNA splicing from a single *MAPT* gene on chromosome 17.[13] These tau variants contain 0–2 inserts in the N-terminal regions and have three (3R) or four repeats (4R) in the C-terminal regions for microtubule binding.[14] The interaction of tau with microtubule is primarily modulated by phosphorylation. Tau gene (*MAPT*) mutations and

aberrant phosphorylation of tau proteins have been found in many neurodegenerative diseases such as frontotemporal dementia and parkinsonism linked to chromosome-17 (FTDP-17), progressive supranuclear palsy (PSP), corticobasal degeneration (CBD), and globular glial tauopathy, showing that tauopathy plays a causative role in neurodegeneration and dementia.[15-16] AD is considered as a secondary tauopathy that requires involvement of amyloidosis for the disease causation. In AD, all six tau isoforms (3R and 4R) are present in the disease filaments.[17] Abnormal phosphorylation of tau proteins disrupts their binding to microtubules in neurons, leading to destabilization of microtubules and mislocalization of the abnormal tau to the soma and dendrites.[18] Aggregation of hyperphosphorylated tau proteins results in the formation of neurotoxic paired helical filaments as well as NFTs. This aberrant signaling cascade is thought to contribute to neuronal death and declined cognition, giving rise to the "tau hypothesis of AD".[7, 19]

Both Aβ plagues and tau tangles are characteristic for their neurotoxicity, however, their mechanistic causality pertaining to which critical toxic species accounts for the clinical AD symptoms is still unclear.[20-21] Nevertheless, recent evidence suggests that Aβ, particularly the soluble Aβ oligomers, is plausibly the pathogenic initiator of AD, while tau aggregation and spreading in the brain cortices correlate more closely to neuronal loss and cognitive decline in AD progression.[22-23] Therapeutic strategies focusing on the Aβ and tau interventions are thought to be promising to impede the pathogenesis and progression of AD rather than ameliorate symptoms, which are attractive for potential AD treatments.[3, 11, 24-26] However, the continued failures of anti-Aβ approaches in AD clinical trials[27-28] drive researchers to embrace more diverse and innovative drug pipelines for AD.[25-26]

1.2. Therapeutic Potentials of C-Glycosylflavones for Alzheimer's Disease

Flavones, a class of polyphenolic compounds widely occurring in plants, are major constituents in the human diet including crops, fruits, vegetables, as well as beverages of plant origin such as juice, tea, wine, and cocoa. They are important phytochemicals displaying diverse benefits to human health.[29] Current studies in animals and humans have demonstrated that many herbal and dietary supplements with flavone-rich extracts can inhibit neurotoxicity, suppress neuroinflammation, and promote memory and cognition.[30-32] In particular, certain types of flavones exert neuroprotective effects via targeting key AD-relevant proteins such as cholinesterases, GSK-3 and CDK5 kinases, and secretases, which are a novel and valuable source of anti-AD agents.[33-35] Conventionally, the neuroprotective action of flavones is thought to be mediated by their anti-oxidative or free radical scavenging activities.[36-37] These classical properties, however, could not fully explain the observed pharmacology of flavones on diverse molecular events in AD pathways. In fact, it has become evident that flavones more likely exert their neuroprotective actions via cell signaling that regulates neuronal apoptosis, survival, differentiation, and proliferation.[33, 35] Flavones can interact with key intracellular receptors or enzymes (e.g., proteases, kinases, and phosphatases) that are involved in signaling cascades of AD responsible for either gene expression or biochemical response.[33, 35]

Flavones in flora mostly exist in forms of *O*-glycosides and *C*-glycosides. While *O*-glycosylflavones present as majority, *C*-glycosylflavones are found to be more stable than the *O*-glycosyl counterpart, and appear to have better therapeutic properties on human health.[38] Many *C*-glycosylflavones of natural and synthetic origins are valuable for disease interventions.[29, 38] For

instance, flavopiridol, a synthetic flavonoid inspired by natural *C*-glycosylflavones, has become an advanced cyclin-dependent kinase (CDK) inhibitor in Phase II clinical trials for cancers.[39-40] With respect to the chemical structure of *C*-glycosylflavones, the presence of a carbon-linked glycosidic bond makes these compounds more resistant to metabolic hydrolysis and degradation. It has been reported that some *C*-glycosyl flavonoids bind to sodium glucose co-transporters (SGLT1/2), which enables their distribution across intestinal barrier through transepithelial transport,[41] and across blood brain barrier (BBB) via secondary active transport.[42-43] Pharmacokinetic and pharmacodynamic studies have shown that *C*-glycosylflavones normally retain higher concentrations and a longer mean residence time in the blood plasma after oral and intravenous administration.[38] The unique features of *C*-glycosylflavones, in conjunction with neuroprotective activities, shed light on their therapeutic potential for the intervention of neurodegenerative diseases such as AD.[32] However, systematic evaluations of *C*-glycosylflavones pertaining to their neuroprotective mechanisms against AD are scarcely reported. Identification and validation of therapeutic targets of *C*-glycosylflavones involving AD pathologies are crucial to convey a better understanding of the molecular mechanisms on the basis of flavone-protein interactions, as well as to assess their therapeutic values in nutraceutical and pharmaceutical applications.

1.3. Current Approaches for Target Identification and Validation in Drug Discovery

Drug discovery aims to search for bioactive molecules that selectively and specifically modulate the functions of target proteins with precise mechanism of actions. Target identification and validation studies play a pivotal role in drug discovery. Traditionally, phenotype-based

screenings are extensively used where compound candidates are directly exposed into the biologically relevant contexts, usually in cells or animals, to observe the perturbative effects on physiological or disease models of interest.[44-45] This approach thus provides the opportunity of discovering bioactive and functional molecules without knowing the exact protein targets in advance. However, it requires follow-up studies to identify and validate single or multiple therapeutic targets involving in biological networks responsible for the observed phenotypes, which in many cases is complicated, laborious, and time-consuming. Given the revolutionary advances in molecular biology and bioassay technology, it is now possible to test compounds for bioactivity on purified proteins in various biochemical assays, particularly for high-throughput screening purposes.[46-48] This target-based approach offers a rapid means to directly link the bioactive molecules with preselected protein targets relevant to the disease of interest. Subsequent functional investigations aim to validate whether the biochemical interactions between the compound and the protein targets could result in expected disease-altered phenotypes in cellular or animal models. Although this approach appears to be straightforward, the direct interaction with a single target may not reflect the actual phenotypic phenomena, as a bioactive molecule often modulates multiple targets simultaneously in a biological context. In general, combinations of phenotype- and target-based approaches are necessary to fully characterize and identify the precise therapeutic targets as well as to elucidate mechanism of actions of bioactive molecules.

Chemical proteomics is an emerging research discipline and a powerful tool for target identification and validation of bioactive molecules. This approach benefits from the tremendous development in the mass spectrometry (MS) technology over the past decade.[49-50] Bioactive molecules such as natural products are well-known for their ability to intervene cell signaling by multifunctional actions on different protein targets, resulting in either a pharmacological synergy

or an undesired toxic effect. Chemical proteomics thus provides a direct, unbiased, and systematic method for global profiling of protein targets of a bioactive molecule.[51-53] By incorporating bioinformatics, it offers comprehensive information with a proteome-wide coverage to elucidate the mechanism of actions of bioactive molecules, and to assess their impacts on biomolecular networks.[54] Compared to traditional methods, this approach overcomes the bottlenecks of phenotype- or target-based screenings, which potentially facilitate the process of drug discovery with time and cost efficiency.

Nowadays, many strategies of chemical proteomics have been applied in drug discovery programs of academia and industry. The most common chemical proteomics strategy harnesses the affinity chromatography coupled with mass spectrometry.[55-56] While this affinity-based chemical proteomics approach has shown many successes for target identification and validation of drugs and natural products, its limitations are noted. This method normally demands for a relatively high amount of proteins and bioactive molecules, and thus a sustainable source of materials is the requisite. Secondly, it is critical to immobilize bioactive molecules without altering bioactivity. Regarding the chemical challenges, the lack of suitable functional groups amenable for chemical modification is a major obstacle. Additionally, in order to minimize the interference on both bioactive molecules and protein targets, the choice of sites on the molecule for modification and of the linker moiety for immobilization are critical, which requires a thoughtful and rational design based on structure-activity relationship (SAR) studies.[57-60] In proteomics considerations, identification of binding proteins does not always correlate to the binding affinity of bioactive molecules (e.g., IC_{50} values), as MS analysis only gives protein ID and spectral counts with respect to their abundance in the protein mixture. Therefore, affinity parameters need to be determined in subsequent competition experiments. In recent years, new experimental design by

combining the affinity-based competition with quantitative proteomics, such as stable isotope labeling with amino acids in cell culture (SILAC)[61] and isobaric tags for relative and absolute quantitation (iTRAQ),[62] has given a practical solution addressing these technical issues. The affinity-based chemical proteomics have shown versatile applications in many research fields and has become a valuable tool implemented in drug discovery paradigm.

1.4. Research Hypotheses and Objectives

The principal objective of this research is to investigate natural and synthetic *C*-glycosylflavones for potential AD therapies. The aforementioned methodologies, e.g., target/phenotype-based screenings and affinity-based chemical proteomics approaches, were adopted and integrated into a rational paradigm for target identification and validation of *C*-glycosylflavones within neuroproteome. The new knowledge gained through this study will be a valuable contribution to the AD biomedical sciences. We expect the findings of this research will broaden the understanding of mechanism of actions of *C*-glycosylflavones for AD prevention and treatment, and eventually develop novel agents in aid of AD drug discovery.

Objective-1. Discovery and validation of natural *C*-glycosylflavones as potential anti-AD agents

Hypothesis*: C*-Glycosylflavones of corn silks are potential selective glycogen synthase kinase-3β (GSK-3β) inhibitors exerting neuroprotection against AD tauopathy.

Key points lead to the hypothesis for Objective 1:

Tau protein hyperphosphorylation is a major component of AD pathology. GSK-3β is a key kinase responsible for aberrant tau hyperphosphorylation in AD. Abnormal tau phosphorylation by GSK-3β undermines the healthy dynamics of tau protein with microtubules and plays a central

role in AD pathology. Selective inhibition of GSK-3β to attenuate tau hyperphosphorylation is a promising therapeutic strategy for AD. Corn silks (CS, *Zea mays* L.) of crop maize are a traditional medicine and recently noted for their neuroprotective benefits.[63] *C*-Glycosylflavones are characteristic in CS.[64] We hypothesize that *C*-glycosylflavones of CS are potential GSK-3β inhibitors exerting neuroprotection against AD tauopathy.

Objective-2. Computer-aided drug design of novel *C*-glycosylflavones as anti-AD agents targeting GSK-3β

Hypothesis*:* Potency and selectivity of *C*-glycosylflavones against GSK-3β can be improved via rational structural modifications.

Key points lead to the hypothesis for Objective 2:

Isoorientin, a 6-*C*-glycosylflavone from CS, alleviates tau hyperphosphorylation and amyloid neurotoxicity through GSK-3β inhibition. Isoorientin selectively inhibits GSK-3β via an ATP-noncompetitive but substrate-competitive mechanism.[65] In addition, it has been reported that isoorientin shows *in vitro* and *in vivo* effects reducing neuroinflammation, oxidative stress, and mitochondrial dysfunction.[66-69] Subchronic toxicity study of CS-derived flavones in mice and rats suggests that isoorientin is a reasonably safe and tolerable agent.[70-71] Isoorientin is a promising natural product drug lead for AD. It is moderately potent to GSK-3β with notable selectivity.[65] We hypothesize that structural modifications of isoorientin by computer-aided drug design approach can offer novel GSK-3β inhibitors with improved potency as potential anti-AD agents.

Objective-3. Elucidation of potential pleiotropic mechanisms of *C*-glycosylflavones in neurons by targeted chemical proteomics

***Hypothesis**:* Isoorientin simultaneously interacts with GSK-3β and other therapeutic targets relevant to AD, which sheds light on its pleiotropic mechanisms and enhances its pharmaceutical values.

Key points lead to the hypothesis for Objective 3:

AD is a complex neurodegenerative disease involving multiple pathogenic mechanisms. An anti-AD agent modulating multiple targets and signaling pathways in a disease-relevant context is valuable in pharmaceutical applications. Flavones are well-known for their multifunctional actions on intervening diseases, which suggests the presence of multiple targets. The feature of pleiotropy can plausibly enhance therapeutic values of flavones by leveraging multiple beneficial activities and outweigh potential toxic effects.[72] Isoorientin and its new analogues have a good safety margin and tolerability, and elicit unique neuroprotection via targeting GSK-3β.[65, 73] We hypothesize that isoorientin also acts on other protein targets to gain a maximal anti-AD effect. Global and unbiased profiling of therapeutic targets by chemical proteomics approaches can provide a full picture of the pleiotropic mechanisms of isoorientin with appreciation of the biomolecular networking of the targets in AD pathways.

CHAPTER 2

2. C-GLYCOSYLFLAVONES AGAINST ALZHEIMER'S DISEASE

2.1. Natural C-Glycosylflavones Alleviate Tau Phosphorylation and Amyloid Neurotoxicity through GSK-3β Inhibition †

Many tau-protein kinases (TPKs) and microtubule affinity-regulating kinases (MARKs) mediate tau phosphorylation.[74] Among them, glycogen synthase kinase-3β (GSK-3β) is one of the most relevant kinases for aberrant tau phosphorylation in AD. In AD brains, over 70% of GSK-3β phosphorylation sites flanking the microtubule-binding domain of tau protein are typically phosphorylated.[75-77] Abnormal tau phosphorylation by GSK-3β undermines the healthy dynamics of tau protein with microtubules. Overactive GSK-3β plays a central role in AD pathology, causing neurodegeneration, inflammatory response, toxic Aβ production as well as synaptic deficit.[76] Therefore, development of GSK-3β inhibitors attenuating tau hyperphosphorylation is a promising therapeutic strategy for AD treatment.[3, 11, 24, 78]

Corn silks (CS) of the food crop maize (*Zea mays* L.) have been an alternative medicine widely adopted by the Asia-Pacific cultures for the treatment of hyperglycemia, hyperlipidemia, cystitis, prostate disorder and urinary infection.[63] Studies have shown that CS extracts are a phytotherapeutic agent with antibiotic, anti-oxidative, anti-inflammatory, anti-diabetic, and anticancer activities.[79-82] Owing to the diverse bioactivities, CS metabolites are of interest to

† Reproduced in part with permission from Liang, Z.; Zhang, B.; Su, W. W.; Williams, P. G.; Li, Q. X. *ACS Chem. Neurosci*. **2016**, *7*, 912-923. Copyright © 2016 American Chemical Society.

natural product and agricultural chemists. Phytochemical and metabolomic studies revealed that CS is rich in flavonoids, polysaccharides, terpenoids, and steroids. Among them, flavones are particularly abundant and characteristic in maize crops.[63-64] It has been proposed that the unique biological properties of CS such as antibiotic, anti-inflammatory and anticancer effects are mainly associated with these flavones. However, there are fewer studies of systematic evaluations of CS-derived flavones for nutraceutical and pharmaceutical applications.

As part of our efforts to look for AD phytopharmaceuticals, we utilized a kinase assay to screen GSK-3β and CDK5/p25 inhibitors. Both GSK-3β and CDK5/p25 have been implicated in tau hyperphosphorylation.[75] Interestingly, an extract of CS selectively inhibited GSK-3β but not CDK5/p25. Successive bioassay-guided fractionation of this CS extract afforded two known 6-*C*-glycosylflavones, isoorientin (**1**) and 3'-methoxymaysin (**2**). In addition to *in silico* studies, *in vitro* enzymatic assays demonstrated an ATP noncompetitive but substrate competitive inhibition by **1** and **2** specific to GSK-3β. A whole-cell lysate assay further confirmed that **1** effectively inhibited tau hyperphosphorylation mediated by GSK-3β *in vitro*.

Aβ induces tau hyperphosphorylation and neurotoxicity in human neuroblastoma SH-SY5Y cells, which is a common cell model for AD research.[83-85] While this cellular system remains limited to represent *in vivo* neuropathology of AD, the inductive effects of exogenous Aβ on SH-SY5Y cells make it possible to study therapeutic interventions involving AD-mimic pathways.[84, 86-87] By implementing this *in vitro* model, immunoblot and cell viability analyses indicated that **1** and **2** are nontoxic agents, but inhibit cellular GSK-3β, and prevent tau hyperphosphorylation and neuronal cytotoxicity from amyloid insult in SH-SY5Y cells.

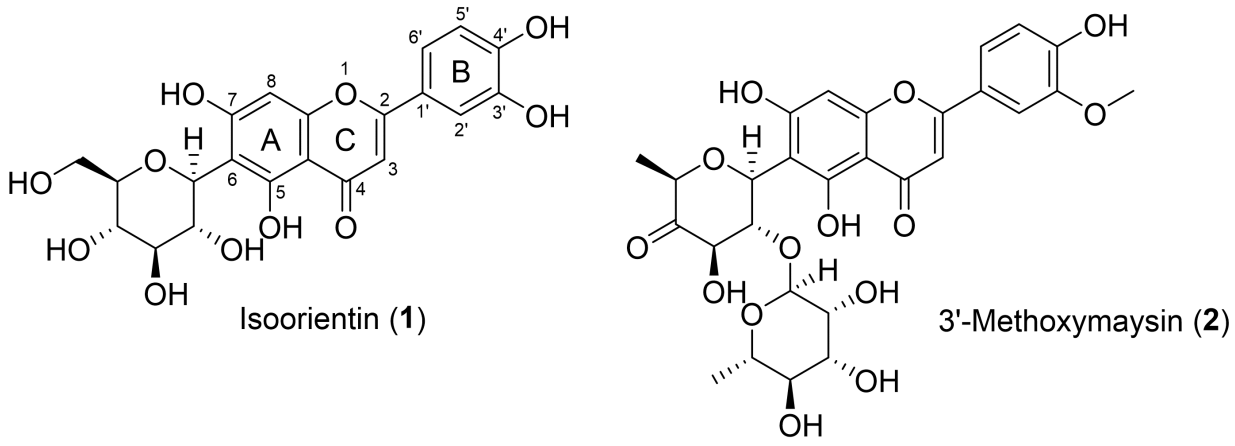

Figure 2.1. 6-*C*-Glycosylflavones from corn silks.
The flavone rings are labeled as A, B, and C, and the positions of atom are labeled in Arabic numbers according to the IUPAC rules.

2.1.1. Isolation and Identification of GSK-3β Inhibitory Compounds from Corn Silks

We recently utilized an *in vitro* universal luminescence-based kinase assay to screen potential GSK-3β and CDK5/p25 inhibitors. In this assay, ADP generated from a kinase reaction is chemically converted to ATP, which then couples with luciferase, such that the intensity of signal from the luciferase reaction is proportional to kinase activity. Kinase inhibitors were isolated from CS extracts via the bioassay-guided fractionation (Figure 2.2). The resulting ethyl acetate (EtOAc) fraction (CS-EA) showed plausible inhibition of GSK-3β activity, giving a 42.7% inhibition at a concentration of 100 μg/mL (Table 2.1). In contrast, no significant inhibition against CDK5/p25 was observed with this fraction at the same concentration (data not shown). LC-QTOF-MS profiling revealed that the EtOAc fraction contained a series of compounds with molecular weights between 480 and 600 amu along with UV maxima at 260 and 350 nm, suggesting the presence of glycosidic flavones.[79] Further bioassay-guided fractionation and HPLC purification of this EtOAc

fraction led to the isolation of two 6-*C*-glycosylflavones, **1** and **2** in over 95% purity as determined by HPLC-UV at 205 nm. Chemical identity of **1** and **2** was determined by NMR spectroscopic comparison with reported data[88-89] in conjunction with ESI-CID-MS/MS analyses.[90] The ESI-QTOF-CID-MS/MS analysis of **2** showed an ion at *m/z* 445.1136 corresponding to $[Y_1]^+$, confirming the presence of a rhamnose, while the observed ion $[^{0,2}B]^+$ at *m/z* 150.6861 indicated a methoxy group at the B-ring of **2** (see Appendix 1). **1** and **2** showed moderate GSK-3β inhibition with an IC_{50} value of 185 and 288 μM, respectively, whereas they were inactive against CDK5/p25 (IC_{50} > 15 mM) (Figure 2.3A).

Flavonoids have been reported as potential colloidal aggregators showing promiscuous inhibition of proteins.[91] These promiscuous inhibitors aggregate with proteins nonspecifically and promote protein unfolding, which is a common cause of false positives in high-throughput screenings. To investigate if the GSK-3β inhibition of **1** was due to this undesired mechanism, **1** was assayed against GSK-3β in a kinase buffer containing varying concentrations of Triton X-100 to disrupt possible aggregation.[92] Intriguingly, GSK-3β inhibition was insensitive to the addition of detergent as the resulting IC_{50} value of **1** did not significantly change (with 0.01% Triton, IC_{50}, 192 μM) (see Appendix 2). This observation was consistent with the inhibitory behavior of staurosporine, a well-known GSK-3β inhibitor without aggregation (with 0.01% Triton, IC_{50}, 3 nM). Conversely, luteolin, a flavone showing GSK-3β inhibition but promoting aggregation,[91] decreased the potency by 16-fold with the addition of 0.01% Triton (increased IC_{50} value from 2 to 32 μM). Structurally, luteolin is the flavone core of **1** without *C*-glycone. The behavioral difference between luteolin and **1** in the promiscuous inhibition assay suggested that the *C*-glycosyl group of **1** plays an essential role in GSK-3β inhibition. Since ruling out the possibility

of promiscuous inhibition, further biological evaluations proceeded with the stronger GSK-3β inhibitor **1**.

Table 2.1. Inhibitory activity of CS extracts against GSK-3β.

Sample ID	Inhibitory Activity % (± SEM %) [a]
	100 μg/mL
CS-EA	42.7 ± 1.0
CS-EA-F	44.5 ± 2.3
CS-EA-F-1	20.1 ± 1.3
CS-EA-F-2 (Compound **1**)	48.4 ± 2.2
CS-EA-F-3 (Compound **2**)	41.5 ± 1.4
CS-EA-F-4	32.3 ± 3.0
CS-EA-F-5	16.8 ± 1.3
Staurosporine (reference)	100.9 ± 1.6

[a] Data were means of quadruplicate of each of two independent experiments with ± SEM (n = 8).

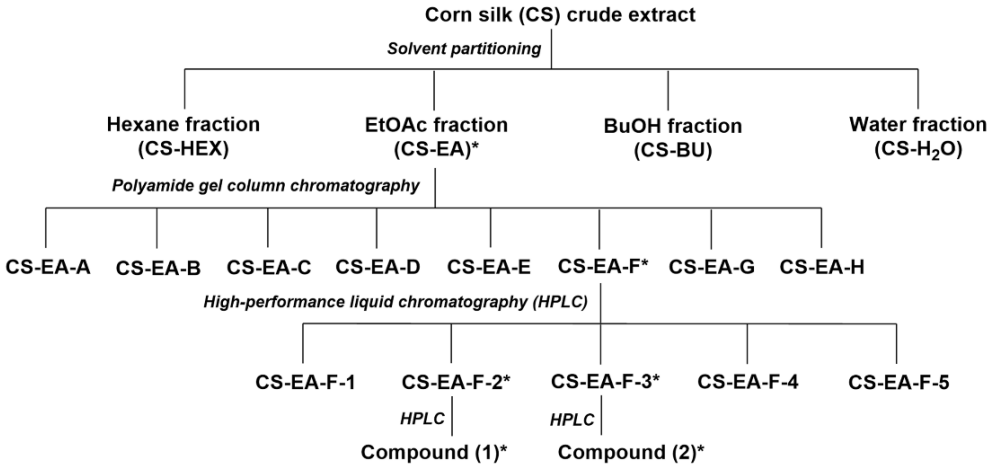

Figure 2.2. Schematic of GSK-3β assay guided fractionation of 1 and 2 from corn silks.
The crude extract was subject to successive partitioning using *n*-hexane, ethyl acetate (EtOAc), *n*-butanol and H_2O to yield four primary fractions. The fractions with the most potent GSK-3β inhibition were further subject to flash column chromatography on a polyamide column using a step gradient of MeOH in H_2O, affording eight fractions (A-H). Separation of fraction F (CS-EA-F) by HPLC afforded five subfractions, whose GSK-3β inhibitory activities were concentrated in subfraction-2 (CS-EA-F-2) and subfraction-3 (CS-EA-F-3). HPLC purification led to the isolation of compound **1** and **2**. *Fractions showed > 40% inhibition at 100 μg/mL in the GSK-3β kinase assay.

2.1.2. Isoorientin Selectively Inhibits GSK-3β in an ATP Noncompetitive Mechanism

To further evaluate the kinase inhibitory selectivity, **1** was assayed on a broad panel of 22 kinases relevant to AD, using the universal kinase assay system. As shown in Figure 2.3B, **1** effectively inhibited GSK-3β (decreased 52.4% kinase activity, $p < 0.0001$) *in vitro* at a concentration of 224 μM compared to the control (100% kinase activity). It is interesting that **1** did not significantly inhibit other 18 kinases ($p > 0.05$) except AKT1, PKC and CK2. Although **1** also showed approximately 30% inhibition against AKT1, PKC and CK2, inhibitory selectivity of GSK-3β was the most distinct in this study. Aside from GSK-3β it has been reported that CDK5, ERK2, JNK, p38, PKA, AKT, PKC, CAMKII, DAPK, AMPK, and CK1/2 contribute positively to tau hyperphosphorylation in human.[75] The selectivity of **1** to GSK-3β over the other AD relevant kinases suggested that **1** interacts with GSK-3β at an allosteric domain rather than the common conserved ATP-binding pocket.

Enzyme kinetic experiments were then performed to elucidate the underlying mechanism of **1** on GSK-3β inhibition. As illustrated in Figure 2.3C, when concentrations of the GSK-3β substrate GS2 (peptide YRRAAVPPSPSLSRHSSPHQ(pS)EDEEE, derived from human muscle glycogen synthase) were held constant at 17 μM, velocities of ATP-ADP conversion at a given concentration of **1** were measured over a period of time. Michealis-Menten kinetic analysis indicated that **1** reduced GSK-3β activity (decreased V_{max}) with an increase of concentration of **1** but not compete with ATP at the active site of GSK-3β, for which it remained an unaltered Michaelis constant (K_m, 76 μM). Moreover, a Dixon plot of enzyme kinetics showed a convergence of intersecting lines on horizontal axis that further corroborated the ATP noncompetitive mechanism of **1** with a K_i value of 210 μM (Figure 2.3D).

GSK-3β is a proline-directed serine/threonine kinase ubiquitously expressed in mammals. It plays a pivotal role in regulating various processes of cell signal transduction including glycogen metabolism, gene transcription, protein translation, cytoskeletal stabilization, cell development and apoptosis. In particular, GSK-3β is a key regulator mediating neural development in human.[93] The normal state of GSK-3β regulates the healthy functioning of neurons, whereas elevated activity of GSK-3β is implicated in AD pathology.[75-76] Inhibiting levels of GSK-3β in an aberrant state is a promising therapeutic strategy for AD treatment. To date, the majority of inhibitors has targeted the highly conserved ATP-binding cavity on GSK-3β.[3] Although GSK-3β inhibitors targeting this active site could achieve high potency, the limited selectivity of ATP competitive inhibitors raises concerns about the safety and tolerability of this class of molecules, which remains a major hurdle in AD drug development.[11] Alternatively, seeking ATP noncompetitive inhibitors is a feasible approach to improve inhibitory selectivity, because these inhibitors tend to bind to uniquely folded domains within GSK-3β instead of simply blocking ATP entrance.[94] In addition, since GSK-3β regulates essential cell signaling events, moderate-to-weak inhibition of aberrant GSK-3β activity may actually normalize GSK-3β functions.[95] The efficacy of many ATP noncompetitive GSK-3β inhibitors of synthetic and natural origins has been demonstrated in a variety of cellular and animal models. Two of them, Tideglusib (a TDZD compound) and lithium ion, have advanced to Phase II clinical trials, which offers a promising prospect.[95] In the present study, because maize is a food crop, it is conceivable that **1** along with its CS-derived *C*-glycosidic flavones, acting as ATP noncompetitive inhibitors of GSK-3β, are safe agents worthy of advanced biological studies.

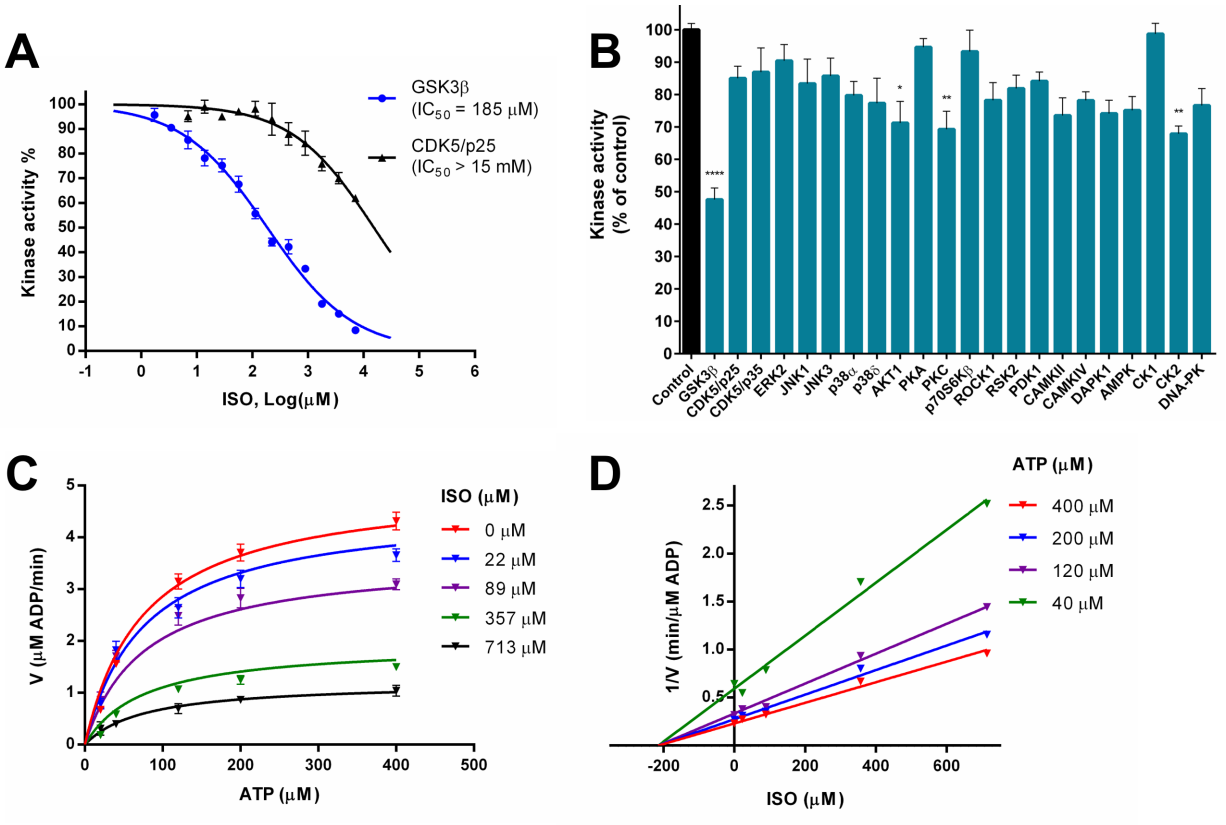

Figure 2.3. Isoorientin (1) selectively inhibits GSK-3β via an ATP noncompetitive mechanism.

Data were means of quadruplicate of each of two independent experiments with ± SEM (n = 8). The data were analyzed by one-way ANOVA with Tukey's multiple comparison test. $^{*}p < 0.05$, $^{**}p < 0.01$, $^{***}p < 0.001$, $^{****}p < 0.0001$ relative to control. ISO, isoorientin. (A) **1** inhibited GSK-3β activity with an IC_{50} value of 185 ± 25 μM. The IC_{50} value of **1** to CDK5/p25 was > 15 mM. Results were presented as the percentage of the kinase activity relative to control (5% DMSO vehicle). Inhibition curves were analyzed by four-parameter regression. (B) Effect of **1** on the activities of 22 protein kinases. Protein kinases were assayed in the presence of 224 μM **1** or control (5% DMSO vehicle). (C) GSK-3β inhibitory kinetics *in vitro*, when GSK-3β substrate GS2 was kept constant at 17 μM. GSK-3β activity was determined by increasing concentrations of **1** in the presence of varying ATP concentrations. The lines represented the result of a non-linear regression analysis of the entire data set using a best-fit kinetic model for enzyme inhibition. The analysis showed a noncompetitive inhibition of ATP with a K_i of 210 ± 22 μM, and a K_m of 76 ± 9 μM. (D) Dixon plots of GSK-3β activity in the presence of varying concentrations of ATP versus **1**. The lines were linear regression plotting of 1/V against concentration of **1** at a given concentration of ATP. Intersecting at the same point on the X axis indicated a noncompetitive inhibition with respect to ATP.

2.1.3. Isoorientin Exerts Inhibition of GSK-3β in a Substrate Competitive Mode

Owing to the aforementioned drawbacks of ATP competitive inhibitors of GSK-3β, new ATP noncompetitive inhibitors with increased selectivity are of high interest in the development of AD pharmaceuticals targeting tauopathy. Comprehensive mapping and identification of the binding sites of GSK-3β by computational simulations has allowed for a better elaboration and evaluation of allosteric kinase inhibitors.[94] For example, some complex small-molecules, such as manzamine A[96] and peptide L803,[95] have been validated as ATP noncompetitive inhibitors with the assistance of molecular modeling.

The interaction of **1** with GSK-3β was therefore examined by computational simulation using the X-ray crystallographic structures of GSK-3β (PDB code 1PYX and 1Q3D). Protein and ligand structures were prepared as described prior to docking. Using these parameters, the ligand staurosporine, a known ATP competitive inhibitor, was successfully re-docked into the active ATP-binding site of GSK-3β, with a RMSD of 0.93 Å compared to its original crystal structure[97] (Figure 2.4A and B). Simulation under the same condition revealed that **1** resides within the substrate-binding site of GSK-3β, an orthosteric cavity immediately near to the ATP-binding pocket (Figure 2.4C). The *C*-glycone of **1** makes polar interactions with GSK-3β residues Leu88, Gln89, Asp90, Lys94 and Arg96 within the substrate-binding pocket to form hydrogen bonds. The aromatic flavone core of **1** shows hydrophobic interactions with residues Phe67 and Val87, and the 7-hydroxyl oxygen atom at the A-ring of the flavone core shows a hydrogen bond with residue Asn95. In conjunction, interactions of the 3'-hydroxyl oxygen atom at the catechol B-ring of the flavone core with the two Mg^{2+} ions in the magnesium-binding site of GSK-3β potentially stabilize

these binding interactions. The role of Mg^{2+} cofactors is known to be essential for the GSK-3β kinase reaction as they assist the key steps in ATP phosphoryl transfer. Competitive replacement of magnesium by lithium significantly inhibits GSK-3β activity.[98] In the present study, interactions of **1** with Mg^{2+} may weaken the binding affinity of ATP with GSK-3β. Furthermore, residues Phe67, Gln89 and Asn95 within the substrate-binding site of GSK-3β are particularly crucial for substrate recognition as mutating any of these amino acids causes the loss of kinase activity.[99] The docking results indicated that interactions of **1** with these key residues in the substrate-binding site of GSK-3β may partially explain its inhibitory action and selectivity (IC_{50}, 185 μM). In comparison, **2** (IC_{50}, 288 μM) shows less favorable interactions with Phe67, Gln89 and Asn95, probably due to steric hindrance from the larger *C*-glycone (Figure 2.4D). Structural features of both flavone and glycone in **1** favor specific interactions with the substrate-binding pocket of GSK-3β, whereas luteolin without *C*-glycone showed nonspecific inhibition of GSK-3β (see Appendix 2). The *C*-glycosidic moiety putatively acts as a key structural element in **1** for GSK-3β specific inhibition and selectivity.

To validate the molecular docking results, we conducted kinetic experiments of GSK-3β when ATP concentrations were fixed at 25 μM. At a given concentration of **1**, rates of ATP conversion were plotted versus different concentrations of substrate GS2. In this case, Michealis-Menten kinetics and corresponding Dixon plot clearly showed a competitive inhibition mode between GS2 and **1** with a K_i value of 125 μM (Figure 2.4E and F), indicating that **1** interacts with the substrate-binding site of GSK-3β as predicted from the docking postulation. Taken together, the enzymological experiments *in silico* and *in vitro* supported an ATP noncompetitive inhibition mechanism by which **1** inhibits GSK-3β via interactions within the substrate-binding pocket.

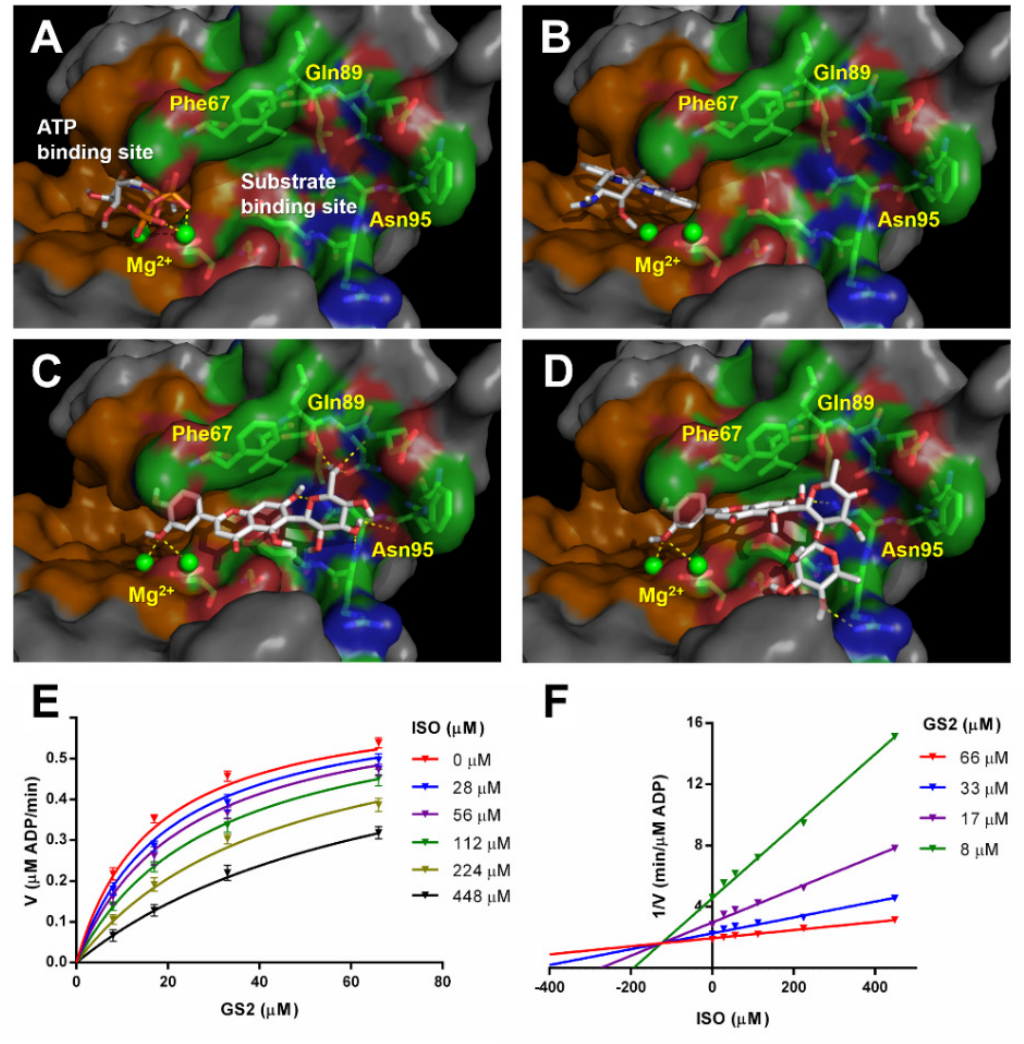

Figure 2.4. Isoorientin (1) is a substrate competitive inhibitor of GSK-3β.
Predicted docking structures of ATP (A), staurosporine (B), **1** (C) and **2** (D) with GSK-3β (PDB code 1PYX). Surface representation of the ATP-binding site of GSK-3β is shown in orange, the substrate-binding site of GSK-3β is shown in green. Within substrate-binding site, surface features are shown with acidic residues in red, basic residues in blue, hydrophobic residues in green. Magnesium ions are shown as bright green spheres. The dotted lines represent interactions with magnesium ions and hydrogen bonds with side chain residues of GSK-3β. (E) GSK-3β inhibitory kinetics *in vitro*, when ATP was kept constant at 25 μM. GSK-3β activity was determined by increasing concentrations of **1** in the presence of varying concentrations of kinase substrate GS2. The lines represented the result of a non-linear regression analysis of the entire data set using a best-fit kinetic model for enzyme inhibition. Data were means of quadruplicate of each of two independent experiments with ± SEM (n = 8). The analysis showed a competitive inhibition of GS2 with a K_i of 125 ± 13 μM, and a V_{max} of 0.66 ± 0.02 μM/min. (F) Dixon plots of GSK-3β activity in the presence of varying concentrations of GS2 versus **1**. The lines were linear regression plotting of 1/V against concentration of **1** at a given concentration of GS2. Intersecting point above the X axis indicated a competitive inhibition with respect to substrate GS2. ISO, isoorientin.

2.1.4. Isoorientin Inhibits GSK-3β-Mediated Tau Hyperphosphorylation in a Whole-Cell Lysate Kinase Assay

Given our hypothesis that **1**, being an ATP noncompetitive inhibitor of GSK-3β, can alleviate tau hyperphosphorylation, we investigated the potential of **1** against GSK-3β-mediated tau phosphorylation. To determine whether the intervention of **1** on tau phosphorylation is ascribed to a direct GSK-3β inhibition in an *ex vivo* matrix, we designed a simple *in vitro* GSK-3β assay to take advantage of a whole-cell lysate of the neuroblastoma SH-SY5Y cells. In this assay, an aliquot of lysate was fortified with exogenous GSK-3β (wt/wt 0.25%), and incubated with **1** (112 μM) or LiCl (10 mM) for 2 h, followed by western blotting probed with anti-tau pS199/pS202 and pS396 antibodies. Tau-5 and GSK-3β antibodies were also applied to assess the respective total protein levels. It has been reported that phosphorylation sites pS199/pS202 and pS396 on tau are GSK-3β specific.[74] Abnormal tau phosphorylation at these sites impairs microtubule stabilization and neurite outgrowth, which is closely linked to AD.[74, 100] Western blot results substantiated that overactive GSK-3β by introducing exogenous GSK-3β significantly increased tau phosphorylation at sites pS199/pS202 and pS396 approximately three fold ($p < 0.0001$) in comparison to their basal phosphorylation levels (lysate spiked with heat-inactivated GSK-3β) (Figure 2.5). Conversely, treatment of **1** or LiCl showed an apparent attenuation on tau phosphorylation for those specific sites mediated by GSK-3β ($p < 0.01$). Noticeably, the anti-tau phosphorylation potency of **1** at 112 μM was comparable to that of LiCl at 10 mM, which the latter is a weak but specific GSK-3β inhibitor (IC_{50}, 2 mM) currently in clinical trials for AD. The encouraging data from the whole-cell lysate kinase assay provided plausible evidence of GSK-3β inhibition and its subsequent effect on GSK-3β-mediated tau hyperphosphorylation upon treatment with **1**.

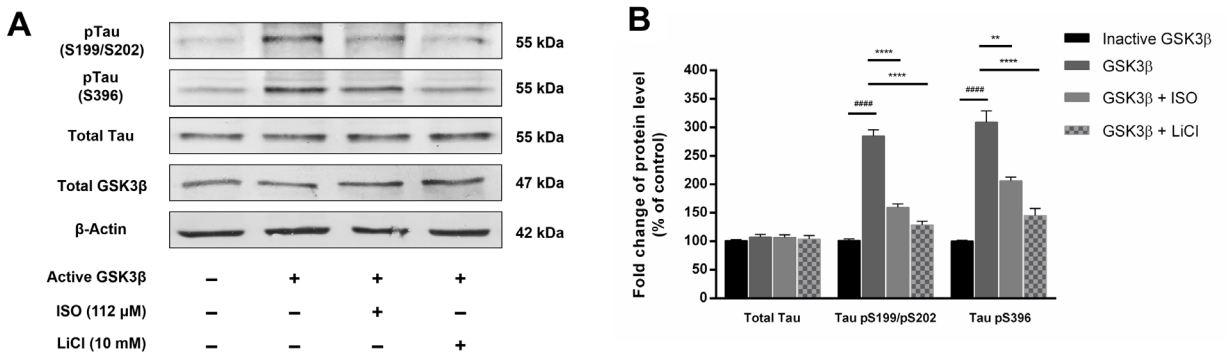

Figure 2.5. Isoorientin (1) attenuates GSK-3β mediated tau phosphorylation in a SH-SY5Y whole-cell lysate kinase assay.
(A) Cell lysate aliquots were spiked with 0.25% (wt/wt) GSK-3β, and incubated with 112 μM **1**, 10 mM LiCl or 5% DMSO vehicle in a kinase buffer at 37 ˚C for 2 h. Immunoblot analysis was performed with antibodies against Tau-5, Tau pS199/pS202, pS396 and GSK-3β. β-Actin level was used as a protein loading control. (B) Densitometric analysis of western blotting for tau protein levels. Optical densities were normalized to β-actin and fold changes were calculated relative to the control with ± SEM (n = 3). The data were analyzed by one-way ANOVA with Tukey's multiple comparison test. $^{\#\#\#\#}p < 0.0001$ relative to inactive GSK-3β spiked control; $^{**}p < 0.01$, $^{***}p < 0.001$, $^{****}p < 0.0001$ relative to the active GSK-3β spiked control. ISO, isoorientin.

2.1.5. Isoorientin Attenuates Aβ-Induced Tau Hyperphosphorylation in SH-SY5Y Cells

Although *in vitro* enzymological studies demonstrated the potential of **1** for GSK-3β inhibition and anti-tau phosphorylation, additional validations for those effects within a cellular level remain necessary. Growing evidence indicated that Aβ activates GSK-3β via PI3K/AKT/GSK-3β signaling in AD, thereby causing downstream tau hyperphosphorylation in neurons.[76, 101] We examined the alleviative effects of **1** on tau hyperphosphorylation in a cell model relevant to Aβ pathology, in which the cells were treated with $A\beta_{42}$. Human neuroblastoma SH-SY5Y cells were used in this research as on differentiation they possess the functionality and molecular features resembling to human neurons.[84-85] Cellular phosphorylation levels were assessed with antibodies

against pS199/pS202 and pS396 on tau protein, while the extent of an inactive form of GSK-3β (phosphorylated GSK-3β at Ser9) with antibody GSK-3β pS9. Those abnormal phosphorylations have been found in AD.[74, 76] Tau-5 and GSK-3β antibodies were used to evaluate the respective total protein expressions.

Figure 2.6 shows that treatment of SH-SY5Y cells with 10 μM $A\beta_{42}$ for 72 h increased tau phosphorylation at sites pS199/pS202 and pS396 approximately 3.5 and 2.3-fold, respectively, relative to untreated cells. In contrast, pretreatment of **1** at varying concentrations (28, 112 and 448 μM) to SH-SY5Y cells for 1 h followed by co-incubation with 10 μM $A\beta_{42}$ for 72 h significantly decreased tau phosphorylation levels at all phosphorylation sites in a dose-dependent manner ($p < 0.01$) (Figure 2.6B). Significant alleviative effects of **1** on tau phosphorylation were achieved even at lower doses (e.g., 28 μM).

No significant change was observed in levels of both GSK-3β pS9 and total GSK-3β in the cells upon treatments (either $A\beta_{42}$ treatment alone or co-incubation of **1** with $A\beta_{42}$) compared to untreated cells ($p > 0.05$) (Figure 2.6A and C). A downregulating effect of Aβ, in particular the $A\beta_{25\text{-}35}$ fragment, on an inactive form of GSK-3β has been postulated to account for GSK-3β activation in certain cell models.[102-103] The results of the present study, however, showed no apparent changes on GSK-3β pS9 levels upon treatments, suggesting complexity in GSK-3β activation. While the exact mechanism between $A\beta_{42}$ stimuli and GSK-3β activation in SH-SY5Y cells is still unclear, the consequential effect of **1** on anti-tau phosphorylation is putatively from a direct inhibition of GSK-3β in the cells (Figure 2.6).

GSK-3β inhibition and anti-tau phosphorylation of **1** were further experimentally supported by co-treatment of **1** with GSK-3β specific inhibitors in $A\beta_{42}$ treated SH-SY5Y cells. LiCl (IC_{50}, 2 mM) and TDZD-8 (IC_{50}, 2 μM) are GSK-3β specific inhibitors and have shown a promise for AD

treatment.[95] We therefore used them as references to compare effects of **1** on anti-tau hyperphosphorylation in the cells. As depicted in Figure 2.7A, brief pretreatment of **1** (112 μM), LiCl (10 mM) or TDZD-8 (10 μM) to SH-SY5Y cells for 1 h followed by co-incubation with 10 μM $A\beta_{42}$ for 72 h displayed an expected decrease of tau phosphorylation at sites pS199/pS202 and pS396 ($p < 0.001$). Notably, when co-treatment of **1** (112 μM) with LiCl (10 mM) to SH-SY5Y cells for 1 h followed by co-incubation with 10 μM $A\beta_{42}$ for 72 h, an effect against tau phosphorylation for sites pS199/pS202 and pS396 was enhanced in comparison with either **1** or LiCl individual treatment (Figure 2.7B). Co-treatment of **1** with LiCl could result in a synergistic effect on anti-tau phosphorylation due to their distinct mechanisms of GSK-3β inhibition – substrate competition by **1** and Mg^{2+} displacement by Li^{+}. On the other hand, TDZD-8 (10 μM) co-treated with **1** (112 μM) did not change the level of anti-tau phosphorylation in comparison with TDZD-8 alone ($p > 0.05$). This phenomenon can be plausibly explained by the fact that TDZDs are ATP noncompetitive and irreversible inhibitors of GSK-3β.[104] While X-ray crystallographic structures of GSK-3β with TDZDs were not available, computational simulation suggested that TDZDs appear to interact within the substrate-binding site of GSK-3β.[105] It is possible that the more potent and irreversible inhibitor TDZD-8 (IC_{50}, 2 μM) overperformed **1** during co-treatment (Figure 2.7A and B). Upon those treatments, little changes in the levels of GSK-3β pS9 and total GSK-3β were observed by western blot analyses ($p > 0.05$) (Figure 2.7C). Nonetheless, the similarity of pharmacological phenomena between **1** and the known GSK-3β specific inhibitors, in conjunction with the findings in the whole-cell lysate kinase assay, indeed conferred that **1** is an effective GSK-3β inhibitor attenuating aberrant tau phosphorylation in the human cells.

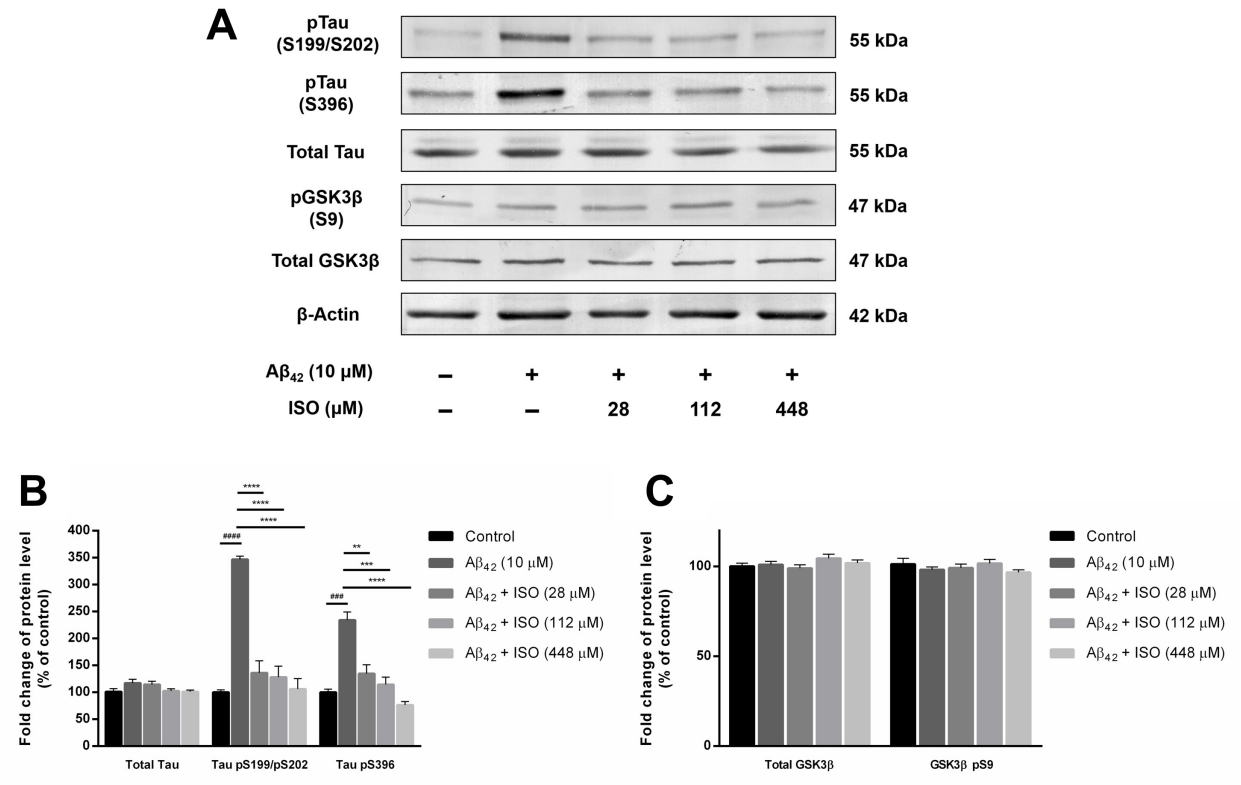

Figure 2.6. Isoorientin (1) attenuates Aβ42 induced tau phosphorylation in SH-SY5Y cells. (A) Cells were pretreated with varying concentrations of **1** or 0.2% DMSO vehicle for 1 h followed by 10 μM Aβ42 treatment and incubated for 72 h. Immunoblot analysis was performed with antibodies against Tau-5, Tau pS199/pS202, Tau pS396, GSK-3β, and GSK-3β pS9. β-Actin level was used as a protein loading control. (B) Densitometric analysis of western blotting for tau protein levels. (C) Densitometric analysis of western blotting for GSK-3β levels. Optical densities were normalized to β-actin and fold changes were calculated relative to the control with ± SEM (n = 3). The data were analyzed by one-way ANOVA with Tukey's multiple comparison test. $^{###}p < 0.001$, $^{####}p < 0.0001$ relative to control; $^{**}p < 0.01$, $^{***}p < 0.001$, $^{****}p < 0.0001$ relative to the 10 μM Aβ42 treatment. ISO, isoorientin.

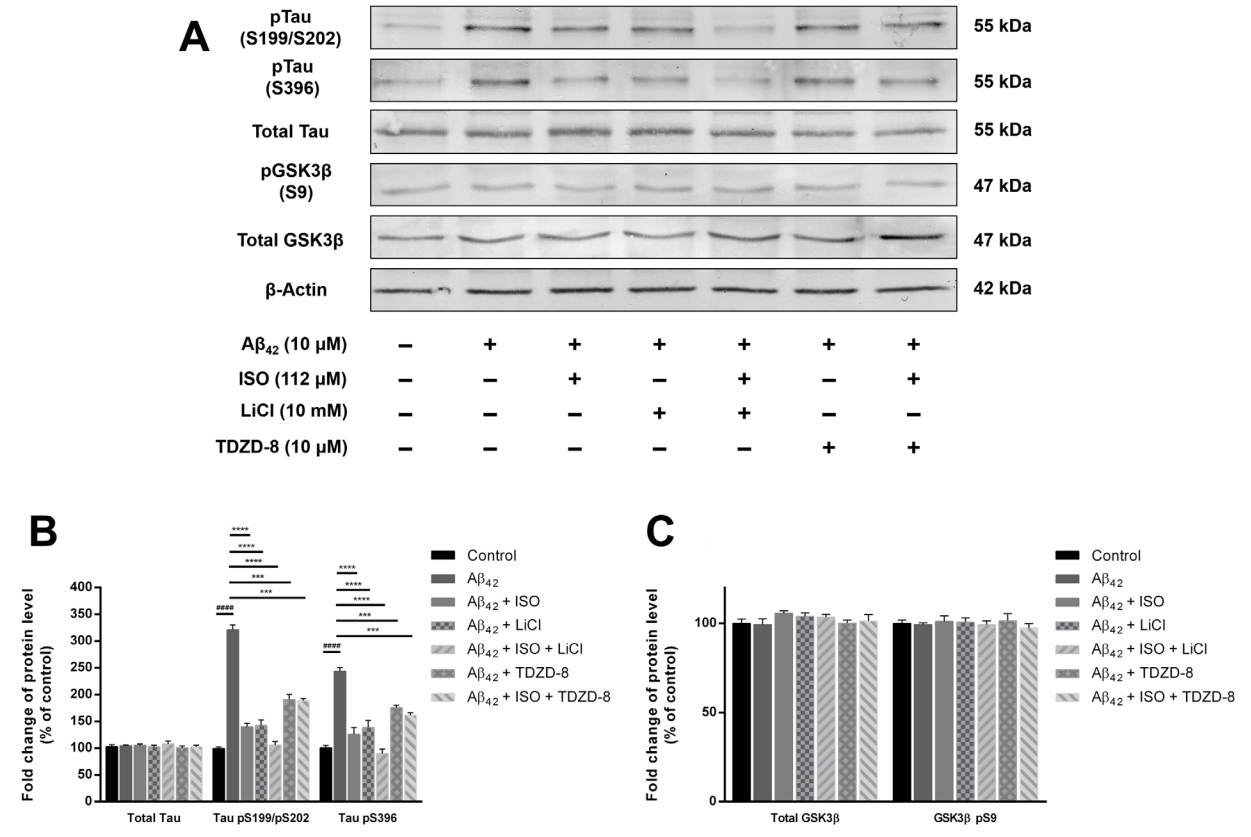

Figure 2.7. Isoorientin (1) attenuates Aβ$_{42}$ induced tau phosphorylation by inhibiting GSK-3β in SH-SY5Y cells.

(A) Cells were pretreated with individual inhibitor (112 μM for **1**; 10 mM for LiCl; 10 μM for TDZD-8) or a combination (**1**/LiCl or **1**/TDZD-8) for 1 h followed by 10 μM Aβ$_{42}$ treatment and incubated for 72 h. Immunoblot analysis was performed with antibodies against Tau-5, Tau pS199/pS202, Tau pS396, GSK-3β, and GSK-3β pS9. β-Actin level was used as a protein loading control. (B) Densitometric analysis of western blotting for tau protein levels. (C) Densitometric analysis of western blotting for GSK-3β levels. Optical densities were normalized to β-actin and fold changes were calculated relative to the control with ± SEM (n = 3). The data were analyzed by one-way ANOVA with Tukey's multiple comparison test. $^{\#\#\#\#}p < 0.0001$ relative to control; $^{***}p < 0.001$, $^{****}p < 0.0001$ relative to the 10 μM Aβ$_{42}$ treatment. ISO, isoorientin.

2.1.6. Isoorientin Exerts Neuroprotection against Aβ-Induced Cytotoxicity in SH-SY5Y Cells

We investigated whether **1** exerts neuroprotective effects against Aβ-induced cytotoxicity in differentiated human SH-SY5Y cells. Oligomers of $A\beta_{42}$ can activate GSK-3β, resulting in tau hyperphosphorylation and microtubule disassembly within axons of neuron.[100] This neurotoxic effect of $A\beta_{42}$ could consequently lead to the axonal and dendritic impairment followed by neuron cell death.[106-108] Such toxic effects were substantiated by a dramatic cell viability reduction after the addition of $A\beta_{42}$ oligomers in SH-SY5Y cells (Figure 2.8A). Since $A\beta_{42}$ at 10 μM inhibited about 50% cell number *in vitro* based on cell viability assay, this dose was used in the subsequent experiments. Pretreatment of SH-SY5Y cells with **1** (112 μM) for 1 h followed by co-incubation with 10 μM $A\beta_{42}$ for 72 h resulted in a neuroprotection against cell viability loss, whose effect was similar to the known GSK-3β inhibitors LiCl and TDZD-8 (Figure 2.8B). Interestingly, co-treatment of **1** (112 μM) with LiCl (10 mM) showed a synergistic neuroprotection, whereas co-treatment with TDZD-8 (10 μM) did not (Figure 2.8B). Quantitative dose-response measurement of cell viability demonstrated effective inhibitions of **1** to neurotoxic induction by 10 μM $A\beta_{42}$ with an EC_{50} value of 47 μM (Figure 2.8C and D). Remarkably, no cytotoxicity of **1** to SH-SY5Y cells was noted up to a dose of 896 μM (Figure 2.8E). Instead, the data showed that **1** slightly stimulated cell proliferation. This result suggested that **1** exhibited a good safety margin and tolerability profile. In addition, microscopic observations illustrated apparent neuronal morphological changes of SH-SY5Y cells upon 10 μM $A\beta_{42}$ treatment, particularly the substantial retraction of neurites (Figure 2.9A and B). In contrast, treatment of **1** effectively prevented the differentiated SH-SY5Y cells from $A\beta_{42}$ intoxication as a large number of healthy cells with extended neurites were observed (Figure 2.9C and D). These observations together with the cell

viability analysis suggested that **1** exhibits effective anti-Aβ neurotoxicity through protecting cell differentiation and neurite extension, whose functions are highly regulated by tau proteins in neuron.

To further verify that *C*-glycosylflavones in the CS extracts are contributive to neuroprotection, we assayed CS fractions on anti-Aβ neurotoxicity. Those fractions active in the GSK-3β assay indeed displayed proportional effects in defense of Aβ-induced cytotoxicity in SH-SY5Y cells (see Appendix 3). Interestingly, **2**, the less potent GSK-3β inhibitor, exerted neuroprotection but with a weaker potency compared to **1** (EC_{50}, 154 μM).

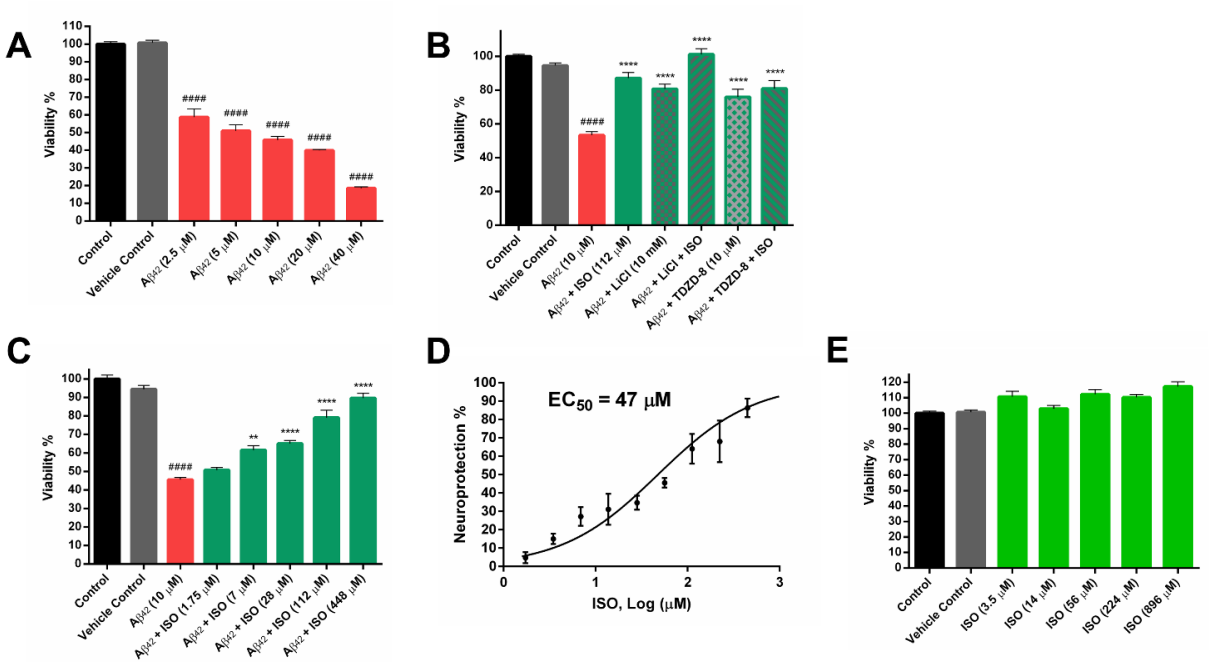

Figure 2.8. Isoorientin (1) alleviates 10 μM $Aβ_{42}$ induced neurotoxicity in differentiated SH-SY5Y cells.
Cell viability was determined using the MTS Cell Proliferation Assay. Colorimetric intensity of nontreated control cells in the MTS assay was normalized as 100% cell viability and that of solvent blank without cell culture was normalized as 0% cell viability. Data were means of triplicate of each of two independent experiments with ± SEM (n = 6). The data were analyzed by one-way ANOVA with Tukey's multiple comparison test. $^{\#\#\#\#}p < 0.0001$ relative to vehicle control; $^{*}p < 0.05$, $^{**}p < 0.01$, $^{***}p < 0.001$, $^{****}p < 0.0001$ relative to the 10 μM $Aβ_{42}$ treatment. ISO, isoorientin. (A) $Aβ_{42}$ induced neurotoxicity in differentiated SH-SY5Y cells. Cells were treated with varying

concentrations of $A\beta_{42}$ or 0.2% DMSO vehicle and incubated for 72 h. (B) Comparison of neuroprotection of **1**, LiCl and TDZD-8 in SH-SY5Y cells. Cells were pretreated with **1** (112 μM), LiCl (10 mM), TDZD-8 (10 μM) or a combination (**1**/LiCl or **1**/TDZD-8) for 1 h followed by 10 μM $A\beta_{42}$ treatment and incubated for 72 h. (C) Cells were pretreated with varying concentrations of **1** or 0.2% DMSO vehicle for 1 h followed by 10 μM $A\beta_{42}$ treatment and incubated for 72 h. (D) **1** inhibited neurotoxicity induced by 10 μM $A\beta_{42}$ with an EC_{50} value of 47 ± 22 μM. Results were presented as the percentage of the neuroprotective activity relative to control (100%) and 10 μM $A\beta_{42}$ treatment (0%). Neuroprotection curve was analyzed by four-parameter regression. (E) Cytotoxicity assessment of **1** in SH-SY5Y cells. Cells were treated with varying concentrations of **1** or 0.2% DMSO vehicle and incubated for 72 h.

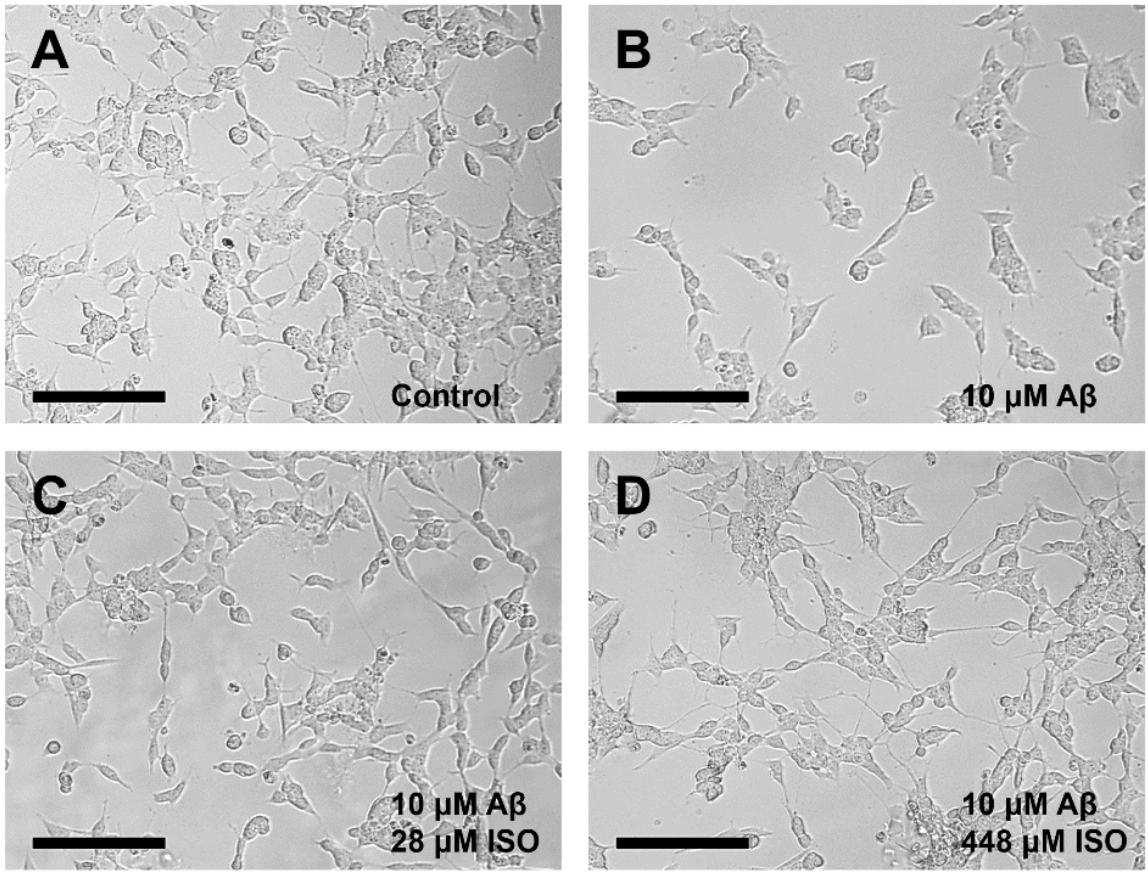

Figure 2.9. Morphological changes of SH-SY5Y cells after treatment for 72 h.
(A) 0.2% DMSO treatment as vehicle control. Differentiated cells with extended neurites. (B) 10 μM $A\beta_{42}$ treatment. Impaired and nondifferentiated cells with retracted neurites. (C) Pretreatment of 28 μM **1** followed by 10 μM $A\beta_{42}$ treatment. Partial differentiated cells with extended neurites. (D) Pretreatment of 448 μM **1** followed by 10 μM $A\beta_{42}$ treatment. Protected differentiated cells with extended neurites. Micrographs represent the average morphologic characteristics of cell cultures under a given condition of 4-6 experimental replicates. Scale bar = 100 μm. ISO, isoorientin.

2.1.7. Discussion

6-*C*-glycosylflavones are a major class of flavones produced in CS via the maysin biosynthetic pathway.[109] These endogenous flavones are well known for their unique activities against corn earworms.[79, 109] While these *C*-glycosylflavones have originally evolved in maize plant for chemical defense purposes, it has been postulated that this class of metabolites can exert biological effects on therapeutic targets such as AD-relevant kinases in human on the basis of their chemical characteristics.[35, 110] With respect to the chemical structure of *C*-glycosylflavones, the presence of carbon-linked glycosidic bond makes these compounds more resistant to metabolic hydrolysis, which is distinct from the *O*-glycosylflavones prevalent in flora. Interestingly, studies reported that CS-derived flavones show neuroprotective activities by inhibiting cholinesterases[111] and reactive oxygen species[112] in different enzyme-based or cell-based models. It is also reported that **1** exerts anticancer activity by intervening the PI3K/AKT signaling in human HepG2 cells,[66, 113] which the pathway is highly associated with neuronal survival relevant to AD.[101] CS-derived flavones including **1** may potentiate a synergistic effect by leveraging multi-activities to gain a maximal neuroprotective profile to tackle AD. Among those activities, anti-tau hyperphosphorylation through GSK-3β inhibition by **1** is a key contributor, as supported by the results of the present study.

Flavones are known for their multi-functional actions.[35, 110] It has become evident that flavones exerting their neuroprotection are probably due to the interaction with key cellular receptors or enzymes that regulate neuronal apoptosis, survival, differentiation and proliferation.[35, 114] AD is a complex neurodegeneration involving Aβ neurotoxicity, tau hyperphosphorylation, Ca^{2+} dysregulation, oxidative stress production, neuroinflammation, and synaptic dysfunction.[1] An anti-AD agent modulating multiple targets and signaling pathways in a disease-relevant context

can offer valuable properties in pharmaceutical applications. In the present study, because $A\beta_{42}$ triggers neurotoxicity through complex pathways in SH-SY5Y cells, the pleiotropic concept[54, 72] may explain the slight discrepancy that **1** is more potent in the cellular assay (EC_{50}, 47 ± 22 μM) than in the GSK-3β assay (substrate-competitive inhibition K_i, 125 ± 13 μM). While **1** showed selective inhibition of GSK-3β among 22 AD-relevant kinases tested, its potential action on multi-targets may be favorable in AD therapies. *C*-glycosylflavones warrant further investigation as AD phytopharmaceuticals.

As of today, four drugs have been approved by the US FDA for AD treatment, while one has been approved by the Chinese FDA. All of them only alleviate short-term cognitive symptoms.[3] There is a critical demand for new agents with greater efficacy and safety to slow, halt, prevent and ideally reverse AD. The present study emphasized a tau-targeted therapeutic strategy to remedy AD. We screened phytochemicals for potential inhibition of AD-relevant kinases. A tandem approach of bioassay-guided fractionation and LC-MS analysis of CS extracts afforded two 6-*C*-glycosylflavones (**1** and **2**) as GSK-3β inhibitors. Isoorientin (**1**) showed moderate potency but apparent selectivity in the kinase assay profile system. *In vitro* enzymatic and cellular evaluations as well as *in silico* molecular modeling revealed a putative mechanism of action by which **1** involves in blocking GSK-3β via a noncompetitive inhibition for ATP to attenuate tau hyperphosphorylation. The results demonstrated the first time that CS-derived *C*-glycosylflavones are ATP noncompetitive inhibitors of GSK-3β. **1** also exerts effective neuroprotection against Aβ-induced cytotoxicity in the human SH-SY5Y cell model, which is plausibly involved in the tau-dependent pathway. **1** can be a potential lead candidate with a good safety margin for AD prevention and treatment. Nevertheless, SAR-based development remains necessary to achieve a better efficacy, bioavailability, and blood-brain barrier permeability of *C*-glycosyl flavonoids.

Experiments using site-directed mutagenesis of the key residues in GSK-3β would help further validate the specific interactions of **1** in the substrate-binding site. It is worthwhile to note that **1** also significantly inhibits AKT1, PKC and CK2 by approximately 30%, the potential multi-target and/or off-target effects should not be neglected. Addressing the kinase selectivity issue is an important aspect in the future SAR-based lead optimization. Further assessments of **1** and its analogues in animal models must be conducted in order to validate their *in vivo* effectiveness for toxic tau clearance as well as the cognitive benefits.

** Methods and experimental procedures are listed in Chapter 3 of the dissertation.*

2.2. Computer-Aided Drug Discovery of Novel C-Glycosylflavones as Anti-Alzheimer's Agents Targeting GSK-3β †

Traditional GSK-3β inhibitors target the highly conserved ATP site. However, the limited selectivity of those inhibitors raises safety concerns owing to off-target effects and, therefore, remains a major challenge in GSK-3β based drug development.[78] Despite substantial efforts in developing GSK-3β inhibitors in the past decades, to date only lithium carbonate and tideglusib (a TDZD compound) have been studied in clinical trials for AD.[24] Lithium carbonate shows a weak inhibition (IC_{50}, 2 mM),[78] while tideglusib (IC_{50}, 100 nM) is an irreversible and time-dependent inhibitor of GSK-3β.[104, 115] In recent years, strategies have been employed to search for selective and reversible GSK-3β inhibitors, particularly those are not ATP-site directed. It is known that the substrate domain of GSK-3β is less conserved with a unique folding different from other kinases.[78, 116] Inhibitors targeting this site are thought to be more specific and selective than the ATP-competitive inhibitors.[78, 116] Yet few substrate-competitive inhibitors of GSK-3β have been reported.[96, 117-119] New, potent, selective and reversible inhibitors targeting the substrate site on GSK-3β are potential disease-modifying therapies for AD.

We have undertaken a different approach to discover potential substrate-competitive inhibitors of GSK-3β from natural sources. Natural products are valuable starting points for drug discovery as they have been naturally selected and optimized under evolutionary pressure and obtained privileged structures for protein binding.[120] *C*-Glycosylflavones and their aglycones (Figure 2.10) omnipresent in plants are important phytochemicals noted for anti-oxidation, anti-

† Reproduced in part with permission from Liang, Z.; Li, Q. X. *ACS Chem. Neurosci*. **2018**, DOI: 10.1021/acschemneuro.8b00010. Copyright © 2018 American Chemical Society.

inflammation, anti-cancer, anti-cardiovascular diseases, and cognitive enhancement.[35, 38, 121] We recently screened corn silks for GSK-3β inhibitors and isolated a 6-*C*-glycosylflavone, isoorientin (**1**) (see Section 2.1).[65] Compound **1** alleviates tau hyperphosphorylation and amyloid neurotoxicity through selective and reversible GSK-3β inhibition,[65] by which the mechanism of action is substrate competition rather than the common ATP competition (see Section 2.1).[65] In addition, a recent study showed that **1** and related natural flavones attenuate Aβ burden and neuroinflammation in an APPswe/PSEN1dE9 mouse model of AD.[69] **1** from maize crop[65] is conceivably safe as supported by *in vivo* subchronic toxicity studies of corn silk-derived flavones in mice and rats.[70-71] **1** is a promising medicinal natural product with a novel mode of action for reducing AD burdens.[65, 69, 71] However, the lack of druggable potency (IC_{50}, 185 μM), commonly suffered by bioactive natural products, makes it challenging in pharmaceutical applications. Potency improvement, through structure-activity relationship (SAR)-based optimization, pharmacological and pharmacokinetic evaluations, as well as testing administration routes *in vivo* are therefore necessary to develop analogues of **1** with therapeutic potential.

In our recent paper, preliminary examination of the predicted 3D structure of the GSK-3β-**1** complex revealed that the substrate pocket of GSK-3β favors specific interactions with both the *C*-glycone and flavone moieties in **1**.[65] In particular, a cleft composed of Phe67, Val87, Leu88, and Phe93 on GSK-3β is critical for substrate recognition (Figure 2.4).[94] This concave cleft could accommodate a hydrophobic moiety favoring ligand binding, which is in the vicinity of the primary hydroxyl group on *C*-glycone of **1**. This raises our hypothesis that introduction of a hydrophobic functional group at this primary alcohol enhances affinity and selectivity of **1** to GSK-3β. In addition, methylation of the phenolic hydroxyls can improve bioavailability, metabolic stability, and potency of flavones.[122]

In the present study, a new series of **1** analogues containing a 6-*C*-glycosylflavone scaffold were semi-synthesized to target the substrate site on GSK-3β. Potency, selectivity, passive membrane permeability, anti-tau hyperphosphorylation, and anti-Aβ neurotoxicity of the new inhibitors were evaluated with molecular and cellular studies, SAR analysis, and molecular modeling.

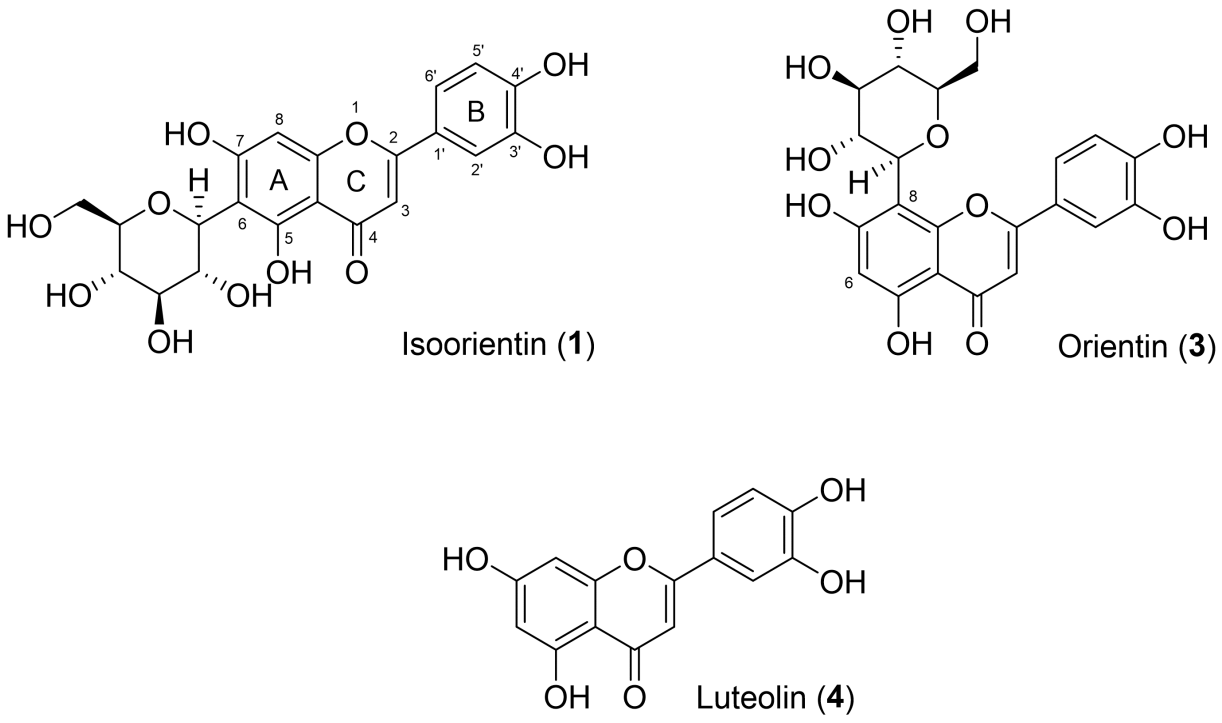

Figure 2.10. Natural *C*-glycosyl and aglycosyl flavones 1, 3 and 4.
The flavone rings are labeled as A, B, and C, and the positions of atom are labeled in Arabic numbers according to the IUPAC rules.

2.2.1. Chemical Design and Synthesis

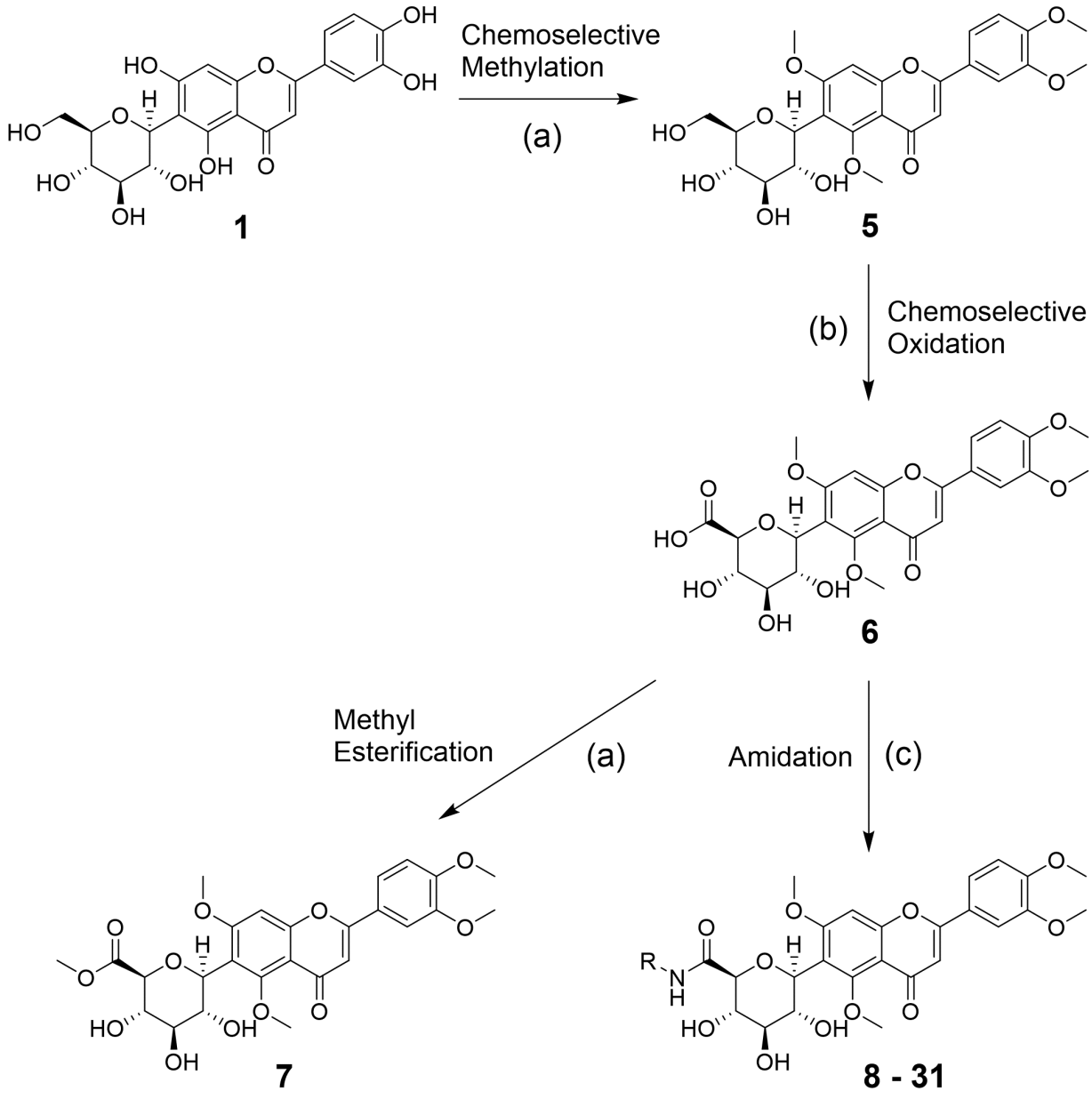

Figure 2.11. Chemical modifications beginning with isoorientin.
[a] Reagents and conditions: (a) $TMSCHN_2$, toluene, methanol, rt, 80%; (b) $[TEMPO]^+[BF_4]^-$, DCM, pyridine, rt, 95%; (c) $R\text{-}NH_2$, HCTU, DIPEA, DMF, DCM, rt, 80-90%.

Based on the strategy noted in Section 2.1 that addition of a hydrophobic moiety around the primary hydroxyl on the *C*-glycone to increase ligand-binding affinity and methylation of phenolic hydroxyls to increase bioavailability and metabolic stability, a series of new analogues of **1** were designed and synthesized (Table 2.2). The semi-synthesis of 6-*C*-glycosylflavones from **1** was carried out according to the route outlined in Figure 2.11. The four phenolic hydroxyls on the flavone core of **1** were first selectively methylated by $TMSCHN_2$ in a methanolic toluene solution according to a previously described method.[123] The resulting tetra-methylated product (**5**) then underwent an oxoammonium salt-mediated oxidation. We optimized an oxidation protocol[124] using a $[TEMPO]^+[BF_4]^-$ salt in a pyridine base solution at room temperature, which chemoselectively transformed the primary alcohol to a carboxylic acid without affecting the secondary hydroxyls on the *C*-glycone. This method successfully afforded the desired product (**6**) in over 95% yield which was confirmed by ESI-TOF-MS and NMR analyses. The carboxylic acid derivative **6** was then subjected to methyl esterification to afford **7**. It is known that an ester bond is susceptible to metabolic hydrolysis. Our chemical design thus focused on amide analogues with better physiochemical stability. A small library of hydrophobic amides (**8**-**31**) was generated by coupling **6** with a series of organic amines via HCTU catalysis. Aliphatic, alicyclic, aromatic and fluorinated amines were selected for the solution-phase amidation (Table 1). The resulting hydrophobic amides were evaluated on their SAR, cytotoxicity, anti-AD activity, and passive membrane permeability. All final products were characterized by NMR and HRMS, and were over 95% purity determined by HPLC-UV at 210, 254, and 340 nm.

Table 2.2. Chemical structures of natural and semi-synthetic *C*-glycosylflavones.

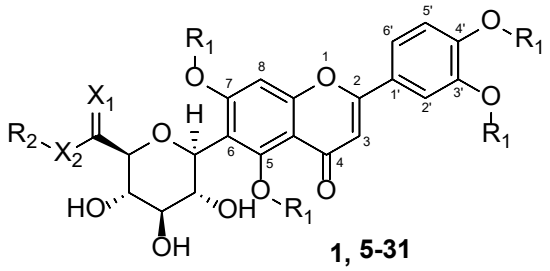

1, 5-31

cmpd no.	Functional group			
	R_1	X_1	X_2	R_2
1	H	H_2	O	H
5	CH_3	H_2	O	H
6	CH_3	O	O	H
7	CH_3	O	O	CH_3
8	CH_3	O	NH	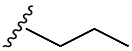
9	CH_3	O	NH	
10	CH_3	O	NH	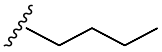
11	CH_3	O	NH	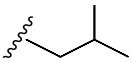
12	CH_3	O	NH	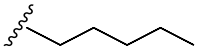
13	CH_3	O	NH	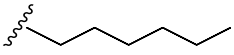
14	CH_3	O	NH	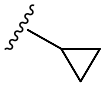
15	CH_3	O	NH	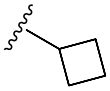
16	CH_3	O	NH	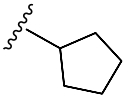
17	CH_3	O	NH	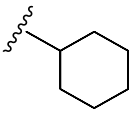

18	CH_3	O	NH	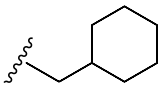
19	CH_3	O	NH	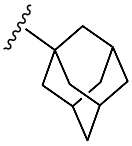
20	CH_3	O	NH	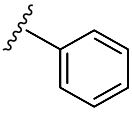
21	CH_3	O	NH	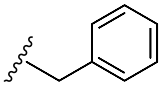
22	CH_3	O	NH	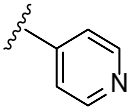
23	CH_3	O	NH	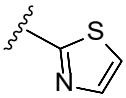
24	CH_3	O	NH	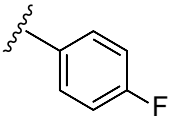
25	CH_3	O	NH	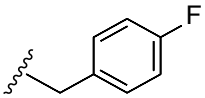
26	CH_3	O	NH	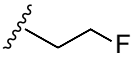
27	CH_3	O	NH	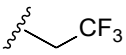
28	CH_3	O	NH	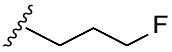
29	CH_3	O	NH	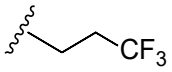
30	CH_3	O	NH	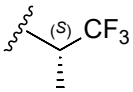
31	CH_3	O	NH	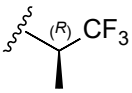

2.2.2. Structure Activity Relationship and Ligand-Lipophilic Efficiency of *C*-Glycosylflavones to GSK-3β

The semi-synthetic 6-*C*-glycosylflavones (**5**-**31**) were assayed on GSK-3β inhibition in comparison to three natural flavones with structural similarities (one 6-*C*-glycosylflavone isoorientin **1**, one 8-*C*-glycosylflavone orientin **3**, and a flavone aglycone luteolin **4**). Among the three flavones (**1**, **3** and **4**, Figure 2.10), **4** showed the highest potency against GSK-3β (IC_{50}, 3.1 μM in Table 2.3), but it is nonspecific and promiscuous as noted in the literature and our previous studies.[65, 125] **1** with *C*-glycosides at 6-position showed a moderate potency against GSK-3β with an IC_{50} value of 185 (Table 2.3). In contrast, **3** with an 8-*C*-glycoside was inactive (IC_{50}, > 5 mM). The results demonstrated that the presence and position of *C*-glycone on the flavone core are critical for GSK-3β inhibition, which agrees with our previous observation.[65]

The tetramethylated alcohol (**5**) and tetramethylated carboxylic acid (**6**) slightly decreased the potency (IC_{50}, 237 and 239 μM, respectively) in comparison with **1**, indicating a trivial contribution of the phenolic hydroxyl groups to GSK-3β inhibition. However, a methyl ester (**7**) (IC_{50}, 135 μM) increased the potency by 1.37-fold as compared to **1** (IC_{50}, 185 μM), suggesting hydrophobic groups at the primary hydroxyl position preferred for GSK-3β inhibition. Remarkably, transforming the primary alcohol to corresponding hydrophobic amides (**8**-**31**) (Table 2) significantly increased the potency against GSK-3β as most analogues displayed IC_{50} values less than 50 μM and ten of them (**9**, **13**, **16**, **17**, **20**, **21**, **27**, **29**, **30** and **31**) were less than 20 μM. As shown in Figure 2.12A, the aliphatic (e.g., **9** and **13**) and alicyclic amides (e.g., **16** and **17**) exhibited a higher affinity to GSK-3β than the aromatic amides (e.g., **20**-**23**). Small (**14** and **15**) or large (**18** and **19**) alicyclic rings showed a less affinity than the cyclopentyl (**16**) or cyclohexyl (**17**)

analogues, plausibly due to the size of the hydrophobic concave cleft in the substrate site on GSK-3β. A branched isopropyl group (**9**, **30**, and **31**) showed a higher affinity than a linear propyl group (**8**, **28**, and **29**). Monofluorination of phenyl (**24**), benzyl (**25**), ethyl (**26**) or propyl (**28**) groups did not improve affinity as compared to nonfluorinated counterparts (e.g., **8**, **20**, and **21**). It is interesting that a trifluoromethyl (CF_3) group has a significant effect on potency. Compounds **27**, **29**, **30** and **31** containing a CF_3 moiety consistently improved binding affinity to GSK-3β in comparison with no fluorine or monofluorinated counterparts (e.g., **8**, **9**, **26** and **28**) (Figure 2.12A). In particular, **30** (IC_{50}, 0.59 μM) with a (*S*)-CF_3 group increased the potency against GSK-3β by 310-fold in comparison with **1**, and is about 4-fold more potent than its epimer **31** with a (*R*)-CF_3 group (IC_{50}, 2.3 μM). All new analogues were not promiscuous or pan-assay interference compounds to GSK-3β as determined with a detergent-based assay.[65, 92]

Ligand-lipophilic efficiency (LiPE) is a parameter commonly used in drug design to assess the quality of compound candidates. Lipophilicity is the most important druglike physiochemical property that highly correlates to absorption, distribution, metabolism, excretion and toxicity (ADMET) profiles and ultimately to the pharmacological response for oral drugs.[126-127] High potency (large pIC_{50}) is a desirable feature in drug candidates, as it reduces the risk of off-target and nonspecific pharmacology. Correlation between lipophilicity (CLog*P*) and potency (pIC_{50}) provides a valuable parameter to estimate druglikeness.[128] Many of the semi-synthetic analogues clustered in an upper-right range of the LiPEs between 2 and 4, indicating that both lipophilicity (CLog*P*) and GSK-3β inhibitory potency (pIC50) have been increased relative to **1** (Figure 2.12B). Particularly, **30** has the highest LiPE value (> 4) among the analogues, suggesting a unique contribution of the CF_3 moiety of **30** to improving potency and lipophilicity.

Table 2.3. Comparison of natural and semi-synthetic *C*-glycosylflavones on GSK-3β inhibition and CLog*P*.

cmpd no.	GSK-3β inhibition IC_{50} (μM) [a]	CLog*P* [b]	cmpd no.	GSK-3β inhibition IC_{50} (μM) [a]	CLog*P* [b]
1	184.9 ± 1.4	0.21	**17**	9.0 ± 1.3	2.55
3	5153 ± 31	0.21	**18**	26.0 ± 1.2	3.16
4	3.1 ± 1.3	2.31	**19**	33.5 ± 0.8	3.17
5	239.2 ± 1.2	1.28	**20**	19.7 ± 1.1	2.21
6	237.3 ± 1.4	0.80	**21**	15.8 ± 1.2	2.34
7	135.0 ± 1.3	1.21	**22**	35.6 ± 1.3	1.54
8	29.2 ± 1.1	1.57	**23**	35.1 ± 1.0	1.45
9	5.4 ± 0.1	1.35	**24**	56.2 ± 1.2	2.61
10	33.3 ± 1.1	2.10	**25**	21.7 ± 1.2	2.48
11	31.1 ± 1.2	1.97	**26**	34.8 ± 1.0	0.77
12	28.0 ± 1.1	2.63	**27**	19.3 ± 0.8	1.31
13	9.4 ± 0.9	3.16	**28**	49.5 ± 1.2	1.00
14	25.8 ± 1.1	1.10	**29**	17.2 ± 0.9	1.29
15	61.9 ± 1.2	1.43	**30**	0.59 ± 0.04	1.62
16	13.1 ± 1.1	1.99	**31**	2.3 ± 0.5	1.62

[a] IC_{50} values were the mean of quadruplicate of each of two independent experiments. [b]CLog*P* values were calculated by a fragment-based method.[129] cmpd, compound.

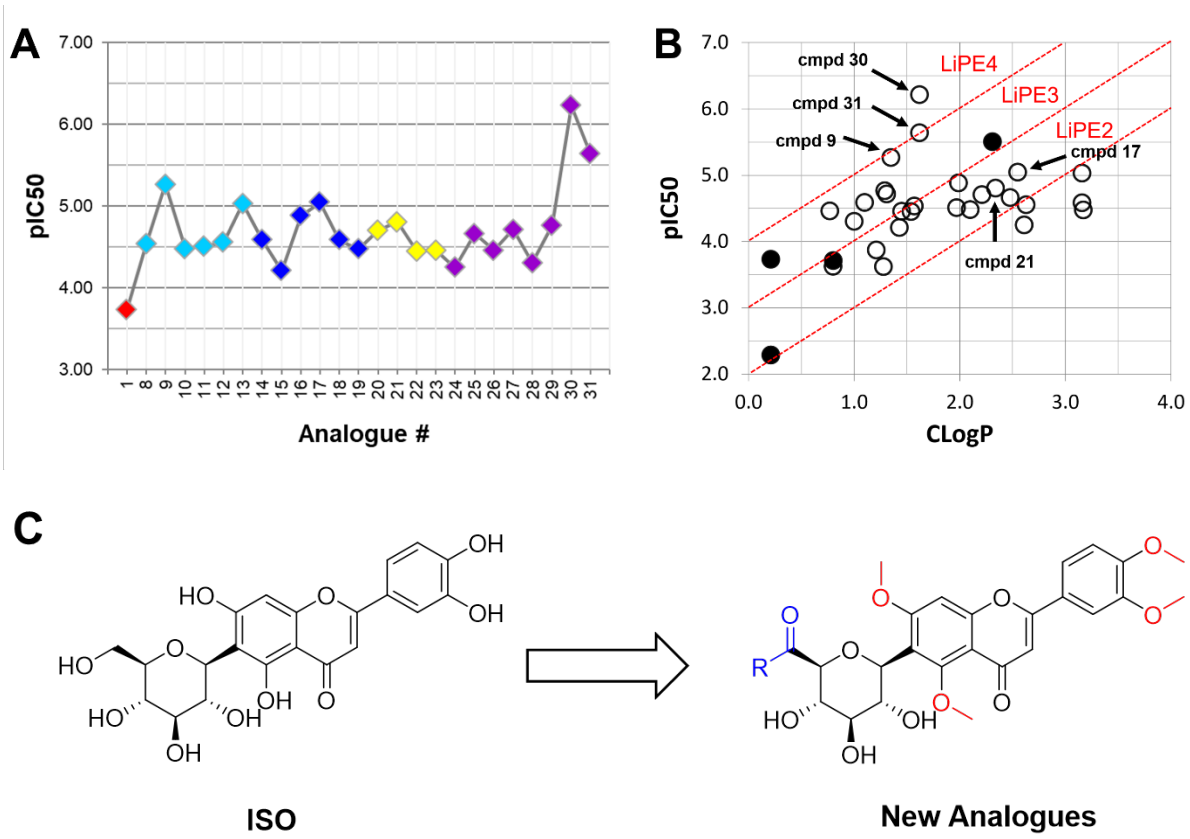

Figure 2.12. Analyses of GSK-3β inhibitory activities for compounds 1-31.
(A) Scatter plot of pIC50 (-LogIC50) for GSK-3β inhibitors **1**, **8-31**. The parent compound isoorientin **1** is shown in red, aliphatic amide analogues are shown in cyan, alicyclic amide analogues are shown in blue, aromatic amide analogues are shown in yellow, and fluorinated amide analogues are shown in purple. (B) Plot of CLog*P* versus pIC50 for GSK-3β inhibitors **1-31**. Diagonal lines represent areas of the same LiPEs to estimate druglikeness. LiPE = pIC50 – CLog*P*. Solid circle, natural flavones; Open circle, semi-synthetic flavones. cmpd, compound. (C) A summary of the important structural changes from ISO to new analogues. R represents hydrophobic functional groups.

2.2.3. Evaluations of New C-Glycosylflavones on Anti-Tau Hyperphosphorylation Mediated by GSK-3β

Compounds **9**, **17**, **21**, and **30** were selected for further evaluation on their effect against GSK-3β mediated tau hyperphosphorylation relative to **1**, as they are the most potent GSK-3β inhibitors

within each of the aliphatic, alicyclic, aromatic and fluorinated amide analogues, respectively. We recently established an *in vitro* GSK-3β assay using a whole-cell lysate of human SH-SY5Y neuroblastomas and demonstrated that the pS396 site on tau protein is GSK-3β specific.[65] This method provides a rapid means to assess intact ligand-kinase interaction in an *ex vivo* protein matrix of a lysate and circumvent compound degradation in a cell system. Direct GSK-3β inhibition by isoorientin **1** led to its consequent effect against GSK-3β–mediated tau hyperphosphorylation on the pS396 site in the SH-SY5Y lysate.[65] In analogy, an aliquot of lysate was fortified with GSK-3β (wt/wt 0.25%), and incubated with **9**, **17**, **21**, or **30** at different concentrations (2, 10, and 50 μM) for 2 h followed by an enzyme-linked immunosorbent assay (ELISA) with an anti-tau pS396 antibody. TDZD-8 (10 μM) and **1** (100 μM) were used as reference controls. Quantitative ELISA measurements substantiated that introducing exogenous GSK-3β significantly increased phosphorylation by approximately 2.5-fold ($p < 0.0001$) at the site pS396 on tau proteins as compared to their basal levels (lysate fortified with heat-inactivated GSK-3β) (Figure 2.13). In contrast, treatment of **9**, **17**, **21**, or **30** effectively attenuated tau hyperphosphorylation in a dose-dependent manner ($p < 0.0001$). All four analogues showed vast improvements of anti-tau hyperphosphorylation in comparison to the natural product **1**. Compound **30** at 10 μM exerted an anti-tau effect comparable to TDZD-8 (a known potent GSK-3β inhibitor, IC_{50} = 2 μM) at the same concentration ($p < 0.05$). These results demonstrated that the new 6-*C*-glycosylflavone analogues indeed alleviate tau hyperphosphorylation, of which **30** is the most promising candidate suitable for further *in vivo* pharmacological assessments.

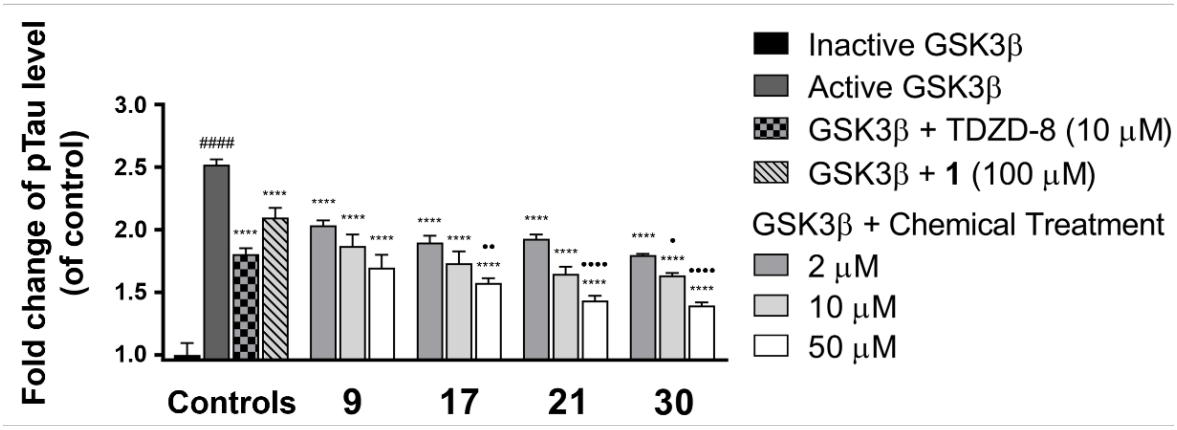

Figure 2.13. Compounds 9, 17, 21 and 30 attenuate GSK-3β-mediated tau phosphorylation in a SH-SY5Y whole-cell lysate kinase assay.
Cell lysate aliquots were fortified with 0.25% (wt/wt) GSK-3β, and incubated with 2–50 μM of **9**, **17**, **21**, **30**, or 5% DMSO vehicle in a kinase buffer at 37 °C for 2 h. 10 μM TDZD-8 and 100 μM isoorientin (**1**) were used as reference controls. ELISA analysis was performed with specific antibody against Tau pS396 to quantify tau phosphorylation levels. Fold changes were calculated relative to the control with ± SEM ($n = 4$). Data were analyzed by one-way ANOVA with Tukey's multiple comparison test. ####$p < 0.0001$ relative to inactive GSK-3β fortified control; ****$p < 0.0001$ relative to the active GSK-3β fortified control; •$p < 0.05$, ••$p < 0.01$ and ••••$p < 0.0001$ relative to the TDZD-8 reference control.

2.2.4. GSK-3β Kinetic Studies on the Inhibition Mode of Compound 30

To determine the GSK-3β inhibitory mechanism, the most potent analogue **30** (Figure 2.14A) was assayed to competitively replace ATP or the GSK-3β substrate GS2 (a peptide derived from human muscle glycogen synthase). Under a constant concentration of the substrate GS2 (17 μM), ATP concentrations varied from 2 to 50 μM and **30** concentrations varied from 0 to 5 μM. The Lineweaver–Burk plots show a convergence of intersecting lines on the x-axis, indicating an unaltered Michaelis–Menten constant (K_m) but a reduced GSK-3β activity (increased $1/V_{max}$) when the concentration of **30** increased (Figure 2.14B(a)). This suggested no competition between ATP

and **30**. In the second set of experiments under a constant concentration of ATP (10 μM), substrate GS2 concentrations varied from 8 to 66 μM and **30** concentrations varied from 0 to 5 μM. The Lineweaver–Burk plots show that all lines intersected at the same point on the y-axis, suggesting an unchanged $1/V_{max}$ but an increase of K_m when the concentration of **30** increased (Figure 2.14B(b)). The data demonstrated that **30** competed with the substrate GS2. The enzyme inhibitory behaviors of **30** are similar to that of the parent compound **1**[65] and therefore confirm that the new analogues are indeed substrate-competitive, ATP-noncompetitive inhibitors of GSK-3β.

2.2.5. Kinase Selectivity Profile of Compound 30

It is prudent to evaluate kinase selectivity in the early phases of drug discovery. Compound **30** was screened against a panel of 41 human protein kinases for selectivity relevant to AD and other CNS disorders.[77] **30** at 5 μM showed an overall good selectivity as it effectively inhibited GSK-3β by decreasing 92.3% kinase activity ($p < 0.0001$) in comparison to the control (100% kinase activity), Besides, **30** also inhibited by approximately 40% kinase activities for CDK1, PDK1, and Aurora B, whereas it showed only smaller inhibition against 37 out of 41 kinases in the test panel (Figure 2.14C). Notably, between the two GSK-3 isoforms (GSK-3α and GSK-3β), **30** at 5 μM displayed a 12.3-fold selectivity to GSK-3β (92.3% inhibition) versus GSK-3α (7.5% inhibition).

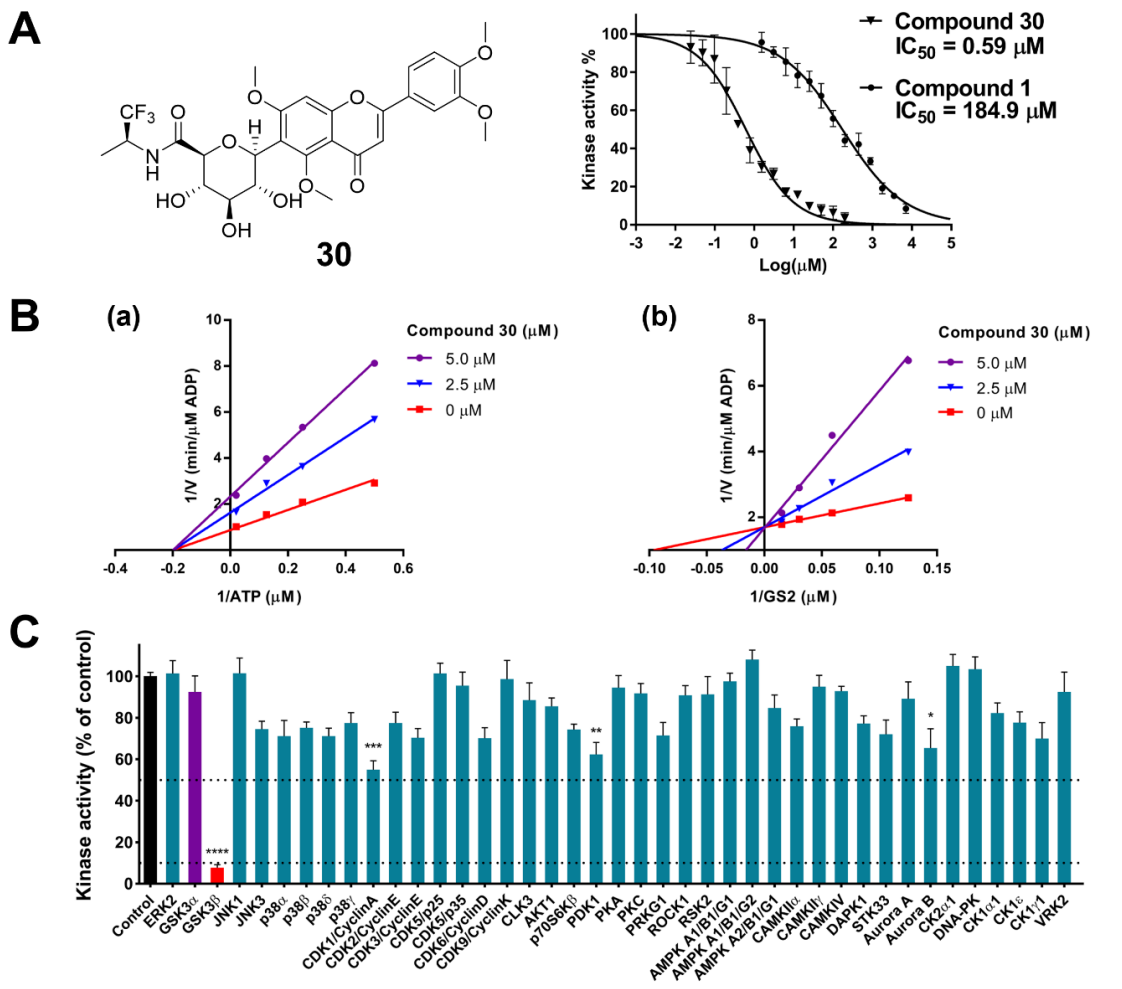

Figure 2.14. Compound 30 selectively inhibits GSK-3β via a substrate-competitive mechanism.

Data were the mean of quadruplicate of each of two independent experiments with ± SEM ($n = 8$). The data were analyzed by one-way ANOVA with Tukey's multiple comparison test. *$p < 0.05$, **$p < 0.01$, ***$p < 0.001$, ****$p < 0.0001$ relative to the control. (A) Structure of **30** and inhibition curves of **30** with an IC_{50} of 0.59 μM and **1** with an IC_{50} of 184.9 μM. The results were presented as the percentage of the kinase activity relative to control (5% DMSO vehicle). Inhibition curves were analyzed by four-parameter regression. (B) Lineweaver–Burk plots of GSK-3β kinetic data at increasing concentrations of **30** from 0 to 5 μM. (a) The lines are linear regression plotting of 1/V against 1/ATP at a given concentration of **30**. ATP concentrations varied from 2 to 50 μM, while the concentration of the GSK-3β substrate GS2 was kept constant at 17 μM. Intersecting at the same point on the x-axis indicates noncompetitive inhibition with respect to ATP. (b) The lines are linear regression plotting of 1/V against 1/GS2 at a given concentration of **30**. Substrate GS2 concentrations varied from 8 to 66 μM, while the ATP concentration was kept constant at 10 μM. Intersecting at the same point on the y-axis indicates competitive inhibition with respect to the substrate GS2. (C) Inhibitory effects of **30** on the activities of 41 kinases. Kinases were assayed in the presence of 5 μM **30** or control (5% DMSO vehicle). Dotted lines represent 10% and 50% inhibition thresholds.

2.2.6. Evaluation of Compound 30 on Cytotoxicity and Anti-Amyloid Neurotoxicity

To investigate whether semi-synthetic 6-*C*-glycosylflavone analogues exert neuroprotection against Aβ-induced neurotoxicity, **30** was assayed in a cellular model where $A\beta_{42}$ oligomers were administrated in human SH-SY5Y neuroblastomas.[65, 85] Compound **30** displayed a good tolerability profile similar to **1** as no observable cytotoxicity up to a dose of 1 mM (Figure 2.15A).[65] On the other hand, treatment of 10 μM $A\beta_{42}$ oligomers decreased cell viability to 40% compared with the controls (Figure 2.15B). However, such $A\beta_{42}$ neurotoxicity was greatly relieved, as pretreatment of SH-SY5Y cells with **30** at concentrations from 1.25 to 20 μM for 1 h followed by coincubation with 10 μM $A\beta_{42}$ for 72 h recovered cell viability from 40% to 100% in a dose-dependent manner. The neuroprotective potency of **30** (EC_{50}, 8.7 μM) (Figure 2.15C) was a 5.4-fold increase in comparison to its parent compound **1** (EC_{50}, 47 μM).[65]

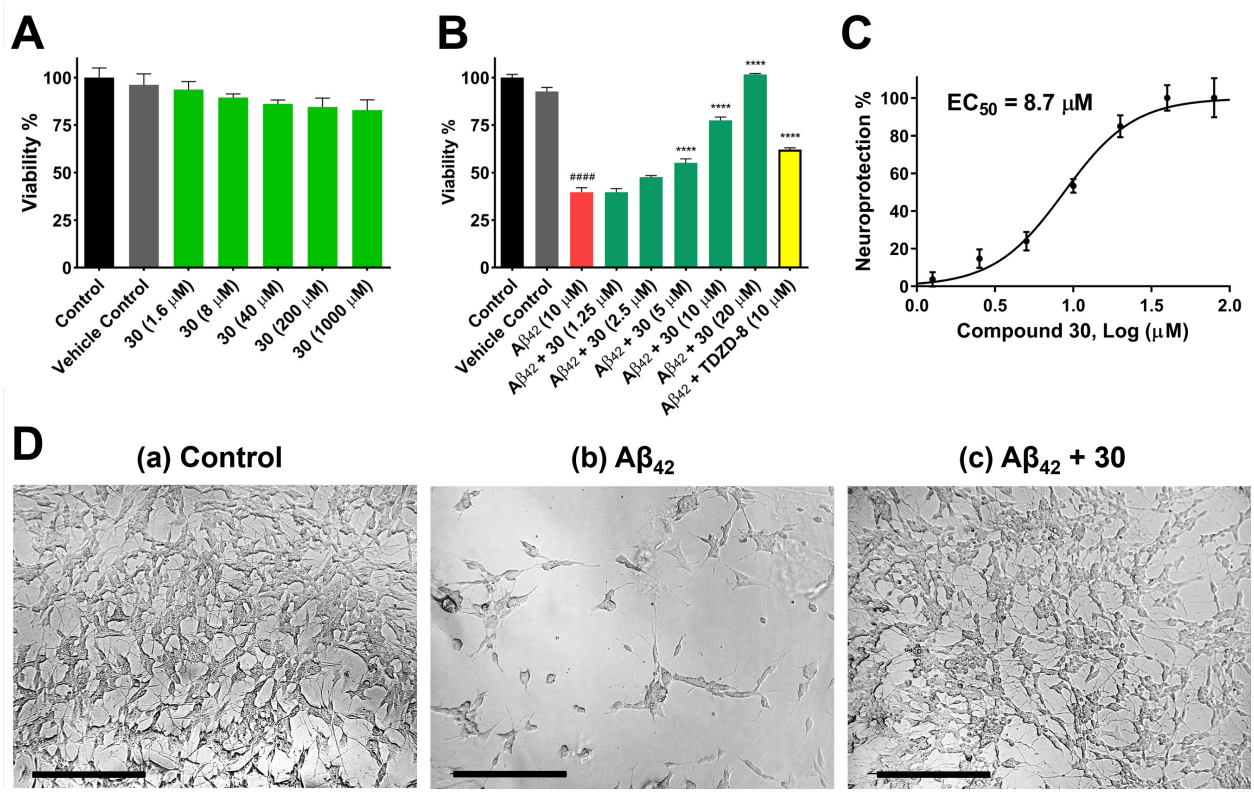

Figure 2.15. Compound 30 alleviates 10 μM Aβ$_{42}$ induced neurotoxicity in differentiated SH-SY5Y cells.

Cell viability was determined using the MTS Cell Proliferation Assay. Colorimetric intensity of nontreated control cells in the MTS assay was normalized as 100% cell viability and that of solvent blank without cell culture was normalized as 0% cell viability. Data were means of triplicate of each of two independent experiments with ± SEM (n = 6). The data were analyzed by one-way ANOVA with Tukey's multiple comparison test. ####p < 0.0001 relative to vehicle control; ****p < 0.0001 relative to the 10 μM Aβ$_{42}$ treatment. (A) Cytotoxicity assessment of **30** in SH-SY5Y cells. Cells were treated with varying concentrations of **30** or 0.2% DMSO vehicle and incubated for 72 h. (B) Cells were pretreated with varying concentrations of **30** or 0.2% DMSO vehicle for 1 h followed by 10 μM Aβ$_{42}$ treatment and incubated for 72 h. 10 μM TDZD-8 was used as a reference control. (C) **30** inhibited neurotoxicity induced by 10 μM Aβ$_{42}$ with an EC$_{50}$ value of 8.7 μM. Results were presented as the percentage of the neuroprotective activity relative to control (100%) and 10 μM Aβ$_{42}$ treatment (0%). Neuroprotection curve was analyzed by four-parameter regression. (D) Morphological changes of SH-SY5Y cells after treatment for 72 h. (a) 0.2% DMSO treatment as vehicle control. Differentiated cells with extended neurites. (b) 10 μM Aβ$_{42}$ treatment. Dying and impaired cells with retracted neurites. (c) Pretreatment of 10 μM **30** followed by 10 μM Aβ$_{42}$ treatment. Protected differentiated cells with extended neurites. Micrographs represent the average morphologic characteristics of cell cultures under a given condition of 4-6 experimental replicates. Scale bar = 100 μm.

Morphological observations also illustrated that pretreatment by **30** at 10 μM effectively protected the SH-SY5Y cells from $A\beta_{42}$ toxicity, as the neuronal cells were healthy and well differentiated with extended neurites (Figure 2.15D). Although a similar neuroprotective activity was observed to **1**, **30** exhibited approximately 20-fold improvement of effectiveness in comparison to its parent compound (EC_{90}: **30** in 10 μM versus **1** in 200 μM).[65] In good agreement with our previous findings, **30** and the other 6-*C*-glycosylflavone analogues exerted anti-Aβ neurotoxicity through protecting neurite outgrowth and neuronal differentiation, whose functions are constitutively regulated by GSK-3β and tau protein within axonal microtubules.[26]

2.2.7. Evaluations of New C-Glycosylflavones on Passive Membrane Permeability

Oral administration is noninvasive and is preferred for chronical diseases such as AD and other CNS disorders. It is advantageous to discover passive membrane permeable AD drugs targeting GSK-3β upon oral administration. The parallel artificial membrane permeability assay (PAMPA) is used to assess passive and transcellular permeability, which is well correlated with *in vivo* oral absorption rates for drugs that cross the gastrointestinal barrier.[130] In the PAMPA model, the amount of target compounds diffused from a donor compartment to an acceptor compartment through a trilayer phospholipid precoated membrane was measured to assess oral-absorption potential of drug candidates. In the present study, **1**, **4**, **9**, **17**, **21**, and **30** were evaluated with the PAMPA assay. Theophylline and atenolol known for their low permeability were used as negative controls. Desipramine known for its high permeability was used as a positive control. The measured effective permeability coefficients (P_e) were compared with the literature data.[130]

Table 2.4. PAMPA permeability and CLog*P* values of compounds tested.

cmpd no.	PAMPA Permeability			CLog*P*
	P_e ($\times 10^{-6}$ cm/s) [a]	*R* (%) [b]	Permeability classification [c]	
Isoorientin (**1**)	0.51 ± 0.01	48	low	0.21
Luteolin (**4**)	1.42 ± 0.07	43	medium	2.31
9	1.55 ± 0.06	46	high	1.35
17	1.77 ± 0.07	20	high	2.55
21	1.35 ± 0.08	30	medium	2.34
30	2.23 ± 0.21	30	high	1.62
Theophylline	0.04 ± 0.01	n/a	low	-0.03
Atenolol [d]	0.29 ± 0.09	40	low	-0.11
Desipramine [d]	13.43 ± 0.91	96	high	4.47

[a] P_e values were the mean of PAMPA measurements (n = 3-4) with ± SD. [b] Percent recovery (*R*%) measures mass retention of compounds trapped inside the PAMPA membrane. [c] PAMPA permeability classification: high ($P_e > 1.5 \times 10^{-6}$ cm/s), medium (1.0×10^{-6} cm/s $\leq P_e \leq 1.5 \times 10^{-6}$ cm/s), low ($P_e < 1.0 \times 10^{-6}$ cm/s). [d] The measured P_e values are comparable to the data in ref.[130]

The new analogues **9**, **17**, **21**, and **30** demonstrated a significant increase of permeability upon 5 h of incubation in comparison with their parent compound **1** (Table 2.4). Methylation of phenolic hydroxyls and transformation of the primary hydroxyl to hydrophobic amides on the *C*-glycone of **1** increased the PAMPA permeability (P_e) ranging from 2.6 to 4.4-fold relative to **1**. Such P_e changes agreed well with the CLog*P* changes (Table 2.4). The best PAMPA permeability of **30** is probably attributed to the CF_3 group. Multiple hydroxyl groups in *C*-glycone and flavone moieties make **1** poorly permeable, which is consistent with the literature reports.[131] For comparison,

luteolin (**4**), an aglycone flavone, had a medium PAMPA permeability similar to **9**, **17**, and **21**, indicating the liability of the polar *C*-glycone of **1** in respect to passive diffusion. Regardless, it is indispensable to assess pharmacokinetics of the new kinase inhibitors for their *in vivo* bioavailability which involves the complexity of active and facilitated transports in addition to passive diffusion.

2.2.8. Key Molecular Interactions between New *C*-Glycosylflavones and the Substrate Site of GSK-3β

To elucidate the molecular mechanisms by which the new 6-*C*-glycosylflavones increase the binding affinity and selectivity to GSK-3β relative to **1**, compounds **5-31** were docked into GSK-3β enzyme. The AutoDock Vina program was used in the present study because it has shown good accuracies for binding pose prediction and scoring function.[132-134] This docking tool has been widely used in drug design and applied in many cases of GSK-3β inhibitor discovery.[94, 118, 135-136]

Two X-ray crystallographic structures of GSK-3β (PDB codes 1PYX[97] and 1H8F[137]) were chosen to take into account for potential induced fit effects upon ligand binding. The GSK-3β in 1PYX contains two Mg^{2+} ions and a ligand ANP, a non-hydrolyzed ATP derivative, at the ATP site. Upon binding of Mg^{2+} ions and an ATP-mimic ligand, it is postulated that GSK-3β undergoes subtle conformational changes in both the ATP and substrate sites for an optimal kinase reaction, a phenomenon known as induced fit effects.[138-139] The GSK-3β structure in 1PYX hence adopts a conformation that resembles the native enzyme ready for substrate recognition. Docking **5-31** into the substrate site of GSK-3β using 1PYX would give more reliable binding poses. On the other hand, the GSK-3β in 1H8F is by far the only available X-ray crystallographic structure containing

the ligand HEPES in the substrate site. HEPES in 1H8F may cause induced fit changes of GSK-3β conformation, particularly for the substrate site. Given the new 6-*C*-glycosylflavones are substrate competitive, we used 1PYX and 1H8F in molecular docking. The docking method was validated by re-docking and cross-docking experiments using both ATP-competitive and substrate-competitive inhibitors (see Appendix 10).

The synthetic 6-*C*-glycosylflavones (**5-31**) and their parent **1** were thus docked into 1PYX and 1H8F with the AutoDock Vina program. Docking scores of 1PYX show a better linear fit to the experimental pIC50 values (R^2 = 0.7844) than that of 1H8F (R^2 = 0.6999) (see Appendix 11), suggesting more accurate predictions of binding poses using 1PYX than 1H8F. The 1PYX docking data set was therefore used in the remainder of the study to analyze the molecular interactions responsible for the improved potency and selectivity to GSK-3β.

The docking results of 1PYX showed that the *C*-glycone moiety of **5-31** forms hydrogen bonds with GSK-3β residues Gln89, Asn95, Arg96 and Glu97 within the substrate pocket, which is similar to **1** (see Appendix 12). Moreover, the newly introduced hydrophobic groups indeed exhibit a favorable ligand pose to the concave surface comprised of Phe67, Val87, Leu88 and Phe93 on GSK-3β. The most potent compounds **30** and **31** (IC_{50}, 0.59 and 2.3 μM, respectively) contain a CF_3 moiety, which may form orthogonal multipolar interactions for protein binding.[140-141] To visualize such molecular interactions, we conducted flexible-residue docking[134, 142] to refine binding poses of **9**, **30**, and **31** in 1PYX. To prepare GSK-3β structure, side chains of Ser66, Phe67, Leu88, Gln89, Asp90, Phe93, Asn95 and Lys183 within the substrate site were treated as flexible. The docking results of **30** suggested formation of orthogonal multipolar interactions. The (*S*)-CF_3 in **30** shows a favorable geometry within typical F···C distances to Leu88 (backbone amide carbonyl carbon, 3.3 Å), Gln89 (backbone amide carbonyl carbon, 3.6 Å) and Asp90 (side chain

carbonyl carbon, 3.3 and 3.8 Å) (Figure 2.16C). It also forms a polar interaction with the backbone NH of Asp90 (F···H distance, 2.6 Å). In contrast, the (*R*)-CF_3 group of **31** is absent from these interactions probably owing to the orientation and steric hindrance by switching CH_3 and CF_3 positions at the stereocenter (Figures 2.16B to C). Therefore, only hydrophobic interactions with Phe67, Val87 and Leu88 of GSK-3β exist in **31** (improper configuration of CF_3 for orthogonal multipolar interactions) as well as **9** (lack of CF_3) (Figures 2.16A to B).

Interestingly, the docking results showed that the catechol B-ring of the flavone core in **9**, **30** and **31** appears to have a π-cation interaction with Lys183.[143-145] The distance between the catechol B-ring center and ε–NH_3^+ cation of Lys183 is 4.1 Å at an angle of 71.5° (Figure 2.16C and Appendix 13). In conjunction, the side chain ε–NH_3^+ of Lys183 forms weak hydrogen bonds with two methoxy oxygen atoms of catechol B-ring (distances of 3.1 and 3.2 Å). The orthogonal multipolar and π-cation interactions potentially enhance the binding affinity to GSK-3β. Nonetheless, additional validations with site-directed mutagenesis and X-ray co-crystallography remain necessary to confirm the molecular docking predictions.

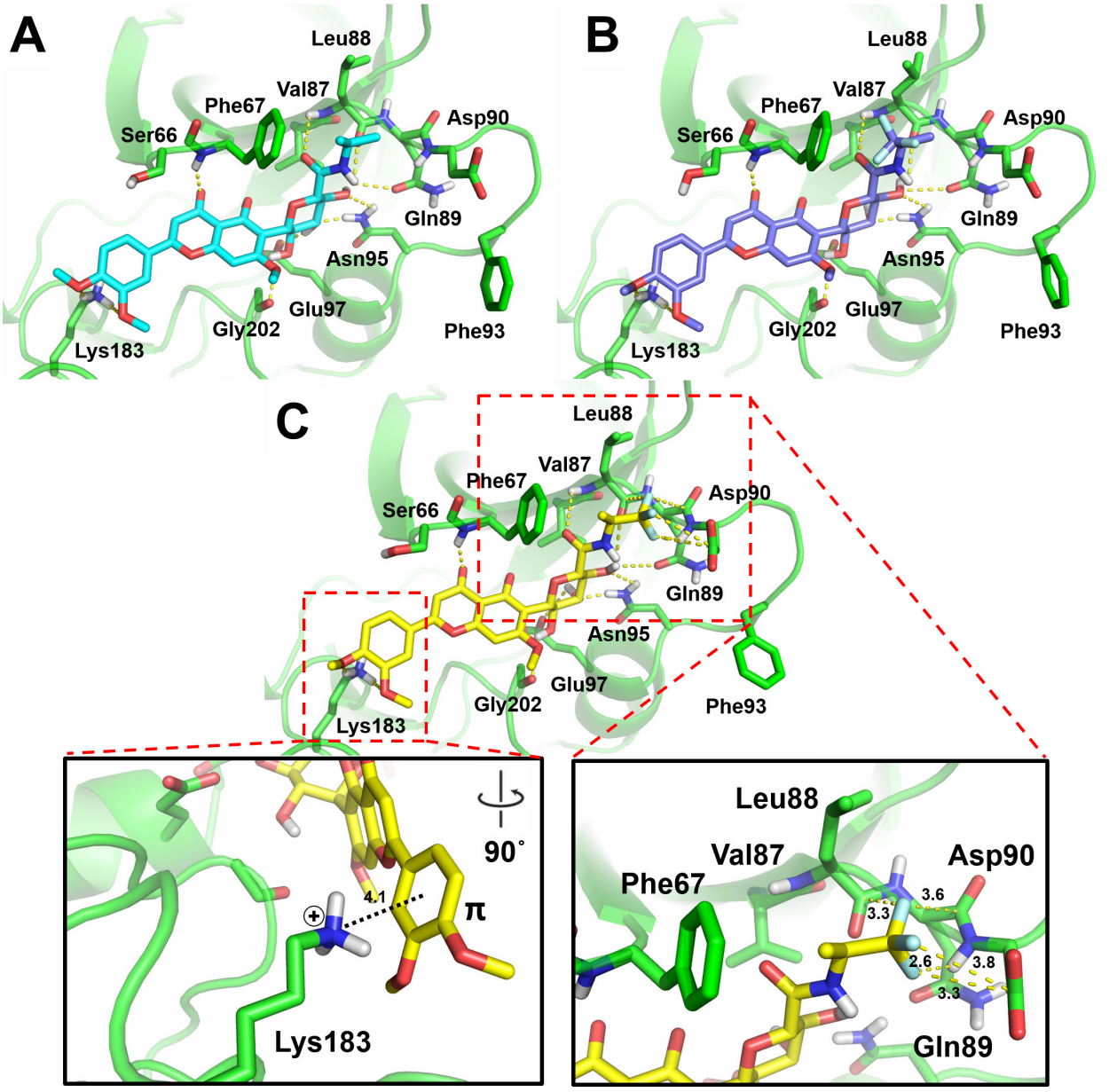

Figure 2.16. Predicted docking poses of 9 (A), 31 (B) and 30 (C) within the substrate site of GSK-3β (PDB code 1PYX).

Dotted lines represent interactions via hydrogen bonding, π-cation interaction or orthogonal multipolar interactions with key amino acid residues of GSK-3β. Key molecular interaction distances are highlighted.

2.2.9. Potential Causes for the Isoform-Selectivity of Compound 30 between GSK-3α and GSK-3β

Isoform-selectivity of **30** to GSK-3β over GSK-3α (Figure 2.14C) was assessed with comparative molecular modeling. Yet no X-ray crystallographic structures of GSK-3α are available in PDB, a homology model of GSK-3α was built with the SWISS-MODEL server[146] (see Appendix 14). A full human GSK-3α amino acid sequence (UniProt code: P49840) was searched against protein databases in BLAST and HHblits and overall 4470 templates were found. A GSK-3β template (PDB code 1PYX) resulted in a top ranking with an overall sequence identity of 82.97%, thereby selected for homology modeling of GSK-3α. A sequence alignment between the two GSK-3 isoforms indicated that GSK-3α has extra amino acid portions flanking the N- and C-termini of GSK-3β (see Appendix 15). Within the matched sequence portion, most amino acid differences occur in the N- and C-terminal regions. In contrast, both the ATP and substrate domains of GSK-3α/β isoforms are conserved as high as 92.37% identical, in which only few amino acid residues are different in these regions. The superposition and comparison of GSK-3β structure (PDB code 1PYX) with the GSK-3α homology model (Figure 2.17A) implied that those subtle differences of amino acid residues in the kinase catalytic domain (both ATP and substrate pockets) may affect substrate recognition as well as ligand binding. Intriguingly, docking experiment using the GSK-3α homology model showed that **30** resides a similar location in the substrate site in comparison to GSK-3β docking data (Figures 2.17B to C). However, the resulting binding pose of **30** in GSK-3α favors neither a π-cation interaction of catechol B-ring nor the orthogonal multipolar interactions of the (*S*)-CF_3 group. It is conceivable that the isoform-specificity of **30** to GSK-3β might be in part due to the lack of these critical molecular interactions in GSK-3α. Instead, the (*S*)-

trifluoroisopropyl group of **30** simply exerts hydrophobic affinity with the homologous residues Phe130, Val150, and Leu151 in the substrate site of GSK-3α (Figure 2.17C).

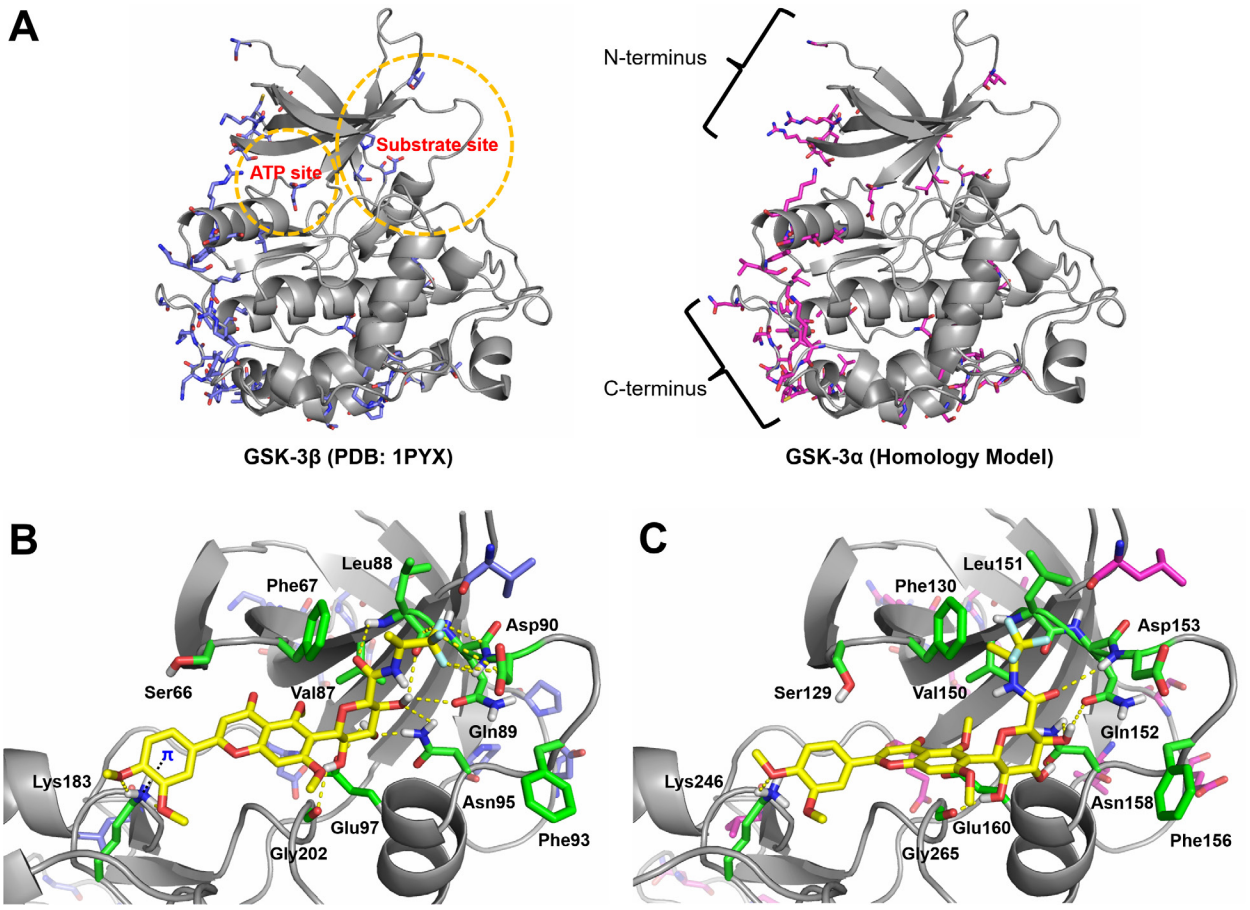

Figure 2.17. Molecular models of GSK-3β and GSK-3α and the docking complexes with compound 30.
(A) Superposition of GSK-3β structure (PDB code 1PYX) and GSK-3α homology model (UniProt code P49840). The ATP and substrate sites are highlighted in circles, and the N- and C-termini are depicted. The ATP and substrate sites of GSK-3α/β isoforms are highly conserved and most of amino acid differences occur in the N- and C-terminal regions. (B) Predicted docking pose of **30** into the substrate site of GSK-3β structure. (C) Predicted docking pose of **30** into the substrate site of GSK-3α homology model. GSK-3 isoforms are shown as gray cartoons. In both isoforms, selected conserved residues are displayed as green sticks. In GSK-3β, nonconserved residues are displayed as blue sticks. In GSK-3α, nonconserved residues are displayed as magenta sticks. The dotted lines represent key molecular interactions.

2.2.10. Discussion

GSK-3β plays a central role in signaling pathways of AD. Accumulating evidence has demonstrated that GSK-3β is activated abnormally by Aβ and in turn hyperphosphorylates tau proteins in neurons. This eventually triggers the tauopathic cascade in AD progression.[1, 26, 76] Development of selective GSK-3β inhibitors as a disease-modifying therapy for AD, therefore, is highly attractive. In recent years, discovery of selective inhibitors targeting the substrate site of GSK-3β has emerged as a rational and feasible strategy in AD drug design.[78] Unlike the ATP-site directed GSK-3β inhibitors that frequently bind to many off-target kinases, inhibitors targeting the substrate site on GSK-3β plausibly overcome this limitation. GSK-3β phosphorylates its specific substrates for biological processes such as glucose homeostasis, immune response, neurogenesis, cell proliferation and apoptosis, and circadian rhythm, which has a plethora of normal functions for human health.[147] However, GSK-3β is aberrantly overactive in AD. Subtle modulation of GSK-3β activity at a normal level rather than complete shut-off to prevent disruption of its normal cellular functions will be highly advantageous in AD therapy.[76] Targeting the substrate site to intervene the GSK-3β-substrate recognition would be a feasible means to find selective inhibitors.[116] Until now, substrate-competitive inhibitors of GSK-3β are limited in the structural classes of marine alkaloid manzamines,[96] labdane diterpenoid andrographolide,[118] peptidomimetic inhibitors,[119] and synthetic compound ITDZ series.[117] These inhibitors were in the low micromolar to sub-micromolar range of potency, but exhibited a good selectivity to GSK-3β under *in vitro* or *in vivo* evaluations. Such findings substantiate the rationale of developing substrate-competitive inhibitors of GSK-3β for AD by which the agents can attain an utmost therapeutic advantage – a high selectivity to avoid potential side effects.

Herein, we reported a new structural class of substrate-competitive inhibitors with significant selectivity for GSK-3β, inspired by isoorientin (**1**), containing a 6-*C*-glycosylflavone scaffold. It is a valuable addition to the known substrate-competitive inhibitors and offers new lead compounds for AD. The inhibitors are new chemical probes allowing to elucidate the underling mechanisms of GSK-3β inhibition and selectivity.

The SAR analysis, *in vitro* enzymatic kinetics, and *in silico* docking studies indicate that both the presence and position of *C*-glycone on the flavone core are essential features binding to the substrate site on GSK-3β. A flavone core (**4**) alone is promiscuous and tends to slide into the ATP site and thus lose the required selectivity (see Appendix 10). The presence of a *C*-glycone at 8-position (**3**, IC_{50}, > 5 mM) rather than 6-position (**1**, IC_{50}, 185 μM) results in an unfavorable binding pose to the substrate site plausibly due to the loss of key hydrogen bonds with Gln89, Asp90, Asn95, and Arg96 (see Appendix 12). Such unique SAR features inspire us to semi-synthesize a series of novel analogues of **1** that selectively inhibit GSK-3β at the substrate site. Data suggest that the new lipophilic amide analogues (**8-31**) increase the potency against GSK-3β for 3–310 fold (Table 2.3) and passive membrane permeability for 2.6–4.4 fold relative to **1** (Table 2.4). Systematic modifications of the carbon-chain length and ring size and bioisosteric replacement in the R_2-group on the *C*-glycone of **1** (Table 2.2) confer a dramatic GSK-3β potency improvement. The structural modifications contribute hydrophobic affinities with Phe67, Val87 and Leu88 in the substrate site of GSK-3β (see Appendix 12), which is concurrently supported by the LiPE analysis (LiPE highlights potency changes to the net of lipophilicity). Compounds **9**, **30**, and **31** containing an isopropyl moiety have IC_{50} values of 5.4, 0.59, and 2.3 μM, respectively, which are most potent among the analogues. It suggests that they adopt a suitable carbon-chain length and topological size within the hydrophobic cleft of the substrate site. LiPE analysis also

indicates that **9**, **30**, and **31** are quality ligands (LiPE values ≥ 4). In addition, the new analogues alleviate tau hyperphosphorylation and Aβ neurotoxicity through GSK-3β inhibition in the human SH-SY5Y neuronal model (Figures 2.13 and 2.15).

With respect to the GSK-3β selectivity of **30**, π-cation interaction and orthogonal multipolar interactions appear to play a critical role. In protein structures, the aromatic side chain of Phe or Tyr usually involves a favorable π-cation interaction with the cationic side chain of Lys or Arg.[143] In analogy, if a small aromatic ligand binds to a protein, potential π-cation interactions would be an important contribution to the binding affinity. Such phenomena have been exemplified in our previous study[144] as well as other investigations.[136, 148-149] Flavonoids seem to be the case – interactions between the aromatic A/B-rings with the cationic Lys or Arg residues.[135, 150] In the docking experiments, we found that the catechol B-ring of the flavone core in **30** forms a π-cation interaction with Lys183 of GSK-3β (distance, 4.1 Å; angle, 71.5°). To a certain extent, this might stabilize the binding conformation and orientation within the substrate site.

It is known that halogen atoms have distinct chemical properties contributing to the molecular recognition. Introduction of halogens such as F, Cl, Br, and I is a common tactic in drug design.[151] Fluorinated compounds commonly form orthogonal multipolar interactions with the backbone and side chain carbonyl carbons (Asp/Glu/Asn/Gln) or the guanidinium carbon (Arg) of amino acid residues in protein structures.[140-141] It is estimated that substitution of CH_3 for CF_3 may improve 5- to 10-fold ligand binding affinity.[141, 152] In the present study, **27** (IC_{50}, 19.3 μM) and **29** (IC_{50}, 17.2 μM) containing a 2,2,2-trifluoroethyl and 3,3,3-trifluoropropyl, respectively, show an improved potency relative to their analogue **8** (IC_{50}, 29.2 μM) without a CF_3 group. In addition, **30** and **31** containing a 1,1,1-trifluoroisopropyl are more potent than their analogue **9** without a CF_3 group. Docking experiments suggest that the isopropyl (*S*)-CF_3 group of **30** interacts with the

backbone and side chain carbonyls of Leu88, Gln89, and Asp90 (Figure 2.16C) within typical interaction distances (F···C, 3.0–3.7 Å).[141] Such orthogonal multipolar interactions might in part give rise to an increased potency of **30** (IC_{50}, 0.59 μM) against GSK-3β approximately 9-fold and 4-fold compared to **9** (IC_{50}, 5.4 μM) and **31** (IC_{50}, 2.3 μM), respectively. Conversely, **31** with a (*R*)-CF_3 group may be lack of these critical molecular interactions (Figures 2.16B to C) and thus has weaker binding affinity than **30**. The differential and stereospecific binding of the CF_3 group between **30** and **31** plausibly explains the high inhibitory selectivity to GSK-3β (Figures 2.12 and 2.14).

Interestingly, **30** exhibits isoform-selectivity to GSK-3β over GSK-3α, which deserves discussion. In humans, GSK-3α (51 kDa) and GSK-3β (47 kDa) are derived from different genes and have distinct functions.[147] Both isoforms share an overall sequence identity of 83%, especially at the ATP catalytic domain with 93% identity.[153] However, they differ substantially in the N- and C-terminal lobes that are thought to cause protein conformational dynamics and differential cellular localization.[147, 153] Subtle amino acid differences in the substrate site between two isoforms putatively affect substrate recognition and preference as noted in the literature.[154-155] Wang et al. reported that GSK-3β phosphorylates a substrate (phosphatase inhibitor-2) 10-time faster than GSK-3α,[154] indicating the differential substrate recognition of GSK-3 isoforms. Soutar et al. demonstrated that the specific sites T231, T235, and S396 on tau proteins are solely phosphorylated by GSK-3β but not GSK-3α,[155] giving an evidence of substrate specificity between two isoforms. Those studies pose a possibility to discover isoform-selective inhibitors via targeting the substrate site of GSK-3β. Compound **30** attains GSK-3β isoform-selectivity probably because of both the π-cation interaction with Lys183 and the orthogonal multipolar interactions with Leu88, Gln89, and Asp90 in GSK-3β on the basis of the comparative docking of GSK-3α/β

(Figures 2.16C and 2.17). In contrast, **30** appears being absent from those key molecular interactions within the substrate site of GSK-3α (Figure 2.17C). In addition, the highly nonconserved regions in GSK-3α, such as the N- and C-terminal domains (Figure 2.17A), can modulate enzyme conformations and thereby may affect the binding of **30**. Notwithstanding, the molecular mechanism suggested by computational modeling requires further verification by conclusive experimental evidence such as site-directed mutagenesis and X-ray co-crystallography.

In summary, we described a new class of substrate-competitive inhibitors of GSK-3β focusing on modifications of the primary hydroxyl group in the *C*-glycone of isoorientin (**1**). The results demonstrated that the 6-*C*-glycone moiety of the new inhibitors defines the specific binding at the substrate site rather than the ATP site on GSK-3β. The data also help explore topological requirements in the substrate site of GSK-3β and highlight the critical SAR. Those inhibitors effectively attenuate tau hyperphosphorylation and amyloid neurotoxicity in molecular and cellular models by which the mechanism is involved in GSK-3β inhibition via an ATP noncompetitive but substrate competitive manner. The inhibitors not only significantly increased the potency, kinase selectivity, and isoform-selectivity, but also improved passive membrane permeability in comparison with the natural product counterparts. Among them, **30** (IC_{50}, 0.59 μM) showed a potency improvement by 310-fold and a promising profile in various biological assessments, which warrants further exploration. SAR analyses and *in silico* mechanistic investigations suggested that the hydrophobic, π-cation and orthogonal multipolar interactions of **30** with the substrate site lead to selective inhibition against GSK-3β, but neither GSK-3α nor a broad panel of kinases tested. Nevertheless, additional SAR knowledge and physiochemical property optimization of the GSK-3β inhibitors based on the 6-*C*-glycosylflavone scaffold are essential to the CNS drug discovery campaign. It is important to conduct experiments on how the

new inhibitors show ATP noncompetitive and how their binding to the substrate site induces the GSK-3β conformational changes affecting ATP affinity in kinase reaction. Such data will help further development of this class of inhibitors in the future. Pharmacokinetics and *in vivo* animal studies of the new GSK-3β inhibitors will help understand drug delivery, target engagement and efficacy, which would suggest the therapeutic potential of these agents for AD and other GSK-3β relevant neuropsychiatric and neurodegenerative diseases.

** Methods and experimental procedures are listed in Chapter 3 of the dissertation.*

2.3. Targeted Chemical Proteomics Analysis of C-Glycosylflavone Reveals Its Pleiotropic Actions in Perturbation of Alzheimer's Signaling

AD is a complex neurodegenerative disease involving multiple pathogenic mechanisms such as Aβ cascade, tau hyperphosphorylation, synaptic dysfunction, neuroinflammation, Ca^{2+} dysregulation, oxidative stress, mitochondria damage, and lysosome/autophagy dysfunction.[1, 5, 26] Current evidence suggests that the AD pathogenic mechanisms are not mutually exclusive but more likely "cross-talk" with each other.[22] The traditional concept of pharmacology that "one drug, one target, one disease" may not be suitable to the complex and chronical diseases such as AD.[72, 156] An anti-AD agent modulating multiple targets and signaling pathways in a disease-relevant context is valuable in pharmaceutical applications.[156-159] Investigation of its potential pleiotropic action makes possible to understand how an anti-AD agent exerts neuroprotective effects to be the outcome of molecular and cellular networks involving multiscale mechanism of actions.[54, 72, 160]

Flavones are well-known for their multifunctional actions for disease intervention.[35, 38, 110] It has become evident that flavones exerting their neuroprotection are due to interactions with multiple cellular receptors or enzymes that regulate neuronal apoptosis, survival, differentiation, and proliferation.[29, 35] The multi-targeted feature of flavones can plausibly enhance therapeutic values by leveraging multiple beneficial activities and outweigh potential toxic effects.[72, 157] We previously demonstrated that the natural *C*-glycosylflavone isoorientin (**1**) and its new synthetic analogues showed a good safety margin and tolerability, and elicited unique neuroprotective activities in neurons.[65, 73] However, an obvious discrepancy between cellular (EC_{50}, 47 μM) and enzymatic (GSK-3β IC_{50}, 185 μM) potencies for **1** was also noted.[65] We hypothesize that the *C*-

glycosylflavones also act on other protein targets in additional to GSK-3β and gain a maximal anti-AD effect. This motivated us to pursue continued investigation.

Chemical proteomics is an emerging research discipline and a powerful tool for target identification of bioactive molecules.[49-50] Global and unbiased profiling of therapeutic targets by chemical proteomics can provide a full picture of the pleiotropic mechanisms of the *C*-glycosylflavone with appreciation of biomolecular networks of the targets in AD pathways.[51-53, 161] In the present study, we applied a targeted chemical proteomics strategy by harnessing the affinity chromatography coupled with the iTRAQ-based quantitative proteomics approach.[55, 162] A schematic of workflow is described in Figure 2.18. Briefly, the 6-*C*-glycosylflavone as a chemical probe was immobilized to matrices (e.g., sepharose resins) and incubated with cell lysates that were derived from an AD-mimic neuronal model. The binding affinity allowed for ligand-protein complexes to be separated from the unbound or nonspecific binding proteins after stringent washing. Captured proteins were then eluted and subjected to tryptic digestion. The digested peptides were labeled with isobaric tags for relative and absolute quantitation (iTRAQ),[62] and analyzed by biological mass spectrometry. The resulting MS data were searched against protein databases (e.g., SwissProt and NCBI) for protein identification and quantification. The protein/function networks were analyzed by bioinformatics tools (e.g., Cytoscape, STRING, and Ingenuity Pathway Analysis), which would reveal potential mechanisms of the *C*-glycosylflavones on neuroprotection.

Human SH-SY5Y neuroblastoma cells are a common *in vitro* cell model. These cells can be differentiated with morphological and biochemical features resembling to human mature neurons.[85, 163-164] The differentiated SH-SY5Y cells express high levels of mature tau isoforms with proper neuronal distribution.[85, 165-166] Furthermore, it has been reported that SH-SY5Y cells express

the AD-relevant proteins APP and Aβ.[167] Therefore, this cell model has been widely adopted as a reproducible, easily accessible, and affordable alternative to the primary neurons for neuroscience, especially in the AD research field.

Chronic Aβ exposure (sub-micromolar to nanomolar levels) in neuronal cells triggers AD-mimic pathologies such as tau hyperphosphorylation, Ca^{2+} homeostatic dysregulation, activation of MAPK/ERK-linked toxicity pathway, mitochondrial dysfunction, and the ultimately loss of neuronal integrity.[84, 107-108] Herein, we adopted human neuroblastoma SH-SY5Y cells treated with Aβ as a cell model.[65, 73] While this cellular system remains limited to represent actual neuropathology of AD in humans, the inductive stress of prolonged Aβ exposure in SH-SY5Y cells would lead to pathological changes within molecular and cellular levels relevant to AD[83-84] as well as make it possible to study therapeutic interventions involving AD-mimic pathways.[84, 86-87, 168-169] In the present targeted chemical proteomics study, we used the cell lysates from the chronic Aβ-treated SH-SY5Y cells as the neuroproteome.

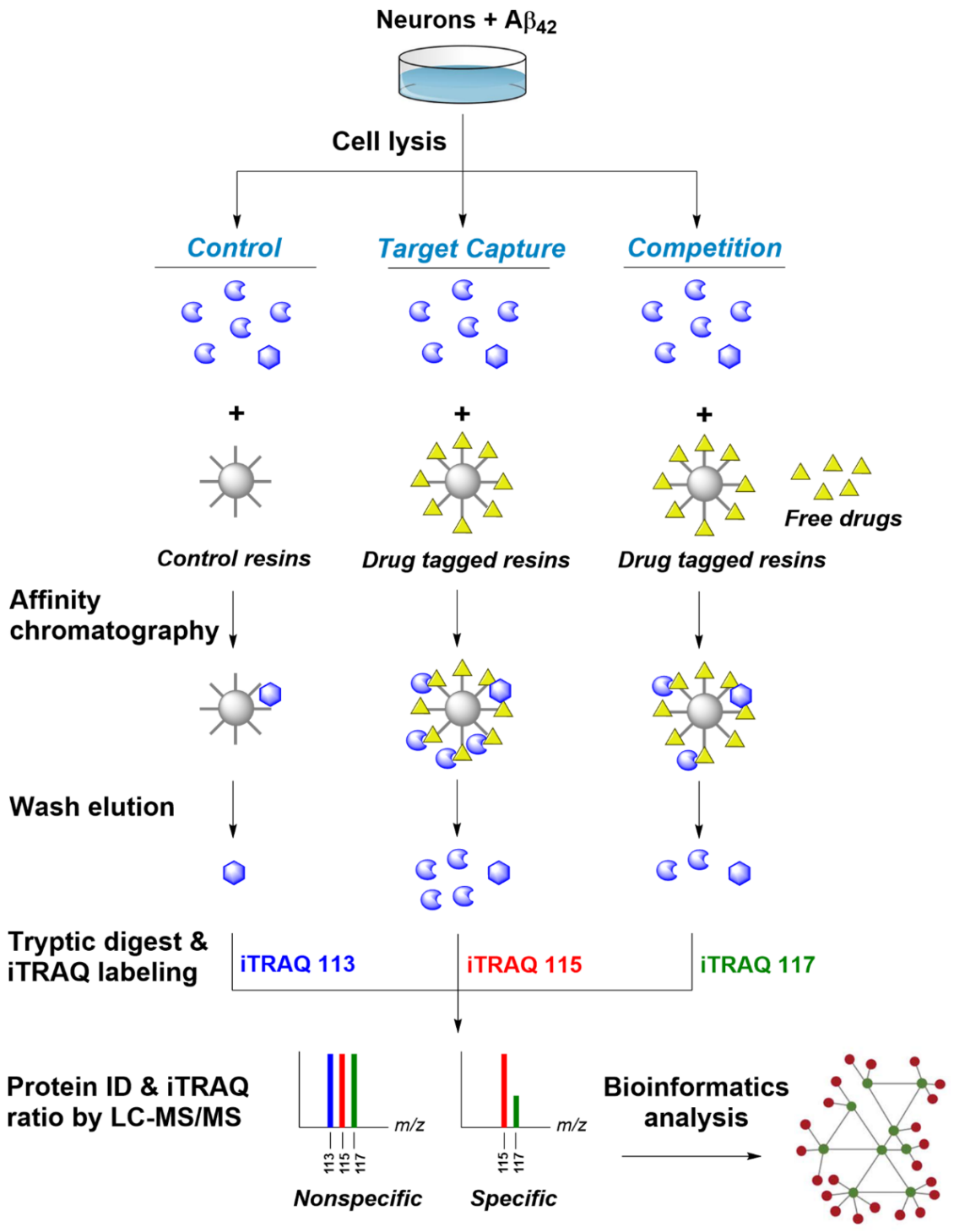

Figure 2.18. Workflow for affinity-based quantitative chemical proteomics analysis.

2.3.1. Design and Synthesis of *C*-Glycosylflavone Probe (CGF-Probe)

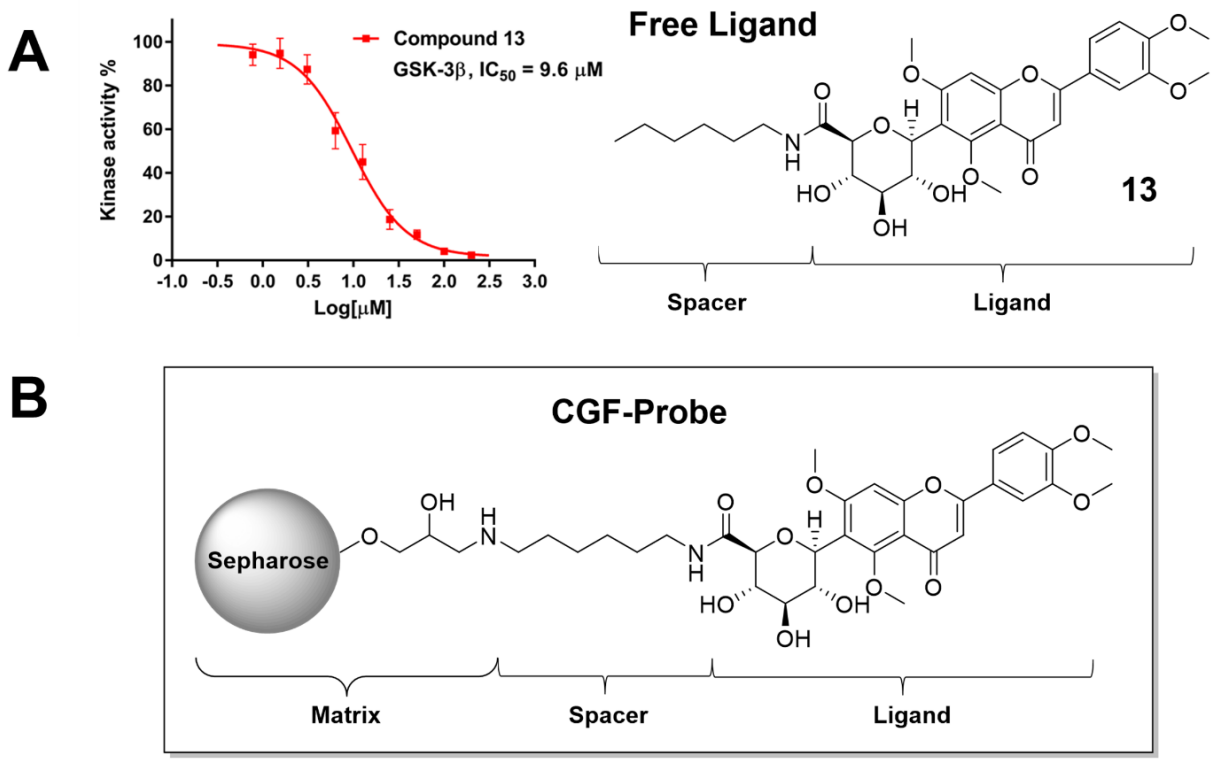

Figure 2.19. Design of the CGF-probe.
(A) Structure of the free ligand **13** and its GSK-3β inhibition curve with an IC_{50} of 9.6 μM. Results were presented as the percentage of the kinase activity relative to control (5% DMSO vehicle). Data were the mean of quadruplicate of each of two independent experiments with ± SEM (n = 8). Inhibition curves were analyzed by four-parameter regression. (B) A design affinity probe (CGF-probe) containing the ligand, spacer, and matrix portions, where the chemical structure composed of the ligand and spacer is the same as the free ligand **13**.

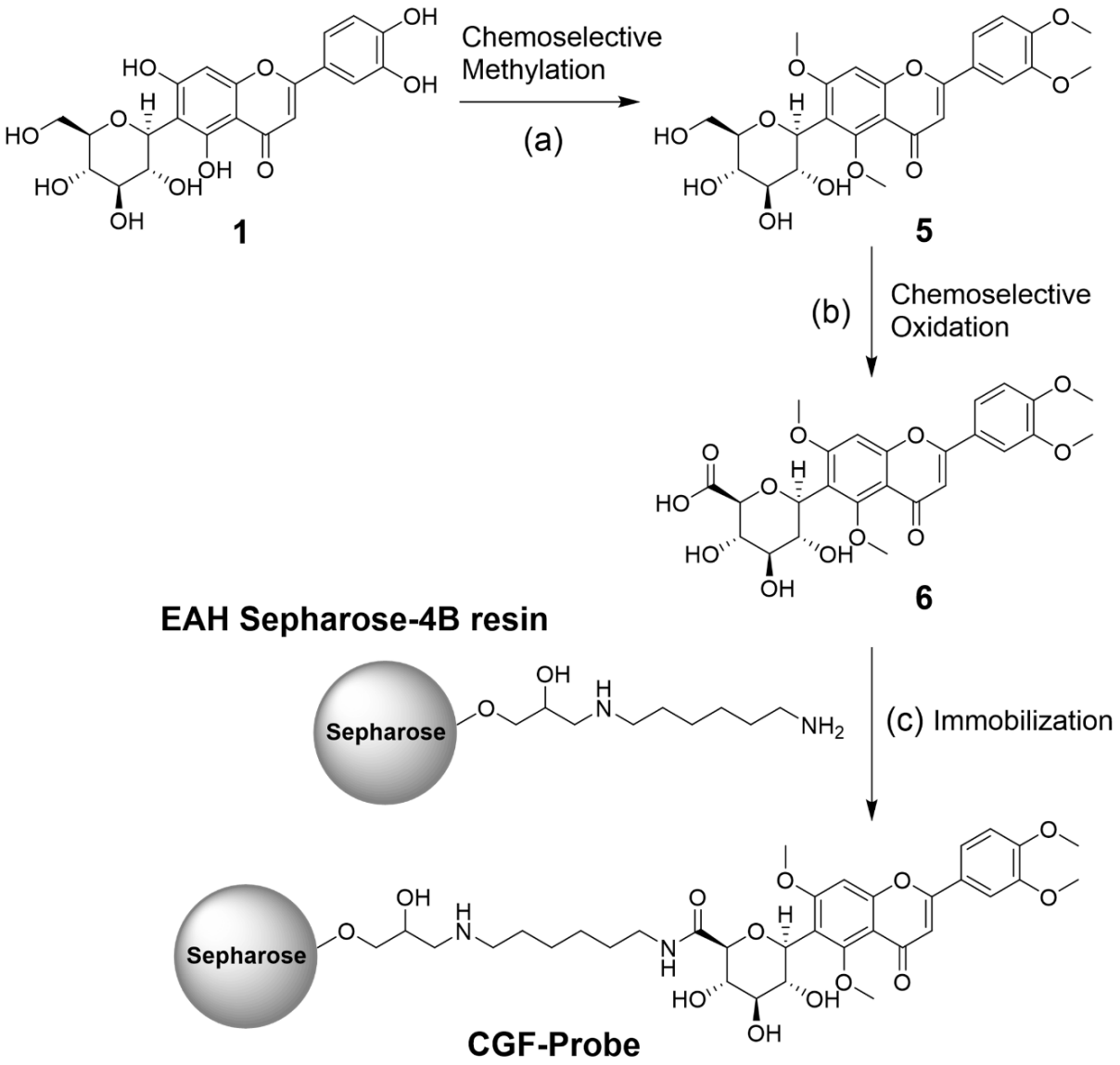

Figure 2.20. Construction of the CGF-probe beginning with isoorientin.
[a] Reagents and conditions: (a) $TMSCHN_2$, toluene, methanol, rt, 80%; (b) $[TEMPO]^+[BF_4]^-$, DCM, pyridine, rt, 95%; (c) Resin-NH_2, excess EDCI, aqueous, pH 5.0, 4 °C, 90%.

With an aim at the unbiased profiling of potential target proteins of *C*-glycosylflavones to assess their pleiotropic actions, the affinity-based chemical proteomics provides the opportunity to better understand on-target and off-target engagement of the ligand in the lysate of SH-SY5Y

cells. In Section 2.2, we have developed a series of selective GSK-3β inhibitors containing the *C*-glycosylflavone scaffold.[73] SAR studies demonstrated that compound **13**, an analogue of isoorientin **1**, with a hexyl amide group on the *C*-glycone inhibited GSK-3β with an IC_{50} value of 9.6 μM (Figure 2.19A). The moderate potency (IC_{50} < 10 μM) and reasonable selectivity of **13** on GSK-3β would allow for the target sampling in the cell lysate in an unbiased manner rather than only capturing GSK-3β (i.e., using compound **30**, which is highly optimized for targeting GSK-3β).

The design of an affinity probe must ensure that the ligand to be immobilized retains appropriate functional activity and binding specificity.[59-60] The probe must have a spacer (commonly 6–15 atom length, flexible chain) linking the ligand to the resin matrix to ensure the binding accessibility and specificity to target proteins.[59-60] Therefore, we designed a CGF-probe by coupling the ligand to the EAH Sepharose-4B resin, which contains a covalent linkage of 1,6-diaminohexane to sepharose as the spacer (Figure 2.19B). The CGF-probe was synthesized according to the route outlined in Figure 2.20. The key step was involved in an amide coupling of the compound **6** with EAH Sepharose-4B resins via EDCI catalysis. The ligand immobilization on resins was in 90% yield as determined by HPLC and readily visualized by the characteristic yellow color of *C*-glycosylflavones in comparison to the original resins (Figure 2.21).

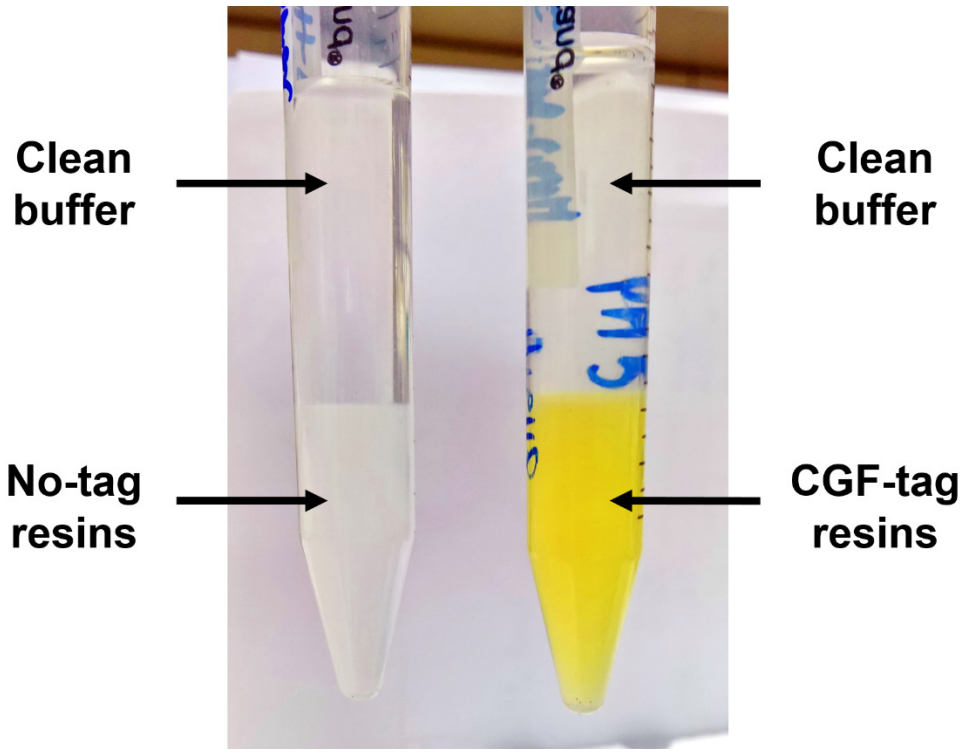

Figure 2.21. Comparison of EAH-4B resins before and after CGF immobilization.

2.3.2. Functional Validation of the CGF-Probe

To confirm that CGF-probe retains the same binding specificity to GSK-3β as the free ligand, an affinity pulldown assay was conducted in parallel using both CGF-tag and no-tag resins. A mixture of standard proteins (i.e., GSK-3β, bovine thyroglobulin, IgA, IgG, ovalbumin, and myoglobin) with different molecular weights and functions was subjected to affinity chromatography followed by 10% SDS-PAGE. As shown in Figure 2.22, the CFG-probe specifically bound to GSK-3β within the protein mixture, which was observed in SDS-gel staining and confirmed by MS analysis (in-gel digestion of the respective band). In contrast, the resins without CGF-tag showed no protein binding at all. The results thus validated the functional activity of the synthetic CGF-probe.

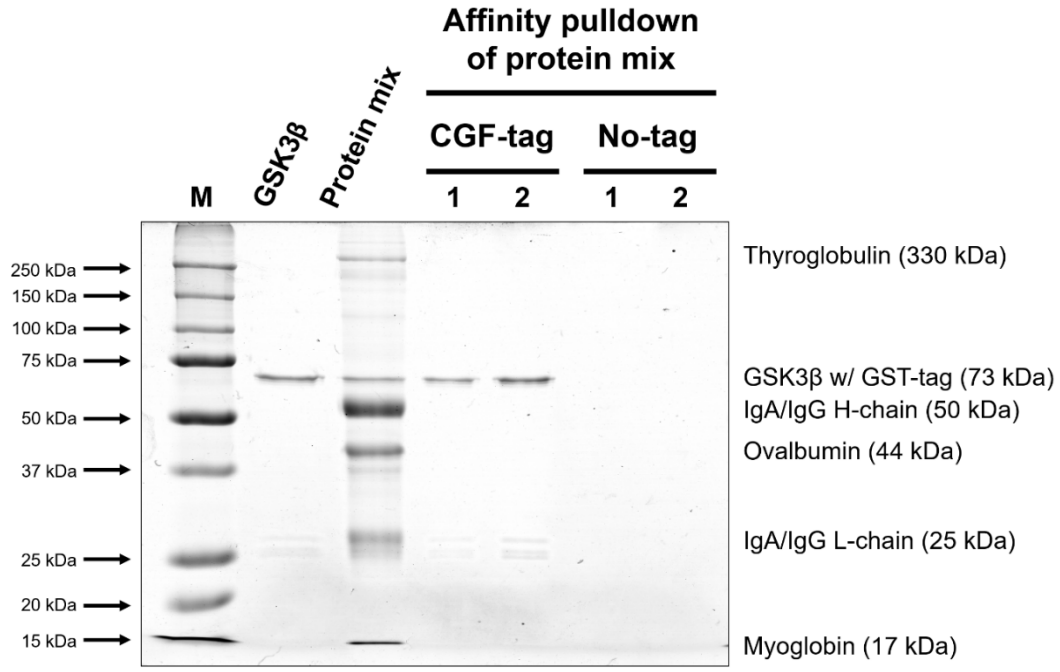

Figure 2.22. Functional validation of the CGF-probe for GSK-3β binding specificity. SDS-PAGE analysis on the protein mixture in the affinity pulldown assays with CGF-tag or no-tag resins. The protein mixture containing bovine thyroglobulin, IgA, IgG, GSK-3β, ovalbumin, and myoglobin. M, protein marker. H-chain, antibody heavy chain. L-chain, antibody light chain.

2.3.3. Identification of Specific Targets of *C*-Glycosylflavone by Affinity-Based Quantitative Chemical Proteomics in a Neuronal Model

Affinity-based quantitative chemical proteomics was performed to profile and identify target proteins in a neuronal cell model. SH-SY5Y cells was treated with 1 μM $A\beta_{42}$ for 72 h. The resulting cells were harvested and lysed. To cope with the experimental variations, the cell lysate was split into eight aliquots for four sets of experiments in duplicate. Each of two aliquots were subjected to the affinity pulldown assay in varied conditions. The resulting eluates were subjected

to in-solution tryptic digestion followed by iTRAQ-8plex labeling. In particular, the iTRAQ labels 113-114 were used on the control samples whose proteins were from the affinity chromatography with no-tag resins; labels 115-116 were used on the samples whose proteins were from the affinity chromatography with CGF-tag resins; labels 117-118 were used on the samples whose proteins were from the low-dose competitive affinity chromatography (50 μM free ligand **13**) with CGF-tag resins; and labels 119-121 were used on the samples whose proteins were from the high-dose competitive affinity chromatography (100 μM free ligand **13**) with CGF-tag resins. After labeling, samples were pooled together and analyzed by nanoLC-ESI-QTOF-MS/MS to identify and quantify target proteins.

For specific target proteins bound to the CGF-probe, the iTRAQ reporter ions 115-116 showed significantly higher signal intensities than 113-114 (reporter ions for those proteins pulled down with no-tag resins) in MS spectra. In addition, the three-set experiments using the CGF-probe showed a MS signal pattern of decreasing intensities of the reporter ions due to the free ligand competition in affinity chromatography (i.e., ion intensities 115-116 > 117-118 > 119-121). Conversely, for nonspecific binding proteins, the iTRAQ reporter ions of all four-set experiments showed similar intensities in MS spectra.

In preliminary experiments, a total of 24 proteins were identified by the MASCOT protein search (Table 2.5). iTRAQ ratios (115-116 versus 113-114) of each identified protein were subjected to statistical analysis and only proteins identified with a significance value of $p < 0.05$ and 1% false discovery rate (FDR) were considered reliable hits. To differentiate specific binding proteins from nonspecific ones, a stringent iTRAQ ratio of 2.5-fold cutoff was established to avoid false positives according to the described procedure.[62] Collectively, six proteins (histone H2A type 1-B/E, histone H1.2, histone H2A.V, calmodulin-1, galectin-3-binding protein, and heterogeneous

nuclear ribonucleoprotein A1-like 2) were identified as specific target proteins of the CGF-probe, and their reporter ion intensities showed a dose-dependent manner in the free ligand competition (Table 2.5).Three proteins (histone H2A type 2-A, nucleolar and coiled-body phosphoprotein 1, and mitochondrial 60 kDa heat shock protein) were identified as nonspecific binding proteins. The remaining 15 proteins were not quantified by iTRAQ. The fold changes of iTRAQ ratios of the identified binding proteins are shown in Figure 2.23.

Table 2.5. Summary of protein identification and iTRAQ-based quantification.

Rank [a]	Mascot score	UniProtKB Accession #	Protein	MW (kDa)	Peptides [b]	SC [c] (%)	iTRAQ ratio [d]
1	234.5	H2A1B_HUMAN	Histone H2A type 1-B/E OS=Homo sapiens GN=HIST1H2AB PE=1 SV=2	14.1	2	22.3	4.46
2	210.4	H12_HUMAN	Histone H1.2 OS=Homo sapiens GN=HIST1H1C PE=1 SV=2	21.4	2	8.9	6.37
3	191.8	H2A2A_HUMAN	Histone H2A type 2-A OS=Homo sapiens GN=HIST2H2AA3 PE=1 SV=3	14.1	1	22.3	0.97
4	154.9	CALM1_HUMAN	Calmodulin-1 OS=Homo sapiens GN=CALM1 PE=1 SV=2	16.8	1	24.8	4.64
5	130.6	NOLC1_HUMAN	Nucleolar and coiled-body phosphoprotein 1 OS=Homo sapiens GN=NOLC1 PE=1 SV=2	73.6	1	2.1	0.73
6	127.1	LG3BP_HUMAN	Galectin-3-binding protein OS=Homo sapiens GN=LGALS3BP PE=1 SV=1	65.3	1	3.4	5.36
7	82.1	ACTB_HUMAN	Actin, cytoplasmic 1 OS=Homo sapiens GN=ACTB PE=1 SV=1	41.7	1	7.7	n/a
8	60.6	H15_HUMAN	Histone H1.5 OS=Homo sapiens GN=HIST1H1B PE=1 SV=3	22.6	3	10.6	n/a
9	52.9	1433G_HUMAN	14-3-3 protein gamma OS=Homo sapiens GN=YWHAG PE=1 SV=2	28.3	2	11.7	n/a
10	48.2	PDS5A_HUMAN	Sister chromatid cohesion protein PDS5 homolog A OS=Homo sapiens GN=PDS5A PE=1 SV=1	150.7	1	2.5	n/a
11	44.7	1433E_HUMAN	14-3-3 protein epsilon OS=Homo sapiens GN=YWHAE PE=1 SV=1	29.2	3	11.4	n/a
12	43.8	MARE1_HUMAN	Microtubule-associated protein RP/EB family member 1 OS=Homo sapiens GN=MAPRE1 PE=1 SV=3	30.0	2	11.9	n/a
13	34.9	TTBK1_HUMAN	Tau-tubulin kinase 1 OS=Homo sapiens GN=TTBK1 PE=1 SV=2	142.6	1	0.9	n/a
14	33.4	RA1L2_HUMAN	Heterogeneous nuclear ribonucleoprotein A1-like 2 OS=Homo sapiens GN=HNRNPA1L2 PE=2 SV=2	34.2	1	3.1	4.08
15	29.5	GRP75_HUMAN	Stress-70 protein, mitochondrial OS=Homo sapiens GN=HSPA9 PE=1 SV=2	73.6	1	6.9	n/a
16	23.5	SNRPA_HUMAN	U1 small nuclear ribonucleoprotein A OS=Homo sapiens GN=SNRPA PE=1 SV=3	31.3	2	11.0	n/a
17	20.8	CH60_HUMAN	60 kDa heat shock protein, mitochondrial OS=Homo sapiens GN=HSPD1 PE=1 SV=2	61.0	1	3.7	0.87
18	20.6	H2AV_HUMAN	Histone H2A.V OS=Homo sapiens GN=H2AFV PE=1 SV=3	13.5	1	22.7	4.34
19	18.8	TNR16_HUMAN	Tumor necrosis factor receptor superfamily member 16 OS=Homo sapiens GN=NGFR PE=1 SV=1	45.2	1	1.6	n/a

20	18.6	SOSB1_HUMAN	SOSS complex subunit B1 OS=Homo sapiens GN=NABP2 PE=1 SV=1	22.3	1	6.2	n/a
21	18.2	1433T_HUMAN	14-3-3 protein theta OS=Homo sapiens GN=YWHAQ PE=1 SV=1	27.7	1	4.9	n/a
22	16.5	RU2A_HUMAN	U2 small nuclear ribonucleoprotein A' OS=Homo sapiens GN=SNRPA1 PE=1 SV=2	28.4	1	5.5	n/a
23	16.3	RAB34_HUMAN	Ras-related protein Rab-34 OS=Homo sapiens GN=RAB34 PE=1 SV=1	29	1	3.9	n/a
24	13.5	H2B1B_HUMAN	Histone H2B type 1-B OS=Homo sapiens GN=HIST1H2BB PE=1 SV=2	13.9	1	11.9	n/a

[a] Ranking based on the Mascot score. [b] Number of identified peptides. [c] Sequence coverage. [d] Median of iTRAQ ratios of reporter ions (115-116)/(113-114), representing ratios of proteins from CGF-tag pulldown versus proteins from no-tag pulldown.

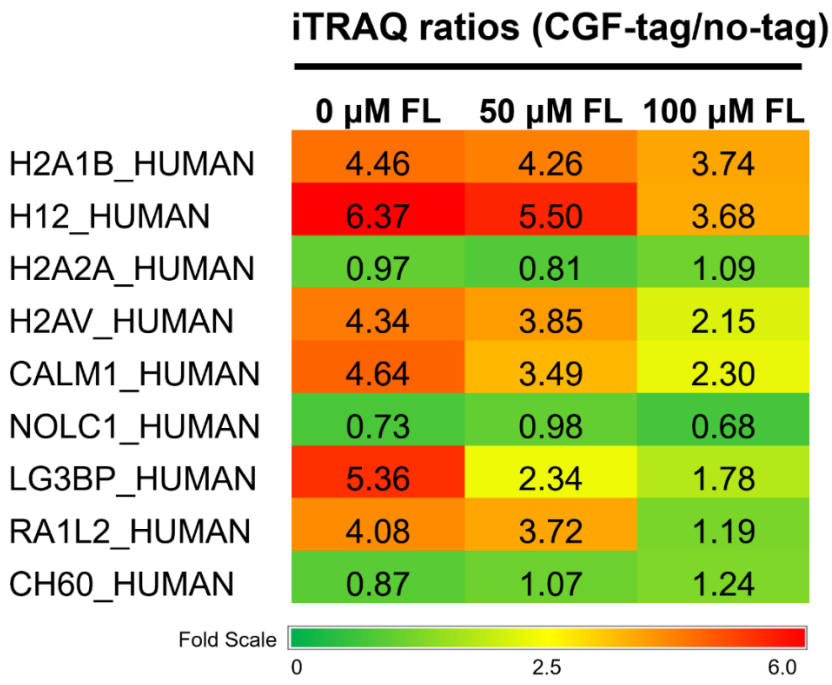

Figure 2.23. Heatmap of iTRAQ ratios of the identified target proteins in the affinity pulldown assays.
A stringent iTRAQ ratio of 2.5-fold cutoff was set to differentiate between the specific and nonspecific binding proteins. Competitive affinity assays (0, 50, and 100 μM free ligand **13**) indicate a decreased binding capacity of the CGF-probe. FL, free ligand.

To further validate the identified specific binding proteins by iTRAQ analysis, the lysate eluates from each of affinity pulldown were analyzed by 12% SDS-PAGE. The resulting stained SDS-gel (Figure 2.24) showed that the CGF-tag resins enriched many proteins with molecular weights ranging from 15 to 50 kDa in comparison with the no-tag resins. Moreover, the competitive affinity assays with the free ligand **13** (0, 50, and 100 μM) decreased target proteins in a dose-dependent manner. Two selected protein bands as depicted were cut and proceeded with in-gel digestion followed by LC-MS protein analysis. They were confirmed as histone H1.2 and histone H2A type 1-B/E, which are the two highest scored proteins identified in the iTRAQ-based proteomic analysis (Table 2.5).

Additional experiments aiming at target/pathway validation using different molecular biology techniques such as immunoblotting, biochemical assay, microarray, ChIP, qPCR, RNA-seq, or CRISPR-Cas9 genome editing to manipulate the SH-SY5Y cells will help elucidate the neuroprotective mechanisms. Nevertheless, the proteomics data by now demonstrated that the 6-*C*-glycosylflavones specifically bind to other target proteins in addition to GSK-3β in the neuronal model.

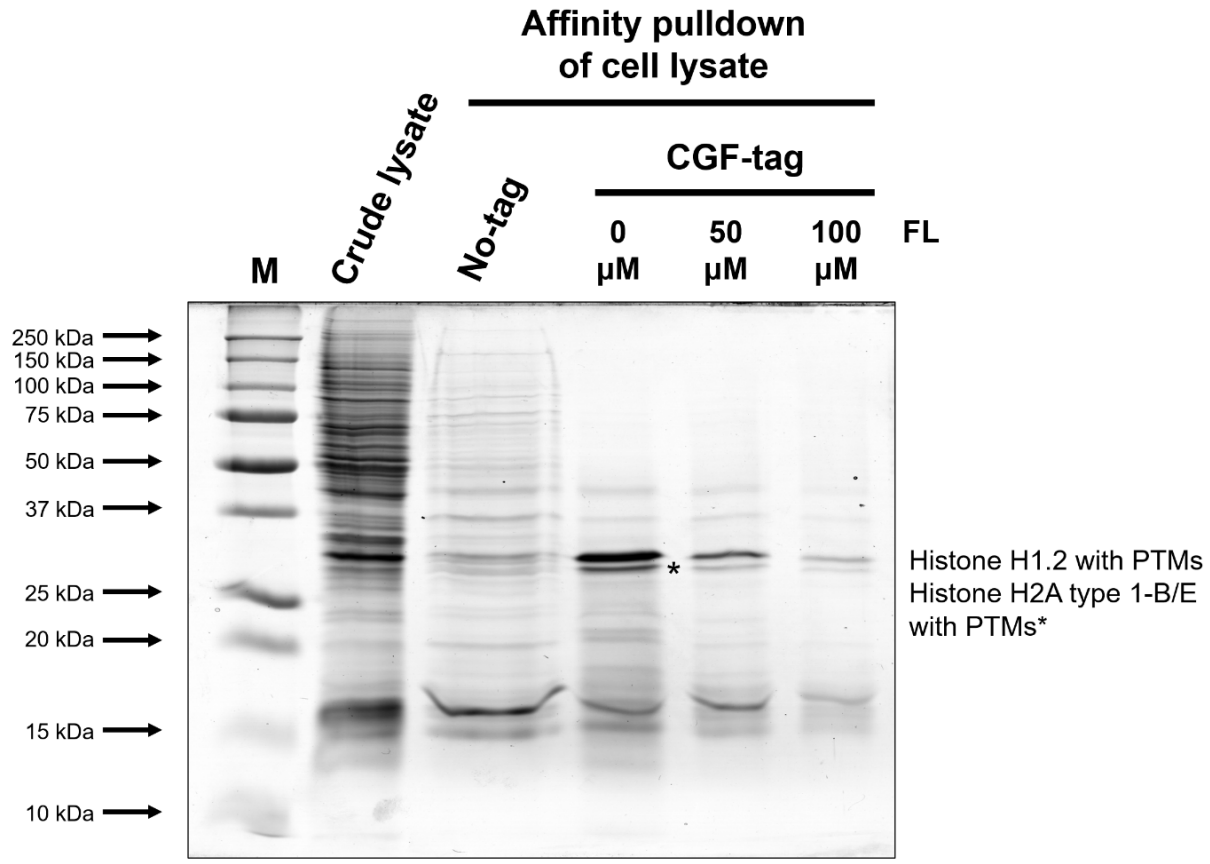

Figure 2.24. Validation of the target proteins deduced from iTRAQ-based proteomics. SDS-PAGE analysis on the proteins from the SH-SY5Y cell lysate in the affinity pulldown using CGF-tag or no-tag resins. The stained SDS-gel showed that the CGF-tag resins enriched many proteins (i.e., range from 15 to 50 kDa) in comparison with the no-tag resins. Affinity competition with the free ligand **13** (0, 50, and 100 μM) showed decreasing target proteins in a dose-dependent manner. Two selected protein bands as depicted were cut and proceeded with in-gel digestion followed by LC-MS protein analysis, which were confirmed as histone H1.2 and histone H2A type 1-B/E. M, protein marker. FL, free ligand. PTMs, post-translational modifications.

2.3.4. Biomolecular Networks Analysis of Target Proteins Reveals Potential Pleiotropic Actions of C-Glycosylflavone

Molecular networking of the identified proteins was visualized and analyzed with Cytoscape 3.6[170] and STRING 10.5[171]. To establish comprehensive molecular networks with rational nodes (i.e., proteins) and edges (i.e., protein-protein associations), a total of 26 proteins identified by iTRAQ chemical proteomics (24 proteins) and by our previous kinase studies (GSK-3β and tau protein) were subjected to bioinformatic analyses. Interestingly, the functional protein networking (Figure 2.25) indicated that most of the identified proteins are biologically connected and show active associations as supported by the literature and curated databases (edge confidence score > 0.400). The resulting protein-protein interaction (PPI) enrichment *p*-value is 0.000486. In particular, three protein clusters including core and linker histones, actin/GSK-3β/tau/calmodulin, and 14-3-3 proteins/MARE1/PDS5A/TNR16 are interconnected. Two small subset clusters including nuclear ribonucleoproteins (RA1L2/RU2A/SNPRA) and mitochondrial chaperone proteins (CH60/GPR75) are isolated. The proteins SOSB1, LG3BP, TTBK1, NOLC1, and RAB34 show a low confidence of PPI (edge confidence score ≤ 0.150).

Gene ontology (GO) annotation on cellular components (Figure 2.26) revealed that *C*-glycosylflavones may perturb 36% of identified proteins involved with nucleus, 22% involved with cytoplasm, 14% involved with chromosome, 10% involved with cytoskeleton, 7% involved with cell membrane, 5% involved with mitochondrion, and 2% involved with phagosome, Golgi, or extracellular matrix.

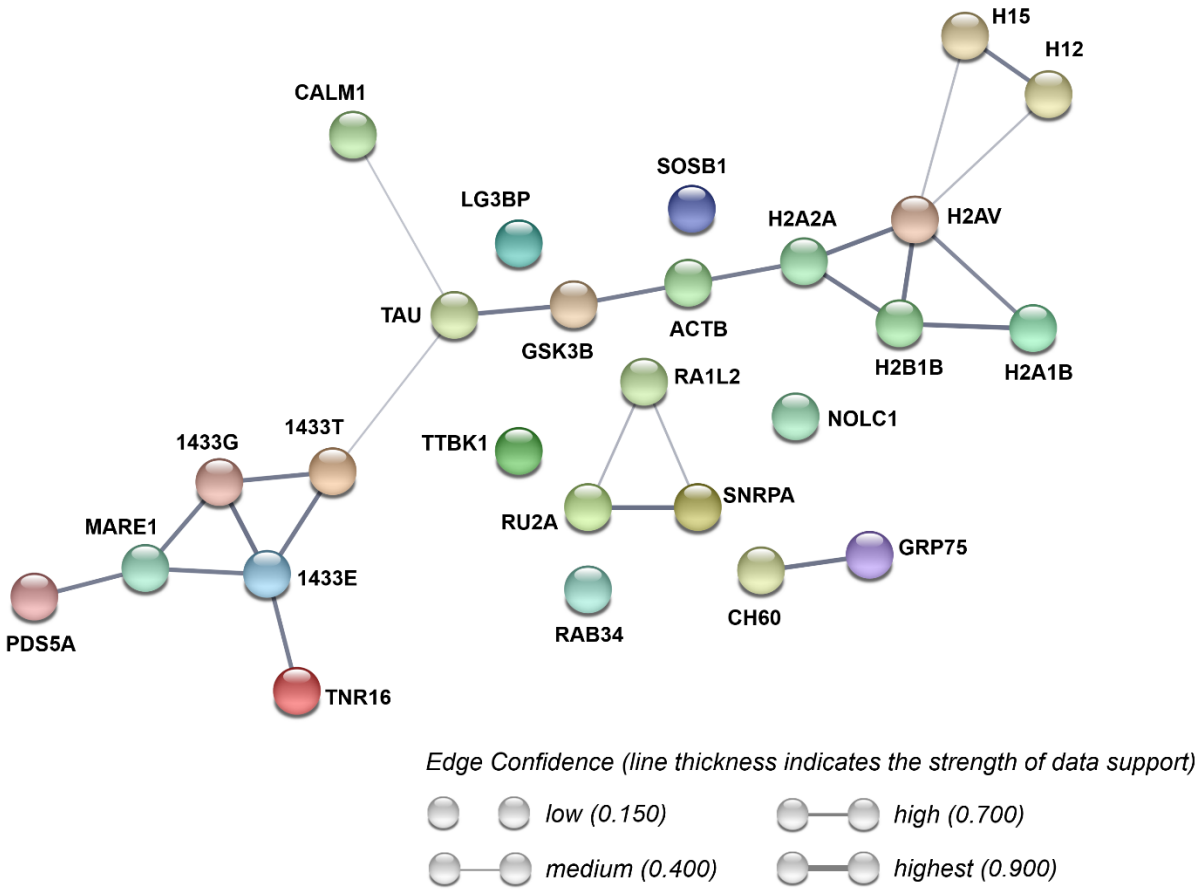

Figure 2.25. Biomolecular networks of the identified proteins bound to *C*-glycosylflavones. The networks were constructed by Cytoscape and STRING programs. The edge thickness represents the statistical data confidence deduced by the literature and curated databases. Colored circles represent protein nodes.

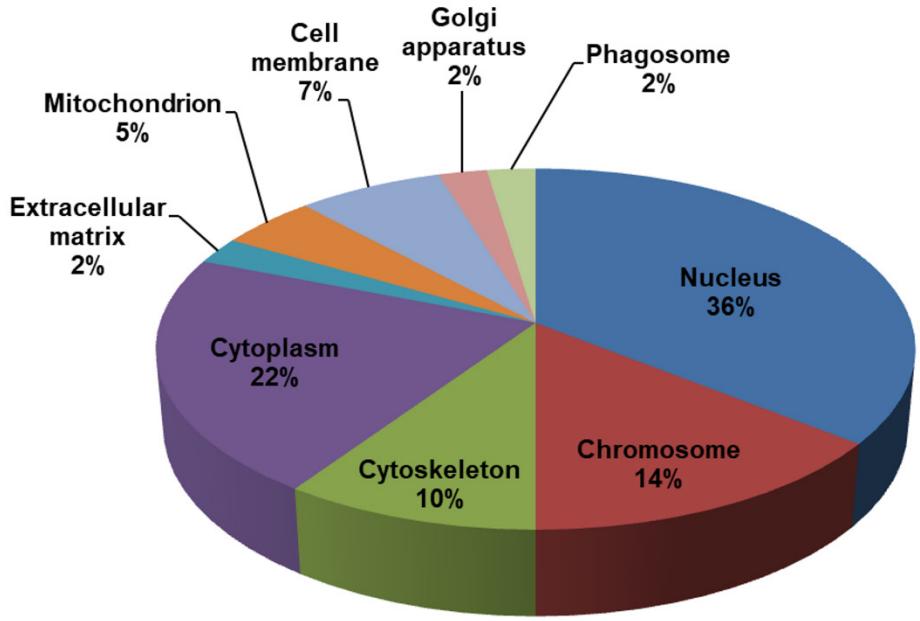

Figure 2.26. Cellular component annotation of the identified proteins bound to *C*-glycosylflavones.

GO annotation on biological process with statistical assessment (FDR threshold, -log(*p*-value) > 1.3) (Figure 2.27) indicated that nervous system development (e.g., substantia nigra/midbrain development, CNS development, and regulation of axonogenesis), apoptosis (both intrinsic and extrinsic pathways), chromatin modulation (e.g., histones and nucleosome assembly, chromatin assembly, and DNA packaging) are of highest probability affected by *C*-glycosylflavones. Small GTPase signaling, microtubule dynamics, intracellular transport, and organelle organization are intervened as well.

Regarding the KEGG pathway enrichments (Figure 2.28), bioinformatic analysis indicated that the Hippo signaling, cell cycle, and neurotrophin signaling are highly affected (-log(*p*-value) > 3.0). The PI3K/Akt signaling that governs cell survival (FDR, -log(*p*-value) > 2.5), the

spliceosomal signaling (FDR, -log(*p*-value) > 1.8), Alzheimer's pathway (FDR, -log(*p*-value) > 1.5), and Rap1 signaling (FDR, -log(*p*-value) > 1.3) are also significantly affected.

Interestingly, GO annotation on the molecular function suggested that most of the identified proteins are associated with enzyme/ligase binding, DNA/RNA binding, and small-molecule binding (Figure 2.29A). Particularly, 19 out of 26 identified proteins show statistically high probabilities of binding with organic cyclic or heterocyclic compounds (Figure 2.29B). Such a prediction is in good agreement with our iTRAQ-based chemical proteomics and the previous GSK-3β inhibition studies that the CGF-probe containing heterocyclic glycone and flavone moieties showed specific binding to histones (i.e., H2A1B, H12, and H2AV), RA1L2, and GSK-3β.

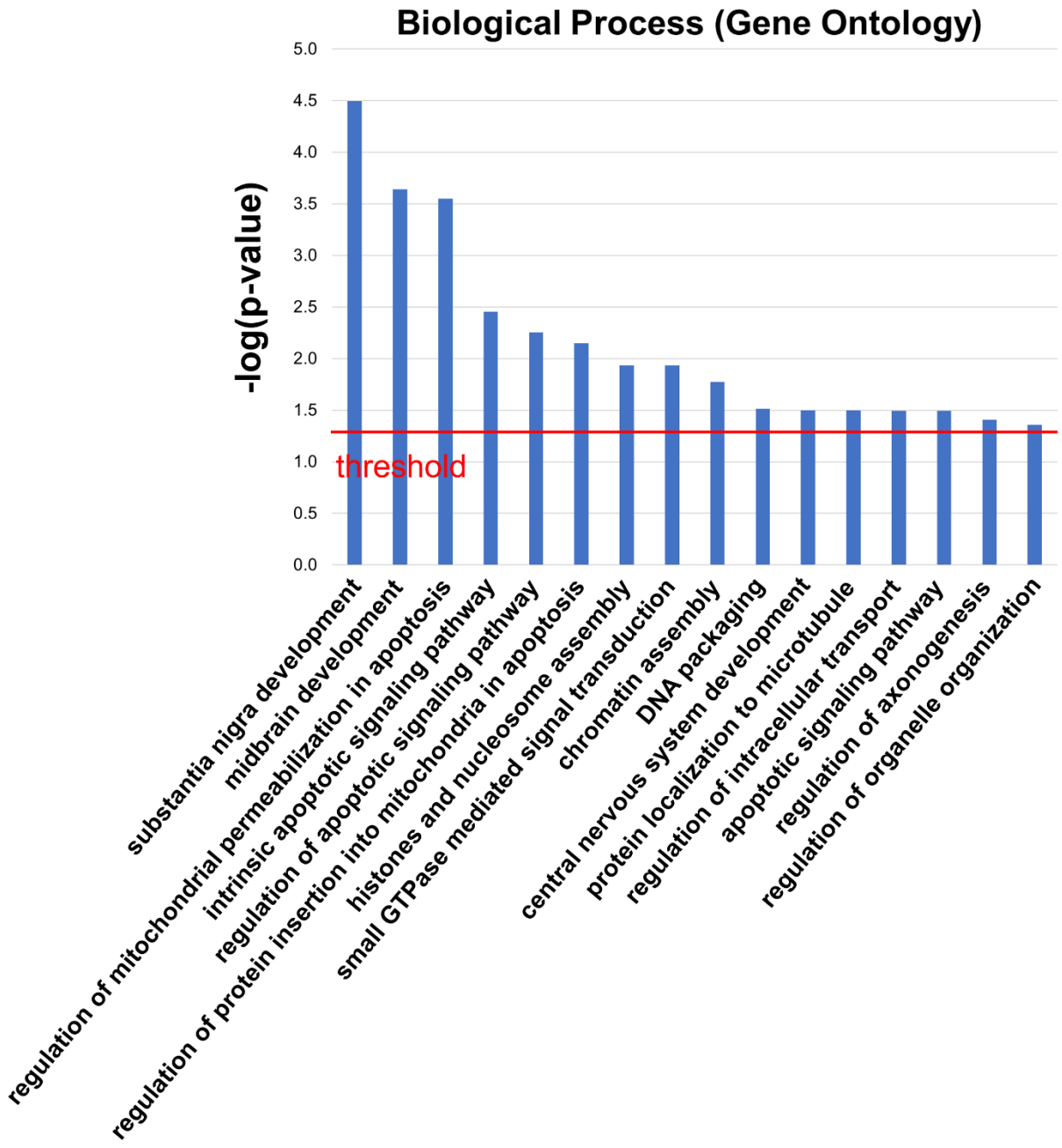

Figure 2.27. Biological process of the identified proteins bound to *C*-glycosylflavones.
The biological process was analyzed by gene ontology (GO) enrichment. FDR threshold, -log(*p*-value) > 1.3, equivalent $p < 0.05$.

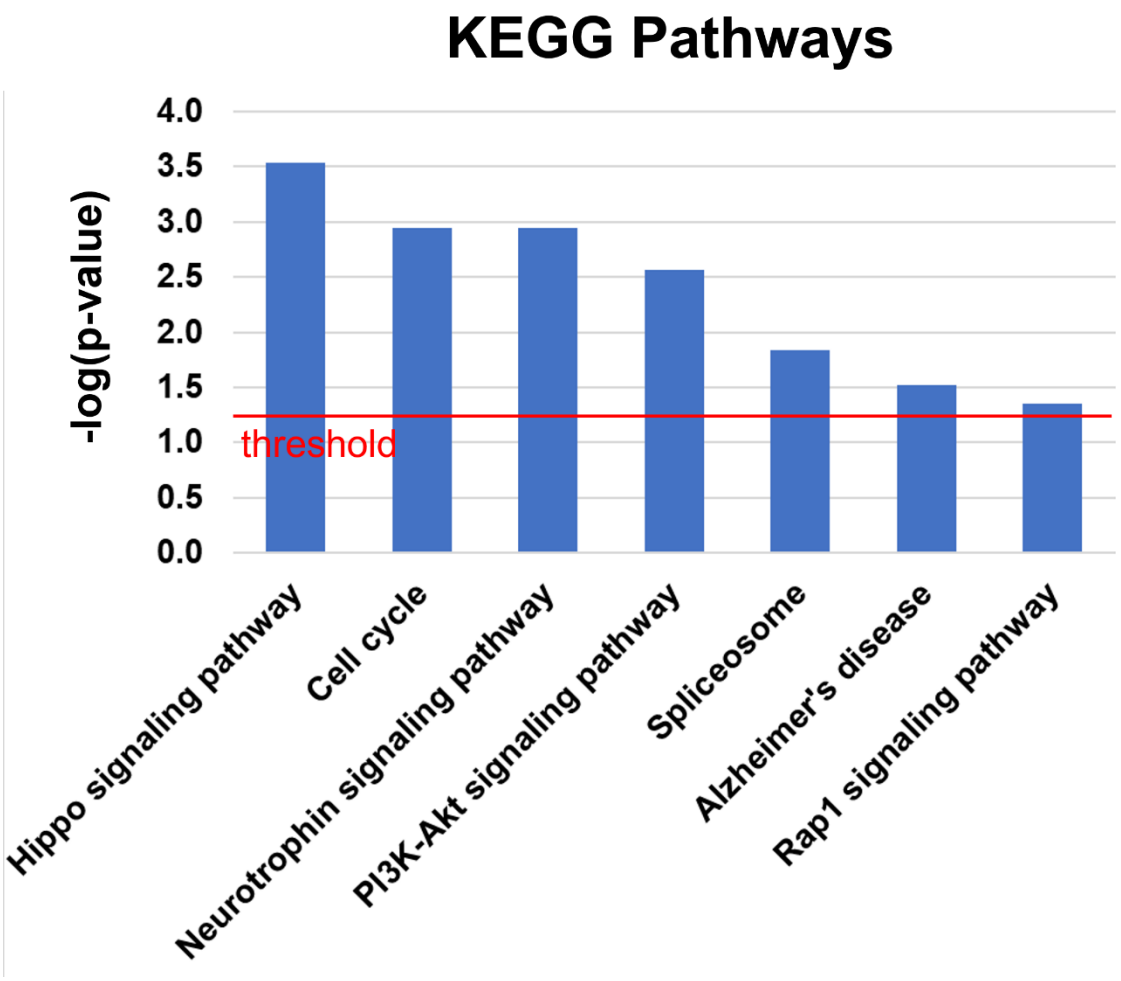

Figure 2.28. KEGG pathways of the identified proteins bound to *C*-glycosylflavones.
The pathways were analyzed by STRING. FDR threshold, -log(*p*-value) > 1.3, equivalent $p < 0.05$.

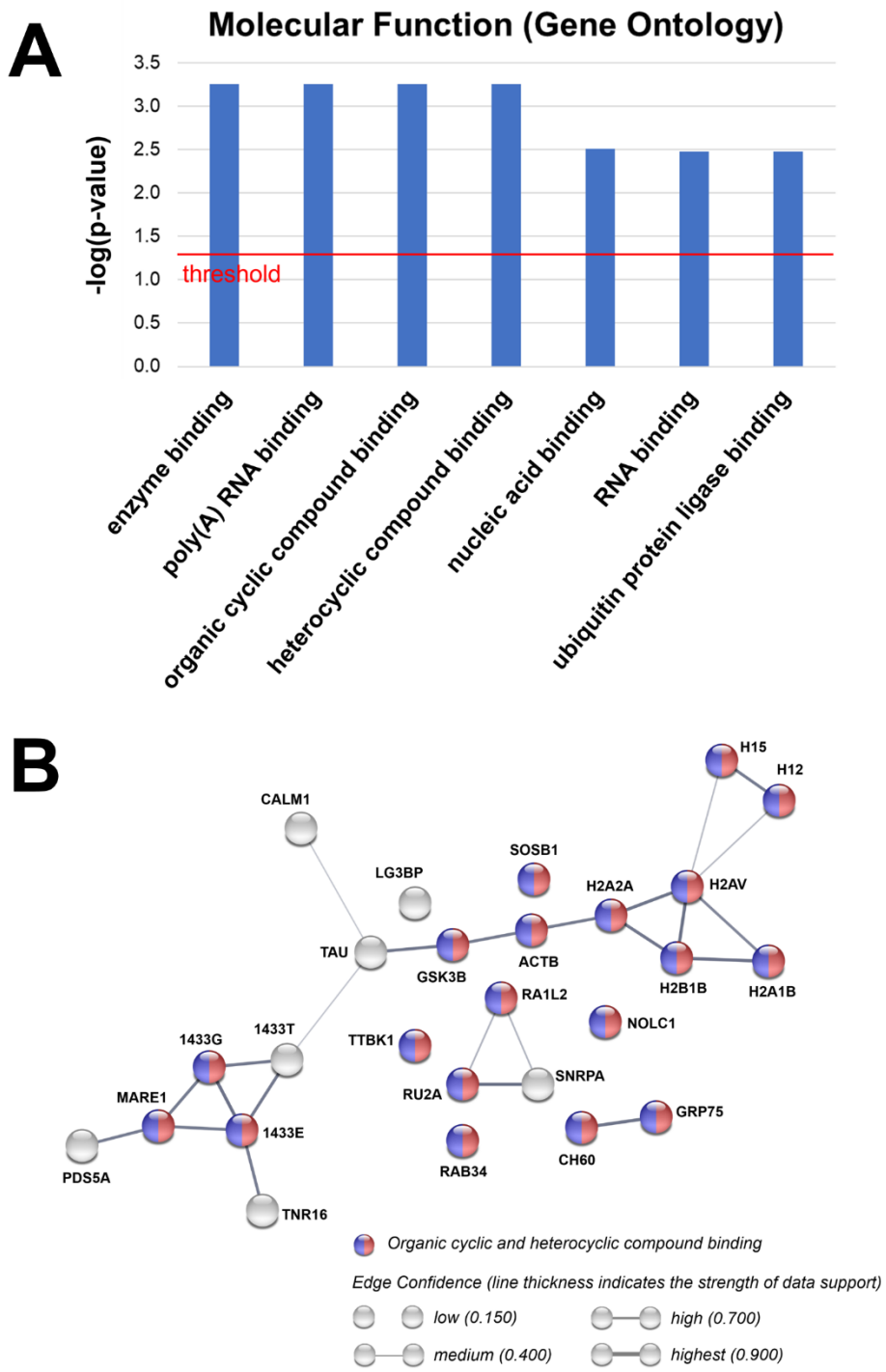

Figure 2.29. Molecular function of the identified proteins bound to *C*-glycosylflavones.
(A) The molecular function was analyzed by gene ontology (GO) enrichment. FDR threshold, -log(*p*-value) > 1.3, equivalent $p < 0.05$. (B) Biomolecular networks of the identified proteins. Bicolored circles represent proteins predicted with high binding affinity to organic cyclic or heterocyclic small-molecule compounds.

2.3.5. Discussion

In the present pilot study, an affinity-based quantitative chemical proteomics followed by comprehensive bioinformatic analyses revealed that the 6-*C*-glycosylflavones are indeed multi-target directed ligands. Such pleiotropic actions may either exert multi-faceted benefits for AD or raise problems of potential toxicity and side effects.[72, 156] Besides GSK-3β inhibition, these compounds specifically bind to histones, calmodulin-1 (CALM1), galectin-3-binding protein (LG3BP), and heterogeneous nuclear ribonucleoprotein A1-like 2 (RA1L2) in SH-SY5Y cells as supported by the iTRAQ quantitative proteomics study.

Histone modulations and the corresponding PTMs have been recognized as a key factor in epigenetic regulation of gene expression in AD and other neurodegenerative disorders.[172-173] In AD condition, small-molecule ligands bound to histones may exert intervention of epigenetic mechanisms in neurons such as DNA methylation and histone acetylation, which may recover neuroplasticity and cell viability.[173-174] Drugs targeting epigenetic changes may reverse AD in genetic level, offering another strategy for the treatment of neurodegenerative disorders.[173-174]

Calmodulin-1 (CALM1) is a multifunctional calcium-binding protein universal in human cells. CALM1 specific binds to Ca^{2+} ions involving in calcium signaling pathway by modifying various target proteins such as kinases or phosphatases.[175] CALM1 also plays an important role in mediating synaptic activity in neurons. Ca^{2+} dysfunction has been implicated in amyloid cascade and AD pathogenesis.[107, 176-177] The present data suggested that *C*-glycosylflavones bind to CALM1 and may intervene aberrant Ca^{2+} signaling in AD. Nonetheless, because calmodulins are essential regulators for the Ca^{2+} homeostasis in all human cells, modulating calmodulin activity by *C*-glycosylflavones, while not necessarily causing cellular toxicity directly, may also affect normal

signaling pathways. Investigation on how *C*-glycosylflavones intervene Ca^{2+} signaling in cells and how to avoid potential toxicity is mandatory.

Galectin-3-binding protein (LG3BP) modulates cell adhesion and cell-matrix interactions. LG3BP has been implicated in immune response associated with natural killer (NK) and lymphokine-activated killer (LAK) cell cytotoxicity, which may stimulate immune defense against viruses and tumor cells.[178] LG3BP interacts with galectin-3 mediating apoptosis. A recent study of AD showed that internalization of tau aggregates damages endosomal membrane, which was detected by galectin-3-binding assay.[179] We hypothesize that tau pathology in AD may disrupt LG3BP functions in neurons that promotes neurodegeneration (i.e., apoptosis), and the *C*-glycosylflavone may intervene this pathological pathway of AD.

Heterogeneous nuclear ribonucleoprotein A1-like 2 (RA1L2) is involved in the processing and transport of mRNA and modulate RNA splicing. Dysfunctions and mutations of RA1L2 have been implicated in neurodegeneration such as amyotrophic lateral sclerosis (ALS) and multisystem proteinopathy (MSP).[180] It has been reported that RA1L2 plays a role in regulation of RNA splicing of β-amyloid precursor protein in AD neurons.[181-182] Our finding suggested *C*-glycosylflavones specifically bind to RA1L2 and may intervene aberrant RNA metabolism in AD.

In summary, the preliminary data suggest pleiotropic actions of *C*-glycosylflavones. Nevertheless, all hypotheses deduced from the proteomics study require further rigorous investigations and more scientific efforts are necessary to advance this line of research. In particular, it should be prudent to investigate potential toxicity of the *C*-glycosylflavones due to their binding to histones, CALM1, LG3BP, or RA1L2, as all these proteins are essential to the normal cellular functions. It is important to perform a parallel proteomics experiment using SH-SY5Y cell without Aβ treatment. A comparison of the chemical proteomics data between untreated

and Aβ-treated cultures would link specific changes with Aβ-induced cellular toxicity to the systems pharmacology/toxicology upon treatment of *C*-glycosylflavones. In addition, it is also advantageous to use primary neurons (i.e., cells isolated from the brain of model animals with Aβ/tau pathology) with better physiological and biochemical relevance instead of the SH-SY5Y cell model.

** Methods and experimental procedures are listed in Chapter 3 of the dissertation.*

2.4. Conclusions and Future Directions

In this dissertation, I have elaborated a hypothesis-driven research on AD drug discovery. I have conducted rigorous and systematic investigations on *C*-glycosylflavones against tau and amyloid pathologies, which is involved with multidisciplinary strategies of natural products chemistry, biochemistry, medicinal chemistry, chemical biology, molecular biology, and neuroscience.

Using target-based screening, the natural 6-*C*-glycosylflavone isoorientin from corn silks was identified as a substrate-competitive, ATP-noncompetitive inhibitor of GSK-3β. Subsequent phenotype-based screening substantiated its promising activities against tau hyperphosphorylation and Aβ neurotoxicity in the SH-SY5Y neuronal cell model for neuroprotection.[65] In addition to our findings, isoorientin has been reported for *in vitro* inhibitory activities against cholinesterases and BACE1.[183-184] Moreover, a recent study showed that the 6-*C*-glycosylflavone maysin, an analogue of isoorientin, attenuates Aβ burden and neuroinflammation in an APPswe/PSEN1dE9 mouse model.[69] Other pharmacological effects of isoorientin for human health have been revealed in the past years. Isoorientin shows selective antiproliferation and induces apoptosis on human hepatoblastoma cells (HepG2) but not on normal liver cells such as the rat liver cells (BRL-3A) and the human liver cell line (HL-7702).[66, 113, 185-188] The anticancer mechanisms are attributed to anti-oxidation, mitochondrial perturbation, and intervention of the ROS-related p53, PI3K/Akt, JNK, and p38 signaling pathways.[66, 113, 185-188] Isoorientin also inhibits human pancreatic and breast cancer cells.[189-190] Moreover, it has been reported that isoorientin inhibits lipopolysaccharide-induced inflammation via down-regulation of MAPK/NF-κB signaling pathway in BV-2 microglia.[67, 191] Isoorientin suppresses secretion of inflammatory cytokines in human keratinocytes (HaCaT).[192] Recently, anti-obesitic and anti-diabetic effects of isoorientin have been reported. It

regulates lipid metabolism by improving mitochondrial function and activates the insulin signaling pathway in 3T3-L1 adipocytes *in vitro*[193-194] as well as prevents hyperlipidemia and liver injury in high-fructose-fed mice.[68] Regarding the toxicological profiles, isoorientin from food crop maize is conceivably safe and tolerable as supported by *in vivo* subchronic toxicity studies of corn silk-derived flavones in mice and rats[70-71] as well as the aforementioned animal studies for diabetes.[68] Taken together, the accumulating evidence indicates that isoorientin is a promising natural product drug lead with medicinal prospects, and our study contributes new knowledge of this agent for potential AD therapy.

Aiming at improving therapeutic potential, computer-aided drug design and SAR-based optimization have led to discovery of a series of new synthetic GSK-3β inhibitors, inspired by the 6-*C*-glycosylflavones, with high kinase selectivity, passive membrane permeability, and anti-AD activities in various biological evaluations.[73, 145] While the results are encouraging, limitations need be noted that most investigations solely rely on techniques such as *in vitro* enzymatic assays, cell-based assays, and *in silico* computational modeling. Additional experiments using site-directed mutagenesis of GSK-3β to generate mutants for kinase inhibitor study and eventually conducting X-ray co-crystallography of inhibitor–GSK-3β complex will offer more conclusive evidence to support the proposed molecular mechanisms and provide guidance for further lead optimization. In addition, it will be useful to investigate the pharmacological effect by co-dosing other known GSK-3β inhibitors with a given *C*-glycosylflavone-based inhibitor in SH-SY5Y cells, which could provide other aspects for functional validation. It would be also worth testing these agents for potential neuroregeneration. As for cell models in the future research, manipulating the SH-SY5Y cells with the CRISPR-Cas9 genome editing technique to generate GSK-3β null/mutant cells can be used as new tools for kinase inhibitor studies. Pharmacological studies of the new GSK-3β

inhibitors in primary neurons, glial cells or *ex vivo* brain slices derived from mouse models of Aβ/tau pathology should be considered. Ultimately, *in vivo* pharmacokinetics, pharmacodynamics, and animal studies are necessary to understand the neuroprotective efficacy of these agents for potential AD prevention.

In a pilot study using the affinity-based chemical proteomics approach, additional protein targets have been identified. We demonstrated that the 6-*C*-glycosylflavones are novel multitarget neuroprotective agents. A proposal of pleiotropic actions by which these agents exert anti-AD activities is briefly summarized in Figure 2.30. The 6-*C*-glycosylflavones intervene tauopathy and amyloid toxicity via GSK-3β inhibition. They bind to calmodulin-1 to interfere Ca^{2+} homeostasis in synaptic transmission. They also bind to histones that would exert epigenetic perturbation in response to the neurodegenerative stress. Binding to LG3BP in conjunction with associated proteins in apoptotic signaling pathways would prevent from neuroinflammation and neuronal death. And interacting with RA1L2 would affect RNA splicing and metabolism in response to AD stresses. Such pleiotropic actions of the 6-*C*-glycosylflavones a least in part support the increasing knowledge in the literature that isoorientin shows diverse benefits in human health. Nonetheless, like an old saying tells that "any medication is a double-edged sword." The 6-*C*-glycosylflavones bind to any of these protein targets may also affect their normal functions in cells. Future work should aim at target/pathway validation using different molecular biology techniques such as immunoblotting, biochemical assay, microarray, qPCR, etc. RNA-seq and ChIP-qPCR analyses will determine if the therapeutic intervention of 6-*C*-glycosylflavones is affecting gene expression or epigenetics in downstream pathways and identify any relationship between them. The metabolomic and biochemical analyses will determine the relationship between specific molecular

pathways and systems pharmacology/toxicology. Bioinformatic analysis will determine if any affected molecular pathways associated with AD pathology.

Collectively, the new knowledge gained through this study confers the therapeutic potential of 6-*C*-glycosylflavones for AD prevention, which is a valuable contribution to the AD biomedical sciences as well as AD drug discovery. Notwithstanding, further investigations through rigorous scientific efforts are still mandatory in the future.

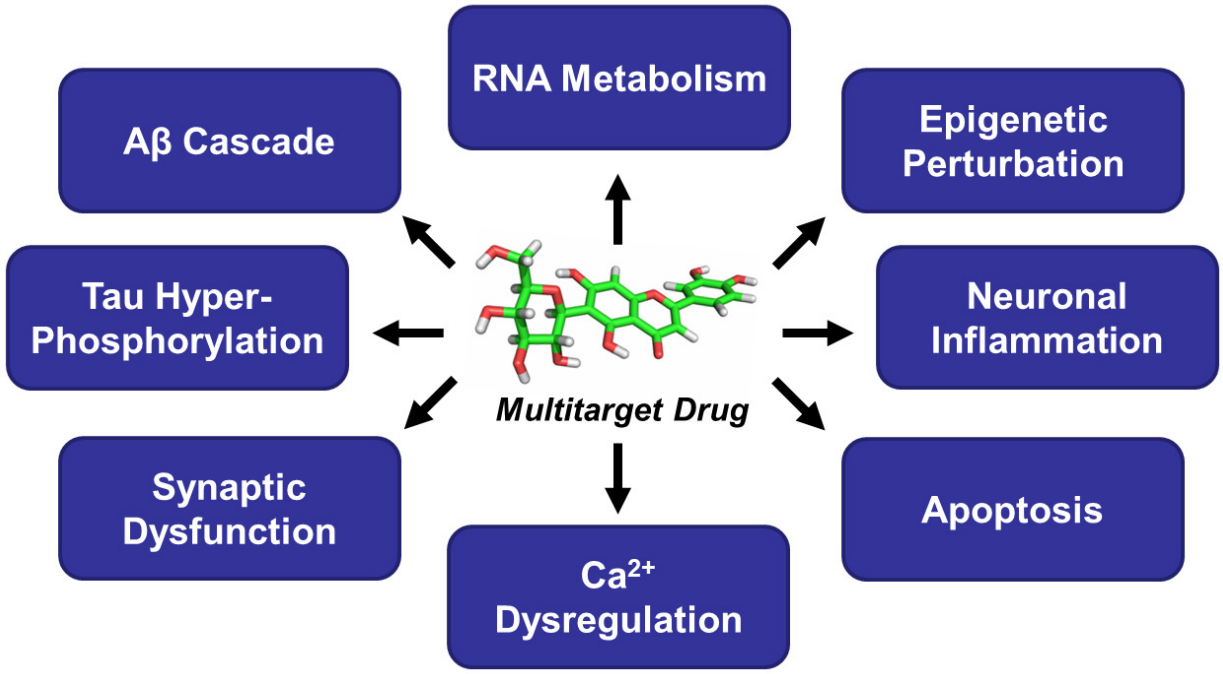

Figure 2.30. A proposed pleiotropic tree of the *C*-glycosylflavones for Alzheimer's disease.

CHAPTER 3

3. EXPERIMENTAL PROCEDURES

3.1. Chemicals and Reagents

All solvents and reagents were from commercial sources and were used without further purification. Natural flavones (isoorientin, orientin, and luteolin), staurosporine, TDZD-8, lithium chloride, theophylline, atenolol, desipramine, $TMSCHN_2$, $[TEMPO]^+[BF_4]^-$, HCTU, retinoic acid, organic amines, Triton X-100, BCIP/NBT reagents, and protease inhibitor cocktail were from Sigma-Aldrich (Saint Louis, MO, USA). β-Amyloid peptide 1-42 ($A\beta_{42}$) was from AnaSpec (Fremont, CA, USA). Trypsin/Lys-C mix, Kinase Selectivity Profiling Assay Kit, ADP-Glo Kinase Assay Kit, and CellTiter 96 AQueous One Solution Cell Proliferation MTS Assay Kit were from Promega (Madison, WI, USA). Precoated PAMPA plate system was from Corning (Tewksbury, MA, USA). iTRAQ Reagent-8plex kit was from SCIEX (Foster City, CA, USA). Antibodies Tau-5, Tau pS199/pS202, Tau pS396, GSK-3β, GSK-3β pS9, human Tau pS396 ELISA Kit, and Cell Extraction Buffer were from Invitrogen (Camarillo, CA, USA). β-Actin antibody was from GenScript (Piscataway, NJ, USA). Alkaline phosphatase-conjugated secondary antibodies were from Southern Biotech (Birmingham, AL, USA). EAH Sepharose 4B resins were from GE Healthcare (Chicago, IL, USA).

3.2. General Procedures for Instrumental Analysis

High-resolution mass spectrometric data were obtained on a Bruker maXis Impact nanoLC-QTOF-MS spectrometer in ESI positive mode. Accurate masses of all analytes were obtained from

the pseudo-molecule $[M+H]^+$ and were within 5 ppm mass error. ^1H, ^{13}C and 2D NMR data were recorded with a Varian Unity Inova 500 MHz spectrometer. NMR spectra were referenced to the appropriate residual solvent signal (δ_H 2.50, δ_C 39.5 for DMSO-d_6) with chemical shifts reported in δ units (ppm). Resonance multiplicities are denoted s, d, t, q, m, and br for singlet, doublet, triplet, quartet, multiplet, and broad, respectively.

All reactions were monitored by LC-MS (Bruker nanoLC-QTOF-MS). Compounds in crude reaction mixtures were separated by flash column chromatography on HyperSep C18 (40–63 μm), and purified by semi-preparative reverse phase Agilent HPLC with a diode array detector (Waters XSELECT CSH Phenyl-Hexyl column, 150 × 10 mm, 5 μm, a linear gradient over 30 min from 10 to 50% aqueous acetonitrile containing 0.1% formic acid, flow rate 2.5 mL/min).

The purity of each compound was determined by analytical reverse phase Agilent HPLC with a diode array detector (Waters XSELECT CSH Fluoro-Phenyl column, 150 × 4.6 mm, 3.5 μm, isocratic elution with 35% aqueous acetonitrile containing 0.1% formic acid, detection at 210, 254, and 340 nm, flow rate of 0.8 mL/min). All the tested compounds were over 95% purity by HPLC-UV at 210 nm.

Luminescent measurement was performed on an Agilent Cary Eclipse fluorescence spectrophotometer. Optical absorbance was measured on a Multiskan GO Microplate spectrophotometer. Microscopic images were observed under a Nikon Diaphot inverted tissue culture microscope with Optronics MicroFire microscope camera.

3.3. Collection of Corn Silks

Fresh corn silks (CS, *Zea mays* L.) were collected from the Waimanalo Research Station, University of Hawaii at Manoa, USA. Upon collection, fresh CS sample was immediately lyophilized and stored at -20 °C until extraction.

3.4. Extraction and Isolation of Natural 6-C-Glycosylflavones

A modified protocol of the bioassay-guided fractionation was used.[195] A 90 g portion of lyophilized CS sample was exhaustively extracted with 1000 mL (×5) of CH_2Cl_2:MeOH (v/v 2:1) to yield 45 g of crude extract. This crude extract was subject to successive solvent partitioning using a modified Kupchan method with *n*-hexane, ethyl acetate (EtOAc), *n*-butanol and H_2O to yield four fractions of 3.7, 0.9, 4.8 and 34.7 g, respectively. The EtOAc fraction (0.9 g) was further subject to flash column chromatography on a DPA-6S polyamide column (50 g) using a step gradient of 25 (×2), 50 (×2), 75 (×2) and 100% (×2) MeOH in H_2O, affording eight fractions (A-H) of 230.5, 80.0, 40.2, 50.8, 30.5, 70.6, 70.1 and 90.5 mg. GSK-3β assay data indicated that the kinase inhibitory activity was concentrated in fraction F (70.6 mg). Separation of fraction F on a reversed-phase HPLC [CSH Fluoro-Phenyl, 150 × 4.6 mm, a linear gradient over 40 min from 10 to 50% acetonitrile in H_2O solvents, flow rate 0.7 mL/min, PDA detection] afforded five subfractions, whose GSK-3β inhibitory activities were concentrated in subfraction-2 (CS-EA-F-2; 3.1 mg) and subfraction-3 (CS-EA-F-3; 5.4 mg). Further purification of these two subfractions under the same conditions led to the isolation of **1** (t_R 17.5 min, 2.5 mg, 0.006% yield) and **2** (t_R 23.1 min, 1.2 mg, 0.003% yield) in over 95% purity as determined by HPLC-UV at 205 nm. The

identity of **1** and **2** was confirmed by ESI-QTOF-CID-MS/MS analysis and comparison with reported NMR spectroscopic data.

3.5. General Procedure for Semi-Synthesis of 6-C-Glycosylflavone Analogues

Preparation of Compound 5. The chemoselective methylation proceeded as described.[123] To a stirred solution of **1** (45 mg, 0.1 mmol) in a mixture of toluene (6 mL) and methanol (4 mL) was added $TMSCHN_2$ (2 M in hexane, 0.5 mL, 1 mmol). The reaction solution was stirred at room temperature for 8 h and the solvent was evaporated. The residue was purified by RP-HPLC (Waters XSELECT CSH Fluoro-Phenyl column, 150 × 4.6 mm, 3.5 μm, isocratic elution with 35% aqueous acetonitrile containing 0.1% formic acid, detection at 210, 254, and 340 nm, flow rate of 0.8 mL/min) to afford **5**.

Preparation of Compound 6. To a stirred solution of **5** (45 mg, 0.09 mmol) in a mixture of dichloromethane (6 mL) and pyridine (3 mL) was added $[TEMPO]^+[BF_4]^-$ (oxoammonium salt, 60 mg, 0.2 mmol). The reaction mixture was stirred at room temperature for 5 h. The reaction was quenched by adding drops of methanol and then evaporated to dryness. The residue was reconstituted in 5% $MeOH/H_2O$ and then eluted on a HyperSep C18 column using the same solvents to remove the red-orange nitroxide. Elution was continued with 90% $MeOH/H_2O$ and the eluate was collected as the crude product, which was further purified by RP-HPLC (Waters XSELECT CSH Fluoro-Phenyl column, 150 × 4.6 mm, 3.5 μm, isocratic elution with 35% aqueous acetonitrile containing 0.1% formic acid, detection at 210, 254, and 340 nm, flow rate of 0.8 mL/min) to afford **6**.

Preparation of Compound 7. To a stirred solution of **6** (1 mg, 2 μmol) in a mixture of toluene (1.5 mL) and methanol (1 mL) was added $TMSCHN_2$ (2 M in hexane, 2 μL, 4 μmol). The reaction solution was stirred at room temperature for 1 h and the solvent was evaporated. The residue was purified by RP-HPLC (Waters XSELECT CSH Fluoro-Phenyl column, 150 × 4.6 mm, 3.5 μm, isocratic elution with 35% aqueous acetonitrile containing 0.1% formic acid, detection at 210, 254, and 340 nm, flow rate of 0.8 mL/min) to afford **7**.

Preparation of Compounds 8-31. To a stirred solution of **6** (5 mg, 9.7 μmol) in a mixture of dimethylformamide (1 mL) and DIPEA (0.5 mL) was added HCTU (10 mg, 24 μmol) and then stirred for 10 min at room temperature. To this solution was added corresponding organic amines (each 50 μmol) and stirred at room temperature for 5 h.

The reaction was quenched by adding 1 *N* HCl followed by evaporation of solvents to dryness. The residue was purified by RP-HPLC (Waters XSELECT CSH Fluoro-Phenyl column, 150 × 4.6 mm, 3.5 μm, isocratic elution with 35% aqueous acetonitrile containing 0.1% formic acid, detection at 210, 254, and 340 nm, flow rate of 0.8 mL/min) to afford the final products.

3.6. Physical Data of Compound Characterization

3.6.1. Natural 6-*C*-Glycosylflavones from Corn Silk

Isoorientin (1): light yellow solid; HRESI-TOFMS *m/z* $[M+H]^+$ 449.1085 (calcd for $C_{21}H_{21}O_{11}^+$, 449.1078, -1.4 ppm error).

3'-Methoxymaysin (2): light yellow solid; HRESI-TOFMS *m/z* $[M+H]^+$ 591.1711 (calcd for $C_{28}H_{31}O_{14}^+$, 591.1708, -0.5 ppm error).

3.6.2. Semi-Synthetic 6-*C*-Glycosylflavones

2-(3,4-Dimethoxyphenyl)-5,7-dimethoxy-6-((2*S*,3*R*,4*R*,5*S*,6*R*)-3,4,5-trihydroxy-6-(hydroxymethyl)tetrahydro-2*H*-pyran-2-yl)-4*H*-chromen-4-one (5). Light yellow solid (80% yield). ^{1}H NMR (DMSO-d_6) δ 7.65 (dd, J = 8.6, 2.2 Hz, 1H), 7.54 (d, J = 2.2 Hz, 1H), 7.12 (d, J = 8.6 Hz, 1H), 7.09 (br s, 1H), 6.72 (br s, 1H), 4.65 (br d, J = 9.7 Hz, 1H), 4.05 (dd, J = 12.7, 9.2 Hz, 1H), 3.89 (s, 3H), 3.86 (s, 3H), 3.81 (s, 3H), 3.77 (s, 3H), 3.72 (dd, J = 12.6, 12.5 Hz, 1H), 3.34 – 3.28 (m, 1H), 3.27 – 3.12 (m, 3H). ^{13}C NMR (DMSO-d_6) δ 175.5, 163.4, 160.2, 158.9, 158.5, 151.8, 149.1, 123.2, 119.7, 111.9, 111.3, 109.4, 107.1, 107.0, 97.0, 82.0, 79.2, 73.1, 71.3, 70.9, 62.6, 62.0, 61.8, 56.4, 55.8. HRESI-TOFMS *m/z* $[M+H]^+$ 505.1710 (calcd for $C_{25}H_{29}O_{11}^+$, 505.1704, -1.1 ppm error). HPLC purity: 97.1% (210 nm).

(2*S*,3*S*,4*R*,5*R*,6*S*)-6-(2-(3,4-Dimethoxyphenyl)-5,7-dimethoxy-4-oxo-4*H*-chromen-6-yl)-3,4,5-trihydroxytetrahydro-2*H*-pyran-2-carboxylic acid (6). Light yellow solid (95% yield). ^{1}H NMR (DMSO-d_6) δ 7.65 (dd, J = 8.5, 2.0 Hz, 1H), 7.54 (d, J = 2.0 Hz, 1H), 7.12 (d, J = 8.5 Hz, 1H), 7.09 (br s, 1H), 6.76 (d, J = 6.6 Hz, 1H), 4.60 (d, J = 10.1 Hz, 1H), 4.02 (m, 1H), 3.89 (s, 3H), 3.85 (s, 3H), 3.82 (s, 3H), 3.75 (s, 3H), 3.30 – 3.16 (m, 3H). ^{13}C NMR (DMSO-d_6) δ 175.5, 173.0, 162.2, 160.4, 158.9, 158.5, 151.9, 149.2, 123.2, 119.7, 111.9, 111.4, 109.4, 107.1, 107.0, 97.1, 79.0, 78.5, 74.1, 72.5, 71.3, 63.5, 62.6, 56.6, 56.1. HRESI-TOFMS *m/z* $[M+H]^+$ 519.1502 (calcd for $C_{25}H_{27}O_{12}^+$, 519.1497, -0.9 ppm error). HPLC purity: 97.8% (210 nm).

Methyl (2*S*,3*S*,4*R*,5*R*,6*S*)-6-(2-(3,4-dimethoxyphenyl)-5,7-dimethoxy-4-oxo-4*H*-chromen-6-yl)-3,4,5-trihydroxytetrahydro-2*H*-pyran-2-carboxylate (7). Light yellow solid (87% yield). ^{1}H NMR (DMSO-d_6) δ 7.69 (dd, J = 8.5, 2.1 Hz, 1H), 7.56 (d, J = 2.1 Hz, 1H), 7.15 (br s, 1H), 7.12 (d, J = 8.5 Hz, 1H), 6.80 (d, J = 5.5 Hz, 1H), 4.57 (d, J = 9.6 Hz, 1H), 4.00 (m, 1H), 3.89 (s, 3H), 3.85 (s, 3H), 3.80 (s, 3H), 3.73 (s, 3H), 3.63 (s, 3H), 3.29 – 3.13 (m, 3H). ^{13}C

NMR (DMSO-d_6) δ 175.6, 172.9, 162.1, 160.1, 159.0, 158.4, 151.8, 149.1, 123.2, 119.7, 111.9, 111.4, 109.4, 107.1, 107.0, 97.0, 79.0, 78.5, 74.1, 72.5, 71.3, 63.4, 62.6, 56.6, 56.0, 51.8. HRESI-TOFMS *m/z* $[M+H]^+$ 533.1656 (calcd for $C_{26}H_{29}O_{12}^+$, 533.1654, -0.5 ppm error). HPLC purity: 97.1% (210 nm).

(2*S*,3*S*,4*R*,5*R*,6*S*)-6-(2-(3,4-Dimethoxyphenyl)-5,7-dimethoxy-4-oxo-4*H*-chromen-6-yl)-3,4,5-trihydroxy-*N*-propyltetrahydro-2*H*-pyran-2-carboxamide (8). Light yellow solid (90% yield). ^{1}H NMR (DMSO-d_6) δ 7.67 (d, *J* = 8.7 Hz, 1H), 7.53 (d, *J* = 2.2 Hz, 1H), 7.13 (s, 1H), 7.12 (d, *J* = 8.7 Hz, 1H), 6.76 (d, *J* = 5.9 Hz, 1H), 4.67 (br d, *J* = 10.1 Hz, 1H), 4.06 (q, *J* = 10.3 Hz, 1H), 3.87 (s, 3H), 3.83 (s, 3H), 3.77 (s, 3H), 3.71 (s, 3H), 3.60 (m, 1H), 3.50 (m, 1H), 3.23 (m, 1H), 2.99 (m, 2H), 1.36 (m, 2H), 0.78 (td, *J* = 7.4, 2.2 Hz, 3H). ^{13}C NMR (DMSO-d_6) δ 175.7, 168.7, 163.4, 160.5, 160.2, 158.4, 151.6, 149.3, 123.1, 120.4, 112.2, 111.9, 109.6, 107.2, 107.0, 96.8, 80.6, 79.0, 74.4, 71.6, 69.6, 63.9, 63.1, 56.7, 56.1, 40.8, 22.6, 11.5. HRESI-TOFMS *m/z* $[M+H]^+$ 560.2135 (calcd for $C_{28}H_{34}NO_{11}^+$, 560.2126, -1.6 ppm error). HPLC purity: 98.6% (210 nm).

(2*S*,3*S*,4*R*,5*R*,6*S*)-6-(2-(3,4-Dimethoxyphenyl)-5,7-dimethoxy-4-oxo-4*H*-chromen-6-yl)-3,4,5-trihydroxy-*N*-isopropyltetrahydro-2*H*-pyran-2-carboxamide (9). Light yellow solid (90% yield). ^{1}H NMR (DMSO-d_6) δ 7.67 (d, *J* = 8.1 Hz, 1H), 7.55 (d, *J* = 2.2 Hz, 1H), 7.14 (br s, 1H), 7.12 (d, *J* = 9.7 Hz, 1H), 6.77 (d, *J* = 5.1 Hz, 1H), 4.67 (d, *J* = 9.7 Hz, 1H), 4.05 (m, 1H), 3.92 (s, 3H), 3.89 (s, 3H), 3.85 (s, 3H), 3.83 (m, 1H), 3.81 (s, 3H), 3.59 (m, 1H), 3.57 (m, 1H), 3.23 (m, 1H), 1.04 (d, *J* = 6.4 Hz, 3H), 1.01 (d, *J* = 6.8 Hz, 3H). ^{13}C NMR (DMSO-d_6) δ 175.5, 168.7, 163.3, 161.7, 160.1, 158.7, 152.1, 149.2, 123.1, 119.5, 111.9, 111.3, 109.4, 107.1, 107.0, 97.0, 79.8, 78.5, 73.8, 71.4, 70.3, 63.4, 62.5, 56.6, 55.8, 40.3, 22.2, 22.2. HRESI-TOFMS *m/z*

$[M+H]^+$ 560.2117 (calcd for $C_{28}H_{34}NO_{11}^+$, 560.2126, 1.7 ppm error). HPLC purity: 97.2% (210 nm).

(2*S*,3*S*,4*R*,5*R*,6*S*)-6-(2-(3,4-Dimethoxyphenyl)-5,7-dimethoxy-4-oxo-4*H*-chromen-6-yl)-3,4,5-trihydroxy-*N*-butyltetrahydro-2*H*-pyran-2-carboxamide (10). Light yellow solid (90% yield). ^{1}H NMR (DMSO-d_6) δ 7.68 (d, J = 8.6 Hz, 1H), 7.55 (d, J = 2.2 Hz, 1H), 7.14 (s, 1H), 7.12 (d, J = 8.6 Hz, 1H), 6.81 (d, J = 6.7 Hz, 1H), 4.67 (br d, J = 10.2 Hz, 1H), 4.06 (m, 1H), 3.89 (s, 3H), 3.85 (s, 3H), 3.80 (s, 3H), 3.74 (s, 3H), 3.58 (m, 1H), 3.50 (m, 1H), 3.23 (m, 1H), 3.02 (m, 2H), 1.34 (m, 2H), 1.23 (m, 2H), 0.83 (m, 3H). ^{13}C NMR (DMSO-d_6) δ 175.9, 168.8, 163.2, 160.3, 160.2, 158.3, 151.8, 149.1, 123.3, 119.7, 111.7, 111.5, 109.2, 107.2, 106.9, 96.5, 80.1, 78.8, 74.0, 71.5, 70.3, 63.8, 62.9, 56.7, 56.1, 38.2, 31.2, 19.6, 13.8. HRESI-TOFMS *m/z* $[M+H]^+$ 574.2289 (calcd for $C_{29}H_{36}NO_{11}^+$, 574.2283, -1.1 ppm error). HPLC purity: 97.4% (210 nm).

(2*S*,3*S*,4*R*,5*R*,6*S*)-6-(2-(3,4-Dimethoxyphenyl)-5,7-dimethoxy-4-oxo-4*H*-chromen-6-yl)-3,4,5-trihydroxy-*N*-isobutyltetrahydro-2*H*-pyran-2-carboxamide (11). Light yellow solid (88% yield). ^{1}H NMR (DMSO-d_6) δ 7.62 (d, J = 8.8 Hz, 1H), 7.49 (d, J = 1.9 Hz, 1H), 7.14 (s, 1H), 7.11 (d, J = 8.6 Hz, 1H), 6.81 (d, J = 6.9 Hz, 1H), 4.68 (br d, J = 10.2 Hz, 1H), 4.07 (m, 1H), 3.89 (s, 3H), 3.84 (s, 3H), 3.80 (s, 3H), 3.75 (s, 3H), 3.62 (m, 1H), 3.49 (m, 1H), 3.24 (m, 1H), 2.87 (t, J = 6.4 Hz, 2H), 1.66 (m, 1H), 0.79 (d, J = 6.7 Hz, 6H). ^{13}C NMR (DMSO-d_6) δ 176.2, 167.3, 163.5, 160.6, 160.7, 158.8, 153.1, 149.5, 123.7, 120.7, 113.0, 112.7, 112.4, 108.3, 107.4, 97.7, 81.0, 79.9, 75.2, 72.8, 71.5, 64.6, 64.1, 57.8, 56.9, 47.2, 29.4, 21.3, 21.3. HRESI-TOFMS *m/z* $[M+H]^+$ 574.2292 (calcd for $C_{29}H_{36}NO_{11}^+$, 574.2283, -1.6 ppm error). HPLC purity: 99.1% (210 nm).

(2*S*,3*S*,4*R*,5*R*,6*S*)-6-(2-(3,4-Dimethoxyphenyl)-5,7-dimethoxy-4-oxo-4*H*-chromen-6-yl)-3,4,5-trihydroxy-*N*-pentyltetrahydro-2*H*-pyran-2-carboxamide (12). Light yellow solid (89% yield). ^{1}H NMR (500 MHz, DMSO-d_6) δ 7.68 (d, J = 8.6 Hz, 1H), 7.55 (d, J = 2.1 Hz, 1H), 7.14 (s, 1H), 7.12 (d, J = 8.6 Hz, 1H), 6.81 (d, J = 6.3 Hz, 1H), 4.67 (br d, J = 10.2 Hz, 1H), 4.06 (m, 1H), 3.89 (s, 3H), 3.85 (s, 3H), 3.80 (s, 3H), 3.74 (s, 3H), 3.58 (m, 1H), 3.50 (m, 1H), 3.22 (m, 1H), 3.03 (m, 2H), 1.35 (m, 2H), 1.23 (m, 2H), 1.20 (m, 2H), 0.83 (m, 3H). ^{13}C NMR (DMSO-d_6) δ 175.9, 168.9, 163.2, 160.5, 160.3, 158.5, 151.9, 149.2, 123.4, 119.7, 111.8, 111.6, 109.3, 107.0, 106.8, 96.4, 80.1, 78.8, 73.5, 71.6, 70.4, 63.5, 62.7, 56.1, 55.9, 38.4, 28.7, 28.6, 21.9, 14.0. HRESI-TOFMS *m/z* $[M+H]^+$ 588.2456 (calcd for $C_{30}H_{38}NO_{11}^+$, 588.2439, -2.8 ppm error). HPLC purity: 98.2% (210 nm).

(2*S*,3*S*,4*R*,5*R*,6*S*)-6-(2-(3,4-Dimethoxyphenyl)-5,7-dimethoxy-4-oxo-4*H*-chromen-6-yl)-3,4,5-trihydroxy-*N*-hexyltetrahydro-2*H*-pyran-2-carboxamide (13). Light yellow solid (90% yield). ^{1}H NMR (DMSO-d_6) δ 7.68 (d, J = 8.6 Hz, 1H), 7.55 (d, J = 2.3 Hz, 1H), 7.14 (s, 1H), 7.12 (d, J = 8.6 Hz, 1H), 6.81 (d, J = 5.9 Hz, 1H), 4.66 (br d, J = 10.5 Hz, 1H), 4.06 (q, J = 8.6 Hz, 1H), 3.89 (s, 3H), 3.84 (s, 3H), 3.80 (s, 3H), 3.74 (s, 3H), 3.60 (m, 1H), 3.50 (m, 1H), 3.23 (m, 1H), 3.01 (m, 2H), 1.40 – 1.15 (m, 8H), 0.82 (m, 3H). ^{13}C NMR (DMSO-d_6) δ 175.6, 168.8, 163.4, 160.3, 160.2, 158.6, 151.8, 149.1, 123.1, 119.6, 112.1, 111.8, 109.3, 107.1, 107.0, 97.1, 79.9, 78.7, 74.5, 71.5, 69.4, 63.5, 62.7, 56.6, 56.0, 38.5, 31.0, 28.9, 26.1, 22.1, 13.9. HRESI-TOFMS *m/z* $[M+H]^+$ 602.2572 (calcd for $C_{31}H_{40}NO_{11}^+$, 602.2596, 3.9 ppm error). HPLC purity: 98.5% (210 nm).

(2*S*,3*S*,4*R*,5*R*,6*S*)-*N*-Cyclopropyl-6-(2-(3,4-dimethoxyphenyl)-5,7-dimethoxy-4-oxo-4*H*-chromen-6-yl)-3,4,5-trihydroxytetrahydro-2*H*-pyran-2-carboxamide (14). Light yellow solid (82% yield). ^{1}H NMR (DMSO-d_6) δ 7.67 (dt, J = 8.3, 2.2 Hz, 1H), 7.54 (d, J = 2.2 Hz, 1H), 7.16

(s, 1H), 7.12 (d, *J* = 8.3 Hz, 1H), 6.78 (d, *J* = 5.7 Hz, 1H), 4.64 (br d, *J* = 9.7 Hz, 1H), 4.06 (q, *J* = 8.9 Hz, 1H), 3.88 (s, 3H), 3.84 (s, 3H), 3.79 (s, 3H), 3.73 (s, 3H), 3.51 (m, 1H), 3.50 (m, 1H), 3.19 (m, 1H), 2.62 (m, 1H), 0.79 (m, 2H), 0.58 (m, 2H). ^{13}C NMR (DMSO-d_6) δ 175.3, 167.6, 163.4, 161.5, 160.3, 159.6, 152.5, 149.3, 123.4, 119.8, 111.8, 111.5, 109.4, 107.7, 107.0, 97.0, 80.2, 78.9, 74.1, 71.3, 70.3, 63.5, 62.8, 56.1, 55.8, 23.1, 10.8, 10.8. HRESI-TOFMS *m/z* $[M+H]^+$ 558.1967 (calcd for $C_{28}H_{32}NO_{11}^+$, 558.1970, 0.5 ppm error). HPLC purity: 98.2% (210 nm).

(2*S*,3*S*,4*R*,5*R*,6*S*)-*N*-Cyclobutyl-6-(2-(3,4-dimethoxyphenyl)-5,7-dimethoxy-4-oxo-4*H*-chromen-6-yl)-3,4,5-trihydroxytetrahydro-2*H*-pyran-2-carboxamide (15). Light yellow solid (85% yield). ^{1}H NMR (DMSO-d_6) δ 7.67 (dt, *J* = 8.6, 2.1 Hz, 1H), 7.54 (d, *J* = 2.1 Hz, 1H), 7.16 (s, 1H), 7.12 (d, *J* = 8.6 Hz, 1H), 6.77 (d, *J* = 7.2 Hz, 1H), 4.66 (br d, *J* = 9.7 Hz, 1H), 4.16 (q, *J* = 7.8 Hz, 1H), 4.05 (td, *J* = 9.3, 5.7 Hz, 1H), 3.88 (s, 3H), 3.84 (s, 3H), 3.78 (s, 3H), 3.74 (s, 3H), 3.54 (m, 1H), 3.51 (m, 1H), 3.21 (m, 1H), 2.09 (m, 2H), 1.86 (m, 2H), 1.58 (m, 2H). ^{13}C NMR (DMSO-d_6) δ 175.5, 167.4, 163.1, 161.4, 160.5, 159.3, 152.2, 149.1, 123.2, 119.6, 111.9, 111.6, 109.1, 107.5, 107.0, 97.1, 80.4, 78.5, 74.2, 71.2, 70.4, 63.3, 62.7, 55.9, 55.7, 43.6, 29.9, 29.9, 14.3. HRESI-TOFMS *m/z* $[M+H]^+$ 572.2120 (calcd for $C_{29}H_{34}NO_{11}^+$, 572.2126, 1.1 ppm error). HPLC purity: 98.3% (210 nm).

(2*S*,3*S*,4*R*,5*R*,6*S*)-*N*-Cyclopentyl-6-(2-(3,4-dimethoxyphenyl)-5,7-dimethoxy-4-oxo-4*H*-chromen-6-yl)-3,4,5-trihydroxytetrahydro-2*H*-pyran-2-carboxamide (16). Light yellow solid (86% yield). ^{1}H NMR (DMSO-d_6) δ 7.66 (d, *J* = 8.4 Hz, 1H), 7.53 (d, *J* = 2.1 Hz, 1H), 7.16 (s, 1H), 7.12 (d, *J* = 8.4 Hz, 1H), 6.75 (d, *J* = 6.5 Hz, 1H), 4.64 (br d, *J* = 10.2 Hz, 1H), 3.95 (m, 1H), 3.87 (s, 3H), 3.82 (s, 3H), 3.79 (m, 1H), 3.77 (s, 3H), 3.71 (s, 3H), 3.53 (m, 1H), 3.51 (m, 1H), 3.21 (m, 1H), 1.79 – 1.40 (m, 8H). ^{13}C NMR (DMSO-d_6) δ 175.4, 167.1, 163.6, 161.4, 160.3, 158.8, 152.1, 149.1, 123.0, 119.8, 112.1, 111.8, 109.2, 107.7, 107.1, 97.3, 80.2, 78.5, 74.2,

71.2, 68.6, 63.6, 62.8, 56.3, 55.9, 50.5, 32.1, 32.1, 23.6, 23.6. HRESI-TOFMS *m/z* $[M+H]^+$ 586.2291 (calcd for $C_{30}H_{36}NO_{11}^+$, 586.2283, -1.4 ppm error). HPLC purity: 96.6% (210 nm).

(2*S*,3*S*,4*R*,5*R*,6*S*)-*N*-Cyclohexyl-6-(2-(3,4-dimethoxyphenyl)-5,7-dimethoxy-4-oxo-4*H*-chromen-6-yl)-3,4,5-trihydroxytetrahydro-2*H*-pyran-2-carboxamide (17). Light yellow solid (88% yield). ^{1}H NMR (DMSO-d_6) δ 7.68 (d, J = 8.4 Hz, 1H), 7.55 (d, J = 2.1 Hz, 1H), 7.14 (s, 1H), 7.12 (d, J = 8.4 Hz, 1H), 6.80 (d, J = 6.5 Hz, 1H), 4.65 (br d, J = 10.2 Hz, 1H), 4.04 (q, J = 8.4 Hz, 1H), 3.88 (s, 3H), 3.84 (s, 3H), 3.79 (s, 3H), 3.74 (s, 3H), 3.58 (m, 1H), 3.51 (m, 1H), 3.49 (m, 1H), 3.21 (m, 1H), 1.74 – 1.47 (m, 6H), 1.27 – 0.99 (m, 4H). ^{13}C NMR (DMSO-d_6) δ 175.5, 167.2, 163.2, 161.3, 160.3, 158.8, 152.0, 149.1, 123.1, 119.8, 112.0, 111.4, 109.4, 107.2, 107.0, 96.9, 80.5, 79.1, 74.1, 71.6, 70.6, 63.9, 62.7, 56.4, 56.0, 47.8, 32.6, 32.6, 29.1, 24.6, 24.6. HRESI-TOFMS *m/z* $[M+H]^+$ 600.2446 (calcd for $C_{31}H_{38}NO_{11}^+$, 600.2439, -1.1 ppm error). HPLC purity: 98.6 % (210 nm).

(2*S*,3*S*,4*R*,5*R*,6*S*)-*N*-(Cyclohexylmethyl)-6-(2-(3,4-dimethoxyphenyl)-5,7-dimethoxy-4-oxo-4*H*-chromen-6-yl)-3,4,5-trihydroxytetrahydro-2*H*-pyran-2-carboxamide (18). Light yellow solid (88% yield). ^{1}H NMR (DMSO-d_6) δ 7.66 (d, J = 8.7 Hz, 1H), 7.54 (d, J = 2.0 Hz, 1H), 7.13 (s, 1H), 7.11 (d, J = 8.7 Hz, 1H), 6.76 (d, J = 6.2 Hz, 1H), 4.66 (br d, J = 9.9 Hz, 1H), 4.05 (q, J = 9.9 Hz, 1H), 3.87 (s, 3H), 3.83 (s, 3H), 3.78 (s, 3H), 3.73 (s, 3H), 3.61 (m, 1H), 3.48 (m, 1H), 3.23 (m, 1H), 2.87 (m, 2H), 1.69 – 1.47 (m, 6H), 1.33 (m, 1H), 1.08 (m, 2H), 0.80 (m, 2H). ^{13}C NMR (DMSO-d_6) δ 176.0, 167.0, 163.7, 160.8, 160.6, 158.9, 152.0, 149.3, 123.4, 119.7, 112.0, 111.7, 109.3, 107.2, 107.1, 96.2, 80.3, 78.7, 74.7, 71.3, 69.9, 63.8, 63.1, 56.9, 56.2, 45.1, 37.1, 30.6, 30.6, 26.3, 25.7, 25.7. HRESI-TOFMS *m/z* $[M+H]^+$ 614.2597 (calcd for $C_{32}H_{40}NO_{11}^+$, 614.2596, -0.1 ppm error). HPLC purity: 98.3% (210 nm).

(2*S*,3*S*,4*R*,5*R*,6*S*)-*N*-(Adamantan-1-yl)-6-(2-(3,4-dimethoxyphenyl)-5,7-dimethoxy-4-oxo-4*H*-chromen-6-yl)-3,4,5-trihydroxytetrahydro-2*H*-pyran-2-carboxamide (19). Light yellow solid (81% yield). ^{1}H NMR (DMSO-d_6) δ 7.67 (d, J = 8.4 Hz, 1H), 7.54 (d, J = 2.1 Hz, 1H), 7.13 (s, 1H), 7.12 (d, J = 8.4 Hz, 1H), 6.78 (d, J = 6.8 Hz, 1H), 4.65 (br d, J = 10.2 Hz, 1H), 4.03 (m, 1H), 3.88 (s, 3H), 3.84 (s, 3H), 3.80 (s, 3H), 3.74 (s, 3H), 3.57 (m, 1H), 3.52 (m, 1H), 3.49 (m, 1H), 1.96 (m, 3H), 1.88 – 1.57 (m, 12H). ^{13}C NMR (DMSO-d_6) δ 175.3, 167.2, 163.3, 161.1, 160.2, 158.9, 152.1, 149.2, 123.2, 119.8, 112.1, 111.6, 109.5, 107.2, 107.0, 97.0, 80.7, 79.2, 74.2, 71.7, 70.5, 63.9, 62.5, 56.4, 56.0, 51.2, 41.2, 41.2, 41.2, 36.1, 36.1, 36.1, 28.9, 28.9, 28.9. HRESI-TOFMS *m/z* $[M+H]^+$ 652.2764 (calcd for $C_{35}H_{42}NO_{11}^+$, 652.2752, -1.8 ppm error). HPLC purity: 97.7% (210 nm).

(2*S*,3*S*,4*R*,5*R*,6*S*)-6-(2-(3,4-Dimethoxyphenyl)-5,7-dimethoxy-4-oxo-4*H*-chromen-6-yl)-3,4,5-trihydroxy-*N*-phenyltetrahydro-2*H*-pyran-2-carboxamide (20). Light yellow solid (88% yield). ^{1}H NMR (DMSO-d_6) δ 7.66 (dd, J = 8.6, 2.2 Hz, 1H), 7.62 (dd, J = 8.2, 2.5 Hz, 2H), 7.55 (d, J = 2.2 Hz, 1H), 7.28 (td, J = 8.1, 2.2 Hz, 2H), 7.16–7.10 (m, 2H), 7.03 (t, J = 7.4 Hz, 1H), 6.77 (d, J = 6.5 Hz, 1H), 4.75 (br d, J = 9.7 Hz, 1H), 4.12 (td, J = 9.7, 2.4 Hz, 1H), 3.94 (s, 3H), 3.89 (s, 3H), 3.85 (s, 3H), 3.84 (m, 1H), 3.79 (s, 3H), 3.66 (m, 1H), 3.29 (m, 1H). ^{13}C NMR (DMSO-d_6) δ 175.4, 167.3, 163.4, 161.9, 160.3, 158.8, 151.8, 149.1, 138.8, 128.6, 128.6, 123.4, 123.1, 119.5, 119.3, 119.3, 112.0, 111.8, 109.4, 107.1, 106.9, 97.1, 81.0, 78.6, 73.7, 71.2, 69.6, 63.4, 62.7, 56.5, 56.0. HRESI-TOFMS *m/z* $[M+H]^+$ 594.1986 (calcd for $C_{31}H_{32}NO_{11}^+$, 594.1970, -2.8 ppm error). HPLC purity: 96.5% (210 nm).

(2*S*,3*S*,4*R*,5*R*,6*S*)-6-(2-(3,4-Dimethoxyphenyl)-5,7-dimethoxy-4-oxo-4*H*-chromen-6-yl)-3,4,5-trihydroxy-*N*-benzyltetrahydro-2*H*-pyran-2-carboxamide (21). Light yellow solid (92% yield). ^{1}H NMR (500 MHz, DMSO-d_6) δ 7.67 (d, J = 10.2 Hz, 1H), 7.54 (d, J = 2.1 Hz,

1H), 7.29 – 7.16 (m, 5H), 7.16 – 7.08 (m, 2H), 6.80 (d, *J* = 6.7 Hz, 1H), 4.68 (dd, *J* = 9.8, 6.7 Hz, 1H), 4.27 (m, 2H), 4.10 (m, 1H), 3.87 (s, 3H), 3.83 (s, 3H), 3.79 (s, 3H), 3.75 (s, 3H), 3.71 (m, 1H), 3.57 (m, 1H), 3.26 (m, 1H). ^{13}C NMR (DMSO-d_6) δ 175.6, 169.1, 163.6, 162.0, 160.3, 158.9, 151.8, 149.1, 139.2, 128.2, 128.2, 127.3, 127.3, 126.7, 123.1, 119.6, 112.1, 111.7, 109.2, 107.1, 107.0, 97.1, 80.2, 78.8, 73.7, 71.6, 71.0, 63.5, 62.8, 56.6, 56.0, 42.0. HRESI-TOFMS *m/z* $[M+H]^+$ 608.2130 (calcd for $C_{32}H_{34}NO_{11}^+$, 608.2126, -0.5 ppm error). HPLC purity: 97.1% (210 nm).

(2*S*,3*S*,4*R*,5*R*,6*S*)-6-(2-(3,4-Dimethoxyphenyl)-5,7-dimethoxy-4-oxo-4*H*-chromen-6-yl)-3,4,5-trihydroxy-*N*-(pyridin-4-yl)tetrahydro-2*H*-pyran-2-carboxamide (22). Light yellow solid (81% yield). ^{1}H NMR (500 MHz, DMSO-d_6) δ 8.40 (d, *J* = 5.0 Hz, 2H), 7.68 (d, *J* = 8.5 Hz, 1H), 7.60 (d, *J* = 5.0 Hz, 2H), 7.55 (s, 1H), 7.15 (s, 1H), 7.12 (d, *J* = 8.5 Hz, 1H), 6.81 (d, *J* = 6.9 Hz, 1H), 4.72 (br d, *J* = 9.7 Hz, 1H), 4.11 (td, *J* = 9.2, 4.1 Hz, 1H), 3.94 (m, 1H), 3.88 (s, 3H), 3.84 (s, 3H), 3.83 (s, 3H), 3.76 (s, 3H), 3.62 (m, 1H), 3.29 (m, 1H). ^{13}C NMR (DMSO-d_6) δ 175.6, 167.5, 163.3, 161.7, 160.2, 158.7, 152.0, 150.9, 150.9, 149.2, 145.3, 123.1, 119.9, 112.1, 113.9, 113.9, 111.5, 109.8, 107.5, 106.8, 97.1, 81.2, 78.8, 74.4, 71.5, 69.8, 63.9, 63.0, 56.5, 56.1. HRESI-TOFMS *m/z* $[M+H]^+$ 595.1921 (calcd for $C_{30}H_{31}N_2O_{11}^+$, 595.1922, 0.1 ppm error). HPLC purity: 97.8% (210 nm).

(2*S*,3*S*,4*R*,5*R*,6*S*)-6-(2-(3,4-Dimethoxyphenyl)-5,7-dimethoxy-4-oxo-4*H*-chromen-6-yl)-3,4,5-trihydroxy-*N*-(thiazol-2-yl)tetrahydro-2*H*-pyran-2-carboxamide (23). Light yellow solid (80% yield). ^{1}H NMR (DMSO-d_6) δ 7.68 (d, *J* = 8.8 Hz, 1H), 7.56 (d, *J* = 2.0 Hz, 1H), 7.53 (d, *J* = 1.7 Hz, 1H), 7.18 (d, *J* = 1.7 Hz, 1H), 7.17 (s, 1H), 7.12 (d, *J* = 8.8 Hz, 1H), 6.82 (d, *J* = 6.8 Hz, 1H), 4.67 (br d, *J* = 10.5 Hz, 1H), 4.03 (m, 1H), 3.89 (s, 3H), 3.84 (s, 3H), 3.82 (s, 3H), 3.76 (s, 3H), 3.60 (m, 1H), 3.55 (m, 1H), 3.23 (m, 1H). ^{13}C NMR (DMSO-d_6) δ 175.4, 168.5,

163.2, 162.3, 161.6, 160.5, 158.9, 151.9, 149.2, 137.2, 123.3, 119.8, 114.1, 111.9, 111.5, 109.5, 107.3, 105.8, 97.3, 80.0, 79.2, 74.3, 72.1, 70.3, 63.7, 62.9, 56.2, 56.0. HRESI-TOFMS *m/z* $[M+H]^+$ 601.1493 (calcd for $C_{28}H_{29}N_2O_{11}S^+$, 601.1487, -1.1 ppm error). HPLC purity: 96.8% (210 nm).

(2*S*,3*S*,4*R*,5*R*,6*S*)-6-(2-(3,4-Dimethoxyphenyl)-5,7-dimethoxy-4-oxo-4*H*-chromen-6-yl)-3,4,5-trihydroxy-*N*-(4-fluorophenyl)tetrahydro-2*H*-pyran-2-carboxamide (24). Light yellow solid (88% yield). ^{1}H NMR (DMSO-d_6) δ 7.70 – 7.61 (m, 3H), 7.54 (d, J = 2.1 Hz, 1H), 7.18 – 7.08 (m, 4H), 6.78 (d, J = 7.1 Hz, 1H), 4.72 (dd, J = 12.0, 9.7 Hz, 1H), 4.11 (q, J = 8.7 Hz, 1H), 3.92 (s, 3H), 3.88 (s, 3H), 3.84 (s, 3H), 3.83 (m, 1H), 3.76 (s, 3H), 3.61 (m, 1H), 3.28 (m, 1H). ^{13}C NMR (DMSO-d_6) δ 175.6, 167.4, 162.8, 160.4, 160.1, 158.6, 156.9, 150.7, 149.2, 136.5, 121.2, 121.2, 123.5, 119.8, 115.5, 115.5, 113.5, 111.8, 109.3, 107.0, 105.7, 97.2, 81.2, 78.5, 74.7, 71.7, 70.4, 63.7, 63.0, 56.1, 55.9. HRESI-TOFMS *m/z* $[M+H]^+$ 612.1892 (calcd for $C_{31}H_{31}FNO_{11}^+$, 612.1876, -2.7 ppm error). HPLC purity: 97.1% (210 nm).

(2*S*,3*S*,4*R*,5*R*,6*S*)-6-(2-(3,4-Dimethoxyphenyl)-5,7-dimethoxy-4-oxo-4*H*-chromen-6-yl)-3,4,5-trihydroxy-*N*-(4-fluorobenzyl)tetrahydro-2*H*-pyran-2-carboxamide (25). Light yellow solid (89% yield). ^{1}H NMR (500 MHz, DMSO-d_6) δ 7.68 (d, J = 8.5 Hz, 1H), 7.55 (d, J = 2.1 Hz, 1H), 7.27 (ddd, J = 8.1, 5.4, 2.2 Hz, 2H), 7.18 – 7.06 (m, 4H), 6.80 (d, J = 6.8 Hz, 1H), 4.67 (t, J = 9.3 Hz, 1H), 4.24 (dd, J = 9.9, 9.0 Hz, 2H), 4.07 (m, 1H), 3.88 (s, 3H), 3.84 (s, 3H), 3.78 (s, 3H), 3.74 (s, 3H), 3.69 (m, 1H), 3.54 (m, 1H), 3.24 (m, 1H). ^{13}C NMR (DMSO-d_6) δ 175.7, 169.1, 163.5, 162.0, 161.2, 160.4, 159.0, 151.9, 149.1, 135.4, 129.3, 129.3, 126.5, 119.7, 115.1, 115.1, 111.8, 111.3, 109.3, 107.1, 105.5, 97.2, 80.2, 78.8, 73.7, 71.9, 71.0, 63.6, 62.9, 56.6, 55.9, 41.3. HRESI-TOFMS *m/z* $[M+H]^+$ 626.2043 (calcd for $C_{32}H_{33}FNO_{11}^+$, 626.2032, -1.7 ppm error). HPLC purity: 97.4% (210 nm).

(2*S*,3*S*,4*R*,5*R*,6*S*)-6-(2-(3,4-Dimethoxyphenyl)-5,7-dimethoxy-4-oxo-4*H*-chromen-6-yl)-3,4,5-trihydroxy-*N*-(2-fluoroethyl)tetrahydro-2*H*-pyran-2-carboxamide (26). Light yellow solid (84% yield). ^{1}H NMR (DMSO-d_6) δ 7.68 (d, J = 8.7 Hz, 1H), 7.56 (d, J = 2.1 Hz, 1H), 7.17 (s, 1H), 7.12 (d, J = 8.7 Hz, 1H), 6.82 (d, J = 6.6 Hz, 1H), 4.67 (br d, J = 10.5 Hz, 1H), 4.45 (m, 1H), 4.35 (m, 1H), 4.07 (t, J = 9.2 Hz, 1H), 3.89 (s, 3H), 3.85 (s, 3H), 3.80 (s, 3H), 3.75 (s, 3H), 3.60 (m, 1H), 3.50 (m, 1H), 3.23 (m, 1H), 3.37 (m, 2H). ^{13}C NMR (DMSO-d_6) δ 175.1, 168.6, 163.5, 161.6, 160.5, 158.9, 151.9, 149.2, 123.6, 119.7, 111.8, 111.4, 109.3, 107.2, 105.5, 97.3, 81.7, 79.9, 79.4, 74.3, 72.3, 70.3, 63.5, 62.9, 56.1, 55.9, 39.1. HRESI-TOFMS *m/z* $[M+H]^+$ 564.1892 (calcd for $C_{27}H_{31}FNO_{11}^+$, 564.1876, -2.9 ppm error). HPLC purity: 97.5% (210 nm).

(2*S*,3*S*,4*R*,5*R*,6*S*)-6-(2-(3,4-Dimethoxyphenyl)-5,7-dimethoxy-4-oxo-4*H*-chromen-6-yl)-3,4,5-trihydroxy-*N*-(2,2,2-trifluoroethyl)tetrahydro-2*H*-pyran-2-carboxamide (27). Light yellow solid (85% yield). ^{1}H NMR (DMSO-d_6) δ 7.68 (dd, J = 8.5, 2.0 Hz, 1H), 7.56 (d, J = 2.0 Hz, 1H), 7.17 (s, 1H), 7.12 (d, J = 8.5 Hz, 1H), 6.81 (d, J = 7.7 Hz, 1H), 4.68 (br d, J = 9.7 Hz, 1H), 4.07 (q, J = 9.1 Hz, 1H), 3.89 (s, 3H), 3.85 (s, 3H), 3.78 (s, 3H), 3.75 (s, 3H), 3.69 (m, 1H), 3.48 (m, 1H), 3.67 (m, 2H), 3.21 (m, 1H). ^{13}C NMR (DMSO-d_6) δ 174.5, 169.5, 163.4, 161.3, 160.4, 158.9, 151.8, 149.1, 125.0, 123.4, 119.7, 112.1, 111.2, 109.4, 107.1, 105.4, 97.2, 80.4, 78.5, 74.8, 71.6, 69.5, 63.6, 62.7, 56.3, 55.9, 41.6. HRESI-TOFMS *m/z* $[M+H]^+$ 600.1700 (calcd for $C_{27}H_{29}F_3NO_{11}^+$, 600.1687, -2.2 ppm error). HPLC purity: 96.8% (210 nm).

(2*S*,3*S*,4*R*,5*R*,6*S*)-6-(2-(3,4-Dimethoxyphenyl)-5,7-dimethoxy-4-oxo-4*H*-chromen-6-yl)-3,4,5-trihydroxy-*N*-(3-fluoropropyl)tetrahydro-2*H*-pyran-2-carboxamide (28). Light yellow solid (86% yield). ^{1}H NMR (DMSO-d_6) δ 7.68 (d, J = 8.7 Hz, 1H), 7.56 (d, J = 2.1 Hz, 1H), 7.17 (s, 1H), 7.12 (d, J = 8.7 Hz, 1H), 6.82 (d, J = 6.4 Hz, 1H), 4.66 (br d, J = 10.6 Hz, 1H), 4.46 (m, 1H), 4.37 (m, 1H), 4.07 (m, 1H), 3.89 (s, 3H), 3.85 (s, 3H), 3.80 (s, 3H), 3.74 (s, 3H), 3.59 (m,

1H), 3.50 (m, 1H), 3.22 (m, 1H), 3.12 (m, 2H), 1.83 – 1.68 (m, 2H). ^{13}C NMR (DMSO-d_6) δ 175.1, 168.5, 163.4, 161.6, 160.6, 158.8, 151.9, 149.3, 123.7, 119.8, 111.9, 111.5, 109.6, 107.3, 105.5, 97.3, 81.9, 80.2, 78.8, 74.2, 71.8, 70.6, 63.6, 62.8, 56.2, 55.8, 34.9, 30.0. HRESI-TOFMS *m/z* $[M+H]^+$ 578.2041 (calcd for $C_{28}H_{33}FNO_{11}^+$, 578.2032, -1.6 ppm error). HPLC purity: 98.3% (210 nm).

(2*S*,3*S*,4*R*,5*R*,6*S*)-6-(2-(3,4-Dimethoxyphenyl)-5,7-dimethoxy-4-oxo-4*H*-chromen-6-yl)-3,4,5-trihydroxy-*N*-(3,3,3-trifluoropropyl)tetrahydro-2*H*-pyran-2-carboxamide (29). Light yellow solid (85% yield). ^{1}H NMR (DMSO-d_6) δ 7.68 (d, J = 8.4 Hz, 1H), 7.55 (d, J = 2.2 Hz, 1H), 7.14 (s, 1H), 7.12 (d, J = 8.4 Hz, 1H), 6.81 (d, J = 5.5 Hz, 1H), 4.68 (br d, J = 10.0 Hz, 1H), 4.07 (m, 1H), 3.89 (s, 3H), 3.85 (s, 3H), 3.80 (s, 3H), 3.74 (s, 3H), 3.61 (m, 1H), 3.49 (m, 1H), 3.28 (m, 2H), 3.21 (m, 1H), 2.40 (m, 2H). ^{13}C NMR (DMSO-d_6) δ 174.6, 169.3, 163.4, 161.1, 160.3, 158.7, 151.8, 149.1, 125.7, 123.1, 119.6, 111.7, 110.9, 109.2, 107.0, 105.2, 97.4, 79.6, 78.3, 73.6, 71.6, 69.5, 63.4, 62.7, 56.0, 55.8, 32.8, 32.1. HRESI-TOFMS *m/z* $[M+H]^+$ 614.1857 (calcd for $C_{28}H_{31}F_3NO_{11}^+$, 614.1844, -2.2 ppm error). HPLC purity: 97.2% (210 nm).

(2*S*,3*S*,4*R*,5*R*,6*S*)-6-(2-(3,4-Dimethoxyphenyl)-5,7-dimethoxy-4-oxo-4*H*-chromen-6-yl)-3,4,5-trihydroxy-*N*-((*S*)-1,1,1-trifluoropropan-2-yl)tetrahydro-2*H*-pyran-2-carboxamide (30). Light yellow solid (82% yield). ^{1}H NMR (500 MHz, DMSO-d_6) δ 7.67 (dd, J = 8.5, 2.1 Hz, 1H), 7.55 (d, J = 2.1 Hz, 1H), 7.15 (br s, 1H), 7.12 (d, J = 8.5 Hz, 1H), 6.78 (d, J = 6.2 Hz, 1H), 4.69 (d, J = 9.6 Hz, 1H), 4.55 (m, 1H), 4.07 (m, 1H), 3.89 (s, 3H), 3.85 (s, 3H), 3.79 (s, 3H), 3.76 (s, 3H), 3.71 (m, 1H), 3.56 (m, 1H), 3.24 (m, 1H), 1.23 (d, J = 6.8 Hz, 3H). ^{13}C NMR (125 MHz, DMSO-d_6) δ 175.5, 168.8, 163.5, 161.7, 160.3, 158.6, 152.1, 149.1, 124.4, 123.1, 119.5, 111.8, 111.3, 109.4, 107.7, 106.9, 96.2, 79.8, 78.3, 73.8, 71.3, 70.3, 62.9, 62.7, 55.9, 55.6, 45.1, 13.3.

HRESI-TOFMS *m/z* $[M+H]^+$ 614.1843 (calcd for $C_{28}H_{31}F_3NO_{11}^+$, 614.1844, 0.1 ppm error). HPLC purity: 98.1% (210 nm).

(2*S*,3*S*,4*R*,5*R*,6*S*)-6-(2-(3,4-Dimethoxyphenyl)-5,7-dimethoxy-4-oxo-4*H*-chromen-6-yl)-3,4,5-trihydroxy-*N*-((*R*)-1,1,1-trifluoropropan-2-yl)tetrahydro-2*H*-pyran-2-carboxamide (31). Light yellow solid (86% yield). ^{1}H NMR (500 MHz, DMSO-d_6) δ 7.66 (dd, *J* = 8.5, 2.0 Hz, 1H), 7.55 (d, *J* = 2.0 Hz, 1H), 7.14 (br s, 1H), 7.12 (d, *J* = 8.5 Hz, 1H), 6.77 (d, *J* = 6.4 Hz, 1H), 4.68 (d, *J* = 9.8 Hz, 1H), 4.54 (m, 1H), 4.06 (m, 1H), 3.88 (s, 3H), 3.84 (s, 3H), 3.79 (s, 3H), 3.75 (s, 3H), 3.71 (m, 1H), 3.55 (m, 1H), 3.24 (m, 1H), 1.23 (d, *J* = 6.8 Hz, 3H). ^{13}C NMR (125 MHz, DMSO-d_6) δ 175.3, 168.6, 163.4, 161.5, 160.2, 158.5, 152.1, 149.0, 124.2, 123.0, 119.4, 111.6, 111.1, 109.3, 107.6, 106.8, 96.4, 79.7, 78.5, 73.9, 71.2, 70.4, 63.1, 62.5, 55.7, 55.4, 45.1, 13.3. HRESI-TOFMS *m/z* $[M+H]^+$ 614.1847 (calcd for $C_{28}H_{31}F_3NO_{11}^+$, 614.1844, -0.5 ppm error). HPLC purity: 96.5% (210 nm).

3.7. Kinase Luminescent Assay

Kinase inhibition was assessed with the ADP-Glo Kinase Assay. For screening, 5 ng/μL of kinase was assayed in a reaction containing 50 ng/μL substrate, 40 mM Tris, pH 7.5, 20 mM $MgCl_2$, 0.1 mg/mL bovine serum albumin, 50 μM dithiothreitol (DTT), 25 μM ATP, varying concentrations of test samples or 5% DMSO as vehicle. The reaction mixture was incubated for 1 h at room temperature followed by the addition of the ADP-Glo reagents according to the manufacturer's protocol. The kinase inhibitor staurosporine was used at 1 μM as a reference control. Each data point was collected in quadruplicate of two independent experiments. Inhibition was presented as the percentage of the kinase activity relative to control (5% DMSO vehicle). Inhibition curves were analyzed by four-parameter regression.

Promiscuous aggregations were assessed with the screening assay in the presence of 0%, 0.001%, 0.01% and 0.05% (v/v) of Triton X-100. Luteolin was used as a reference control for promiscuous inhibition. All natural *C*-glycosylflavones and their new analogues were not promiscuous or pan-assay interference compounds as determined with a detergent-based assay.[65, 92]

To study the GSK-3β kinetics, a reaction solution contained 5 ng/μL kinase, 40 mM Tris, pH 7.5, 20 mM $MgCl_2$, 0.1 mg/mL BSA, 50 μM DTT, and varying concentrations of ATP or substrate GS2 (peptide YRRAAVPPSPSLSRHSSPHQ(pS)EDEEE that is derived from human muscle glycogen synthase) versus test samples. The mixture was incubated for 5, 15, 30, and 60 min at room temperature followed by the addition of the ADP-Glo reagents according to the manufacturer's protocol. The Dixon and Lineweaver−Burk representations are derived from the single and double reciprocal plotting of the enzyme kinetic data, respectively.

3.8. Cell Culture

Human neuroblastoma SH-SY5Y cell line (ATCC CRL-2266; Sigma-Aldrich, Saint Louis, MO) was cultured in DMEM/F12 (v/v 1:1) media supplemented with 2 mM glutamine, 10% heat-inactivated fetal bovine serum (FBS) and 1% antibiotics including penicillin and streptomycin. After reaching 70-80% confluence, cells were then subcultured on poly-L-lysine plates with 10 μM retinoic acid in a reduced serum media (1% FBS) to promote differentiation as described.[85] Differentiation was confirmed by the change to polygonal morphology and extension of long neurites. Cell cultures were incubated at 37 °C in a fully humidified atmosphere containing 5% CO_2.

3.9. Whole-Cell Lysate GSK-3β Assay

The assay procedure was followed as described.[65] SH-SY5Y cells were washed with phosphate buffered saline (PBS) and lysed with cell extraction buffer containing 10 mM Tris, pH 7.4, 100 mM NaCl, 1 mM EDTA, 1 mM EGTA, 1 mM NaF, 20 mM $Na_4P_2O_7$, 2 mM Na_3VO_4, 1% Triton X-100, 10% glycerol, 0.1% sodium dodecyl sulfate (SDS), 0.5% sodium deoxycholate, 1 mM phenylmethanesulfonyl fluoride (PMSF) and a protease inhibitor cocktail. Lysate was diluted with kinase buffer (40 mM Tris, pH 7.5, 20 mM $MgCl_2$, 50 μM DTT, 400 μM ATP) to afford a concentration of 5 μg/μL of total protein, and split into aliquots. Recombinant human GSK-3β was fortified into lysate aliquots to a final concentration of 0.25% (wt/wt) of total protein. A lysate aliquot fortified with heat-inactivated GSK-3β was used as a negative control. The fortified lysate aliquots were incubated with test sample or 5% DMSO vehicle at 37 °C for 2 h followed by ELISA analysis. The GSK-3β inhibitor TDZD-8 was used at 10 μM as a reference control.

3.10. Western Blot Analysis

SH-SY5Y cells were seeded at a density of 3×10^5 cells/mL in a 24-well plate in DMEM/F12 media containing 1% FBS. Cells were pretreated with different concentrations of test samples or the 0.2% DMSO vehicle for 1 h followed by co-incubation with 10 μM $A\beta_{42}$ for 72 h. The cultures were then washed with PBS and lysed with phosphate protein extraction buffer (20 mM $Na_4P_2O_7$, pH 7.4, 115 mM NaCl) containing 1 mM PMSF and a protease inhibitor cocktail. Concentrations of the harvested proteins were determined by Bradford assay. Equal amounts of total proteins for each sample (10 μg per lane) were resolved by 10% SDS-PAGE and transferred onto PVDF membranes. The membranes were blocked with 5% BSA overnight and hybridized with primary

antibodies against Tau-5 (total tau), Tau pS199/pS202, Tau pS396, GSK-3β (total GSK-3β), GSK-3β pS9 or β-actin (loading control) at room temperature for 2 h. After washes, the membranes were incubated with corresponding alkaline phosphatase-conjugated secondary antibodies at room temperature for 1 h, and the immunoreactive bands were detected by the BCIP/NBT reagent. Densitometric analysis was performed on three independent blots per experiment.

3.11. Human Tau pS396 ELISA

The quantitative determination of phosphorylated human tau at GSK-3β specific pS396 site was conducted by taking 50 µL diluted cell lysate and using a specific antibody against human tau [pS396] in a sandwich ELISA according to the manufacturer's protocol. Tau phosphorylation was quantified by measuring the absorbance at 450 nm in a microtiter plate reader. The analysis was collected in quadruplicate of two independent experiments.

3.12. $A\beta_{42}$ Oligomer Preparation

The toxic oligomers of $A\beta_{42}$ were prepared as described.[65] Briefly, lyophilized $A\beta_{42}$ peptide was dissolved in hexafluoroisopropanol, dried under vacuum, and stored at -20 °C. Immediately prior to use, the peptide residue was reconstituted in DMEM/F12 media to make a stock solution at 0.1 mM and incubated at 4 °C for 24 h to form diffusible oligomers. $A\beta_{42}$ oligomers at a final concentration of 10 µM were assayed for cell viability.

3.13. Anti-Aβ$_{42}$ Neurotoxicity Assay

SH-SY5Y cells were seeded at a density of 3×10^5 cells/mL in a 96-well plate in DMEM/F12 media containing 10 μM retinoic acid and 1% FBS to induce postmitotic differentiation. Cells were incubated under regular culture conditions for attachment. After 24 h of plating, the cells were pretreated with different concentrations of test samples or the 0.2% DMSO as a vehicle control for 1 h and then co-incubated with 10 μM Aβ$_{42}$ for 72 h. After the experimental treatment, the cells were subject to a CellTiter 96 AQueous One Solution Cell Proliferation MTS Assay according to the manufacturer's instruction. Staurosporine at 1 μM was used as a reference control for cytotoxicity, while 10 μM TDZD-8 was used as a reference control for GSK-3β inhibition. Each data point was collected in triplicate of two independent experiments. Colorimetric intensity of nontreated control cells in the MTS assay was normalized as 100% cell viability and that of solvent blank without cell culture was normalized as 0% cell viability.

Neuroprotection was presented as the percentage of the cell viability relative to control (100%) and 10 μM Aβ$_{42}$ treatment (0%). Neuroprotection curve was analyzed by four-parameter regression.

3.14. PAMPA Studies

A 96-well filter plate with 0.45 μm polyvinylidene fluoride (PVDF) membrane was precoated with trilayer phospholipids. Then 300 μL of sample solutions (20 μM) in 5% DMSO-PBS at pH 7.4 were added to the donor wells. The acceptor plate containing 200 μL 5% DMSO-PBS was then placed on top of the donor plate so that the artificial membrane was in contact with the solution below. The PAMPA system was covered with a lid and incubated for 5 h at room temperature. The

concentration of compound in the donor and acceptor wells was quantified by LC-ESI-QTOF-MS. Theophylline and atenolol known for their low permeability were used as negative controls, and desipramine known for its high permeability was used as a positive control. Samples were run in quadruplicate. P_e values and R% were calculated according to the manufacturer's instruction.

3.15. Molecular Docking Studies

Compounds of interest were docked with AutoDock Vina 1.1.2[133-134] using the X-ray crystallographic structures of GSK-3β (PDB codes 1PYX[97] and 1H8F[137]). To streamline the docking process, the PDB crystallographic structures were treated without water molecules according to the published GSK-3β docking protocols,[40, 94, 118, 134] although the explicit hydration effect of water molecules is known to affect the binding of small molecules to GSK-3β.[139] Proteins were prepared by adding polar hydrogens and Gasteiger charges using AutoDockTools.[134] The molecular model of ligands were drawn using ChemBioDraw Ultra 12.0 (PerkinElmer Inc.) and constructed in the ChemBio3D interface. Ligands were optimized for their energy and geometry using MMFF94 and AM1 force fields prior to docking as described.[196] All bonds of ligands were treated as rotatable except for the aromatic, alkenyl, carbonyl bonds and rings. The dimensions of the grid map were 30 × 30 × 30 points with a grid-point spacing of 1 Å. Docking was proceeded with an exhaustiveness value of 500 and a maximum output of 100 structures. Details for the docking method validation was elaborated in Appendix 10. Re-docking experiments were conducted using the ligands ANP and HEPES for 1PYX and 1H8F, respectively. ANP showed a binding pose at the ATP site of GSK-3β (PDB code 1PYX) with a RMSD of 0.33 Å as compared to its original crystal structure. HEPES showed a binding pose at the substrate site of GSK-3β (PDB code 1H8F) with a RMSD of 0.62 Å as compared to its original crystal structure.

AutoDockTools[134] was used to analyze the docking data of compounds of interest on molecular interactions including hydrogen bonds, hydrophobic contact, π-cation interactions, π-π interactions, and multipolar interactions.

3.16. Homology Modeling

The GSK-3α homology model was built with the SWISS-MODEL server.[146] The full sequence of human GSK-3α (UniProt code P49840) was obtained from the Universal Protein Resource. The target sequence was searched against BLAST and HHblits databases for evolutionary related protein structures. A total of 4470 templates were found. For each identified template, the template's quality was predicted from features of the target-template alignment. A template of the GSK-3β structure (PDB code 1PYX) showing the highest quality (sequence identity, 82.97%) in the template ranking was selected for model building. The model was built based on the target-template alignment using ProMod3. Coordinates that are conserved between the target and the template were copied from the template to the model. Insertions and deletions were remodeled using a fragment library. Side chains were then rebuilt. Finally, the geometry and energy minimization of the resulting model was performed using the OpenMM molecular mechanics force field. The model quality assessment was performed based on the global and per-residue model quality using the QMEAN scoring function (see Appendix 14).

3.17. SH-SY5Y Cell Culture with $A\beta_{42}$ Challenge for Proteomics

SH-SY5Y cells were seeded at a density of 3×10^5 cells/mL on poly-L-lysine plates in DMEM/F12 media containing 2 mM glutamine, 10 μM retinoic acid and 1% FBS to induce postmitotic differentiation. Cells were incubated under regular culture conditions for attachment.

After 24 h of plating, the cells were co-incubated with 1 μM $A\beta_{42}$ for additional 72 h at 37 °C in a fully humidified atmosphere containing 5% CO_2.

3.18. Cell Lysis and Protein Extraction

SH-SY5Y cells were washed with phosphate buffered saline (PBS) and lysed with cell extraction buffer containing 10 mM Tris, pH 7.4, 100 mM NaCl, 1 mM EDTA, 1 mM EGTA, 1 mM NaF, 20 mM $Na_4P_2O_7$, 2 mM Na_3VO_4, 1% Triton X-100, 10% glycerol, 0.1% sodium dodecyl sulfate (SDS), 0.5% sodium deoxycholate, 1 mM phenylmethanesulfonyl fluoride (PMSF) and a protease inhibitor cocktail. Lysates were centrifuged for 15 min at 13,000 rpm and 4 °C. Supernatant was transferred to a clean tube. Lysis buffer of supernatant was exchanged to binding buffer (PBS, pH 7.4, with 1 mM PMSF and a protease inhibitor cocktail) using an Amicon Ultra-4 mL 3K MWCO centrifugal filter device (Millipore, Burlington, MA). Concentrations of the harvested proteins were determined by Bradford assay. The protein sample was stored at -80 °C.

3.19. C-Glycosylflavone Coupling with EAH Sepharose-4B Resins

EAH Sepharose-4B resin contains a covalent linkage of 1,6-diaminohexane to agarose (4 % agarose, 45-165 μm, exclusion limit 20,000 kDa), which has reactive primary amine groups at the end of 11-atom spacer arms. EAH Sepharose-4B resins are used to couple ligands containing carboxyl groups with the carbodiimide coupling method.

To a solution of the synthetic compound **6** (50 mg, 0.1 mmol) in acidic distilled water (4 mL, pH 4.5) was added with the EAH-4B matrix in a matrix-ligand solution ratio of 1:0.5. Excess of EDCI (1.9 g, 10 mmol) was added to the matrix suspension to a final concentration of 0.1 M at pH 4.5-5.0. The mixture was rotated end-over-end for 48 h at 4 °C. After coupling, the product was

thoroughly washed in sequence with 0.1 M sodium acetate buffer pH 4.0 containing 0.5 M NaCl, 0.1 M Tris-HCl buffer pH 8.5 containing 0.5 M NaCl, and distilled water pH 7.5. The product matrix was stored at 2-8 °C.

3.20. C-Glycosylflavone-Probe Affinity Pulldown Assay

A 1.5 × 10 cm chromatography column was packed with 2 ml of ligand-tag resin (binding capacity: 1 ml of the ligand-tag resin can bind 7-12 mg/ml of target proteins). The column was equilibrated with 12 ml of binding buffer (PBS, pH 7.4, with 1 mM PMSF and a protease inhibitor cocktail). 2 ml of protein sample (10 mg/mL of total protein) was added carefully to the column without disturbing the surface of the packing resins, and affinity chromatography was proceeded at 4 °C. For competitive affinity assay, 2 ml of protein sample (10 mg/mL of total protein) containing varied concentrations of free ligands was added to the column. To maximize binding capacity, the column was connected to a peristaltic pump to circulate the protein sample where eluates passed through the resin bed were reloaded to column. After 24 h, the resins were washed with 12 ml of binding buffer.

The bound proteins were eluted by applying 12 mL of elution buffer (0.1 M glycine-HCl, pH 2.5-3.0, 1 mM PMSF, and a protease inhibitor cocktail). The resulting eluate was collected and neutralized by adding 50 μL of neutralization buffer (1 M Tris-HCl, pH 8.5) per 1 mL of collected eluate. The resulting buffer was exchanged to 1 M triethylammonium bicarbonate (TEAB) buffer, pH 8.5, using an Amicon Ultra-4 mL 3K MWCO centrifugal filter device (Millipore, Burlington, MA). The eluate sample was concentrated to 250 μL and stored at -80 °C.

The column containing ligand-tag resins was regenerated by washing in sequence with 12 ml of distilled water, 12 ml of 0.1 M Tris-HCl (pH 8.5) containing 0.5 M NaCl, and 12 mL of binding buffer. The ligand-tag resins were stored at 2-8 °C in presence of 20% ethanol.

3.21. SDS-PAGE Analysis

The lysate eluates from affinity chromatography were resolved by 10-12% SDS-PAGE. A mixture of standard proteins (bovine thyroglobulin, IgA, IgG, GSK-3β, ovalbumin, myoglobin) was used to validate the binding specificity of the CFG-tag resins. Concentrations of the protein samples were determined by Bradford assay. Equal amounts of total proteins for each sample (10 μg per lane) were resolved by SDS-PAGE with a MiniProtean apparatus (Bio-Rad, Hercules, CA). The gel was stained with Bio-Safe Coomassie Stain according to the Bio-Rad protocol. Densitometric analysis was performed in triplicate.

3.22. Tryptic Digestion of Proteins

For in-solution digest, 100 μg of each protein sample were transferred to new tubes and volume was adjusted to 80 μL with TEAB buffer, pH 8.5. Proteins were denatured and reduced using 0.05% v/v SDS and 5 mM tris(2-carboxyethyl)phosphine (TCEP) and incubated at 60 °C for 1 h. Cysteine residues were alkylated with 10 mM methylmethanethiosulfate (MMTS) for 10 min at room temperature. Proteins were subjected to in-solution digestion by adding 5 μg of the mass spec grade Trypsin/Lys-C (protein:(Trypsin/Lys-C) ratio of 20:1) mix resuspended in TEAB buffer, pH 8.5, and incubated at 37 °C for 16 h.

For in-gel digest, the target protein band was cut and chopped into pieces (about 1 mm^3) and transferred to a microcentrifuge tube. The gel pieces were destained with 25 mM NH_4HCO_3 in 50%

acetonitrile and dried completely in a speed-vacuum at 45 °C. Proteins in gel were denatured and reduced with 10 mM DTT at 56 °C for 30 min. Cysteine residues were alkylated with 55 mM iodoacetamide (IAA) for 30 min in the dark at room temperature. The gel pieces were dehydrated with 100% acetonitrile at 37 °C until becoming an opaque-white color and shrink, then dried completely in a speed-vacuum. Proteins were subjected to in-gel digestion by adding 5 μg of the mass spec grade Trypsin/Lys-C (protein:(Trypsin/Lys-C) ratio of 20:1) mix resuspended in 25 mM NH_4HCO_3 buffer, pH 8.5, and incubated at 37 °C for 16 h. The digested peptides were extracted with 50% acetonitrile in 5% formic acid aqueous solution and transferred to a new tube. Sample was desalted with C18 ZipTip prior to LC-MS analysis.

3.23. iTRAQ Labeling of the Tryptic Peptides

Labeling was performed using iTRAQ Reagent-8plex kit (reporter ions 113, 114, 115, 116, 117, 118, 119, and 121) according to the manufacturer's protocol. iTRAQ reagents resuspended in 50 μL of isopropanol were reacted with the digested protein samples in TEAB buffer, pH 8.5, for 3 h at room temperature. The iTRAQ labels 113-114 were used on the control samples whose proteins were from the affinity chromatography with no-tag resins; labels 115-116 were used on the samples whose proteins were from the affinity chromatography with CGF-tag resins; labels 117-118 were used on the samples whose proteins were from the low-dose competitive affinity chromatography (50 μM free ligand **13**) with CGF-tag resins; and labels 119-121 were used on the samples whose proteins were from the high-dose competitive affinity chromatography (100 μM free ligand **13**) with CGF-tag resins. After labeling, samples were pooled together in TEAB buffer. Samples were stored at -80 °C. Samples were desalted and cleaned up using C18 ZipTip prior to LC-MS proteomics analysis.

3.24. Nano-UPLC-ESI-MS/MS Analysis for Proteomics

An nano-Advance UHPLC coupled to a maXis Impact QTOF mass spectrometer (Bruker, Billerica, MA) equipped with a CaptiveSpray source. The digested peptide mixtures were eluted on a ProntoSIL C18AQ column (0.1 × 150 mm, 3 μm, 200 Å pore size) with a linear gradient over 80 min from 5 to 45% aqueous acetonitrile containing 0.1% formic acid, flow rate of 500 nL/min. Samples were measured in auto MS/MS mode, a mass range of *m/z* 50-2200 with a fixed cycle time of 3 s. Acquisition speed was 2 Hz in MS and 4 or 16 Hz in MS/MS mode depending on precursor intensity. Precursors were selected in the *m/z* 300-2200 range with charge states at 2-5 (singly charge ions were excluded). Active exclusion was activated after 1 spectrum for 2 min. The collision energy was adjusted between 23–65 eV as a function of the *m/z* value. Data were collected in three technical replicates per sample.

3.25. Protein Identification and Quantification

Raw MS data were converted into peak list files in xml or mascot generic file (mgf) format using Daltonics DataAnalysis software 4.2 (Bruker, Billerica, MA). Peak lists were submitted to ProteinScape version 3.2 (Bruker, Billerica, MA) and searched against the SwissProt database with MASCOT 2.3 server (Matrix Science, London, UK). Search parameters were set as followed the Bruker's proteomics application manual: the peptide and MS/MS tolerance were set to 10 ppm and 0.06 Da, respectively; trypsin was set as the cleaving enzyme and two missed cleavages were allowed; methylthio (C) and iTRAQ-8plex (K and N-term) were set as fixed modifications, and oxidation (M) and iTRAQ-8plex (Y) were set as variable modifications; the peptide decoy and percolator strategies were applied to evaluate the database search results; the significance value

was set at $p < 0.05$ for protein identification, and the false discovery rate (FDR) for peptide identification was set at 1%; proteins with a Mascot score ≥ 13 and peptides with a Mascot score ≥ 13 were accepted.

Quantification ratios were obtained using WARP-LC (Bruker, Billerica, MA). Combinations of iTRAQ ratios were calculated for the accepted proteins (114/113, 115/113, 116/113, 117/113, 118/113, 119/113, 121/113, 115/114, 116/114, 117/114, 118/114, 119/114, and 121/114). The median of all ratios was calculated for each protein and a stringent 2.5-fold cutoff to avoid false positives was applied to differentiate between the specific and nonspecific binding proteins according to the described procedure.[62]

3.26. Molecular Interaction Networks Analysis

Molecular interaction networks and biological pathways were visualized, integrated, and analyzed with open source software platforms Cytoscape 3.6[170] and STRING 10.5[171].

3.27. Statistical Analysis

Data were presented as the mean ± SEM or ± SD. The data were analyzed by one-way ANOVA with Bonferroni's multiple comparison test, Tukey's multiple comparison posthoc test, as well as Student's *t* test. The *p* values less than 0.05 were considered statistically significant. Analyses were performed using Excel and GraphPad Prism.

APPENDICES

Appendix 1. Proposed fragmentations of (A) **1** and (B) **2** in tandem mass spectrometry (ESI-CID-MS/MS)

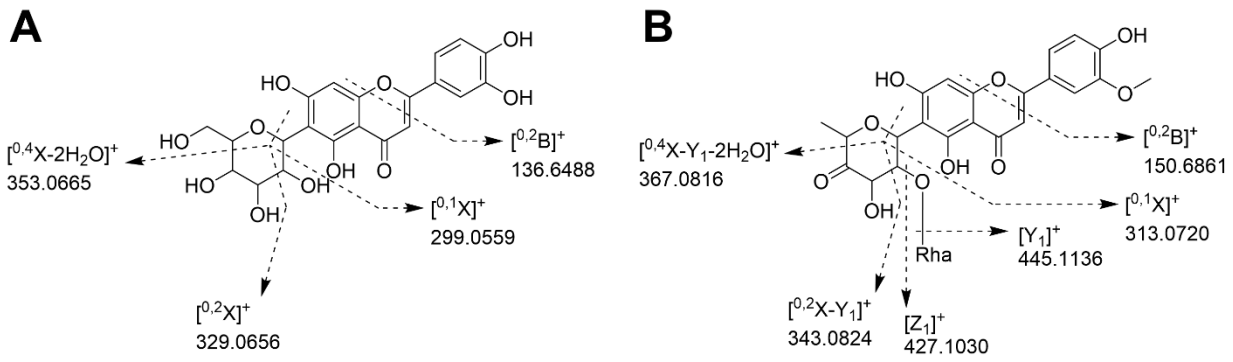

Appendix 2. GSK3β specific inhibition of **1** that is insensitive to the detergent Triton X-100

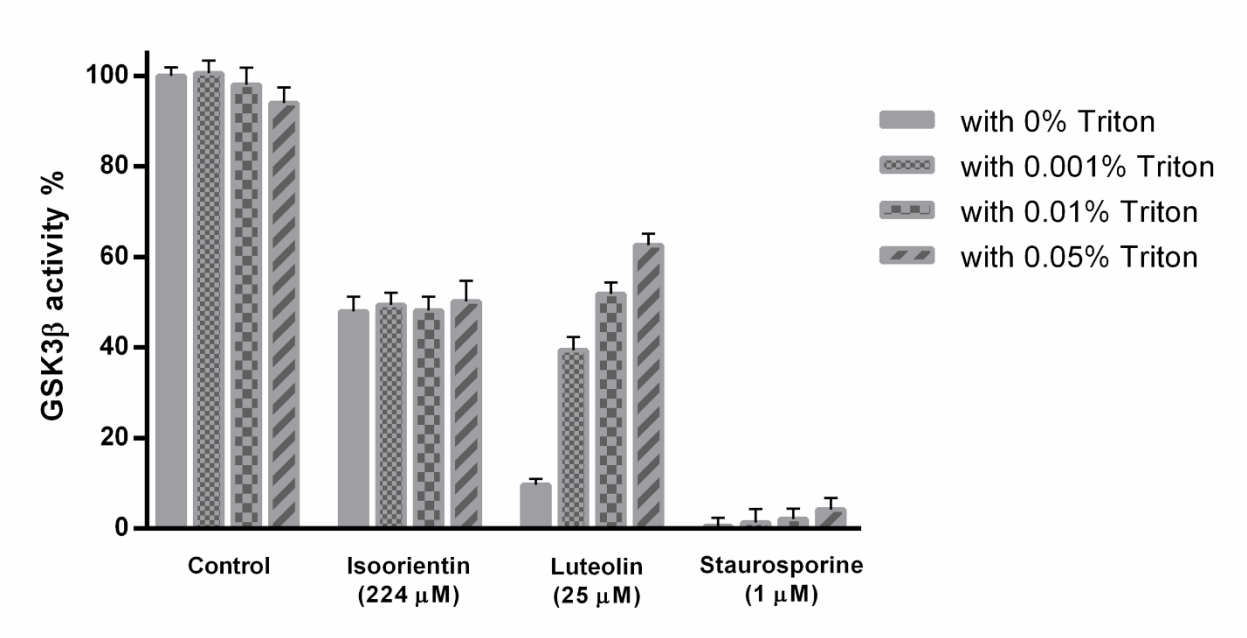

GSK3β was assayed in the presence of 224 μM **1** with increasing concentrations of Triton X-100 (v/v 0%, 0.001%, 0.01% and 0.05%). Luteolin (IC_{50}, 2 μM; assay concentration, 25 μM) and staurosporine (IC_{50}, 2 nM; assay concentration, 1 μM) were used as reference controls for promiscuous aggregations. Data were means of quadruplicate of each of two independent experiments with ± SEM.

Appendix 3. CS fractions with GSK3β inhibition alleviate neurotoxicity induced by Aβ42 in SH-SY5Y cells

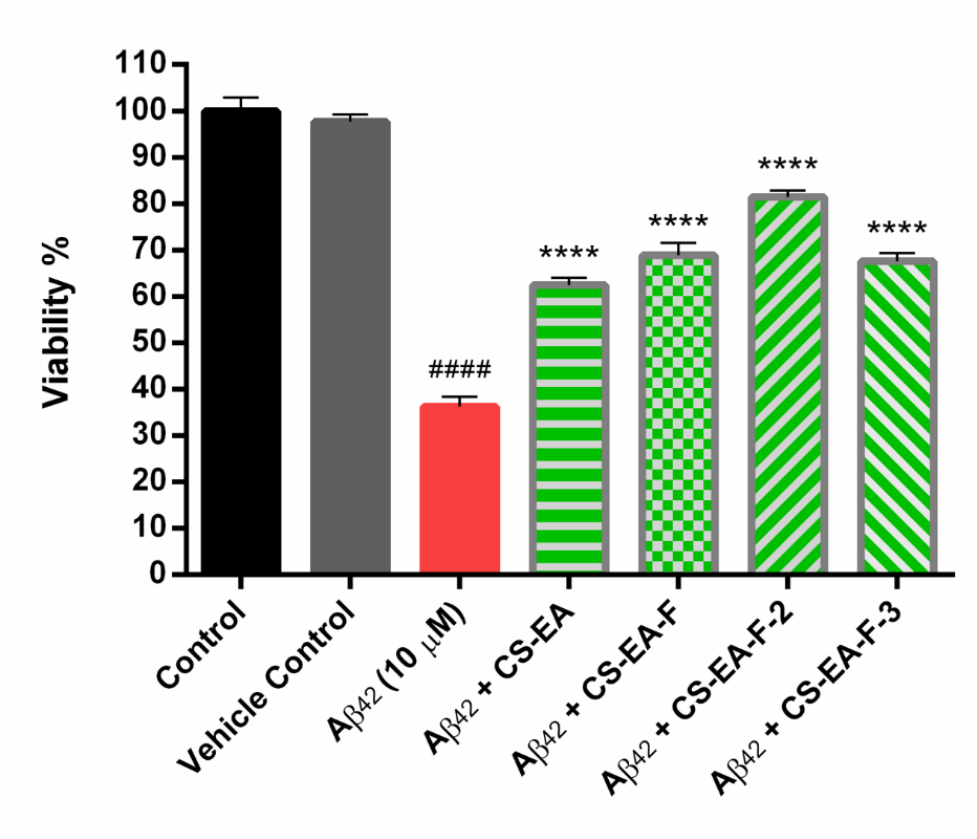

Cells were pretreated with 100 μg/mL of CS fractions or 0.2% DMSO vehicle for 1 h followed by 10 μM Aβ42 treatment and incubated for 72 h. Results were presented as the percentage of the cell viability relative to control. Data were means of triplicate of each of two independent experiments with ± SEM. $^{\#\#\#\#}p < 0.0001$ relative to vehicle control; $^{****}p < 0.0001$ relative to the 10 μM Aβ42 treatment.

Appendix 4. HPLC chromatogram of CS fractions

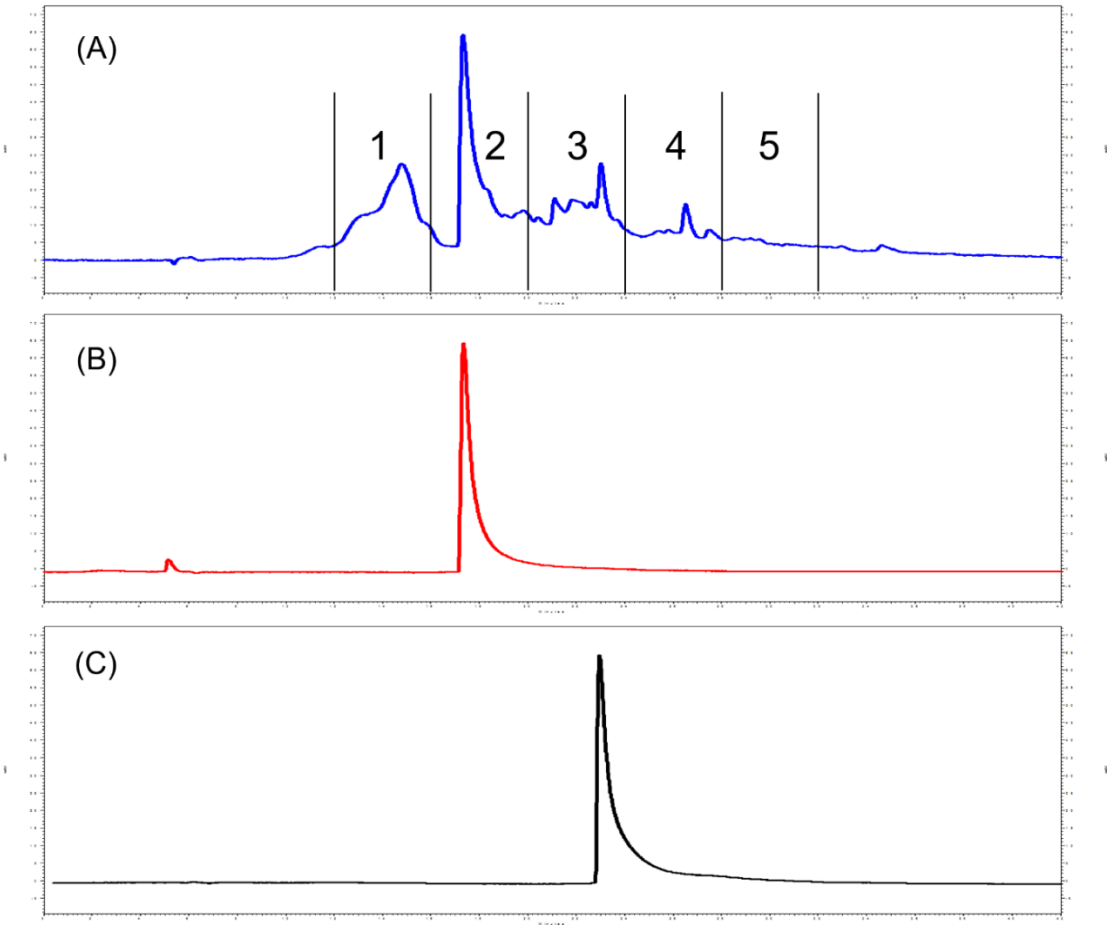

(A) HPLC chromatogram of fraction CS-EA-F. Numbers 1 to 5 correspond to collection windows for subfractions CS-EA-F-1 through CS-EA-F-5. (B) HPLC chromatogram of fraction CS-EA-F-2 (**1**) after purification. (C) HPLC chromatogram of fraction CS-EA-F-3 (**2**) after purification.

Appendix 5. Mass spectrometry spectra of **1**

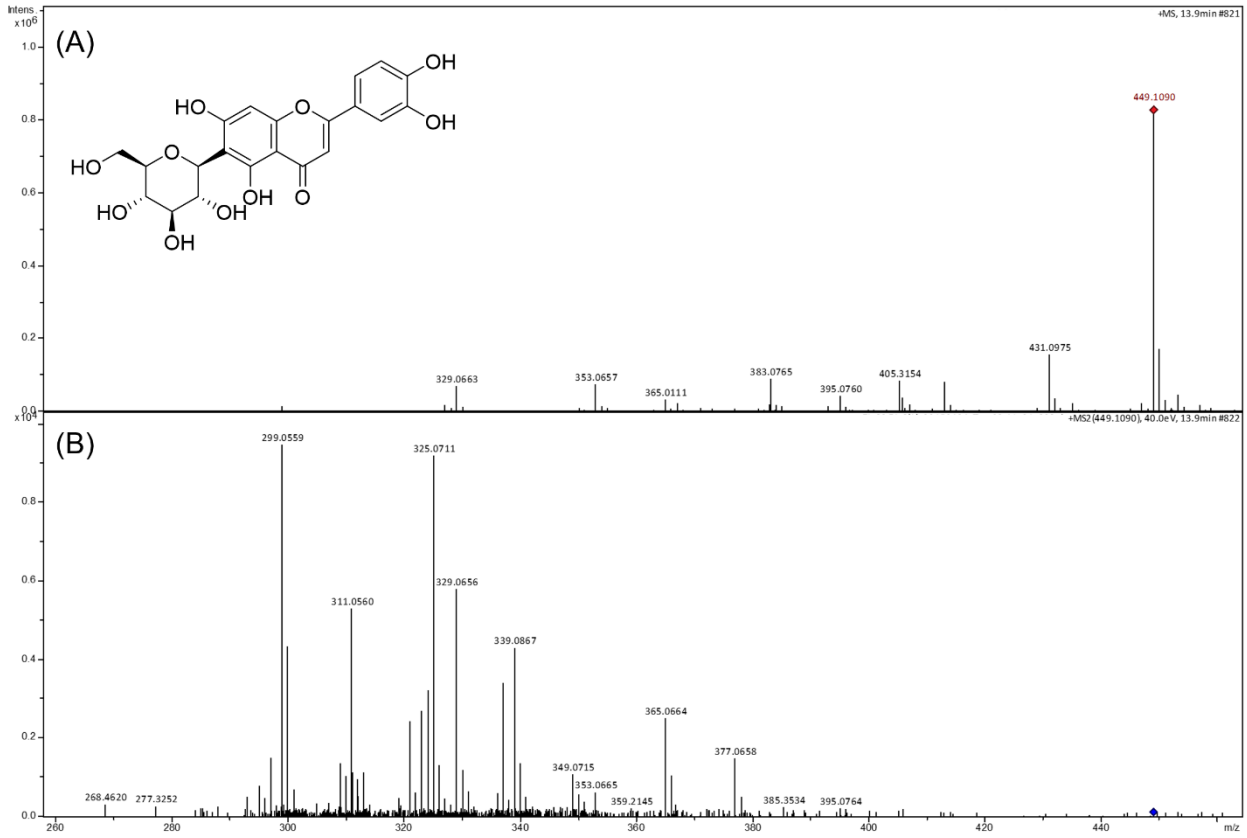

(A) MS1 spectrum. (B) CID-MS/MS spectrum

Appendix 6. Mass spectrometry spectra of **2**

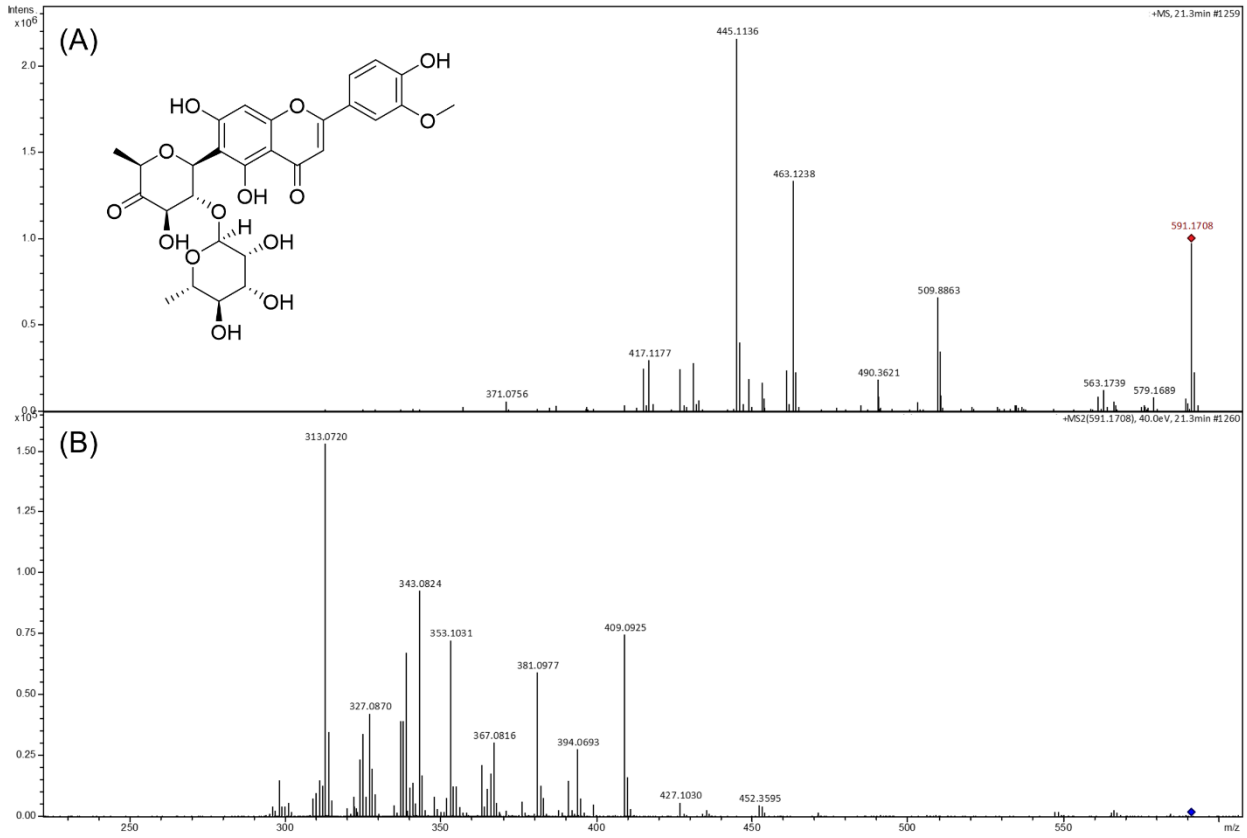

(A) MS1 spectrum. (B) CID-MS/MS spectrum.

Appendix 7. ^{1}H NMR spectrum of **1** (from fraction CS-EA-F-2, > 95% purity) in DMSO-d_6

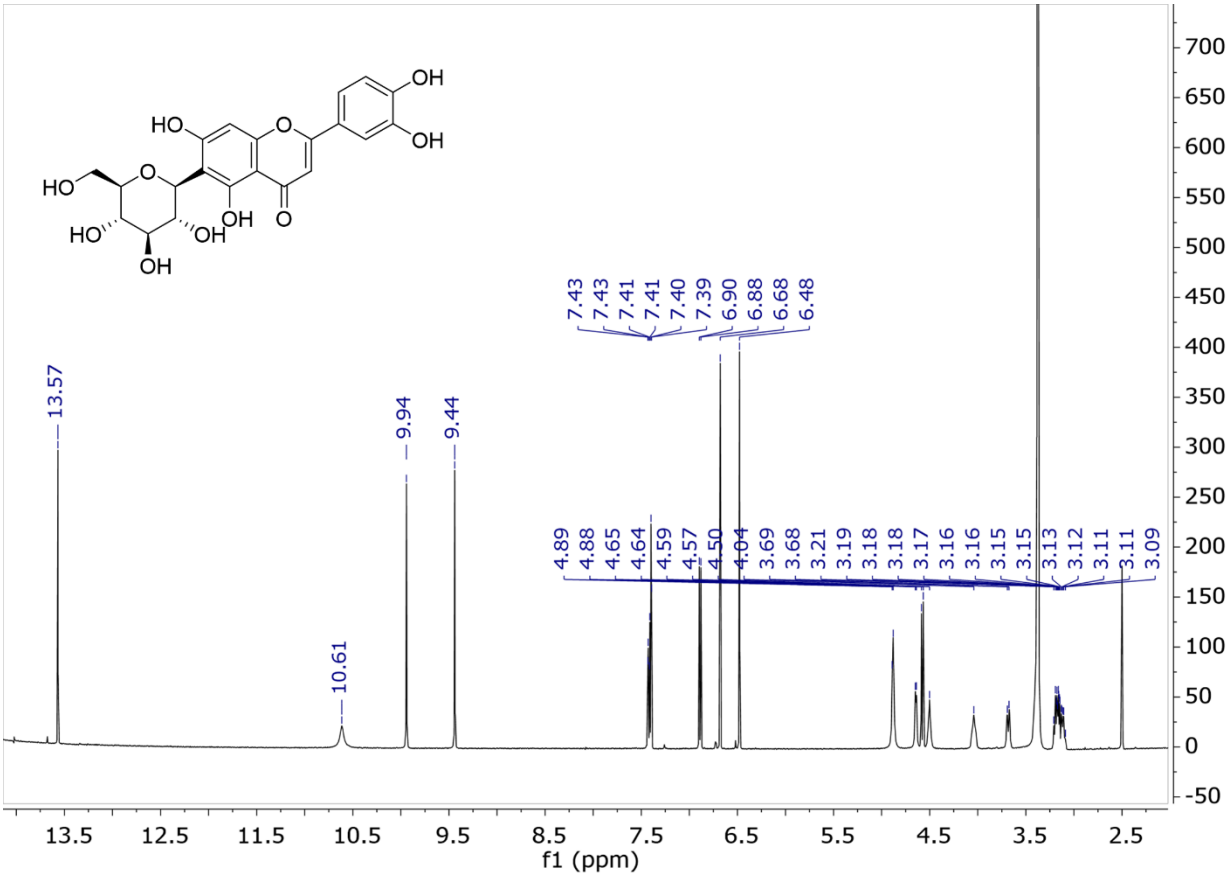

Appendix 8. ^{13}C NMR spectrum of **1** (from fraction CS-EA-F-2, > 95% purity) in DMSO-d_6

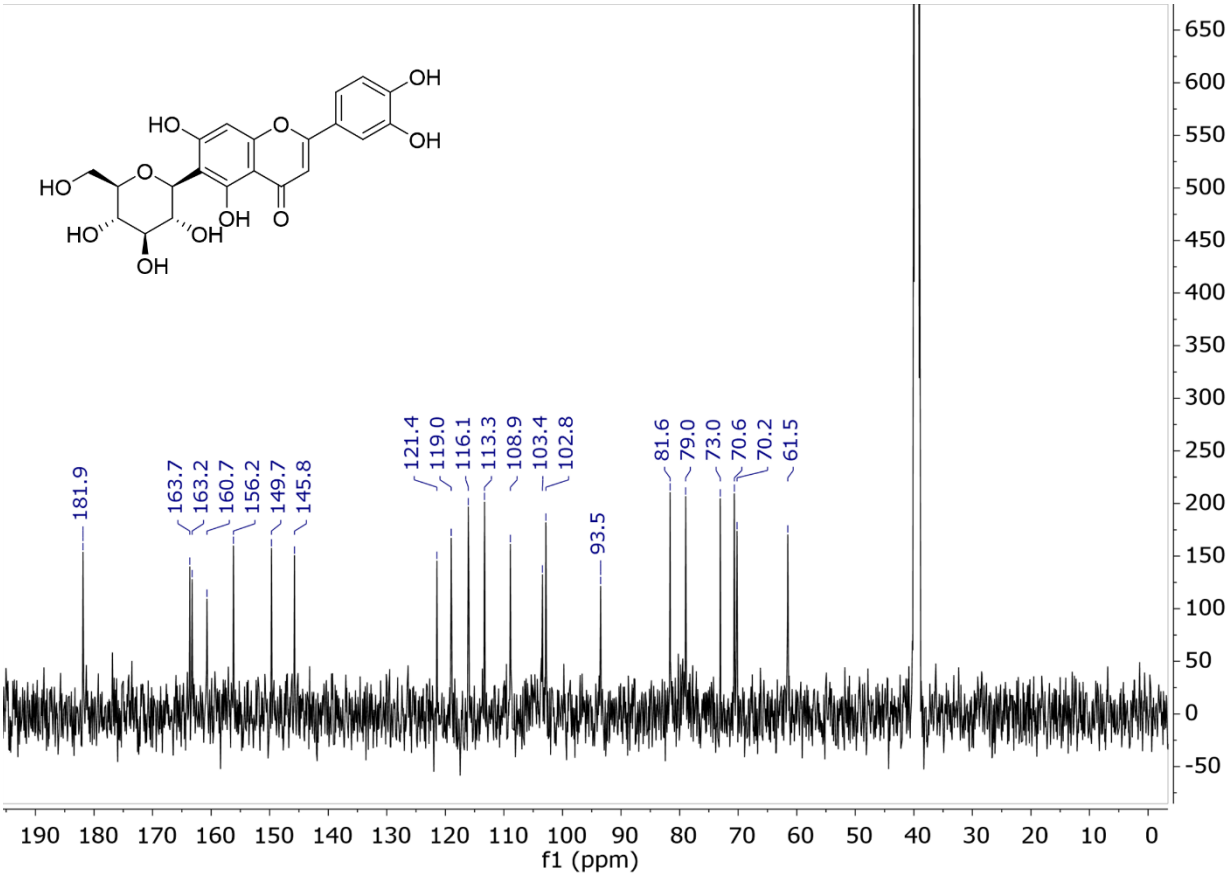

Appendix 9. ^{1}H NMR spectrum of **2** (from fraction CS-EA-F-3, > 95% purity) in DMSO-d_6

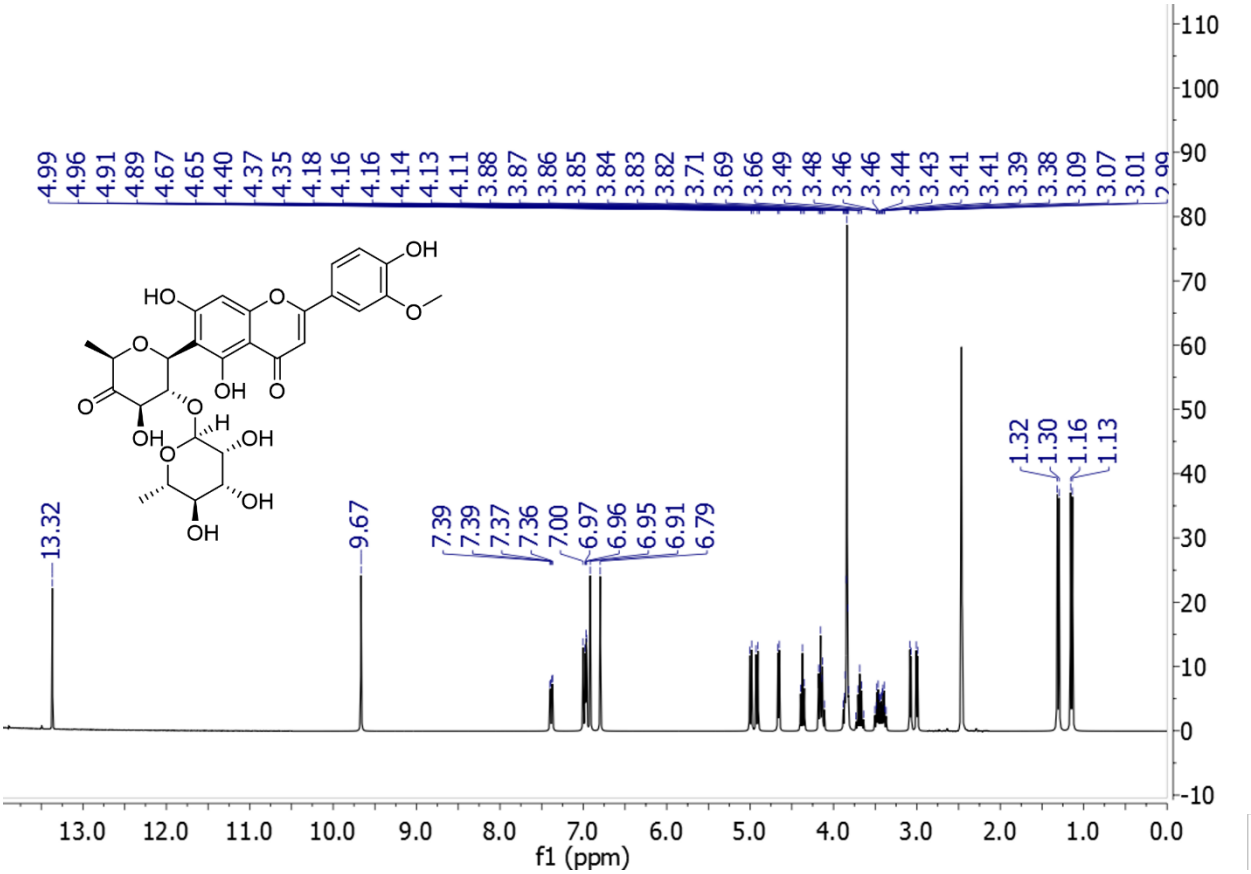

Appendix 10. Docking Method Validation by Re-docking and Cross-docking Experiments with Known GSK-3β Inhibitors

We chose two X-ray crystallographic structures of GSK-3β (PDB codes 1PYX[97] and 1H8F[137]). The docking method was validated by re-docking and cross-docking experiments using both ATP-competitive and substrate-competitive inhibitors.

Re-docking the native ligand ANP to 1PYX resulted in a binding pose at the ATP site of GSK-3β with a RMSD of 0.33 Å as compared to its original crystal structure.[97] Under the same parameters, docking with the known ATP-competitive inhibitors, staurosporine and luteolin, led to the binding to the ATP site of GSK-3β, of which the binding poses and positions are similar to the reported data.[97, 197] The ligands HEPES, manzamine A and isoorientin are known GSK-3β inhibitors bound to the substrate site. Docking these ligands to 1PYX confirmed their binding to the substrate site, and the predicted poses are comparable to the reported data.[65, 96, 137] Cross-docking of the same ligands to the 1H8F demonstrated that ANP, staurosporine, and luteolin reside the ATP site of GSK-3β, whereas HEPES, manzamine A, and isoorientin are in the substrate site. Re-docking experiment using the native ligand HEPES of 1H8F resulted in a binding pose at the substrate site of GSK-3β with a RMSD of 0.62 Å as compared to its original crystal structure.[137]

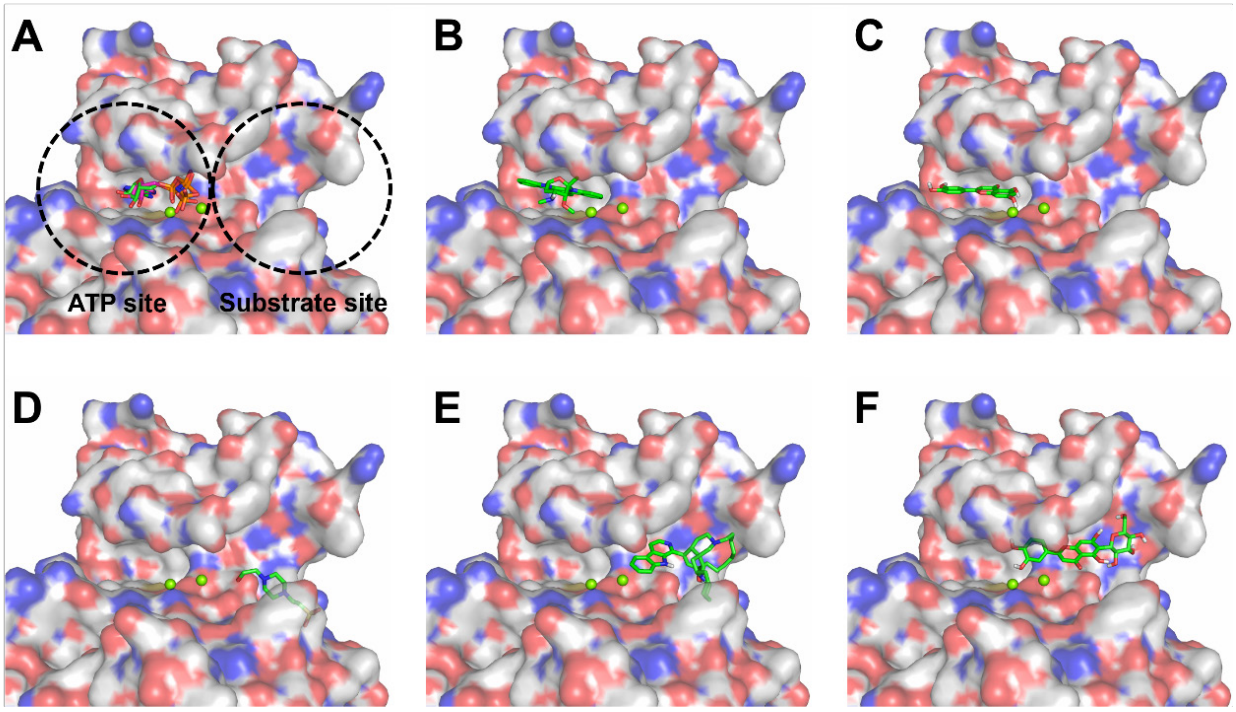

Predicted docking poses of ANP (A), staurosporine (B), luteolin (C), HEPES (D), manzamine A (E), and isoorientin (F) in GSK-3β (PDB code 1PYX). Ligands in magenta color are original structures in X-ray crystallographic complex, ligands in green color are docking structures.

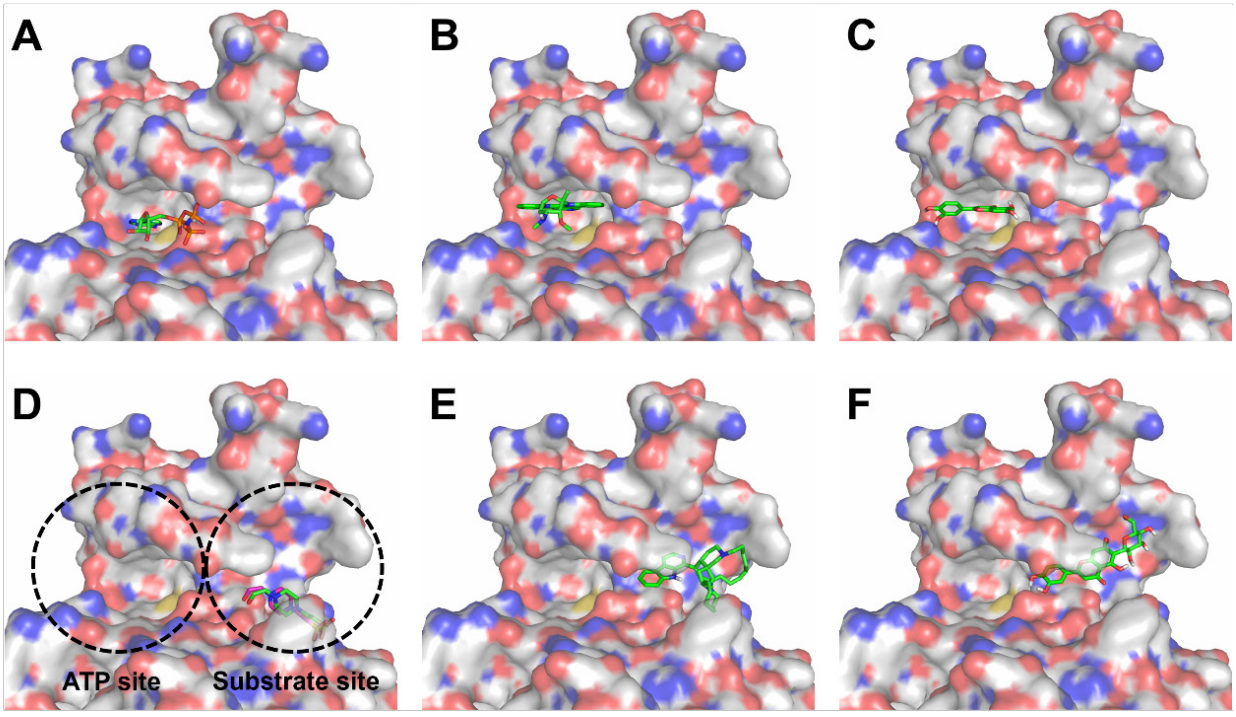

Predicted docking poses of ANP (A), staurosporine (B), luteolin (C), HEPES (D), manzamine A (E), and isoorientin (F) into GSK-3β (PDB code 1H8F). Ligands in magenta color are original structures in X-ray crystallographic complex, ligands in green color are docking structures.

Appendix 11. Inhibitions and Docking Scores of C-Glycosylflavones and Reference Inhibitors to GSK3β

cmpd	GSK3β inhibition	Docking Score [b]: Affinity (-kcal/mol)		cmpd	GSK3β inhibition	Docking Score [b]: Affinity (-kcal/mol)	
no.	IC_{50} (μM) [a]	1PYX	1H8F	no.	IC_{50} (μM) [a]	1PYX	1H8F
1	184.9 ± 1.4	7.3	7.1	**21**	15.8 ± 1.2	8.4	8.4
3	5153 ± 31	6.8	6.3	**22**	35.6 ± 1.3	8.1	8.4
4	3.1 ± 1.3	8.3	8.2	**23**	35.1 ± 1.0	8.2	8.3
5	239.2 ± 1.2	7.4	7.8	**24**	56.2 ± 1.2	8.5	8.6
6	237.3 ± 1.4	7.3	7.6	**25**	21.7 ± 1.2	8.4	8.5
7	135.0 ± 1.3	7.6	7.8	**26**	34.8 ± 1.0	7.8	7.9
8	29.2 ± 1.1	7.7	7.9	**27**	19.3 ± 0.8	8.2	8.0
9	5.4 ± 0.1	8.3	8.3	**28**	49.5 ± 1.2	7.3	7.7
10	33.3 ± 1.1	7.9	7.9	**29**	17.2 ± 0.9	8.2	7.9
11	31.1 ± 1.2	7.8	8.0	**30**	0.59 ± 0.04	9.1	8.9
12	28.0 ± 1.1	8.0	7.8	**31**	2.3 ± 0.5	8.7	8.5
13	9.4 ± 0.9	8.4	7.8	**Staurosporine**	0.0023 ± 0.0006	10.2	10.0
14	25.8 ± 1.1	7.6	8.0	**Manzamine A**	10.2 [c]	9.0	8.9
15	61.9 ± 1.2	7.4	8.1	**ANP**	n/a	9.7	9.3
16	13.1 ± 1.1	7.7	8.4	**HEPES**	n/a	4.4	4.5
17	9.0 ± 1.3	8.3	8.4				
18	26.0 ± 1.2	8.1	8.4				
19	33.5 ± 0.8	8.4	8.8				
20	19.7 ± 1.1	8.4	8.4				

[a] IC_{50} values were the mean of quadruplicate of each of two independent experiments. [b]Docking scores were binding affinities calculated by AutoDock Vina. [c] IC_{50} value from ref [198].

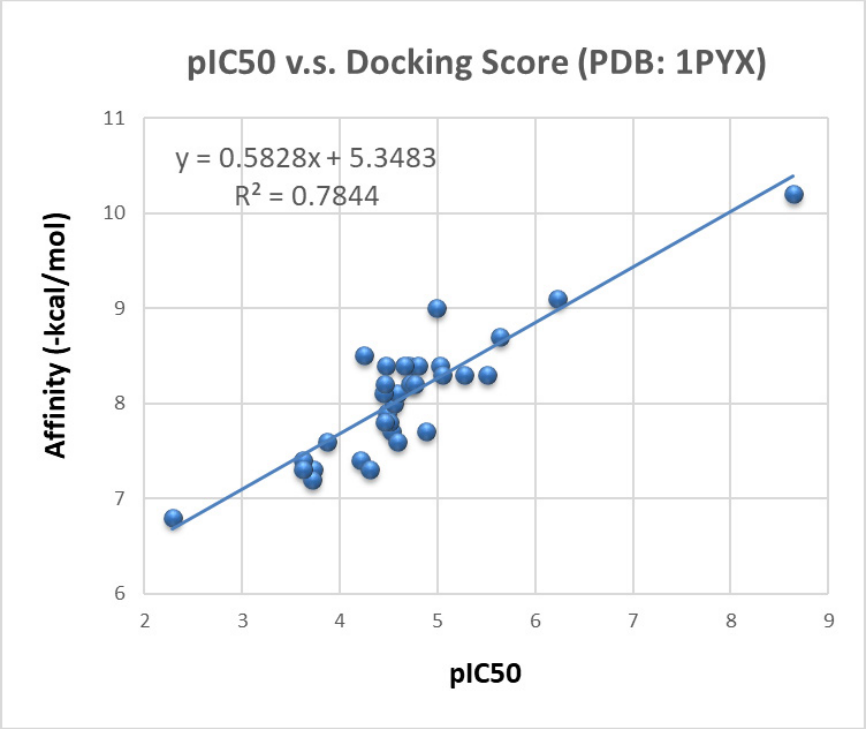

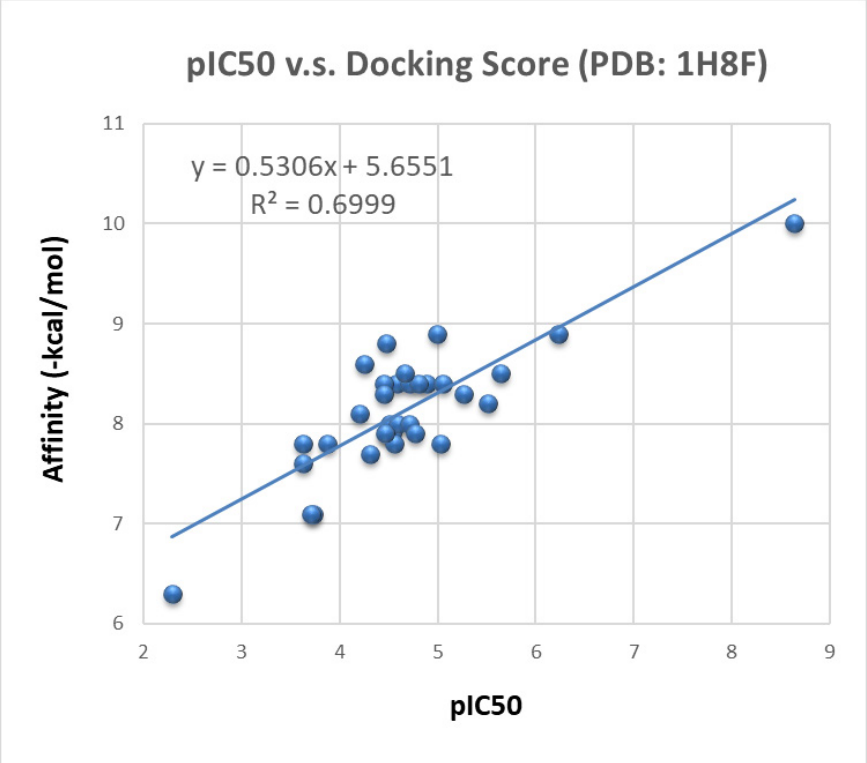

Linear plots of pIC50 (-LogIC50) versus calculated binding affinity (PDB codes 1PYX and 1H8F) for GSK-3β inhibitors

Appendix 12. Predicted Docking Poses of Flavones with GSK-3β (PDB Code 1PYX)

Docking poses of flavones **1** (A), **9** (B), **17** (C), **21** (D), **3** (E), and **4** (F) with GSK-3β (PDB code 1PYX). Surface representation of the ATP site of GSK-3β is shown in orange, the substrate site of GSK-3β is shown in green. Within the substrate site, surface features are shown with acidic residues in red, basic residues in blue, and hydrophobic residues in green. Mg^{2+} ions are shown as bright green spheres. The dotted lines represent interactions with Mg^{2+} ions and hydrogen bonds with side chain residues of GSK-3β.

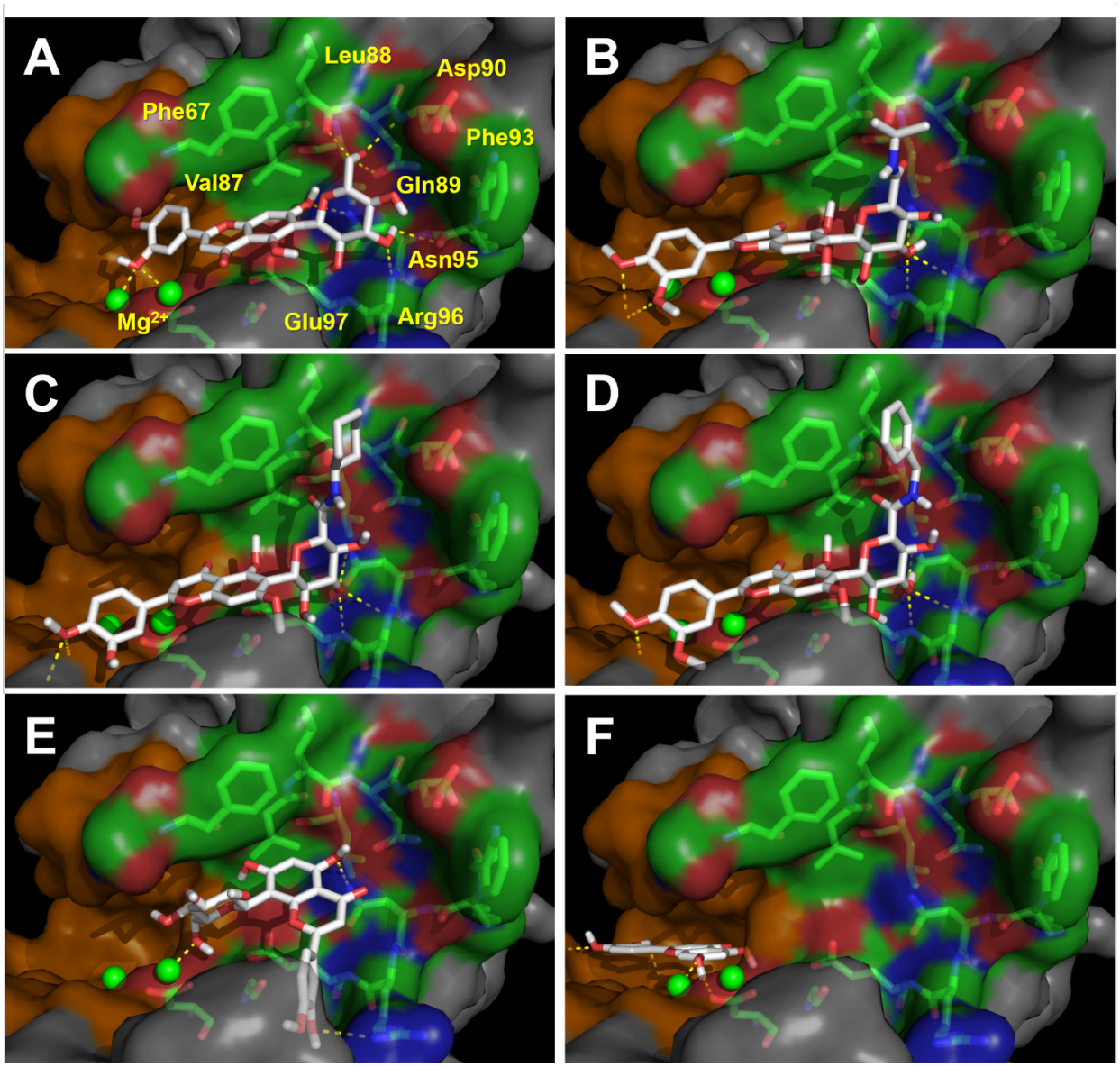

Appendix 13. Summary of Molecular Interaction Distances of Compound 30 with GSK3β (PDB Code 1PYX) in Molecular Docking

Interaction type	**Interaction residue**	**Distance (Å)**
Hydrogen bonds	Carbonyl O···HN (Phe67)	2.3
	Methoxy O···HN (Lys183)	3.1, 3.2
	Glycone HO···HN (Leu88)	3.4
	Glycone HO···HN (Asn95)	1.8, 2.6
	Glycone OH···O=C (Leu88)	2.8
	Glycone OH···O=C (Gln89)	3.2
	Glycone OH···O=C (Glu97)	2.8
	Glycone OH···O=C (Gly202)	2.5
Hydrophobic interactions	Isopropyl Me (Phe67)	
	Methoxy Me (Val87)	
	Isopropyl CF_3 (Leu88)	
π-cation interaction	Catechol B-ring···NH_3^+ (Lys183)	4.1 (angle 71.5°)
Orthogonal multipolar interactions	Isopropyl F···C=O (Leu88)	3.3
	Isopropyl F···C=O (Gln89)	3.6
	Isopropyl F···C=O (Asp90)	3.3, 3.8
Fluorine polar interaction	Isopropyl F···HN (Asp90)	2.6

Appendix 14. GSK-3α Homology Modeling Method

The SWISS-MODEL[146] template library (SMTL version 2017-09-21, PDB release 2017-09-15) was searched with BLAST and HHBlits for evolutionary related structures matching the target sequence GSK-3α (UniProt Code P49840). For each identified template, the template's quality has been predicted from features of the target-template alignment. The templates with the highest quality have then been selected for model building. Overall 4470 templates were found to match the target sequence. The top templates are:

	Name	Title	Coverage	Identity	Method	Oligo State	Ligands
☐	5air.1.A	LOW-DENSITY LIPOPROTEIN RECEPTOR-RELATED PROTEIN 6, GLYCOGEN SYNTHASE KINASE-3 BETA		81.87	X-ray, 2.5Å	homo-dimer	None
☐	5air.1.B	LOW-DENSITY LIPOPROTEIN RECEPTOR-RELATED PROTEIN 6, GLYCOGEN SYNTHASE KINASE-3 BETA		81.87	X-ray, 2.5Å	homo-dimer	None
☑ ✓	1pyx.1.A	Glycogen synthase kinase-3 beta		82.97	X-ray, 2.4Å	homo-dimer	4 x MG, 2 x ANP
☐	1q5k.1.A	Glycogen synthase kinase-3 beta		82.97	X-ray, 1.9Å	homo-dimer	2 x TMU
☐	4j1r.1.A	Glycogen synthase kinase-3 beta		82.97	X-ray, 2.7Å	monomer	1 x K, 1 x I5R
☐	1q3d.1.B	GLYCOGEN SYNTHASE KINASE-3 BETA		82.97	X-ray, 2.2Å	homo-dimer	2 x STU
☐	1j1b.1.A	Glycogen synthase kinase-3 beta		82.97	X-ray, 1.8Å	homo-dimer	2 x ANP
☐	4acg.1.A	GLYCOGEN SYNTHASE KINASE-3 BETA		82.97	X-ray, 2.6Å	homo-dimer	2 x 6LQ
☐	4e7w.1.A	Glycogen Synthase Kinase 3		69.16	X-ray, 3.3Å	monomer	None
☐	4e7w.1.A	Glycogen Synthase Kinase 3		70.39	X-ray, 3.3Å	monomer	None
☐	1h27.1.A	CELL DIVISION PROTEIN KINASE 2		40.14	X-ray, 2.2Å	hetero-oligomer	None
☐	1h1p.2.A	CELL DIVISION PROTEIN KINASE 2		40.14	X-ray, 2.1Å	hetero-oligomer	1 x CMG
☐	1h28.1.A	CELL DIVISION PROTEIN KINASE 2		40.14	X-ray, 2.8Å	hetero-oligomer	None
☐	1h24.2.A	CELL DIVISION PROTEIN KINASE 2		40.14	X-ray, 2.5Å	hetero-oligomer	None
☐	1h1q.2.A	CELL DIVISION PROTEIN KINASE 2		40.14	X-ray, 2.5Å	hetero-oligomer	1 x 2A6
☐	1vyw.2.A	CELL DIVISION PROTEIN KINASE 2		39.43	X-ray, 2.3Å	hetero-oligomer	1 x 292

The GSK-3α homology model was built based on the GSK-3β template PDB code 1PYX:

Template	Sequence identity	Oligo-state	Found by	Method	Resolution	Sequence similarity	Range	Coverage	Description
1pyx.1.A	82.97	homodimer	BLAST	X-ray	2.40 Å	0.55	98–449	0.77	GSK-3β
Built with	**Oligo-State**	**Ligands**	**GMQE**	**QMEAN**					
ProMod3 Version 1.0.2.	monomer	Mg^{2+} ion	0.72	-0.90					

Model Quality Estimation:

The global and per-residue model quality has been assessed using the QMEAN scoring function. For improved performance, weights of the individual QMEAN terms have been trained specifically for SWISS-MODEL.

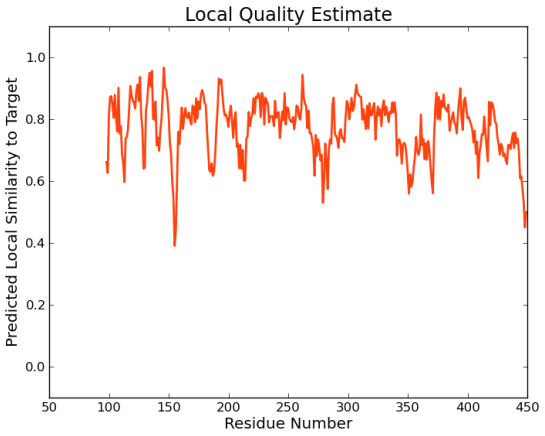

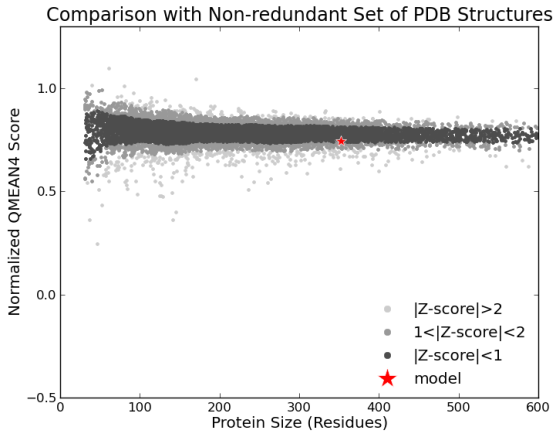

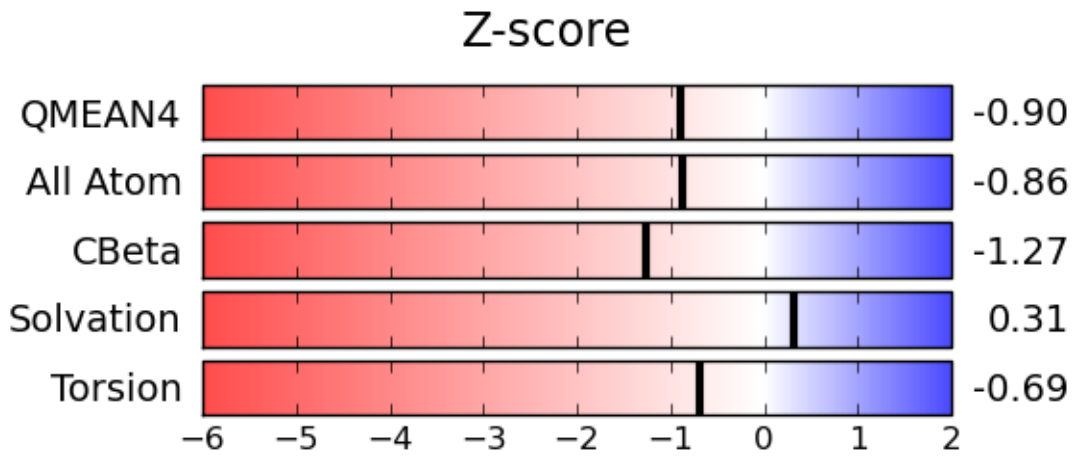

Appendix 15. Protein Sequence Alignment Between Human GSK-3α (UniProt Code P49840) and Human GSK-3β (PDB Code 1PYX)

Identical residues are unpainted, nonidentical residues are yellow highlighted, unmatched residues are green highlighted; key residues comprised of ATP site are colored in red, key residues comprised of substrate site are colored in blue. It is obvious that the kinase catalytic domain comprised of both ATP and substrate pocket sequences (D121-H208 and C241-L270 in GSK-3α; D58-H145 and C178-L207 in GSK-3β) are conserved as high as 93% identical. Only nine amino acid residues are nonidentical in these regions between two isoforms.

P49840_hGSK3A	MSGGGPSGGGPGGSGRARTSSFAEPGGGGGGGGGGPGGSASGPGGTGGGKASVGAMGGGV	60
1PYX_hGSK3B	--	
P49840_hGSK3A	GASSSGGGPGGSGGGGSGGPGAGTSFPPPGVKLGRDSGKVTTVVATLGQGPERSQEVAYT	120
1PYX_hGSK3B	------------------------------VSRDKDGSKVTTVVATPGQGPDRPQEVSYT	57
P49840_hGSK3A	DIKVIGNGSFGVVYQARLAETRELVAIKKVLQDKRFKNRELQIMRKLDHCNIVRLRYFFY	180
1PYX_hGSK3B	DTKVIGNGSFGVVYQAKLCDSGELVAIKKVLQDKRFKNRELQIMRKLDHCNIVRLRYFFY	117
P49840_hGSK3A	SSGEKKDELYLNLVLEYVPETVYRVARHFTKAKLTIPILYVKVYMYQLFRSLAYIHSQGV	240
1PYX_hGSK3B	SSGEKKDEVYLNLVLDYVPETVYRVARHYSRAKQTLPVIYVKLYMYQLFRSLAYIHSFGI	177
P49840_hGSK3A	CHRDIKPQNLLVDPDTAVLKLCDFGSAKQLVRGEPNVSYICSRYYRAPELIFGATDYTSS	300
1PYX_hGSK3B	CHRDIKPQNLLLDPDTAVLKLCDFGSAKQLVRGEPNVSYICSRYYRAPELIFGATDYTSS	237
P49840_hGSK3A	IDVWSAGCVLAELLLGQPIFPGDSGVDQLVEIIKVLGTPTREQIREMNPNYTEFKFPQIK	360
1PYX_hGSK3B	IDVWSAGCVLAELLLGQPIFPGDSGVDQLVEIIKVLGTPTREQIREMNPNYTEFKFPQIK	297
P49840_hGSK3A	AHPWTKVFKSRTPPEAIALCSSLLEYTPSSRLSPLEACAHSFFDELRCLGTQLPNNRPLP	420
1PYX_hGSK3B	AHPWTKVFRPRTPPEAIALCSRLLEYTPTARLTPLEACAHSFFDELRDPNVKLPNGRDTP	357
P49840_hGSK3A	PLFNFSAGELSIQPSLNAILIPPHLRSPAGTTTLTPSSQALTETPTSSDWQSTDATPTLT	480
1PYX_hGSK3B	ALFNFTTQELSSNPPLATILIPPHARIQAAASTPTNATAA--------------------	397
P49840_hGSK3A	NSS	483
1PYX_hGSK3B	---	

Appendix 16. HPLC Analysis for Purity Determination of Compounds 5-31[a]

The purity of compounds **5-31** was determined by analytical reverse phase Agilent HPLC with a diode array detector (Waters XSELECT CSH Fluoro-Phenyl column, 150 × 4.6 mm, 3.5 µm, isocratic elution with 35% aqueous acetonitrile containing 0.1% formic acid for over 20 min, detection at 210 nm, flow rate of 0.8 mL/min). All tested compounds were over 95% purity.

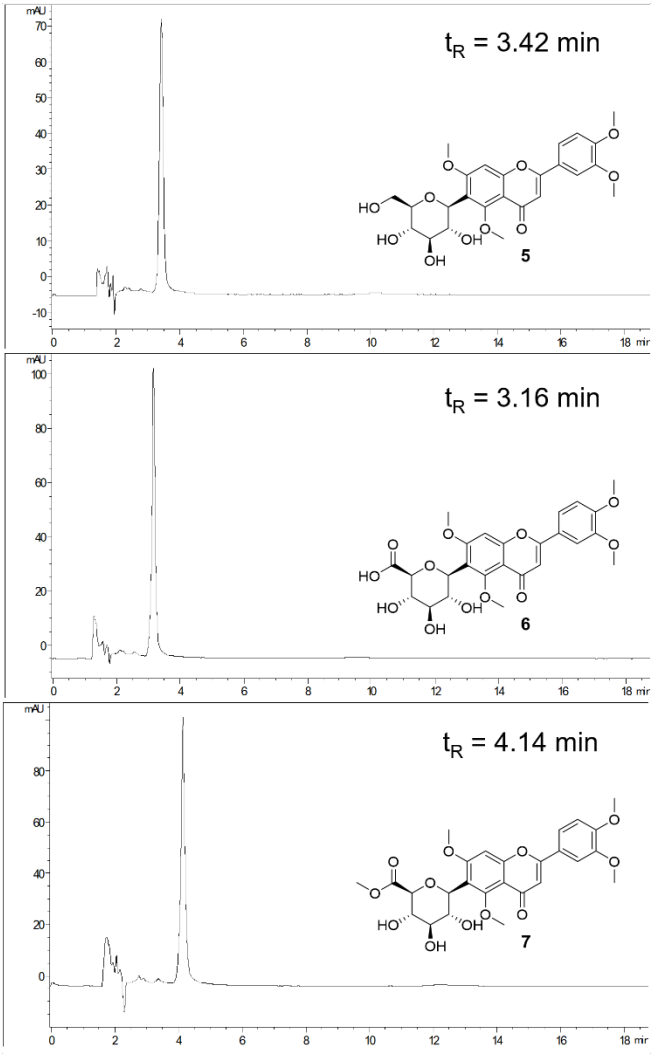

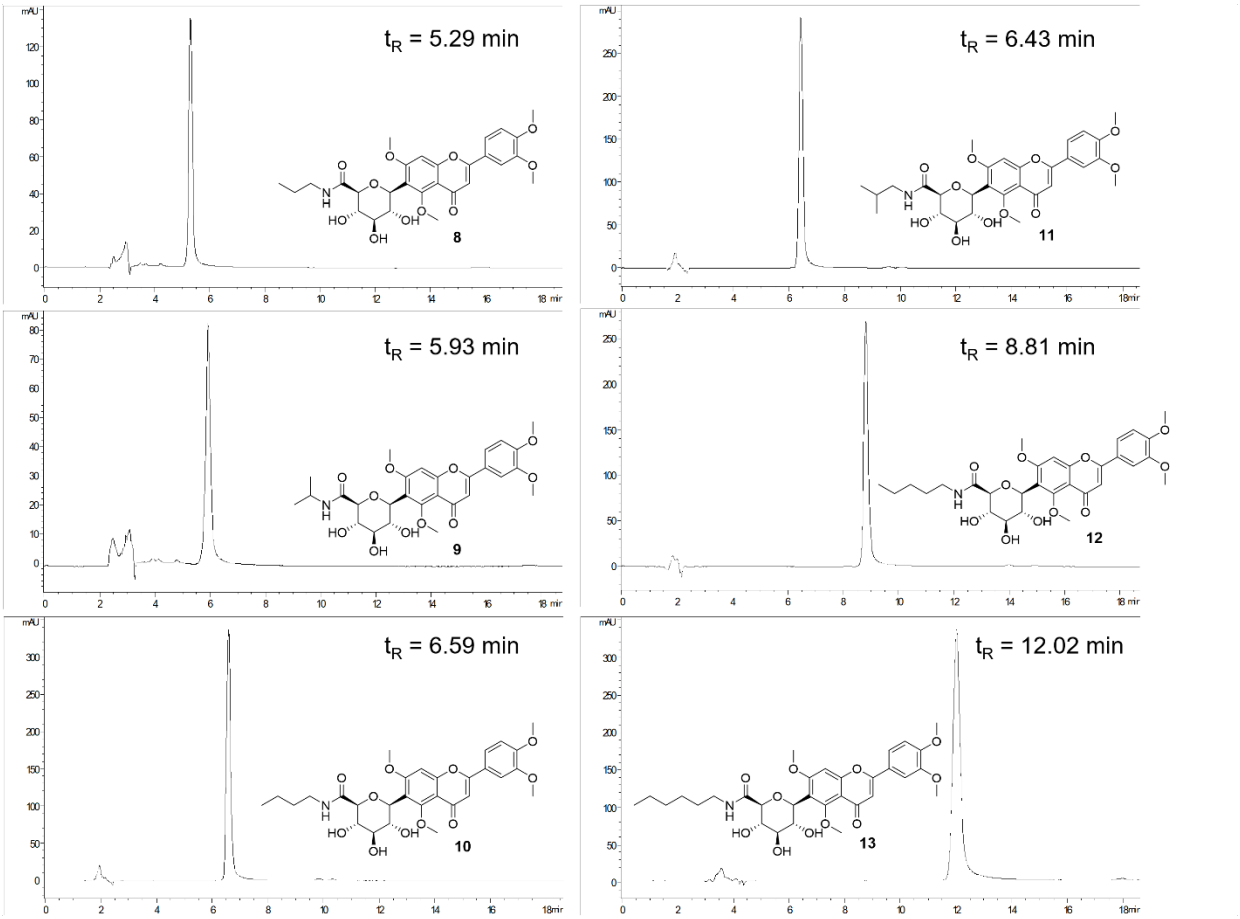
t_R = 5.29 min
8
t_R = 6.43 min
11
t_R = 5.93 min
9
t_R = 8.81 min
12
t_R = 6.59 min
10
t_R = 12.02 min
13

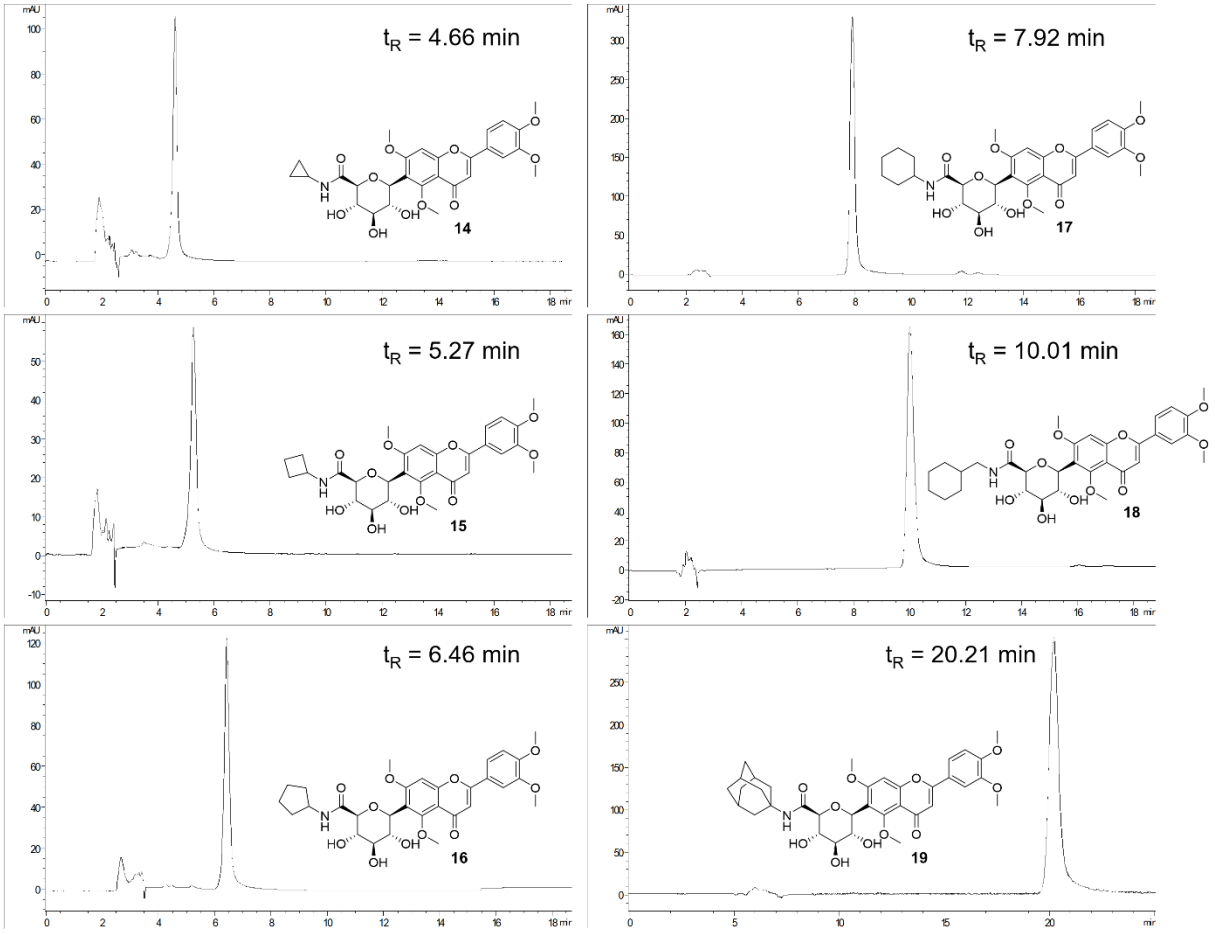
t_R = 4.66 min
14
t_R = 7.92 min
17
t_R = 5.27 min
15
t_R = 10.01 min
18
t_R = 6.46 min
16
t_R = 20.21 min
19

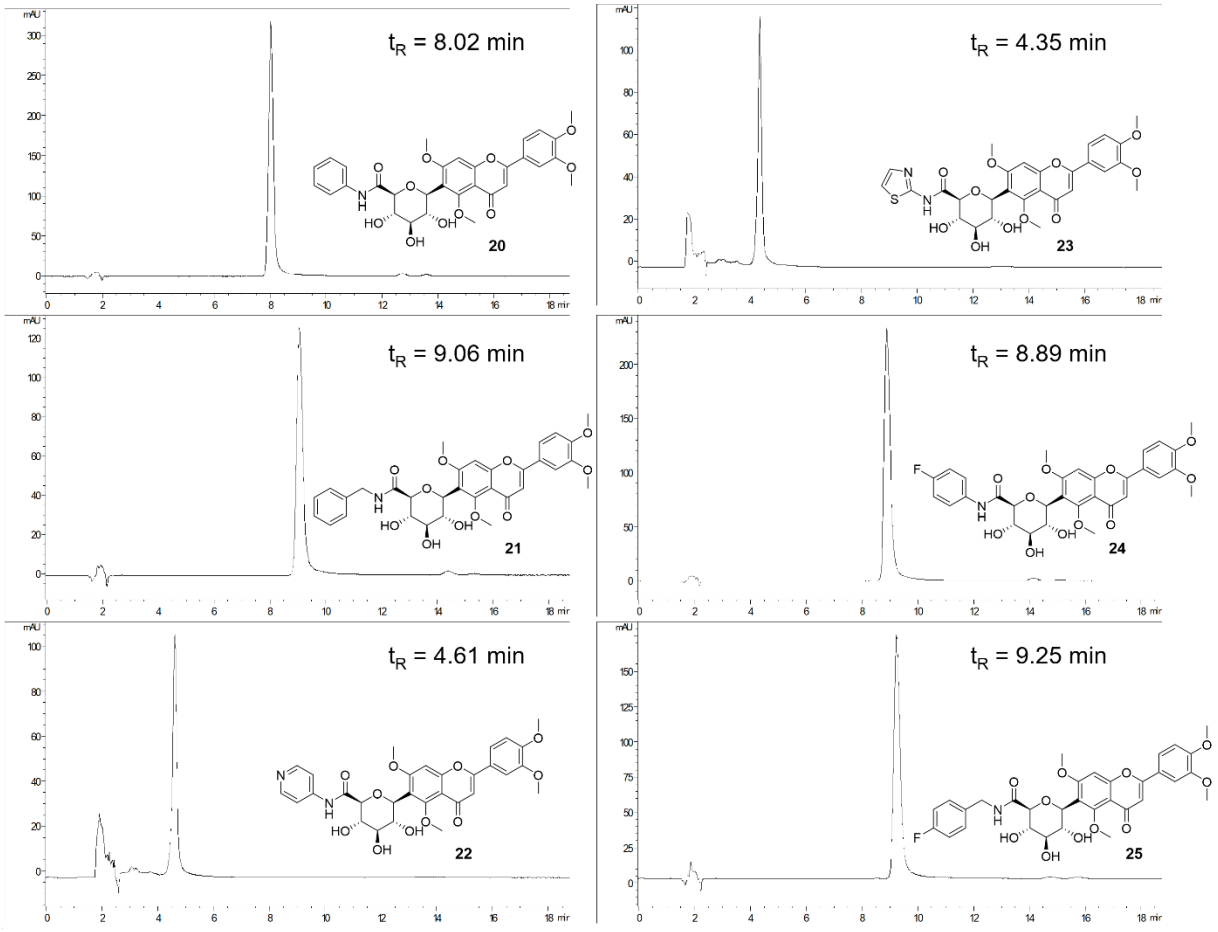
t_R = 8.02 min
20
t_R = 4.35 min
23
t_R = 9.06 min
21
t_R = 8.89 min
24
t_R = 4.61 min
22
t_R = 9.25 min
25

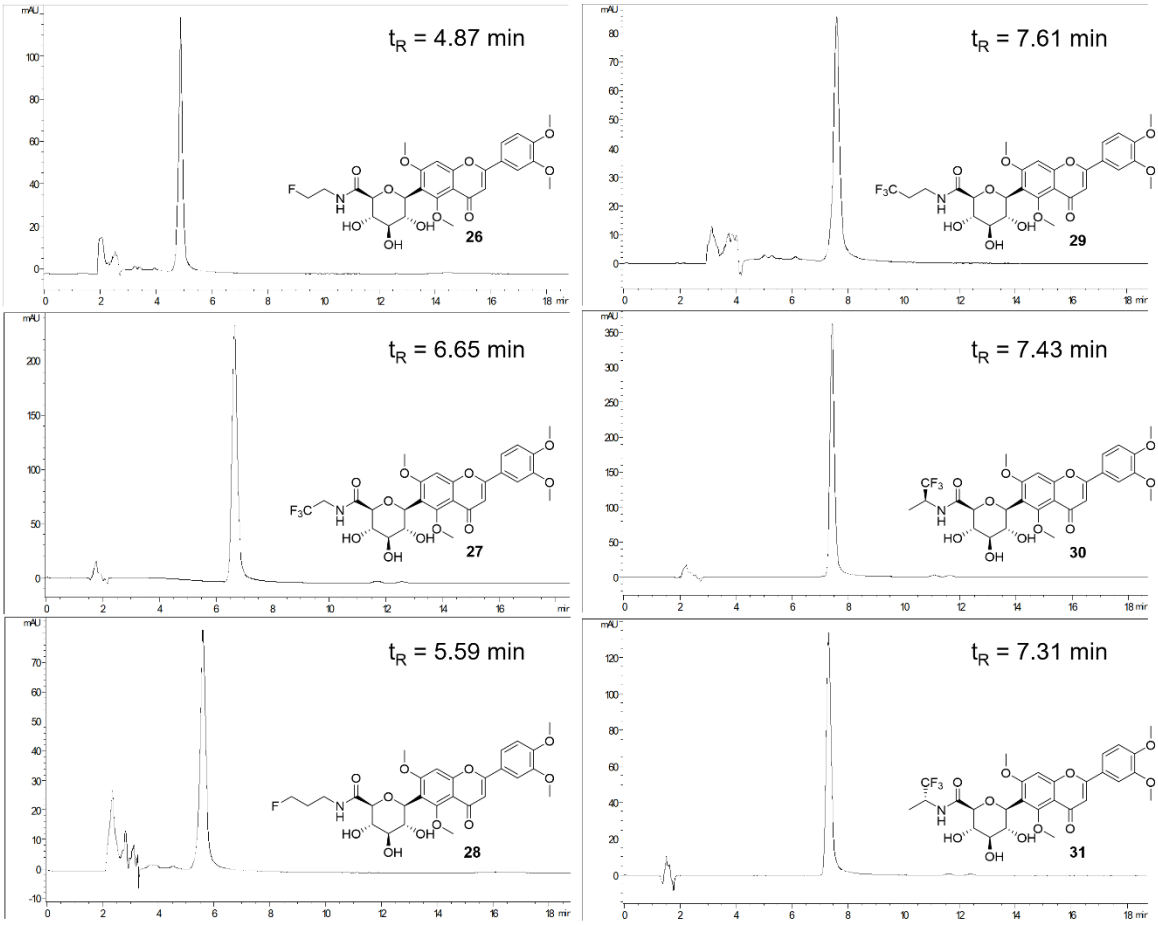
t_R = 4.87 min
26
t_R = 7.61 min
29
t_R = 6.65 min
27
t_R = 7.43 min
30
t_R = 5.59 min
28
t_R = 7.31 min
31

Appendix 17. In Vitro Kinase Selectivity Screening for Compound 30

The Kinase Selectivity Profiling System includes kinase and substrate pairs. Percentage kinase activities upon treatment of compound **30** at 5 μM in a panel of human protein kinases were measured by the ADP-Glo Kinase Assay Kit according to the manufacturer's protocol. The kinase inhibitor staurosporine was used at 1 μM as a reference control. Each data point was collected in quadruplicate of two independent experiments.

Assay Kinase	Substrate/Co-Factor	Kinase Activity (%)
ERK2	MBP	101.3
GSK3α	GSK3 Substrate	92.5
GSK3β	GSK3 Substrate	7.7
JNK1	p38 Substrate	101.4
JNK3	p38 Substrate	74.5
p38α	p38 Substrate	71.1
p38β	p38 Substrate	75.2
p38δ	p38 Substrate	71.2
p38γ	p38 Substrate	77.5
CDK1/CyclinA2	Histone H1 Protein	55.1
CDK2/CyclinE1	Histone H1 Protein	77.5
CDK3/CyclinE1	Histone H1 Protein	70.4
CDK5/p25	Histone H1 Protein	101.3
CDK5/p35	Histone H1 Protein	95.5
CDK6/CyclinD3	Histone H1 Protein	70.1
CDK9/CyclinK	PDKtide	98.7
CLK3	MBP	88.5
AKT1	AKT (PKB) Substrate	85.5
p70S6Kβ	RSK Substrate	74.3
PDK1	PDKtide	62.3
PKA	Kemptide	94.5
PKC	Neurogranin Peptide Substrate	91.8
PRKG1	RSK Substrate	71.5
ROCK1	S6K Substrate	90.8
RSK2	RSK Substrate	91.3

AMPK A1/B1/G1	SAMStide	97.6
AMPK A1/B1/G2	SAMStide	108.1
AMPK A2/B1/G1	SAMStide	84.7
CAMK2α	Autocamtide-2	75.9
CAMK2γ	Autocamtide-2	94.9
CAMK4	Autocamtide-2	92.8
DAPK1	MBP	77.2
STK33	MBP	72.0
Aurora A	MBP	89.2
Aurora B	MBP	65.4
CK2α1	Casein	105.0
DNA-PK	DNA-PK Peptide Substrate	103.4
CK1α1	De-Phospho Casein	82.3
CK1ε	De-Phospho Casein	77.7
CK1γ1	Casein	70.1
VRK2	Casein	92.5

Appendix 18. LC-MS Method for Determination of the PAMPA Permeability

At the end of the incubation period, 10 μL sample from each donor and acceptor well was quantified by LC-ESI-QTOF-MS analysis under a positive mode and used a 7-point calibration with appropriate dilution of the samples. A sum of pseudo-molecular ions $[M+H]^+$, $[M+Na]^+$ and $[M+K]^+$ for each target analyte was extracted from total ion chromatogram (TOC) for quantification. Samples were run in quadruplicate.

Permeability of the compounds (P_e) were calculated using the following formula:

Permeability (cm/s): $P_e = \{-\ln[1-C_A(t)/C_{eq}]\}/[A*(1/V_D+1/V_A)*t]$

where A = filter area (0.3 cm^2), V_D = donor well volume (0.3 mL), V_A = acceptor well volume (0.2 mL), t = incubation time (5 hours = 18000 seconds), $C_A(t)$ = compound concentration in acceptor well at time t, $C_D(t)$ = compound concentration in donor well at time t,

$C_{eq} = [C_D(t)*V_D+C_A(t)*V_A]/(V_D+V_A)$.

Mass retention (*R*%) is calculated using the following formula:

$R\% = \{1-[C_D(t)*V_D+C_A(t)*V_A]/(C0*V_D)\}*100$

where C0 is the initial compound concentration in donor well.

Appendix 19. Structures of the Reference Compounds

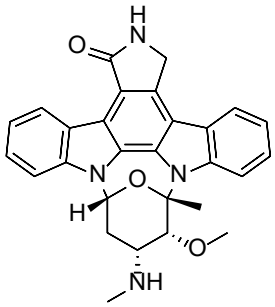

Staurosporine

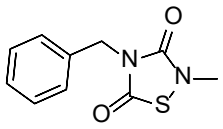

TDZD-8

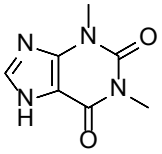

Theophylline

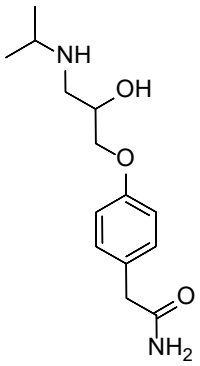

Atenolol

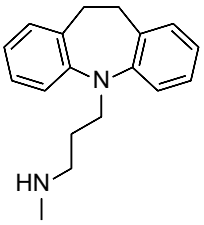

Desipramine

REFERENCES

1. Querfurth, H. W.; LaFerla, F. M., Alzheimer's disease. *N. Engl. J. Med.* **2010**, *362*, 329-344.
2. National Institutes of Health. https://www.nia.nih.gov/.
3. Mangialasche, F.; Solomon, A.; Winblad, B.; Mecocci, P.; Kivipelto, M., Alzheimer's disease: Clinical trials and drug development. *Lancet Neurol.* **2010**, *9*, 702-716.
4. Scheuner, D.; Eckman, C.; Jensen, M.; Song, X.; Citron, M.; Suzuki, N.; Bird, T. D.; Hardy, J.; Hutton, M.; Kukull, W.; Larson, E.; Levy-Lahad, L.; Viitanen, M.; Peskind, E.; Poorkaj, P.; Schellenberg, G.; Tanzi, R.; Wasco, W.; Lannfelt, L.; Selkoe, D.; Younkin, S., Secreted amyloid beta-protein similar to that in the senile plaques of Alzheimer's disease is increased in vivo by the presenilin 1 and 2 and APP mutations linked to familial Alzheimer's disease. *Nat. Med.* **1996**, *2*, 864-870.
5. Selkoe, D. J.; Hardy, J., The amyloid hypothesis of Alzheimer's disease at 25 years. *EMBO Mol. Med.* **2016**, *8*, 595-608.
6. Hong, M.; Zhukareva, V.; Vogelsberg-Ragaglia, V.; Wszolek, Z.; Reed, L.; Miller, B. I.; Geschwind, D. H.; Bird, T. D.; McKeel, D.; Goate, A.; Morris, J. C.; Wilhelmsen, K. C.; Schellenberg, G. D.; Trojanowski, J. Q.; Lee, V. M.-Y., Mutation-specific functional impairments in distinct tau isoforms of hereditary FTDP-17. *Science* **1998**, *282*, 1914-1917.
7. Ballatore, C.; Lee, V. M. Y.; Trojanowski, J. Q., Tau-mediated neurodegeneration in Alzheimer's disease and related disorders. *Nat. Rev. Neurosci.* **2007**, *8*, 663-672.
8. Corder, E. H.; Saunders, A. M.; Strittmatter, W. J.; Schmechel, D. E.; Gaskell, P. C.; Small, G. W.; Roses, A. D.; Haines, J. L.; Pericak-Vance, M. A., Gene dose of apolipoprotein E type 4 allele and the risk of Alzheimer's disease in late onset families. *Science* **1993**, *261*, 921-923.
9. Kim, J.; Basak, J. M.; Holtzman, D. M., The role of apolipoprotein E in Alzheimer's disease. *Neuron* **2009**, *63*, 287-303.
10. Citron, M., Alzheimer's disease: Strategies for disease modification. *Nat. Rev. Drug Discov.* **2010**, *9*, 387-398.
11. Huang, Y.; Mucke, L., Alzheimer mechanisms and therapeutic strategies. *Cell* **2012**, *148*, 1204-1222.

12. Conde, C.; Caceres, A., Microtubule assembly, organization and dynamics in axons and dendrites. *Nat. Rev. Neurosci.* **2009**, *10*, 319-332.
13. Goedert, M.; Spillantini, M. G.; Jakes, R.; Rutherford, D.; Crowther, R. A., Multiple isoforms of human microtubule-associated protein tau: Sequences and localization in neurofibrillary tangles of Alzheimer's disease. *Neuron* **1989**, *3*, 519-526.
14. Himmler, A.; Drechsel, D.; Kirschner, M. W.; Martin, D. W., Tau consists of a set of proteins with repeated C-terminal microtubule-binding domains and variable N-terminal domains. *Mol. Cell. Biol.* **1989**, *9*, 1381-1388.
15. Lee, V. M.-Y.; Goedert, M.; Trojanowski, J. Q., Neurodegenerative tauopathies. *Annu. Rev. Neurosci.* **2001**, *24*, 1121-1159.
16. Brunden, K. R.; Trojanowski, J. Q.; Lee, V. M. Y., Advances in tau-focused drug discovery for Alzheimer's disease and related tauopathies. *Nat. Rev. Drug Discov.* **2009**, *8*, 783-793.
17. Fitzpatrick, A. W. P.; Falcon, B.; He, S.; Murzin, A. G.; Murshudov, G.; Garringer, H. J.; Crowther, R. A.; Ghetti, B.; Goedert, M.; Scheres, S. H. W., Cryo-EM structures of tau filaments from Alzheimer's disease. *Nature* **2017**, *547*, 185-190.
18. Hoover, B. R.; Reed, M. N.; Su, J.; Penrod, R. D.; Kotilinek, L. A.; Grant, M. K.; Pitstick, R.; Carlson, G. A.; Lanier, L. M.; Yuan, L.-L.; Ashe, K. H.; Liao, D., Tau mislocalization to dendritic spines mediates synaptic dysfunction independently of neurodegeneration. *Neuron* **2010**, *68*, 1067-1081.
19. Morris, M.; Maeda, S.; Vossel, K.; Mucke, L., The many faces of tau. *Neuron* **2011**, *70*, 410-426.
20. Ittner, L. M.; Götz, J., Amyloid-β and tau - a toxic pas de deux in Alzheimer's disease. *Nat. Rev. Neurosci.* **2011**, *12*, 65-72.
21. Bloom, G. S., Amyloid-β and tau: The trigger and bullet in Alzheimer disease pathogenesis. *JAMA Neurology* **2014**, *71*, 505-508.
22. Holtzman, D. M.; Morris, J. C.; Goate, A. M., Alzheimer's disease: The challenge of the second century. *Sci. Transl. Med.* **2011**, *3*, 77sr71.
23. McDade, E.; Bateman, R. J., Stop Alzheimer's before it starts. *Nature* **2017**, *547*, 153-155.
24. Schneider, L. S.; Mangialasche, F.; Andreasen, N.; Feldman, H.; Giacobini, E.; Jones, R.; Mantua, V.; Mecocci, P.; Pani, L.; Winblad, B.; Kivipelto, M., Clinical trials and late-stage

drug development for Alzheimer's disease: An appraisal from 1984 to 2014. *J. Intern. Med.* **2014**, *275*, 251-283.

25. Khanna, M. R.; Kovalevich, J.; Lee, V. M. Y.; Trojanowski, J. Q.; Brunden, K. R., Therapeutic strategies for the treatment of tauopathies: Hopes and challenges. *Alzheimers Dement.* **2016**, *12*, 1051-1065.
26. Iqbal, K.; Liu, F.; Gong, C.-X., Tau and neurodegenerative disease: The story so far. *Nat. Rev. Neurol.* **2016**, *12*, 15-27.
27. Reardon, S., Alzheimer antibody drugs show questionable potential. *Nat. Rev. Drug Discov.* **2015**, *14*, 591-592.
28. Honig, L. S.; Vellas, B.; Woodward, M.; Boada, M.; Bullock, R.; Borrie, M.; Hager, K.; Andreasen, N.; Scarpini, E.; Liu-Seifert, H.; Case, M.; Dean, R. A.; Hake, A.; Sundell, K.; Hoffmann, V. P.; Carlson, C.; Khanna, R.; Mintun, M.; DeMattos, R.; Selzler, K. J.; Siemers, E., Trial of solanezumab for mild dementia due to Alzheimer's disease. *N. Engl. J. Med.* **2018**, *378*, 321-330.
29. Verma, A. K.; Pratap, R., The biological potential of flavones. *Nat. Prod. Rep.* **2010**, *27*, 1571-1593.
30. Singh, M.; Arseneault, M.; Sanderson, T.; Murthy, V.; Ramassamy, C., Challenges for research on polyphenols from foods in Alzheimer's disease: Bioavailability, metabolism, and cellular and molecular mechanisms. *J. Agric. Food Chem.* **2008**, *56*, 4855-4873.
31. Vauzour, D.; Vafeiadou, K.; Rodriguez-Mateos, A.; Rendeiro, C.; Spencer, J. E., The neuroprotective potential of flavonoids: A multiplicity of effects. *Genes Nutr* **2008**, *3*, 115-126.
32. Solanki, I.; Parihar, P.; Mansuri, M. L.; Parihar, M. S., Flavonoid-based therapies in the early management of neurodegenerative diseases. *Adv. Nutr.* **2015**, *6*, 64-72.
33. Hwang, S.-L.; Shih, P.-H.; Yen, G.-C., Neuroprotective effects of citrus flavonoids. *J. Agric. Food Chem.* **2012**, *60*, 877-885.
34. Anand, P.; Singh, B., Flavonoids as lead compounds modulating the enzyme targets in Alzheimer's disease. *Med. Chem. Res.* **2013**, *22*, 3061-3075.
35. Baptista, F. I.; Henriques, A. G.; Silva, A. M. S.; Wiltfang, J.; da Cruz e Silva, O. A. B., Flavonoids as therapeutic compounds targeting key proteins involved in Alzheimer's disease. *ACS Chem. Neurosci.* **2014**, *5*, 83-92.

36. Pietta, P.-G., Flavonoids as antioxidants. *J. Nat. Prod.* **2000**, *63*, 1035-1042.

37. Heim, K. E.; Tagliaferro, A. R.; Bobilya, D. J., Flavonoid antioxidants: Chemistry, metabolism and structure-activity relationships. *J. Nutr. Biochem.* **2002**, *13*, 572-584.

38. Xiao, J.; Capanoglu, E.; Jassbi, A. R.; Miron, A., Advance on the flavonoid C-glycosides and health benefits. *Crit. Rev. Food Sci. Nutr.* **2016**, *56*, S29-S45.

39. Shapiro, G. I., Cyclin-dependent kinase pathways as targets for cancer treatment. *J. Clin. Oncol.* **2006**, *24*, 1770-1783.

40. Nguyen, T. B.; Lozach, O.; Surpateanu, G.; Wang, Q.; Retailleau, P.; Iorga, B. I.; Meijer, L.; Guéritte, F., Synthesis, biological evaluation, and molecular modeling of natural and unnatural flavonoidal alkaloids, inhibitors of kinases. *J. Med. Chem.* **2012**, *55*, 2811-2819.

41. Lies, B.; Martens, S.; Schmidt, S.; Boll, M.; Wenzel, U., Flavone potently stimulates an apical transporter for flavonoids in human intestinal Caco-2 cells. *Mol. Nutr. Food Res.* **2012**, *56*, 1627-1635.

42. Jesus, A. R.; Vila-Viçosa, D.; Machuqueiro, M.; Marques, A. P.; Dore, T. M.; Rauter, A. P., Targeting type 2 diabetes with C-glucosyl dihydrochalcones as selective sodium glucose co-transporter 2 (SGLT2) inhibitors: Synthesis and biological evaluation. *J. Med. Chem.* **2017**, *60*, 568-579.

43. Li, Y.; Shi, Z.; Chen, L.; Zheng, S.; Li, S.; Xu, B.; Liu, Z.; Liu, J.; Deng, C.; Ye, F., Discovery of a potent, selective renal sodium-dependent glucose cotransporter 2 (SGLT2) inhibitor (HSK0935) for the treatment of type 2 diabetes. *J. Med. Chem.* **2017**, *60*, 4173-4184.

44. Clemons, P. A., Complex phenotypic assays in high-throughput screening. *Curr. Opin. Chem. Biol.* **2004**, *8*, 334-338.

45. Prior, M.; Chiruta, C.; Currais, A.; Goldberg, J.; Ramsey, J.; Dargusch, R.; Maher, P. A.; Schubert, D., Back to the future with phenotypic screening. *ACS Chem. Neurosci.* **2014**, *5*, 503-513.

46. Mayr, L. M.; Bojanic, D., Novel trends in high-throughput screening. *Curr. Opin. Pharmacol.* **2009**, *9*, 580-588.

47. Macarron, R.; Banks, M. N.; Bojanic, D.; Burns, D. J.; Cirovic, D. A.; Garyantes, T.; Green, D. V. S.; Hertzberg, R. P.; Janzen, W. P.; Paslay, J. W.; Schopfer, U.; Sittampalam, G. S., Impact of high-throughput screening in biomedical research. *Nat. Rev. Drug Discov.* **2011**, *10*, 188-195.

48. Williams, P.; Sorribas, A.; Liang, Z., New methods to explore marine resources for Alzheimer's therapeutics. *Curr. Alzheimer Res.* **2010**, *7*, 210-213.

49. Rix, U.; Superti-Furga, G., Target profiling of small molecules by chemical proteomics. *Nat. Chem. Biol.* **2009**, *5*, 616-624.

50. Schirle, M.; Bantscheff, M.; Kuster, B., Mass spectrometry-based proteomics in preclinical drug discovery. *Chem. Biol.* **2012**, *19*, 72-84.

51. Sutton, C. W., The role of targeted chemical proteomics in pharmacology. *Br. J. Pharmacol.* **2012**, *166*, 457-475.

52. Yao, Z.; Petschnigg, J.; Ketteler, R.; Stagljar, I., Application guide for omics approaches to cell signaling. *Nat. Chem. Biol.* **2015**, *11*, 387-397.

53. Wang, J.; Gao, L.; Lee, Y. M.; Kalesh, K. A.; Ong, Y. S.; Lim, J.; Jee, J.-E.; Sun, H.; Lee, S. S.; Hua, Z.-C.; Lin, Q., Target identification of natural and traditional medicines with quantitative chemical proteomics approaches. *Pharmacol. Ther.* **2016**, *162*, 10-22.

54. Zhao, S.; Iyengar, R., Systems pharmacology: Network analysis to identify multiscale mechanisms of drug action. *Annu. Rev. Pharmacol. Toxicol.* **2012**, *52*, 505-521.

55. Moulick, K.; Ahn, J. H.; Zong, H.; Rodina, A.; Cerchietti, L.; Gomes DaGama, E. M.; Caldas-Lopes, E.; Beebe, K.; Perna, F.; Hatzi, K.; Vu, L. P.; Zhao, X.; Zatorska, D.; Taldone, T.; Smith-Jones, P.; Alpaugh, M.; Gross, S. S.; Pillarsetty, N.; Ku, T.; Lewis, J. S.; Larson, S. M.; Levine, R.; Erdjument-Bromage, H.; Guzman, M. L.; Nimer, S. D.; Melnick, A.; Neckers, L.; Chiosis, G., Affinity-based proteomics reveal cancer-specific networks coordinated by Hsp90. *Nat. Chem. Biol.* **2011**, *7*, 818-826.

56. Wright, M. H.; Sieber, S. A., Chemical proteomics approaches for identifying the cellular targets of natural products. *Nat. Prod. Rep.* **2016**, *33*, 681-708.

57. Li, Q. X.; Casida, J. E., 1,3-Dithianes with acid functionalities: Potent inhibitors and candidate affinity probes for the GABA-gated chloride channel. *Bioorg. Med. Chem. Lett.* **1993**, *3*, 2671-2674.

58. Li, Q. X.; Casida, J. E., Structure-activity studies leading to potent chloride channel blockers: 5e-tert-Butyl-2-[4-(substituted-ethynyl)phenyl]-1,3-dithianes. *Bioorg. Med. Chem.* **1994**, *2*, 1423-1434.

59. Li, Q. X.; Casida, J. E., Affinity probes for the GABA-gated chloride channel: Selection of 5e-tert-butyl-2e-[4-(substituted-ethynyl)phenyl]-1,3-dithianes and optimization of linker moiety. *Bioorg. Med. Chem.* **1995**, *3*, 1667-1674.

60. Li, Q. X.; Casida, J. E., Affinity probes for the GABA-gated chloride channel: 5e-tert-Butyl-2e-[4-(substituted-ethynyl)phenyl]-1,3-dithianes with photoactivatable, fluorescent, biotin, agarose and protein substituents. *Bioorg. Med. Chem.* **1995**, *3*, 1675-1684.

61. Ong, S.-E.; Blagoev, B.; Kratchmarova, I.; Kristensen, D. B.; Steen, H.; Pandey, A.; Mann, M., Stable isotope labeling by amino acids in cell culture, SILAC, as a simple and accurate approach to expression proteomics. *Mol. Cell. Proteomics* **2002**, *1*, 376-386.

62. Unwin, R. D.; Griffiths, J. R.; Whetton, A. D., Simultaneous analysis of relative protein expression levels across multiple samples using iTRAQ isobaric tags with 2D nano LC-MS/MS. *Nat. Protoc.* **2010**, *5*, 1574-1582.

63. Hasanudin, K.; Hashim, P.; Mustafa, S., Corn silk (Stigma maydis) in healthcare: A phytochemical and pharmacological review. *Molecules* **2012**, *17*, 9697-9715.

64. Casas, M. I.; Duarte, S. M.; Doseff, A. I.; Grotewold, E., Flavone-rich maize: An opportunity to improve the nutritional value of an important commodity crop. *Front. Plant Sci.* **2014**, *5*, 440.

65. Liang, Z.; Zhang, B.; Su, W. W.; Williams, P. G.; Li, Q. X., *C*-Glycosylflavones alleviate tau phosphorylation and amyloid neurotoxicity through GSK3β inhibition. *ACS Chem. Neurosci.* **2016**, *7*, 912-923.

66. Yuan, L.; Wang, J.; Xiao, H.; Xiao, C.; Wang, Y.; Liu, X., Isoorientin induces apoptosis through mitochondrial dysfunction and inhibition of PI3K/Akt signaling pathway in HepG2 cancer cells. *Toxicol. Appl. Pharmacol.* **2012**, *265*, 83-92.

67. Yuan, L.; Wu, Y.; Ren, X.; Liu, Q.; Wang, J.; Liu, X., Isoorientin attenuates lipopolysaccharide-induced pro-inflammatory responses through down-regulation of ROS-related MAPK/NF-κB signaling pathway in BV-2 microglia. *Mol. Cell. Biochem.* **2014**, *386*, 153-165.

68. Yuan, L.; Han, X.; Li, W.; Ren, D.; Yang, X., Isoorientin prevents hyperlipidemia and liver injury by regulating lipid metabolism, antioxidant capability, and inflammatory cytokine release in high-fructose-fed mice. *J. Agric. Food Chem.* **2016**, *64*, 2682-2689.

69. Song, Y.; Kim, H.-D.; Lee, M.-K.; Hong, I.-H.; Won, C.-K.; Bai, H.-W.; Lee, S. S.; Lee, S.; Chung, B. Y.; Cho, J.-H., Maysin and its flavonoid derivative from centipedegrass attenuates amyloid plaques by inducting humoral immune response with Th2 skewed cytokine response in the Tg (APPswe, PS1dE9) Alzheimer's mouse model. *PLoS ONE* **2017**, *12*, e0169509.

70. Wang, C.; Zhang, T.; Liu, J.; Lu, S.; Zhang, C.; Wang, E.; Wang, Z.; Zhang, Y.; Liu, J., Subchronic toxicity study of corn silk with rats. *J. Ethnopharmacol.* **2011**, *137*, 36-43.

71. Peng, K.-Z.; Zhang, S.-Y.; Zhou, H.-L., Toxicological evaluation of the flavonoid-rich extract from Maydis stigma: Subchronic toxicity and genotoxicity studies in mice. *J. Ethnopharmacol.* **2016**, *192*, 161-169.

72. Anighoro, A.; Bajorath, J.; Rastelli, G., Polypharmacology: Challenges and opportunities in drug discovery. *J. Med. Chem.* **2014**, *57*, 7874-7887.

73. Liang, Z.; Li, Q. X., Discovery of selective, substrate-competitive, and passive membrane permeable glycogen synthase kinase-3β inhibitors: Synthesis, biological evaluation, and molecular modeling of new *C*-glycosylflavones. *ACS Chem. Neurosci.* **2018**, DOI: 10.1021/acschemneuro.1028b00010.

74. Hanger, D. P.; Anderton, B. H.; Noble, W., Tau phosphorylation: The therapeutic challenge for neurodegenerative disease. *Trends Mol. Med.* **2009**, *15*, 112-119.

75. Mazanetz, M. P.; Fischer, P. M., Untangling tau hyperphosphorylation in drug design for neurodegenerative diseases. *Nat. Rev. Drug Discov.* **2007**, *6*, 464-479.

76. Hooper, C.; Killick, R.; Lovestone, S., The GSK3 hypothesis of Alzheimer's disease. *J. Neurochem.* **2008**, *104*, 1433-1439.

77. Martin, L.; Latypova, X.; Wilson, C. M.; Magnaudeix, A.; Perrin, M.-L.; Yardin, C.; Terro, F., Tau protein kinases: Involvement in Alzheimer's disease. *Ageing Res. Rev.* **2013**, *12*, 289-309.

78. Pandey, M. K.; DeGrado, T. R., Glycogen synthase kinase-3 (GSK-3) – targeted therapy and imaging. *Theranostics* **2016**, *6*, 571-593.

79. Elliger, C. A.; Chan, B. G.; Waiss Jr, A. C.; Lundin, R. E.; Haddon, W. F., C-Glycosylflavones from Zea mays that inhibit insect development. *Phytochemistry* **1980**, *19*, 293-297.

80. Wang, G.-Q.; Xu, T.; Bu, X.-M.; Liu, B.-Y., Anti-inflammation effects of corn silk in a rat model of carrageenin-induced pleurisy. *Inflammation* **2012**, *35*, 822-827.

81. Liu, J.; Wang, C.; Wang, Z.; Zhang, C.; Lu, S.; Liu, J., The antioxidant and free-radical scavenging activities of extract and fractions from corn silk (Zea mays L.) and related flavone glycosides. *Food Chem.* **2011**, *126*, 261-269.

82. Tian, J.; Chen, H.; Chen, S.; Xing, L.; Wang, Y.; Wang, J., Comparative studies on the constituents, antioxidant and anticancer activities of extracts from different varieties of corn silk. *Food Funct.* **2013**, *4*, 1526-1534.

83. Ferrari, A.; Hoerndli, F.; Baechi, T.; Nitsch, R. M.; Götz, J., β-Amyloid induces paired helical filament-like tau filaments in tissue culture. *J. Biol. Chem.* **2003**, *278*, 40162-40168.

84. Datki, Z.; Papp, R.; Zádori, D.; Soós, K.; Fülöp, L.; Juhász, A.; Laskay, G.; Hetényi, C.; Mihalik, E.; Zarándi, M.; Penke, B., In vitro model of neurotoxicity of Aβ 1–42 and neuroprotection by a pentapeptide: Irreversible events during the first hour. *Neurobiol. Dis.* **2004**, *17*, 507-515.

85. Agholme, L.; Lindström, T.; Kågedal, K.; Marcusson, J.; Hallbeck, M., An in vitro model for neuroscience: Differentiation of SH-SY5Y cells into cells with morphological and biochemical characteristics of mature neurons. *J. Alzheimer's Dis.* **2010**, *20*, 1069-1082.

86. Zheng, X.; Xie, Z.; Zhu, Z.; Liu, Z.; Wang, Y.; Wei, L.; Yang, H.; Yang, H.; Liu, Y.; Bi, J., Methyllycaconitine alleviates amyloid-β peptides-induced cytotoxicity in SH-SY5Y cells. *PLoS ONE* **2014**, *9*, e111536.

87. Gray, N. E.; Morré, J.; Kelley, J.; Maier, C. S.; Stevens, J. F.; Quinn, J. F.; Soumyanath, A., Caffeoylquinic acids in Centella asiatica protect against amyloid-β toxicity. *J. Alzheimer's Dis.* **2014**, *40*, 359-373.

88. Kato, T.; Morita, Y., C-Glycosylflavones with acetyl substitution from Rumex acetosa L. *Chem. Pharm. Bull.* **1990**, *38*, 2277-2280.

89. Snook, M. E.; Gueldner, R. C.; Widstrom, N. W.; Wiseman, B. R.; Himmelsbach, D. S.; Harwood, J. S.; Costello, C. E., Levels of maysin and maysin analogs in silks of maize germplasm. *J. Agric. Food Chem.* **1993**, *41*, 1481-1485.

90. Abad-García, B.; Garmón-Lobato, S.; Berrueta, L. A.; Gallo, B.; Vicente, F., New features on the fragmentation and differentiation of C-glycosidic flavone isomers by positive

electrospray ionization and triple quadrupole mass spectrometry. *Rapid Commun. Mass Spectrom.* **2008**, *22*, 1834-1842.

91. Sassano, M. F.; Doak, A. K.; Roth, B. L.; Shoichet, B. K., Colloidal aggregation causes inhibition of G protein-coupled receptors. *J. Med. Chem.* **2013**, *56*, 2406-2414.
92. Feng, B. Y.; Shoichet, B. K., A detergent-based assay for the detection of promiscuous inhibitors. *Nat. Protoc.* **2006**, *1*, 550-553.
93. Hur, E.-M.; Zhou, F.-Q., GSK3 signalling in neural development. *Nat. Rev. Neurosci.* **2010**, *11*, 539-551.
94. Palomo, V.; Soteras, I.; Perez, D. I.; Perez, C.; Gil, C.; Campillo, N. E.; Martinez, A., Exploring the binding sites of glycogen synthase kinase 3. Identification and characterization of allosteric modulation cavities. *J. Med. Chem.* **2011**, *54*, 8461-8470.
95. Eldar-Finkelman, H.; Martinez, A., GSK-3 inhibitors: Preclinical and clinical focus on CNS. *Front. Mol. Neurosci.* **2011**, *4*, 32.
96. Peng, J.; Kudrimoti, S.; Prasanna, S.; Odde, S.; Doerksen, R. J.; Pennaka, H. K.; Choo, Y.-M.; Rao, K. V.; Tekwani, B. L.; Madgula, V.; Khan, S. I.; Wang, B.; Mayer, A. M. S.; Jacob, M. R.; Tu, L. C.; Gertsch, J.; Hamann, M. T., Structure-activity relationship and mechanism of action studies of manzamine analogues for the control of neuroinflammation and cerebral infections. *J. Med. Chem.* **2010**, *53*, 61-76.
97. Bertrand, J. A.; Thieffine, S.; Vulpetti, A.; Cristiani, C.; Valsasina, B.; Knapp, S.; Kalisz, H. M.; Flocco, M., Structural characterization of the GSK-3β active site using selective and non-selective ATP-mimetic inhibitors. *J. Mol. Biol.* **2003**, *333*, 393-407.
98. Forlenza, O. V.; De-Paula, V. J. R.; Diniz, B. S. O., Neuroprotective effects of lithium: Implications for the treatment of Alzheimer's disease and related neurodegenerative disorders. *ACS Chem. Neurosci.* **2014**, *5*, 443-450.
99. Ilouz, R.; Kowalsman, N.; Eisenstein, M.; Eldar-Finkelman, H., Identification of novel glycogen synthase kinase-3β substrate-interacting residues suggests a common mechanism for substrate recognition. *J. Biol. Chem.* **2006**, *281*, 30621-30630.
100. Busciglio, J.; Lorenzo, A.; Yeh, J.; Yankner, B. A., β-Amyloid fibrils induce tau phosphorylation and loss of microtubule binding. *Neuron* **1995**, *14*, 879-888.
101. Takashima, A., GSK-3 is essential in the pathogenesis of Alzheimer's disease. *J. Alzheimer's Dis.* **2006**, *9*, 309-317.

102. Ma, R.; Xiong, N.; Huang, C.; Tang, Q.; Hu, B.; Xiang, J.; Li, G., Erythropoietin protects PC12 cells from β-amyloid25–35-induced apoptosis via PI3K/Akt signaling pathway. *Neuropharmacology* **2009**, *56*, 1027-1034.

103. Li, L.; Liu, Z.; Liu, J.; Tai, X.; Hu, X.; Liu, X.; Wu, Z.; Zhang, G.; Shi, M.; Zhao, G., Ginsenoside Rd attenuates beta-amyloid-induced tau phosphorylation by altering the functional balance of glycogen synthase kinase 3beta and protein phosphatase 2A. *Neurobiol. Dis.* **2013**, *54*, 320-328.

104. Domínguez, J. M.; Fuertes, A.; Orozco, L.; del Monte-Millán, M.; Delgado, E.; Medina, M., Evidence for irreversible inhibition of glycogen synthase kinase-3β by tideglusib. *J. Biol. Chem.* **2012**, *287*, 893-904.

105. Martinez, A.; Alonso, M.; Castro, A.; Dorronsoro, I.; Gelpí, J. L.; Luque, F. J.; Pérez, C.; Moreno, F. J., SAR and 3D-QSAR studies on thiadiazolidinone derivatives: Exploration of structural requirements for glycogen synthase kinase 3 inhibitors. *J. Med. Chem.* **2005**, *48*, 7103-7112.

106. Yankner, B. A.; Duffy, L. K.; Kirschner, D. A., Neurotrophic and neurotoxic effects of amyloid β protein: Reversal by tachykinin neuropeptides. *Science* **1990**, *250*, 279-282.

107. Arora, K.; Alfulaij, N.; Higa, J. K.; Panee, J.; Nichols, R. A., Impact of sustained exposure to β-amyloid on calcium homeostasis and neuronal integrity in model nerve cell system expressing α4β2 nicotinic acetylcholine receptors. *J. Biol. Chem.* **2013**, *288*, 11175-11190.

108. Arora, K.; Cheng, J.; Nichols, R. A., Nicotinic acetylcholine receptors sensitize a MAPK-linked toxicity pathway on prolonged exposure to β-amyloid. *J. Biol. Chem.* **2015**, *290*, 21409-21420.

109. McMullen, M. D.; Byrne, P. F.; Snook, M. E.; Wiseman, B. R.; Lee, E. A.; Widstrom, N. W.; Coe, E. H., Quantitative trait loci and metabolic pathways. *Proc. Natl. Acad. Sci. U.S.A.* **1998**, *95*, 1996-2000.

110. Williams, P.; Sorribas, A.; Howes, M.-J. R., Natural products as a source of Alzheimer's drug leads. *Nat. Prod. Rep.* **2011**, *28*, 48-77.

111. Kan, A.; Orhan, I.; Coksari, G.; Sener, B., In-vitro neuroprotective properties of the Maydis stigma extracts from four corn varieties. *Int. J. Food Sci. Nutr.* **2012**, *63*, 1-4.

112. Choi, D. J.; Kim, S.-L.; Choi, J. W.; Park, Y. I., Neuroprotective effects of corn silk maysin via inhibition of H2O2-induced apoptotic cell death in SK-N-MC cells. *Life Sci.* **2014**, *109*, 57-64.

113. Pacifico, S.; Scognamiglio, M.; D'Abrosca, B.; Piccolella, S.; Tsafantakis, N.; Gallicchio, M.; Ricci, A.; Fiorentino, A., Spectroscopic characterization and antiproliferative activity on HepG2 human hepatoblastoma cells of flavonoid C-glycosides from Petrorhagia velutina. *J. Nat. Prod.* **2010**, *73*, 1973-1978.

114. Yang, S.; Liu, W.; Lu, S.; Tian, Y.-Z.; Wang, W.-Y.; Ling, T.-J.; Liu, R.-T., A novel multifunctional compound camellikaempferoside B decreases Aβ production, interferes with Aβ aggregation, and prohibits Aβ-mediated neurotoxicity and neuroinflammation. *ACS Chem. Neurosci.* **2016**, *7*, 505-518.

115. Swinney, Z. T.; Haubrich, B. A.; Xia, S.; Ramesha, C.; Gomez, S. R.; Guyett, P.; Mensa-Wilmot, K.; Swinney, D. C., A four-point screening method for assessing molecular mechanism of action (MMOA) identifies tideglusib as a time-dependent inhibitor of Trypanosoma brucei GSK3β. *PLoS Negl. Trop. Dis.* **2016**, *10*, e0004506.

116. Huggins, D. J.; Sherman, W.; Tidor, B., Rational approaches to improving selectivity in drug design. *J. Med. Chem.* **2012**, *55*, 1424-1444.

117. Palomo, V.; Perez, D. I.; Perez, C.; Morales-Garcia, J. A.; Soteras, I.; Alonso-Gil, S.; Encinas, A.; Castro, A.; Campillo, N. E.; Perez-Castillo, A.; Gil, C.; Martinez, A., 5-Imino-1,2,4-thiadiazoles: First small molecules as substrate competitive inhibitors of glycogen synthase kinase 3. *J. Med. Chem.* **2012**, *55*, 1645-1661.

118. Tapia-Rojas, C.; Schüller, A.; Lindsay, C. B.; Ureta, R. C.; Mejías-Reyes, C.; Hancke, J.; Melo, F.; Inestrosa, N. C., Andrographolide activates the canonical Wnt signalling pathway by a mechanism that implicates the non-ATP competitive inhibition of GSK-3β: Autoregulation of GSK-3β in vivo. *Biochem. J.* **2015**, *466*, 415-430.

119. Licht-Murava, A.; Paz, R.; Vaks, L.; Avrahami, L.; Plotkin, B.; Eisenstein, M.; Eldar-Finkelman, H., A unique type of GSK-3 inhibitor brings new opportunities to the clinic. *Sci. Signal.* **2016**, *9*, ra110.

120. Rodrigues, T.; Reker, D.; Schneider, P.; Schneider, G., Counting on natural products for drug design. *Nature Chem.* **2016**, *8*, 531-541.

121. Sciacca, M. F. M.; Romanucci, V.; Zarrelli, A.; Monaco, I.; Lolicato, F.; Spinella, N.; Galati, C.; Grasso, G.; D'Urso, L.; Romeo, M.; Diomede, L.; Salmona, M.; Bongiorno, C.; Di Fabio, G.; La Rosa, C.; Milardi, D., Inhibition of Aβ amyloid growth and toxicity by silybins: The crucial role of stereochemistry. *ACS Chem. Neurosci.* **2017**, *8*, 1767-1778.

122. Walle, T., Methylation of dietary flavones greatly improves their hepatic metabolic stability and intestinal absorption. *Mol. Pharm.* **2007**, *4*, 826-832.

123. Liang, Z.; Sorribas, A.; Sulzmaier, F. J.; Jiménez, J. I.; Wang, X.; Sauvage, T.; Yoshida, W. Y.; Wang, G.; Ramos, J. W.; Williams, P. G., Stictamides A–C, MMP12 inhibitors containing 4-amino-3-hydroxy-5-phenylpentanoic acid subunits. *J. Org. Chem.* **2011**, *76*, 3635-3643.

124. Bobbitt, J. M.; Bartelson, A. L.; Bailey, W. F.; Hamlin, T. A.; Kelly, C. B., Oxoammonium salt oxidations of alcohols in the presence of pyridine bases. *J. Org. Chem.* **2014**, *79*, 1055-1067.

125. Baell, J. B., Feeling nature's PAINS: Natural products, natural product drugs, and pan assay interference compounds (PAINS). *J. Nat. Prod.* **2016**, *79*, 616-628.

126. Leeson, P. D.; Springthorpe, B., The influence of drug-like concepts on decision-making in medicinal chemistry. *Nat. Rev. Drug Discov.* **2007**, *6*, 881-890.

127. Wager, T. T.; Hou, X.; Verhoest, P. R.; Villalobos, A., Central nervous system multiparameter optimization desirability: Application in drug discovery. *ACS Chem. Neurosci.* **2016**, *7*, 767-775.

128. Freeman-Cook, K. D.; Hoffman, R. L.; Johnson, T. W., Lipophilic efficiency: The most important efficiency metric in medicinal chemistry. *Future Med. Chem.* **2013**, *5*, 113-115.

129. Chou, J. T.; Jurs, P. C., Computer-assisted computation of partition coefficients from molecular structures using fragment constants. *J. Chem. Inf. Comput. Sci.* **1979**, *19*, 172-178.

130. Chen, X.; Murawski, A.; Patel, K.; Crespi, C. L.; Balimane, P. V., A novel design of artificial membrane for improving the PAMPA model. *Pharm. Res.* **2008**, *25*, 1511-1520.

131. Courts, F. L.; Williamson, G., The occurrence, fate and biological activities of C-glycosyl flavonoids in the human diet. *Crit. Rev. Food Sci. Nutr.* **2015**, *55*, 1352-1367.

132. Wang, Z.; Sun, H.; Yao, X.; Li, D.; Xu, L.; Li, Y.; Tian, S.; Hou, T., Comprehensive evaluation of ten docking programs on a diverse set of protein-ligand complexes: The

prediction accuracy of sampling power and scoring power. *Phys. Chem. Chem. Phys.* **2016**, *18*, 12964-12975.

133. Trott, O.; Olson, A. J., AutoDock Vina: Improving the speed and accuracy of docking with a new scoring function, efficient optimization, and multithreading. *J. Comput. Chem.* **2010**, *31*, 455-461.
134. Forli, S.; Huey, R.; Pique, M. E.; Sanner, M. F.; Goodsell, D. S.; Olson, A. J., Computational protein-ligand docking and virtual drug screening with the AutoDock suite. *Nat. Protoc.* **2016**, *11*, 905-919.
135. Hassandarvish, P.; Rothan, H. A.; Rezaei, S.; Yusof, R.; Abubakar, S.; Zandi, K., In silico study on baicalein and baicalin as inhibitors of dengue virus replication. *RSC Advances* **2016**, *6*, 31235-31247.
136. Neri-Bazán, R. M.; García-Machorro, J.; Méndez-Luna, D.; Tolentino-López, L. E.; Martínez-Ramos, F.; Padilla-Martínez, I. I.; Aguilar-Faisal, L.; Soriano-Ursúa, M. A.; Trujillo-Ferrara, J. G.; Fragoso-Vázquez, M. J.; Barrón, B. L.; Correa-Basurto, J., Design, in silico studies, synthesis and in vitro evaluation of oseltamivir derivatives as inhibitors of neuraminidase from influenza A virus H1N1. *Eur. J. Med. Chem.* **2017**, *128*, 154-167.
137. Dajani, R.; Fraser, E.; Roe, S. M.; Young, N.; Good, V.; Dale, T. C.; Pearl, L. H., Crystal structure of glycogen synthase kinase 3β: Structural basis for phosphate-primed substrate specificity and autoinhibition. *Cell* **2001**, *105*, 721-732.
138. Gadakar, P. K.; Phukan, S.; Balaji, V. N., Pose prediction accuracy in docking studies and enrichment of actives in the active site of GSK-3β. *J. Chem. Inf. Model.* **2007**, *47*, 1446-1459.
139. Fu, G.; Sivaprakasam, P.; Dale, O. R.; Manly, S. P.; Cutler, S. J.; Doerksen, R. J., Pharmacophore modeling, ensemble docking, virtual screening, and biological evaluation on glycogen synthase kinase-3β. *Mol. Inform.* **2014**, *33*, 610-626.
140. Müller, K.; Faeh, C.; Diederich, F., Fluorine in pharmaceuticals: Looking beyond intuition. *Science* **2007**, *317*, 1881-1886.
141. Bissantz, C.; Kuhn, B.; Stahl, M., A medicinal chemist's guide to molecular interactions. *J. Med. Chem.* **2010**, *53*, 5061-5084.

142. Abreu, R. M. V.; Froufe, H. J. C.; Queiroz, M.-J. R. P.; Ferreira, I. C. F. R., Selective flexibility of side-chain residues improves VEGFR-2 docking score using AutoDock Vina. *Chem. Biol. Drug Des.* **2012**, *79*, 530-534.

143. Gallivan, J. P.; Dougherty, D. A., Cation-π interactions in structural biology. *Proc. Natl. Acad. Sci. U.S.A.* **1999**, *96*, 9459-9464.

144. Pellequer, J.-L.; Zhao, B.; Kao, H.-I.; Bell, C. W.; Li, K.; Li, Q. X.; Karu, A. E.; Roberts, V. A., Stabilization of bound polycyclic aromatic hydrocarbons by a π-cation interaction. *J. Mol. Biol.* **2000**, *302*, 691-699.

145. Liang, Z.; Li, Q. X., π–Cation interactions in molecular recognition: Perspectives on pharmaceuticals and pesticides. *J. Agric. Food Chem.* **2018**, *66*, 3315-3323.

146. Biasini, M.; Bienert, S.; Waterhouse, A.; Arnold, K.; Studer, G.; Schmidt, T.; Kiefer, F.; Cassarino, T. G.; Bertoni, M.; Bordoli, L.; Schwede, T., SWISS-MODEL: Modelling protein tertiary and quaternary structure using evolutionary information. *Nucleic Acids Res.* **2014**, *42*, W252-W258.

147. Beurel, E.; Grieco, S. F.; Jope, R. S., Glycogen synthase kinase-3 (GSK3): Regulation, actions, and diseases. *Pharmacol. Ther.* **2015**, *148*, 114-131.

148. Xiong, L.; Zhu, X.-L.; Shen, Y.-Q.; Kandergama Wasala Mudiyanselage Wishwajith, W.; Li, K.; Yang, G.-F., Discovery of N-benzoxazol-5-yl-pyrazole-4-carboxamides as nanomolar SQR inhibitors. *Eur. J. Med. Chem.* **2015**, *95*, 424-434.

149. Liang, S. H.; Chen, J. M.; Normandin, M. D.; Chang, J. S.; Chang, G. C.; Taylor, C. K.; Trapa, P.; Plummer, M. S.; Para, K. S.; Conn, E. L.; Lopresti-Morrow, L.; Lanyon, L. F.; Cook, J. M.; Richter, K. E. G.; Nolan, C. E.; Schachter, J. B.; Janat, F.; Che, Y.; Shanmugasundaram, V.; Lefker, B. A.; Enerson, B. E.; Livni, E.; Wang, L.; Guehl, N. J.; Patnaik, D.; Wagner, F. F.; Perlis, R.; Holson, E. B.; Haggarty, S. J.; El Fakhri, G.; Kurumbail, R. G.; Vasdev, N., Discovery of a highly selective glycogen synthase kinase-3 inhibitor (PF-04802367) that modulates tau phosphorylation in the brain: Translation for PET neuroimaging. *Angew. Chem., Int. Ed.* **2016**, *55*, 9601-9605.

150. Wei, J.; Jin, F.; Wu, Q.; Jiang, Y.; Gao, D.; Liu, H., Molecular interaction study of flavonoid derivative 3d with human serum albumin using multispectroscopic and molecular modeling approach. *Talanta* **2014**, *126*, 116-121.

151. Wilcken, R.; Zimmermann, M. O.; Lange, A.; Joerger, A. C.; Boeckler, F. M., Principles and applications of halogen bonding in medicinal chemistry and chemical biology. *J. Med. Chem.* **2013**, *56*, 1363-1388.

152. Pollock, J.; Borkin, D.; Lund, G.; Purohit, T.; Dyguda-Kazimierowicz, E.; Grembecka, J.; Cierpicki, T., Rational design of orthogonal multipolar interactions with fluorine in protein–ligand complexes. *J. Med. Chem.* **2015**, *58*, 7465-7474.

153. Ali, A.; Hoeflich, K. P.; Woodgett, J. R., Glycogen synthase kinase-3: Properties, functions, and regulation. *Chem. Rev.* **2001**, *101*, 2527-2540.

154. Wang, Q. M.; Park, I. K.; Fiol, C. J.; Roach, P. J.; DePaoli-Roach, A. A., Isoform differences in substrate recognition by glycogen synthase kinases 3.alpha. and 3.beta. in the phosphorylation of phosphatase inhibitor 2. *Biochemistry* **1994**, *33*, 143-147.

155. Soutar, M. P. M.; Kim, W.-Y.; Williamson, R.; Peggie, M.; Hastie, C. J.; McLauchlan, H.; Snider, W. D.; Gordon-Weeks, P. R.; Sutherland, C., Evidence that glycogen synthase kinase-3 isoforms have distinct substrate preference in the brain. *J. Neurochem.* **2010**, *115*, 974-983.

156. Cavalli, A.; Bolognesi, M. L.; Minarini, A.; Rosini, M.; Tumiatti, V.; Recanatini, M.; Melchiorre, C., Multi-target-directed ligands to combat neurodegenerative diseases. *J. Med. Chem.* **2008**, *51*, 347-372.

157. Chiruta, C.; Schubert, D.; Dargusch, R.; Maher, P., Chemical modification of the multitarget neuroprotective compound fisetin. *J. Med. Chem.* **2012**, *55*, 378-389.

158. León, R.; Garcia, A. G.; Marco-Contelles, J., Recent advances in the multitarget-directed ligands approach for the treatment of Alzheimer's disease. *Med. Res. Rev.* **2013**, *33*, 139-189.

159. Hughes, R. E.; Nikolic, K.; Ramsay, R. R., One for all? Hitting multiple Alzheimer's disease targets with one drug. *Front. Neurosci.* **2016**, *10*, 177.

160. Hopkins, A. L., Network pharmacology: The next paradigm in drug discovery. *Nat. Chem. Biol.* **2008**, *4*, 682-690.

161. Moya-Alvarado, G.; Gershoni-Emek, N.; Perlson, E.; Bronfman, F. C., Neurodegeneration and Alzheimer's disease (AD). What can proteomics tell us about the Alzheimer's brain? *Mol. Cell. Proteomics* **2016**, *15*, 409-425.

162. Pan, S.; Zhang, H.; Wang, C.; Yao, S. C. L.; Yao, S. Q., Target identification of natural products and bioactive compounds using affinity-based probes. *Nat. Prod. Rep.* **2016**, *33*, 612-620.

163. Shamir, D. B.; Rosenqvist, N.; Rasool, S.; Pedersen, J. T.; Sigurdsson, E. M., Internalization of tau antibody and pathological tau protein detected with a flow cytometry multiplexing approach. *Alzheimers Dement.* **2016**, *12*, 1098-1107.

164. Jahn, K.; Wieltsch, C.; Blumer, N.; Mehlich, M.; Pathak, H.; Khan, A. Q.; Hildebrandt, H.; Frieling, H., A cell culture model for investigation of synapse influenceability: epigenetics, expression and function of gene targets important for synapse formation and preservation in SH-SY5Y neuroblastoma cells differentiated by retinoic acid. *J. Neural. Transm.* **2017**, *124*, 1341-1367.

165. Uberti, D.; Rizzini, C.; Spano, P.; Memo, M., Characterization of tau proteins in human neuroblastoma SH-SY5Y cell line. *Neurosci. Lett.* **1997**, *235*, 149-153.

166. Jämsä, A.; Hasslund, K.; Cowburn, R. F.; Bäckström, A.; Vasänge, M., The retinoic acid and brain-derived neurotrophic factor differentiated SH-SY5Y cell line as a model for Alzheimer's disease-like tau phosphorylation. *Biochem. Biophys. Res. Commun.* **2004**, *319*, 993-1000.

167. Zheng, L.; Roberg, K.; Jerhammar, F.; Marcusson, J.; Terman, A., Autophagy of amyloid beta-protein in differentiated neuroblastoma cells exposed to oxidative stress. *Neurosci. Lett.* **2006**, *394*, 184-189.

168. Meng, P.; Yoshida, H.; Tanji, K.; Matsumiya, T.; Xing, F.; Hayakari, R.; Wang, L.; Tsuruga, K.; Tanaka, H.; Mimura, J.; Kosaka, K.; Itoh, K.; Takahashi, I.; Kawaguchi, S.; Imaizumi, T., Carnosic acid attenuates apoptosis induced by amyloid-β 1–42 or 1–43 in SH-SY5Y human neuroblastoma cells. *Neurosci. Res.* **2015**, *94*, 1-9.

169. González-Sarrías, A.; Núñez-Sánchez, M. Á.; Tomás-Barberán, F. A.; Espín, J. C., Neuroprotective effects of bioavailable polyphenol-derived metabolites against oxidative stress-induced cytotoxicity in human neuroblastoma SH-SY5Y cells. *J. Agric. Food Chem.* **2017**, *65*, 752-758.

170. Shannon, P.; Markiel, A.; Ozier, O.; Baliga, N. S.; Wang, J. T.; Ramage, D.; Amin, N.; Schwikowski, B.; Ideker, T., Cytoscape: A software environment for integrated models of biomolecular interaction networks. *Genome Res.* **2003**, *13*, 2498-2504.

171. Szklarczyk, D.; Morris, J. H.; Cook, H.; Kuhn, M.; Wyder, S.; Simonovic, M.; Santos, A.; Doncheva, N. T.; Roth, A.; Bork, P.; Jensen, L. J.; von Mering, C., The STRING database in 2017: Quality-controlled protein–protein association networks, made broadly accessible. *Nucleic Acids Res.* **2017**, *45*, D362-D368.

172. Anderson, K. W.; Turko, I. V., Histone post-translational modifications in frontal cortex from human donors with Alzheimer's disease. *Clin. Proteomics* **2015**, *12*, 26.

173. Sanchez-Mut, J. V.; Gräff, J., Epigenetic alterations in Alzheimer's disease. *Front. Behav. Neurosci.* **2015**, *9*, 347.

174. Cacabelos, R.; Torrellas, C., Epigenetics of aging and Alzheimer's disease: Implications for pharmacogenomics and drug response. *Int. J. Mol. Sci.* **2015**, *16*, 30483-30543.

175. Chin, D.; Means, A. R., Calmodulin: A prototypical calcium sensor. *Trends Cell Biol.* **2000**, *10*, 322-328.

176. Berridge, M. J., Calcium signalling and Alzheimer's disease. *Neurochem. Res.* **2010**, *36*, 1149-1156.

177. Fernández-Morales, J.-C.; Arranz-Tagarro, J.-A.; Calvo-Gallardo, E.; Maroto, M.; Padín, J.-F.; García, A. G., Stabilizers of neuronal and mitochondrial calcium cycling as a strategy for developing a medicine for Alzheimer's disease. *ACS Chem. Neurosci.* **2012**, *3*, 873-883.

178. Tinari, N.; Kuwabara, I.; Huflejt, M. E.; Shen, P. F.; Iacobelli, S.; Liu, F. T., Glycoprotein 90K/MAC-2BP interacts with galectin-1 and mediates galectin-1-induced cell aggregation. *Int. J. Cancer* **2001**, *91*, 167-172.

179. Calafate, S.; Flavin, W.; Verstreken, P.; Moechars, D., Loss of Bin1 promotes the propagation of tau pathology. *Cell Rep.* **2016**, *17*, 931-940.

180. Kim, H. J.; Kim, N. C.; Wang, Y.-D.; Scarborough, E. A.; Moore, J.; Diaz, Z.; MacLea, K. S.; Freibaum, B.; Li, S.; Molliex, A.; Kanagaraj, A. P.; Carter, R.; Boylan, K. B.; Wojtas, A. M.; Rademakers, R.; Pinkus, J. L.; Greenberg, S. A.; Trojanowski, J. Q.; Traynor, B. J.; Smith, B. N.; Topp, S.; Gkazi, A.-S.; Miller, J.; Shaw, C. E.; Kottlors, M.; Kirschner, J.; Pestronk, A.; Li, Y. R.; Ford, A. F.; Gitler, A. D.; Benatar, M.; King, O. D.; Kimonis, V. E.; Ross, E. D.; Weihl, C. C.; Shorter, J.; Taylor, J. P., Mutations in prion-like domains in hnRNPA2B1 and hnRNPA1 cause multisystem proteinopathy and ALS. *Nature* **2013**, *495*, 467-473.

181. Donev, R.; Newall, A.; Thome, J.; Sheer, D., A role for SC35 and hnRNPA1 in the determination of amyloid precursor protein isoforms. *Mol. Psychiatry* **2007**, *12*, 681-690.

182. Berson, A.; Barbash, S.; Shaltiel, G.; Goll, Y.; Hanin, G.; Greenberg, D. S.; Ketzef, M.; Becker, A. J.; Friedman, A.; Soreq, H., Cholinergic-associated loss of hnRNP-A/B in Alzheimer's disease impairs cortical splicing and cognitive function in mice. *EMBO Mol. Med.* **2012**, *4*, 730-742.

183. Conforti, F.; Rigano, D.; Menichini, F.; Loizzo, M. R.; Senatore, F., Protection against neurodegenerative diseases of Iris pseudopumila extracts and their constituents. *Fitoterapia* **2009**, *80*, 62-67.

184. Choi, J. S.; Islam, M. N.; Ali, M. Y.; Kim, Y. M.; Park, H. J.; Sohn, H. S.; Jung, H. A., The effects of C-glycosylation of luteolin on its antioxidant, anti-Alzheimer's disease, anti-diabetic, and anti-inflammatory activities. *Arch. Pharm. Res.* **2014**, *37*, 1354-1363.

185. Lim, J.; Park, H.-S.; Choi, J.-K.; Lee, I.-S.; Choi, H., Isoorientin induces Nrf2 pathway-driven antioxidant response through phosphatidylinositol 3-kinase signaling. *Arch. Pharm. Res.* **2007**, *30*, 1590-1598.

186. Yuan, L.; Wei, S.; Wang, J.; Liu, X., Isoorientin induces apoptosis and autophagy simultaneously by reactive oxygen species (ROS)-related p53, PI3K/Akt, JNK, and p38 signaling pathways in HepG2 cancer cells. *J. Agric. Food Chem.* **2014**, *62*, 5390-5400.

187. Yuan, L.; Wang, J.; Wu, W.; Liu, Q.; Liu, X., Effect of isoorientin on intracellular antioxidant defence mechanisms in hepatoma and liver cell lines. *Biomed. Pharmacother.* **2016**, *81*, 356-362.

188. Lin, X.; Wei, J.; Chen, Y.; He, P.; Lin, J.; Tan, S.; Nie, J.; Lu, S.; He, M.; Lu, Z.; Huang, Q., Isoorientin from Gypsophila elegans induces apoptosis in liver cancer cells via mitochondrial-mediated pathway. *J. Ethnopharmacol.* **2016**, *187*, 187-194.

189. Ye, T.; Su, J.; Huang, C.; Yu, D.; Dai, S.; Huang, X.; Chen, B.; Zhou, M., Isoorientin induces apoptosis, decreases invasiveness, and downregulates VEGF secretion by activating AMPK signaling in pancreatic cancer cells. *Onco Targets Ther.* **2016**, *9*, 7481-7492.

190. Czemplik, M.; Mierziak, J.; Szopa, J.; Kulma, A., Flavonoid C-glucosides derived from Flax Straw extracts reduce human breast cancer cell growth in vitro and induce apoptosis. *Front. Pharmacol.* **2016**, *7*, 282.

191. Lee, W.; Ku, S.-K.; Bae, J.-S., Vascular barrier protective effects of orientin and isoorientin in LPS-induced inflammation in vitro and in vivo. *Vascul. Pharmacol.* **2014**, *62*, 3-14.

192. Wedler, J.; Daubitz, T.; Schlotterbeck, G.; Butterweck, V., In vitro anti-inflammatory and wound-healing potential of a Phyllostachys edulis leaf extract – identification of isoorientin as an active compound. *Planta Med.* **2014**, *80*, 1678-1684.

193. Luan, G.; Wang, Y.; Wang, Z.; Zhou, W.; Hu, N.; Li, G.; Wang, H., Flavonoid glycosides from Fenugreek seeds regulate glycolipid metabolism by improving mitochondrial function in 3T3-L1 adipocytes in vitro. *J. Agric. Food Chem.* **2018**, *66*, 3169-3178.

194. Alonso-Castro, A. J.; Zapata-Bustos, R.; Gómez-Espinoza, G.; Salazar-Olivo, L. A., Isoorientin reverts TNF-α-induced insulin resistance in adipocytes activating the insulin signaling pathway. *Endocrinology* **2012**, *153*, 5222-5230.

195. Higa, J. K.; Liang, Z.; Williams, P. G.; Panee, J., Phyllostachys edulis compounds inhibit palmitic acid-induced monocyte chemoattractant protein 1 (MCP-1) production. *PLoS ONE* **2012**, *7*, e45082.

196. Liang, Z.; Sulzmaier, F. J.; Yoshida, W. Y.; Kelly, M.; Ramos, J. W.; Williams, P. G., Neopetrocyclamines A and B, polycyclic diamine alkaloids from the sponge Neopetrosia cf exigua. *J. Nat. Prod.* **2015**, *78*, 543-547.

197. Johnson, J. L.; Rupasinghe, S. G.; Stefani, F.; Schuler, M. A.; Gonzalez de Mejia, E., Citrus flavonoids luteolin, apigenin, and quercetin inhibit glycogen synthase kinase-3β enzymatic activity by lowering the interaction energy within the binding cavity. *J. Med. Food* **2011**, *14*, 325-333.

198. Hamann, M.; Alonso, D.; Martín-Aparicio, E.; Fuertes, A.; Pérez-Puerto, M. J.; Castro, A.; Morales, S.; Navarro, M. L.; del Monte-Millán, M.; Medina, M.; Pennaka, H.; Balaiah, A.; Peng, J.; Cook, J.; Wahyuono, S.; Martínez, A., Glycogen synthase kinase-3 (GSK-3) inhibitory activity and structure–activity relationship (SAR) studies of the manzamine alkaloids. Potential for Alzheimer's disease. *J. Nat. Prod.* **2007**, *70*, 1397-1405.